Dissertation
submitted to the
Combined Faculties for the Natural Sciences and for Mathematics
of the Ruperto-Carola University of Heidelberg, Germany
for the degree of
Doctor of Natural Sciences

Put forward by:

Diplom-Physiker	Markus Schmalzl
born in	Neumarkt i.d.OPf

Oral Examination: Feb 2, 2011

The Earliest Stages

of

Isolated Low-Mass Star Formation

Referees	Prof. Dr.	Thomas Henning
	PD Dr.	Henrik Beuther

Mahalo

Die frühesten Phasen der Entstehung von Sternen niedriger Masse

Ein Schlüssel zum Verständnis des Sternentstehungsprozesses liegt in der Kenntnis der genauen Anfangsbedingungen des protostellaren Kollaps. Diese Doktorarbeit konzentriert sich dabei gezielt auf Sterne mit niedriger Masse, die in Isolation entstehen, und deckt dabei drei räumliche Größenordnungen ab: Angefangen von der Analyse eines Filaments mit einer Länge von mehreren Parsec, bis hin zur Untersuchung von Strukturen von der Größe von nur einigen hundert AE in einem isolierten, prästellaren Kern.

Der erste Teil der Doktorarbeit befasst sich mit der Studie des Filaments L 1495, wo mit Hilfe einer NIR Extinktionskarte die fragmentartige Substruktur aufgelöst wird. Einige Bereiche des Filaments befinden sich noch in der Phase der Fragmentation, wohingegen in anderen Bereichen schon dichte Kerne, die üblicherweise durch etwa eine Jeans-Länge voneinander getrennt sind, aus dem Filament auskondensiert sind. Eine Analyse zeigt, dass diese Kerne dicht genug sind, um zu kollabieren und Sterne zu bilden.

Im zweiten Teil dieser Arbeit, wende ich mich gezielt dem isolierten Globul CB 17 zu. Interessanterweise beherbergt es neben einem Klasse I Protostern noch einen prästellaren Kern, der sich in nur etwa 5000 AE befindet. Fern-infrarot und (sub)mm Beobachtungen der Staubemission erlauben Rückschlüsse auf die Dichte- und Temperaturestruktur, sowie die Staubeigenschaften. In hochauflösenden Interferometer-Aufnahmen zeigt sich eine komplexe Geschwindigkeitsstruktur des prästellaren Kerns, die wahrscheinlich durch Wechselwirkung mit dem Protostern zustande kommt.

The Earliest Stages of Isolated Low-Mass Star Formation

The knowledge of the initial conditions of low-mass star formation is a key to understand the process of protostellar collapse and protostar formation. This thesis focuses on the earliest stages of isolated low-mass star formation and covers spatial scales which spread over three orders of magnitude. It includes the study of a filament with a length of a few parsecs, down to the in-depth analysis of an isolated prestellar core, where structures of the order of a few hundred AU are resolved.

In the first part, a NIR extinction map of the filament L 1495 reveals its small scale, highly fragmented structure, and a high star-forming potential in all its parts. In some regions, the initial filament collapse and fragmentation is still taking place and star formation is yet to occur, whereas in other parts, I identify a population of dense cores with separations of the order of the locals Jeans length, which are likely to collapse and form stars.

The second part of the thesis focuses on the isolated core CB 17, which hosts two sources at very different evolutionary stages (Class I vs. prestellar core) at a projected distance of only 5500 AU. With the aid of FIR and (sub)mm observations of the dust emission, I determine its density and temperature structure and draw conclusions about the dust properties. Interferometric observations at high angular resolution reveal a complex velocity structure in the prestellar core, which might be result of interaction with the protostar.

Acknowledgements

This thesis, although my personal work, would not have been possible with the aid and support of countless people.

First of all, I would like to thank Thomas Henning for giving me the opportunity to write my PhD thesis at such a renowned institution as the MPIA. I appreciate the scientific and financial support I have received during this time.

I would like to thank my thesis committee, namely Ralf Klessen, Werner Aeschbach-Hertig, and my thesis referees Thomas Henning and Henrik Beuther.

I also would like to thank my supervisor Ralf Launhardt for his excellent supervision, for his support in many respects, for his guidance, and for the conversations about science – and beyond.

I am also indebted to my co-workers, in particular Jouni Kainulainen, Tyler Bourke and Ralf Launhardt, João Alves, Alyssa Goodman, Thomas Henning, Sascha Quanz, Jaime Pineda, Carlos Roman-Zuniga, Amy Stutz, and many others here at MPIA.

I also would like to thank Tyler Bourke for his support, his guidance, and for giving me the opportunity to spend time at some of the best places to study and do astronomy.

Vielen herzlichen Dank auch an Frank Witzel und Ina Beckmann, mit denen ich stets über Gott und die Welt quatschen konnte, was mir eine willkommene Abwechslung zur Wissenschaft war. Dies gilt auch uneingeschränkt für die MPIA Studenten-Kaffeerunde.

A big thanks also to all the flatmates I had during the course of my thesis in Schlierbach, Cambridge, and Handschuhsheim. Furthermore I would like to thank all my friends, which accompany me in my life, and show me many different aspects of life beyond science and astronomy.

Zuletzt möchte ich mich bei meiner zukünftigen Frau Eva bedanken, die ich getrost in jeglicher Hinsicht als meine bessere Hälfte bezeichnen kann. Gleichermaßen möchte ich mich bei meinen Eltern, Großeltern und Geschwistern bedanken, die mich nicht nur während des Studiums und der Doktorarbeit, sondern schon immer in meinem Leben in jeglicher nur erdenklichen Art unterstützt haben.

Contents

1. Low-Mass Star Formation in a Nutshell **1**
1.1. Stars Form in Filaments 2
1.2. Stars Form in Dense Cores 4
1.3. The Role of Dust 5

2. The Tools to Study Star Formation **9**
2.1. A Few Words on Light 9
2.2. A Radiative Transfer 101 10
2.3. Observational Techniques 14
  2.3.1. Near Infrared 14
  2.3.2. Radio Astronomy – Single Dish Antenna 16
  2.3.3. Radio Astronomy – Interferometry 23
2.4. Cosmic Dust 29
  2.4.1. FIR/Millimetre Wavelengths 30
  2.4.2. Optical/NIR Wavelengths 31
2.5. Molecules in Space 35
  2.5.1. Molecular Structure 36
  2.5.2. Level Population 37
  2.5.3. Molecular Line Emission 41
  2.5.4. Column Density Derivation 42

3. Star Formation in the Taurus Filament L 1495: From Dense Cores to Stars **45**
3.1. Introduction 46
3.2. Observations and Data Reduction 47
3.3. Results 49
  3.3.1. Dust Extinction in the Taurus Filament 49
  3.3.2. The Dense Core Population 52
  3.3.3. Reddening Law 58
3.4. Discussion 58
  3.4.1. Star Formation in the Filament 58
  3.4.2. The Nature of the Dense Cores 60
3.5. Summary 62

4. CB 17 – A Herschel View **65**
4.1. Introduction 66
4.2. Observations and Data Reduction 67
  4.2.1. Herschel Space Observatory 67
  4.2.2. (Sub)mm Maps 68

4.2.3. NIR observations . . . 68
4.3. Results . . . 69
4.3.1. NIR Extinction Map . . . 69
4.3.2. Dust Emission Maps . . . 69
4.4. Discussion . . . 77
4.4.1. Modified Blackbody vs. Raytracing . . . 77
4.4.2. Temperature and Density Distribution . . . 81
4.4.3. Dust Properties . . . 83
4.5. Summary and Outlook . . . 84

5. CB 17 – Molecular Abundances and Freeze-out 87
5.1. Introduction . . . 88
5.2. Observations and Data Reduction . . . 88
5.2.1. IRAM-30m . . . 88
5.3. Results . . . 89
5.3.1. Molecular Column Density . . . 89
5.3.2. Velocity Structure . . . 92
5.4. Discussion . . . 95
5.4.1. Molecular Abundances . . . 95
5.4.2. Velocity Structure . . . 99
5.5. Summary and Outlook . . . 101

6. CB 17 – Zooming into the Dense Core 103
6.1. Introduction . . . 104
6.2. Observations and Data Reduction . . . 104
6.2.1. Formylium (HCO^+) . . . 104
6.2.2. Dyazenulium (N_2H^+) . . . 105
6.2.3. Carbon Monosulphide (CS) . . . 105
6.3. Results . . . 106
6.3.1. Formylium . . . 106
6.3.2. Diazenulium . . . 108
6.4. Discussion . . . 110
6.4.1. Envelope Structure . . . 110
6.4.2. Structure of the Dense Core . . . 113
6.4.3. CB 17-SMM1 – A First Core? . . . 117
6.5. Summary . . . 120

A. Appendices 121
A.1. Molecular Line Parameters . . . 122
A.2. IRAM-30m Telescope Efficiencies . . . 123

Bibliography 125

1

Low-Mass Star Formation in a Nutshell

> We choose to go to the moon in this decade and do the other things, not because they are easy, but because they are hard, because that goal will serve to organize and measure the best of our energies and skills, because that challenge is one that we are willing to accept, one we are unwilling to postpone, [. . .].
>
> — *John F. Kennedy*

In contrast to low-mass star formation, which is well understood, many questions in high-mass star formation still remain unanswered. Many publications in the field of high-mass star formation begin with sentences similar to this one. Although the authors simply attempt to emphasise the fact that high-mass star formation does show an increased level of complexity, some certainly do underestimate the amount of open questions which are still to be answered in the field of low-mass star formation.

Although most stars form in clusters (Lada and Lada, 2003), which are embedded in Giant Molecular Clouds, these are certainly not the best places to study the detailed physical processes that accompany the protostellar collapse of molecular cloud cores. Stellar feedback, tidal interaction, and competitive accretion – to name a few effects – will influence the evolution of the molecular cloud, and, thus, star formation can be most comprehensively viewed in the global context of the entire star-forming region. In this context, the net effect of the myriad of forces acting to form stars and disrupt their nascent molecular clouds can become hard to disentangle. The problem becomes more tractable in simpler, smaller regions of isolated star formation, although one has to keep in mind that star formation in clustered environments may be governed by different physical processes than those that dominate in isolated regions.

The goal of this thesis is to study the initial conditions of low-mass star formation in isolation by observations at near and far infrared, at sub-mm and mm wavelengths, with ground based and space-borne observatories. The spatial scales that are covered range from a few parsecs in the study of the filamentary structure of the Taurus Molecular Cloud, down to a few hundred AU in search for a First Hydrostatic Core in CB 17 (Figure 1.1).

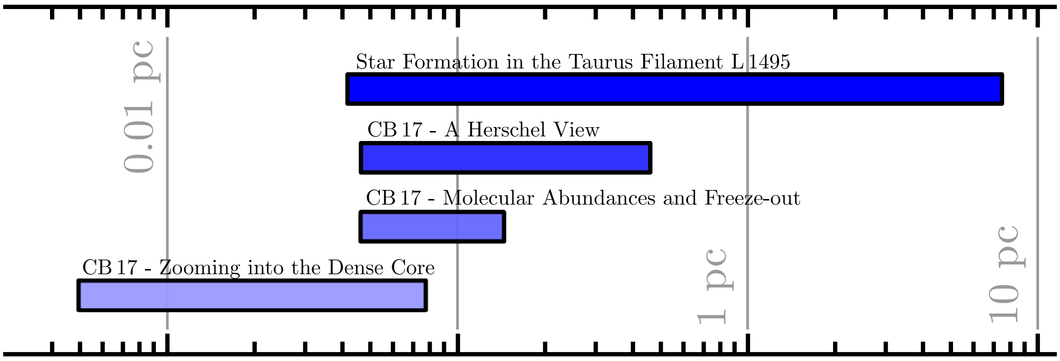

Figure 1.1.: The spatial scales, which are covered in the different chapters of this thesis. In total, they span over three orders of magnitude.

In this chapter I will give a brief introduction to the general field of star-formation, with an emphasis on subjects particularly relevant to this thesis. Chapter 2 will focus on the tools which are necessary to study star formation. This includes both the introduction of physics (e.g., radiative transfer, molecular line emission) and observational tools (e.g., telescope types, data reduction). In Chapter 3 follows a study of the dense core population in the Taurus Filament L 1495, which was obtained with the aid of a near infrared extinction map. Chapters 4-6 focus on the isolated globule CB 17, which was observed at various wavelengths and at various spatial resolutions to characterise its structure.

1.1. Stars Form in Filaments

“Hier ist wahrhaftig ein Loch im Himmel[†]!” This quote is attributed to Sir William Herschel, as he observed an apparently starless spot towards the constellation Scorpius (Houghton, 1942). Large scale photographic surveys at the beginning of the 20th century (e.g., Barnard et al., 1927) revealed a plethora of such dark spots and lanes all over the sky, and provided evidence that these are indeed not empty patches on the sky, but rather caused by dense foreground material, which obscures the light of background stars (Figure 1.2). The connection of these dark clouds and star formation was only made by Bok and Reilly (1947). Later, optical surveys like the Palomar Observatory Sky Survey (POSS) and the ESO/SERC Southern Sky Survey proved to be an excellent tool to find these dark clouds in the sky (e.g., Lynds, 1962; Hartley et al., 1986).

Almost two hundred years after his death, Sir William Herschels impact on the area of star formation is larger than ever. Observations of the *Herschel Space Observatory* (Pilbratt et al., 2010), which was named after him in recognition of his discovery of infrared light (Herschel, 1800), reveal a plethora of filamentary structures in various low-mass star-forming regions (e.g., André et al., 2010, and references therein). Although astronomers since long know of their existence, the question of how these filaments form is still under debate. However, filament formation poses not the only big question, but also the origin of the observed low star formation efficiency is not understood. In the simple picture of a

---

[†] English: “Here is truly a hole in the heavens!”

Figure 1.2.: *Nebulous Region in Taurus* (Barnard et al., 1927, Copyright: Carnegie Institution of Washington, Carnegie Observatories, Pasadena California). The dark patch in the centre right with the dark lane emanating towards the south east is L 1495 (Lynds, 1962), which will be investigated in more detail in Chapter 3.

gravity-only dominated regime, one would expect a considerably higher star formation rate. The two basic hypotheses to explain these problems are the *quasi-static* the *dynamic* cloud evolution.

The first mode explains lifetimes of the order of 10 Myr by seeing clouds as quasi-static objects close to equilibrium (Shu, 1977). Support against gravitational instability is provided by magnetic fields. Magnetically subcritical clouds, i.e., the magnetic fields are strong enough to resist the gravitational pull, collapse can only happen via the so-called “ambipolar diffusion”. This term describes the slow drift of neutral particles, which are not frozen to the magnetic field. Star formation can now occur, when enough mass is accumulated to make the cloud supercritical. However, this process is efficient, but very slow.

A second, opposing mode of star formation is the so called dynamic mode, which is also known as *gravoturbulent fragmentation* (Klessen et al., 2000; Heitsch et al., 2001; Klessen et al., 2004). In this scenario, molecular clouds form from convergent flows without ever reaching an equilibrium state. In these flows, self-gravity can become the dominant force when the Jeans critical mass is reached in local density enhancements, which then leads to a quick formation of stars. However, if gravity is not powerful enough, these local density enhancements are dispersed by the turbulence, and makes the star formation inefficient.

Recently, Myers (2009) pointed out that all nearby star-forming regions exhibit a so-called *hub-filament structure*, which consists of a central hub with low aspect ratio and high column density, from which several filaments with high aspect ratios and lower column densities emanate. It was pointed out that many of these filaments exhibit very regular spacings, which other models do not explain, and introduces the idea of self-gravitating layers being responsible for the observed phenomenology, but not without mentioning that this model also possesses caveats, and should rather be seen as a starting point for further investigation. One of the hub-filament structures in his sample is the filament L 1495 (Lynds, 1962), which is part of the Taurus Molecular Cloud (Figure 1.2) and will be investigated in more detail in Chapter 3.

Filamentary structure in general can be explained as a fractal (e.g., Stutzki et al., 1998). The self-similarity is likely to be caused in a spatial range, where turbulence dominates. Column density distributions of molecular clouds very often exhibit log-normal character, which is often believed to be a result of supersonic turbulent motions. However, only recently Tassis et al. (2010) reported, that supersonic turbulence is not the only agent, which can cause log-normal distributions. Kainulainen et al. (2009) observed a break from this log-normal behaviour in regions with star-forming activity, and attributed the column density excess towards high densities to the influence of self-gravity.

A different approach to characterise a filament is hierarchical fragmentation. The largest scales, i.e, the scale of the complete star-forming region is called *cloud*. Smaller regions inside this cloud (e.g., filaments) are called *clumps*, and even smaller, gravitationally bound entities are denoted *cores* (Table 1.1). The approach to classify molecular clouds in this hierarchical scheme, and the previous approach of assuming a scale-free fractal is only a contradiction at first sight. Clump/core mass spectra exhibit a power-law behaviour, which essentially represents the scale-free character of the fractal analysis. Motte et al. (1998) observed a clump mass spectrum in the star-forming region ρOph, which can be fitted with a power-law, and a slope of $\Gamma = 1.5$. Recalling, that the stellar initial mass (IMF) is best described by a slope of $\Gamma = 1.35$ (e.g., Salpeter, 1955), these authors therefore interpreted these cores to be the direct precursors of stars. Alves et al. (2007) and Rathborne et al. (2009) report to have found a break-point in the dense core mass function, which they directly relate to a similar break-point in the IMF (Kroupa, 2002). They establish a direct relation between the mass functions by introducing an efficiency factor of $\epsilon \sim 0.3$. Recent observations with Herschel exhibit similar shapes for the dense core mass functions, therefore giving this theory some more weight (André et al., 2010).

Table 1.1.: Hierarchical structure of clouds, clumps, and cores (Bergin and Tafalla, 2007)

	Clouds	**Clumps**	**Cores**
Mass [$M_\odot$]	$10^3 - 10^4$	50 – 500	0.5 – 5
Size [pc]	2 – 15	0.3 – 3	0.03 – 0.2
Mean density [cm^{-3}]	50 – 500	$10^3 - 10^4$	$10^4 - 10^5$
Gas temperature [K]	~ 10	10 – 20	8 – 12

1.2. Stars Form in Dense Cores

In the domain of the cores with densities of the order of $n_{\mathrm{H}_2} \sim 10^5\,\mathrm{cm}^{-3}$, self-gravity dominates. Collapse starts, when at temperatures of the order of 10 K thermal energy (in conjunction with magnetic fields and/or turbulence) cannot balance the gravitational pull. As long as the envelope is optically thin, the released gravitational energy is efficiently radiated away, and the core will develop a power-law density profile $\rho \propto r^{-2}$, which flattens towards the centre. The collapse ends with the formation of an opaque, hydrostatic core with a temperature of a few 100 K a size of a few AU, which mainly consists of hydrogen molecules (Larson, 1969; Boss and Yorke, 1995). Due to its short lifetime, its deeply embedded nature, and its small size it was so far not possible to confirm the tentative detections (Enoch et al., 2010; Chen et al., 2010) of such a *first hydrostatic core* (FHSC). However, with the capability of contemporary (Herschel) and upcoming (ALMA) observing facilities, the confirmed detection of a FHSC seems to be only a question of time. Theoretical simulations also already predict the launch of a low-velocity outflow at this early stage (Machida et al., 2008). Upon further heating, the FHSC loses its hydrostatic support due to thermal dispersion of hydrogen molecules, which then leads to a second collapse. This is then stopped by the formation of the protostar. All this happens within the order of a few so-called *free-fall times* (Stahler and Palla, 2005)

$$t_{\mathrm{ff}} = \sqrt{\frac{3\pi}{32\,G\,\rho}}, \tag{1.1}$$

where G is the gravitational constant, and conforms to the time, a pressure-free sphere of uniform density ρ would need to collapse to zero radius. For a molecular cloud core with $n_{\mathrm{H}_2} = 10^5\,\mathrm{cm}^{-3}$ it is therefore of the order of $t_{\mathrm{ff}} \sim 10^5$ yr.

However, the initial conditions of this core collapse are still only poorly understood. A detailed study of *Dense Cores in Dark Clouds* was initiated by Myers et al. (1983), who identified 90 small, visually opaque regions from the Palomar Sky Atlas prints. In subsequent papers, these were systematically analysed for, e.g., velocity structure and shapes (e.g., Myers, 1983; Myers et al., 1991; Fuller and Myers, 1992; Goodman et al., 1993), and chemical composition (e.g., Myers et al., 1983; Myers and Benson, 1983; Benson and Myers, 1983; Benson et al., 1998; Caselli et al., 2002). They find evidence for complex motions (i.e., infall, rotation, outflow) around pre- and protostellar cores, and a rich chemistry, which strongly differs from the interstellar medium. Some of these cores were part of a larger star-forming complex (e.g., Taurus), but some could be found with no immediate connection to a star-forming regions. These cores are the ideal testbed to understand the physics behind the star formation.

1.3. The Role of Dust

Although molecular clouds consist of 99% gas, the 1% of dust is actually found to play a key role in the formation of stars. Interstellar dust grains, which are mainly formed in the envelopes of evolved AGB stars (e.g., Woitke et al., 2000), have typical sizes of $a = 0.005\ldots1\,\mu$m and consists mainly of silicates and graphite (MRN, Mathis et al., 1977).

Dust grains are responsible for both the emission at FIR and (sub)mm wavelengths, and the dark appearance of molecular clouds at optical wavelength. The key to quantify the dust properties is the so-called *dust opacity* κ_ν, which is the absorption cross section per dust mass, and has contributions by both scattering and absorption of electromagnetic waves. Opacity curves are calculated from assumed chemical composition and optical material properties and size distributions, and constrained by lab measurements as well as

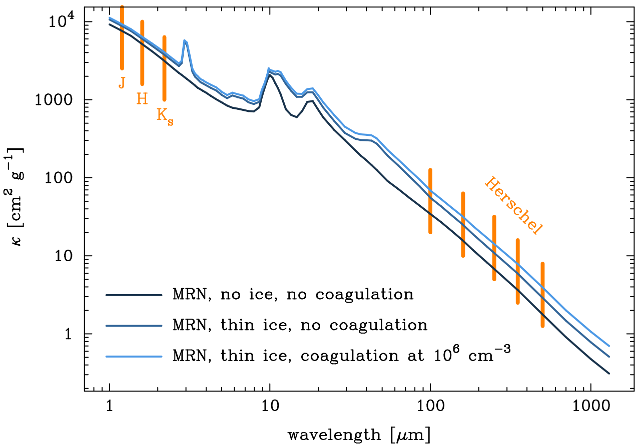

Figure 1.3.: Dust opacity model of Ossenkopf and Henning (1994) with different dust composition. The initial grain size distribution was taken from MRN. The wavelengths of *Herschel* observations, and near infrared J, H, K_s filters, which were used in this work, are indicated.

observations of interstellar dust. Figure 1.3 shows some dust opacity curves for protostellar cores (Ossenkopf and Henning, 1994), where dust can be coagulated and/or coated with ice mantles. Knowing the dust temperature then allows to draw conclusions about the dust column density, and under the assumption of a constant abundance ratio between gas and dust, also about the gas.

Due to the relatively higher dust opacity at shorter wavelengths, dust grains efficiently shield interiors of molecular clouds from the UV radiation of the interstellar radiation field, and prohibit heating of the dense core interiors. Additional contribution to the cooling of molecular cloud cores is provided by collisions of molecules with dust grains, which heat up and re-radiate the energy, which was gained from the collision, as thermal emission. These processes cause a net cooling, that lead inevitably to the core collapse due to insufficient thermal support, and a core becomes supercritical.

Furthermore, the only efficient way to form the main constituent in molecular clouds, namely molecular H_2, is that the dust grain surface catalyses this reaction (Gould and Salpeter, 1963). The gas phase reaction

$$\mathrm{H} + \mathrm{H} \longrightarrow \mathrm{H}_2 + \gamma \tag{1.2}$$

poses a very small recombination cross-section, as the emitted photon γ must result from a forbidden transition. But not only molecular hydrogen, but also many other molecules form on dust grains, and form the field of grain-surface chemistry. In the dense cores with low temperatures and lack of UV radiation, certain molecular species cannot desorb from the grain surface, which leads to a selective freeze-out. This effect is particularly strong in the case of carbonaceous molecules. Nitrogen-bearing molecules, e.g., N_2H^+, which are destroyed by CO can therefore exist in this environment (e.g., Bergin et al., 2001). However, Öberg et al. (2005) found that N_2, which is the parent molecule of N_2H^+ should freeze-out at the same temperature as CO, which then still leaves open the question of why nitrogen-bearing molecules are so enhanced in the dense core centres. Effects like this have to be included in sophisticated chemical networks, which are constantly updated (e.g., the UMIST database of astrochemistry contains several thousand possible reactions among 420 species, Woodall et al. 2007). Astronomers use these to model chemical abundances at various stages of the early phases of stellar evolution (e.g., Wiebe et al., 2003; Semenov et al., 2004), including gas-phase and grain-surface reactions.

Emphasising the importance of dust for the formation of stars, obviously gives rise to the question of how stars were formed in the early universe. In the absence of dust (and also other metals, which provide a non-negligible contribution to the cooling in present star formation), cooling is mostly provided by an inefficient, ro-vibrational transition of small traces of H_2, which provides cooling only down to temperatures of $T \sim 200\,\mathrm{K}$ (Tan and McKee, 2008). This is by an order of magnitude higher, compared to temperatures in galactic star formation today, and therefore leads to completely different processes which are involved. However, I leave the study of these primordial, and certainly interesting objects for another PhD student, and will focus in this work on star formation in the current-day universe and in solar neighbourhood.

2

The Tools to Study Star Formation

Thats one small step for a man
One giant leap for mankind.

— Neil A. Armstrong, Apollo 11, 1st man on the Moon

OUTLINE:

This chapter focuses not so much on the science, but more on the physics behind the science. This is done in a rather extensive way, to serve as a sort of reference book. Most concepts are, if not stated otherwise, taken from Rohlfs and Wilson (2004), Stahler and Palla (2005), and Carroll and Ostlie (2006). In §2.1 and §2.2 I will give a quick introduction into light and the propagation of light through non-empty medium. How *astronomers observe the light coming from outer space is then described in §2.3, before I will focus on the physics, and explain* why *it is possible to observe dust (§2.4) and molecules (§2.5).*

2.1. A Few Words on Light

Until man will be able to directly travel to other star-forming regions, the only way to obtain information is incorporated into the electromagnetic information we receive from them. Although astronomers do also enjoy a beautiful night sky, they have since the very early days also tried to understand the physics behind it. It is known, that the Greek astronomer and philosopher Hipparchus already compiled one of the first star catalogues in the Western world by separating stars into six groups according to their apparent brightness. Of course,

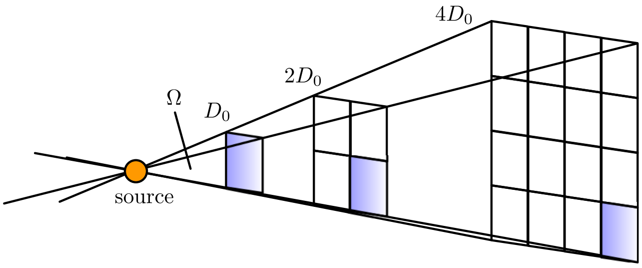

Figure 2.1.: Illustration of the *inverse square law*. With increasing distance D, the energy, which is emitted into the solid angle Ω, is distributed over a larger area. Therefore, the flux density is related to the energy via $\propto D^{-2}$.

today astronomers use more sophisticated and less subjective tools than Hipparchus' eyes, and with the aid of photometric plates, CCD chips or heterodyne receivers – just to name a few – they can now objectively quantify the amount of light, which reaches us here on earth (if the photons do not end up on a dead pixel, which would be quite disappointing after travelling tens or even millions of light years).

Brightness of a source is in astronomy generally measured by *flux density* F_ν, which is defined as the energy per unit wavelength, unit area and unit time. It is more convenient to express the brightness on a magnitude scale, which is defined as

$$m_\nu = -2.5 \log\left(\frac{F_\nu}{F_{\nu,0}}\right), \tag{2.1}$$

where $F_{\nu,0}$ is a conveniently defined zero-point, which is in general the flux density of the star Vega[†]. The flux depends on the distance of the source from the observer via an inverse square law (Figure 2.1). Therefore, stars appear brighter or dimmer at smaller or larger distance, and Equation (2.1) defines the so-called *apparent magnitude*. A distance-independent scale is the so-called *absolute magnitude*, which conforms to the apparent magnitude of a source at a distance of 10 pc, and is thus given by

$$M_\nu = -2.5 \log\left(\frac{F_\nu(10\,\mathrm{pc})}{F_0}\right). \tag{2.2}$$

The connection between the apparent and absolute magnitudes is given by the distance modulus μ, which is the same for all frequencies, and defined as

$$\mu = m_\nu - M_\nu. \tag{2.3}$$

A colour in the astronomical sense is defined as the difference of magnitudes at two different wavelengths. Its big advantage is, that it is independent of distance, as the distance modulus μ cancels out, and we obtain

$$m_{\nu_1} - m_{\nu_2} = M_{\nu_1} - M_{\nu_2} \tag{2.4}$$

2.2. A Radiative Transfer 101

The previous section only dealt with the light that reaches earth, and how astronomers defined their magnitude scale. This section focuses more on *how* the light travels through

---

[†] Consequently, by definition Vega has a magnitude $m_\nu = 0$ mag at all wavelengths

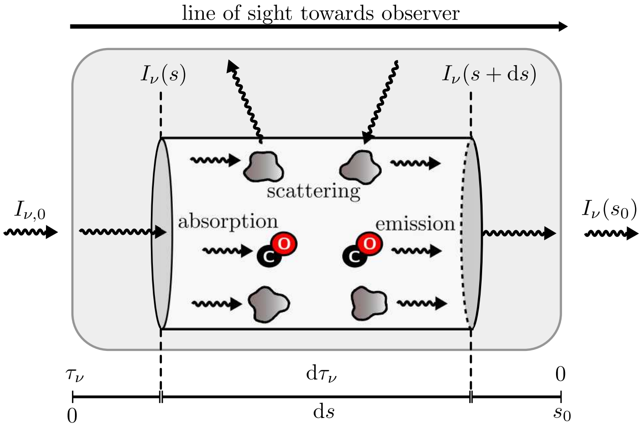

Figure 2.2.: Light passing through a slab of thickness ds inside a molecular cloud of size s_0 can be altered by various processes. The incident brightness I_ν changes due to absorption, emission and scattering caused by dust grains and/or molecules. It should be noted that the directions of the optical thickness τ and linear distance s are opposing each other.

space, before it reaches earth. It is convenient to express the radiative transfer in terms of *specific intensity*[†] I_ν, which expresses the amount of energy per unit frequency passing through a unit area per unit time from a region of unit solid angle on the sky, and is therefore independent of distance. Simply speaking, the independence of the specific intensity on the distance is reflected by the fact, that the energy within the solid angle remains constant (Figure 2.1).

The connection between the flux density and specific intensity is given by integration over the source size

$$F_\nu = \int_{\Omega_\mathrm{s}} I_\nu \, \cos\vartheta \, \mathrm{d}\Omega \tag{2.5}$$

where $\cos\vartheta$ is the cosine of the angle with respect to the normal of the area. The solid angle of a cone with apex angle θ is given by

$$\Omega = 2\pi \left[1 - \cos\left(\frac{\theta}{2}\right)\right] \tag{2.6}$$

For a circular source, this then yields in the small angle approximation the simple relation

$$\Omega_\mathrm{s} = \frac{r^2\pi}{D^2}, \tag{2.7}$$

where r and D are the radius and the distance of the source, respectively. However, in non-empty space there exist various effects, which provide attenuation or amplification of the light rays along the line of sight, and therefore also the specific intensity is not constant. Such effects are depicted in Figure 2.2, and will be discussed in more detail in the following paragraphs.

The intensity can be reduced by absorption, or by scattering of light away from the line of sight. Scattering is of considerable importance only for wavelengths $\lesssim 1\,\mu$m, and therefore will be neglected in the course of this work. The absorption is quantified by the *opacity* κ_ν, which is usually measured in units of cm^{2}g^{-1} and strongly depends on the properties of

---

[†] strictly speaking, I_ν is *spectral radiance* and not an intensity. However, it is nevertheless commonly used in astronomy.

the absorbing material. In a slab of thickness ds the opacity provides an attenuation of the specific intensity of

$$\mathrm{d}I_{\nu^-} = -\kappa_\nu \, \rho \, I_\nu \, \mathrm{d}s \tag{2.8}$$

where ρ is the mass density. It is convenient to define the parameter $\alpha_\nu \equiv \rho \, \kappa_\nu$, which can be interpreted as the inverse of the mean free path of a photon. Furthermore, one can define the *optical depth*[†] $\mathrm{d}\tau_\nu = -\alpha_\nu \, \mathrm{d}s$, which is a dimensionless parameter. Under the assumption of constant absorption coefficient κ_ν along the line of sight, the optical depth is given by

$$\begin{aligned}\tau_\nu &= \int_0^{s_0} \kappa_\nu \, \rho \, \mathrm{d}s \\ &= \kappa_\nu \, m_\mathrm{p} \int_0^{s_0} n_\mathrm{p} \, \mathrm{d}s \\ &= \kappa_\nu \, m_\mathrm{p} \, N_\mathrm{p},\end{aligned} \tag{2.9}$$

where m_p is the mass, n_p the number density, and N_p the column density of the particles, which are responsible for the absorption.

If the optical depth $\tau_\nu \ll 1$, one can say that the photon can escape the medium unscathed, whereas $\tau_\nu \gg 1$ means that it most likely gets absorbed.

Alongside absorption, there are also effects which increase the specific intensity. This can be thermal emission of dust grains, line emission of molecules, and/or scattering of light into the line of sight (which will again be neglected for my case, but can also play an important role, e.g. Pagani et al. 2010). These positive contributions are then given by

$$\mathrm{d}I_{\nu^+} = j_\nu \, \mathrm{d}s, \tag{2.10}$$

where j_ν is the so called *emissivity*.

Positive and negative contributions yield the total change of brightness $\mathrm{d}I_\nu = \mathrm{d}I_{\nu^-} + \mathrm{d}I_{\nu^+}$, which can then be rewritten into the form of the so-called *equation of radiative transfer*

$$\frac{\mathrm{d}I_\nu}{\mathrm{d}s} = -\alpha_\nu \, I_\nu + j_\nu. \tag{2.11}$$

which can be reformed in terms of optical depth to

$$\frac{\mathrm{d}I_\nu}{\mathrm{d}\tau} = I_\nu - \frac{j_\nu}{\alpha_\nu} \tag{2.12}$$

In the case of thermal equilibrium, but also already at local thermal equilibrium, emission and absorption balance each other, i.e., $\mathrm{d}I_\nu/\mathrm{d}\tau = 0$. Then the specific intensity can be derived from Equation (2.12) to be

$$\frac{j_\nu}{\alpha_\nu} = I_\nu \equiv B_\nu \tag{2.13}$$

[†] Due to convenience the direction of ds is towards the observer, whereas the optical depth dτ is defined to rise with rising distance from the observer. One has to take that into account when defining the integration boundaries.

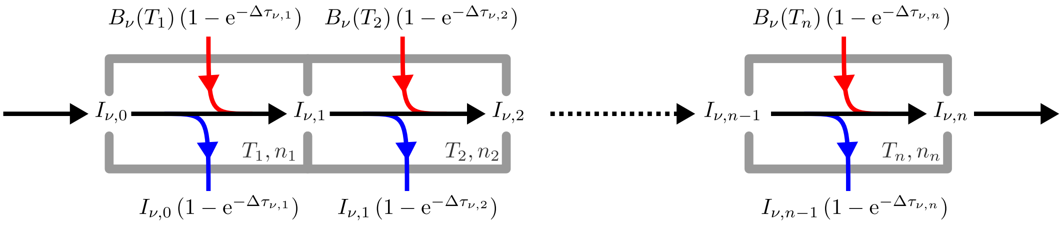

Figure 2.3.: Illustrative principle of raytracing. Under the assumption of constant conditions T_i and n_i in an arbitrarily small region i (indicated by the grey cells) one can derive the specific intensity $I_{\nu,i}$ along a ray (black arrows) by considering both positive and negative contributions. Positive contributions (blue arrows) arise from the thermal emission, which is described by the Planck law $B_\nu(T)$, negative contributions (red arrows) originate from the exponential attenuation of radiation.

where B_ν is the so-called *Planck function*. It describes the specific intensity of a blackbody in thermal equilibrium, and is defined as

$$B_\nu = \frac{2\,h\,\nu^3/c^2}{\exp\left(h\nu/k_\text{B}T\right)-1}. \tag{2.14}$$

The remarkable feature of the Planck function is that its spectrum is completely described by a single parameter only, the temperature T.

Multiplication of Equation (2.12) by $\exp(-\tau_\nu)$ and integration by parts then yields the specific intensity $I_\nu(s_0)$, which is emitted by the molecular cloud

$$I_\nu(s_0) = I_{\nu,0}\,e^{-\tau_\nu} + B_\nu\,(1-e^{-\tau_\nu}). \tag{2.15}$$

This relation only holds in case of constant conditions along the line-of-sight, which will in most cases not be true. In this case, one can approximate the intensity by applying a simple *raytracing* algorithm. The principle of this procedure is depicted in Figure 2.3. Although the conditions might not be the same throughout the whole molecular cloud, one can assume that within an arbitrarily small region i, the temperature T_i and number density n_i are constant. The molecular cloud can therefore be separated into n cells, and iterative application of Equation (2.15) for all cells along the ray, quite accurately reproduces the true specific intensity, which then eventually reaches the observer.

For astronomers, two limiting cases are of particular interest. The first one is, that all emission originates from the molecular cloud, i.e., $I_{\nu,0} = 0$. Equation (2.15) can then be approximated for two cases of optically thick and thin medium:

$$I_\nu(s_0) \sim \begin{cases} B_\nu & \tau_\nu \gg 1 \\ \tau_\nu\,B_\nu & \tau_\nu \ll 1 \end{cases} \tag{2.16}$$

Another very common case is, when a medium does not emit significantly ($B_\nu = 0$), but one rather studies the attenuation of background light

$$I_\nu(s_0) = I_{\nu,0}\,e^{-\tau_\nu}. \tag{2.17}$$

Recalling Equations (2.1) and (2.5) this furthermore means that the received flux density also gets attenuated by $e^{-\tau}$, and thus the apparent magnitude is given by

$$\begin{aligned} m_{\nu,\tau} &= -2.5\ \log\left(\frac{F_\nu\, e^{-\tau_\nu}}{F_{\nu,0}}\right) \\ &= -2.5\ \log\left(\frac{F_\nu}{F_{\nu,0}}\right) + A_\nu \\ &= m_\nu + A_\nu, \end{aligned} \tag{2.18}$$

where the *extinction* A_ν describes the attenuation due to an intervening medium, and is given by

$$\begin{aligned} A_\nu &\equiv -2.5\ \log(e^{-\tau_\nu}) \\ &\sim 1.086\,\tau_\nu \end{aligned} \tag{2.19}$$

2.3. Observational Techniques

After a first introduction into radiative transfer, the next section focuses more on *how* astronomers actually measure things. During my PhD thesis I observed at both near infrared and radio wavelengths, and therefore will quickly introduce the general principles.

2.3.1. Near Infrared

Detectors

The advent of charge-coupled devices (CCDs) and infrared detectors in the 1980s has revolutionised the way astronomers obtain their images at optical and near infrared wavelengths. Such semi-conductor based detectors are sensitive to light due to a relatively small bandgap of only a few electron volts, which allows incident photons to lift electrons from the valence into the conduction band. In the early days, the standard material for was silicon. Its bandgap of $\Delta E = 1.1\,\mathrm{eV}$ restricts the sensitivity to light to wavelengths $\lambda < 1\,\mu$m. The sensitivity at NIR wavelengths was achieved by developing other semiconductors, and nowadays the most commonly used ones are Mercury-cadmium-telluride (MgCdTe, $\Delta E \sim 0.5\,\mathrm{eV}$, $\lambda \lesssim 2.5\,\mu$m), Indium-antimonide (InSb, $\Delta E = 0.23\,\mathrm{eV}$, $\lambda < 5.4\,\mu$m) or silicon doped with arsenic (Si:As, $\Delta E \sim 0.05\,\mathrm{eV}$, $\lambda < 27\,\mu$m), but many more exist (Fassbender, 2003).

The relatively narrow bandgap of these materials does not only allow light to lift electrons into the conduction band, but also the thermal energy of the electrons is sufficient to overcome this barrier. This effect can be suppressed by cooling down the detector to temperatures of liquid nitrogen (77 K), or even below. Early detectors were semiconductor elements with only a few pixels, but today commonly used arrays offer 1k×1k or 2k×2k pixel elements.

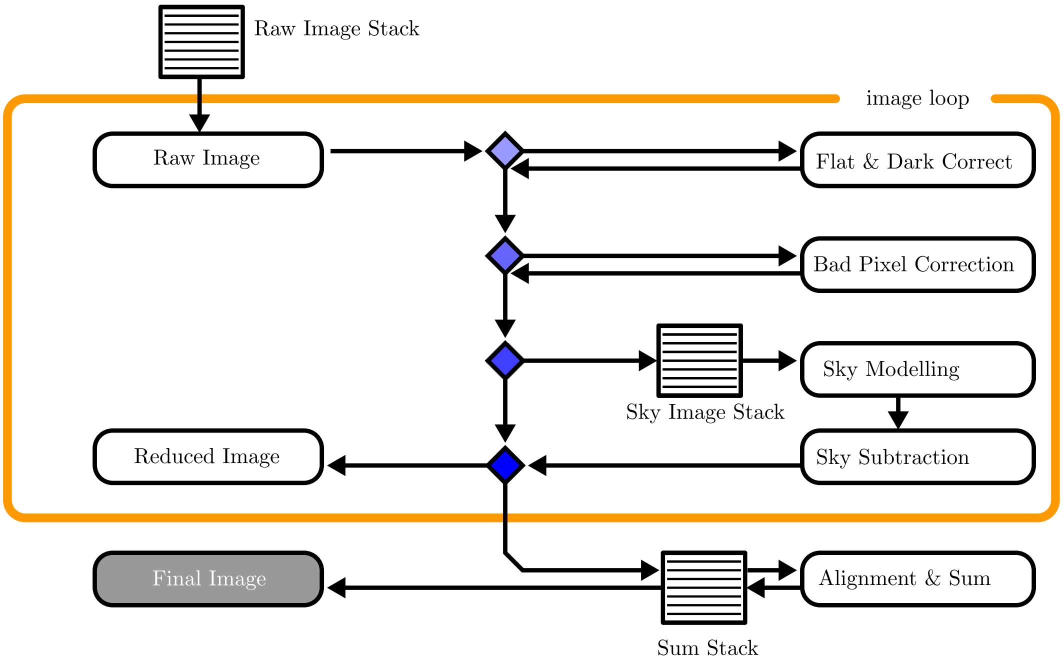

Figure 2.4.: NIR reduction scheme (based on Fassbender, 2003). See text for more descriptions.

Observations and Calibration

Observations at NIR wavelengths always consist of a set of calibration and the actual science observations. The calibrations are necessary to quantify the following things:

- **Dark Current:** Although the low temperature suppresses the release of thermal electrons into the conduction band, this effect cannot completely be avoided. A Dark Current calibration is generally a set of observations with linearly varying exposure time, which then allows to estimate the thermal signal for a scientific observation at a given exposure time. An additional effect is the so-called bias, which is the signal caused by the electronics during a read-out out of the detector.
- **Flatfield:** An infrared detector does show quantum efficiency and pixel-to-pixel sensitivity variations, i.e., the probability of detecting an incoming photon varies in dependence on the position on the chip. Flatfields are observations of a uniformly illuminated object (twilight sky, dome screen), which then gives a good estimate of the relative pixel response.
- **Bad Pixel:** Pixels, which do not show a linear relation with exposure time are known as bad pixels. Astronomers distinguish two types of bad pixels, namely the *dead pixels*, which show no signal at all, and *hot pixels*, which do show a signal, but do not exhibit the expected linear relation.

The general image reduction scheme, which is based on the Omega2000 pipeline (Fassbender, 2003), is illustrated in Figure 2.4. First, the dark current (which already includes the bias) is subtracted from the raw image, before it is normalised by the flatfield.

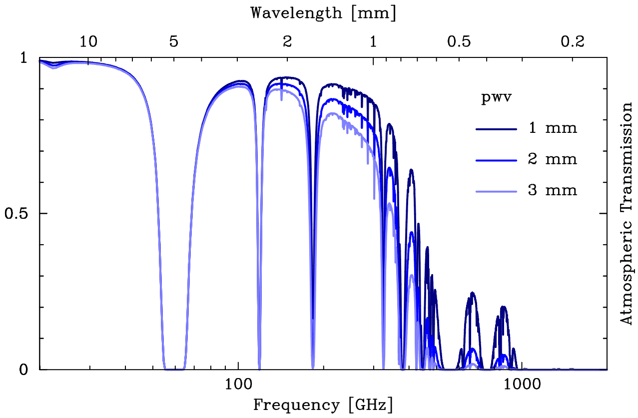

Figure 2.5.: Atmospheric transmission at mm and sub-mm wavelengths at the IRAM-30m telescope. The different curves represent the transition in dependence on the atmospheric water content (precipitable water vapour = pwv).

The next step is to remove the sky signal, which can be achieved by either observing a nearby, empty region on the sky, or by the more convenient way of using the scientific observations to get an estimate of the signal. The general observing strategy is to induce little offsets (*dithering*) between two subsequent, short exposures. The latter one avoids saturation of bright stars, whereas the first one ensures that, e.g., a star does not always end up on a dead pixel. Due to the dithering a pixel will, therefore, in most cases only receive the signal of empty sky. A median filter applied on typically 5 frames, which were taken before and after the frame in question, thus accurately recovers the sky emission, which can then be subtracted from the reduced image.

This loop is repeated for every image in the raw image stack. The reduced single images are then aligned, searched for traces of cosmic radiation (which are removed, if necessary), and summed up to yield the final image.

2.3.2. Radio Astronomy – Single Dish Antenna

Earth's atmosphere is not only transparent at optical wavelength, but it also has some more spectral regions with no or low opacity. Among these is the so called radio window. Its big advantage is that at this wavelength range many objects exhibit considerable thermal emission, plus it also shows many molecular transition lines. The atmospheric transmission at the site of the IRAM-30m telescope is shown in Figure 2.5, and one can clearly see the bands of high atmospheric transmission. The IRAM-30m telescope offers receivers, which operate in the 3, 2, 1 and 0.9 mm atmospheric windows. Operations at shorter wavelengths are not feasible, as the access to these atmospheric windows is mostly restricted by the atmospheric water content. At other sites (e.g., Mauna Kea in Hawai'i, the ALMA-site in Chile, or DOME-C at Concordia-Station/Antarctica) it is possible to observe also at wavelengths as low as 500 μm, but only for a limited time of the year. Complete access to the wavelength range $\lesssim$ 500 μm can only be given by space-borne observatories like Herschel (Pilbratt et al., 2010) or Spitzer (Werner et al., 2004).

Radio telescopes are most commonly built as Cassegrain or Gregorian systems. The electromagnetic radiation of the source reaches the telescope, where it is reflected by the primary and secondary mirror, before it reaches the receivers.

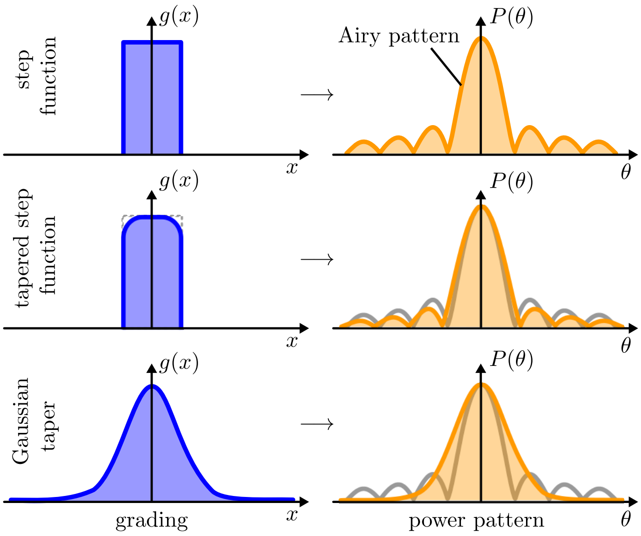

Figure 2.6.: Power pattern for single dish telescopes with different grading functions. For a step function, the resulting power response is the so-called *Airy pattern*. For the tapered grading functions, the Airy pattern is plotted as a reference (grey line). The size of the sidelobes is exaggerated.

In a *bolometer*, incoming photons are absorbed, which then in turn provides a small temperature increase. This can be measured, as the material does have a temperature dependent ohmic resistance. Commonly used bolometer arrays are SCUBA/SCUBA-2 (at the JCMT in Hawai'i), MAMBO/MAMBO2 (at the IRAM-30m telescope in Spain), and LABOCA/SABOCA (at the APEX in Chile). However, bolometers are not able to retain any spectral information, which can on the other hand be preserved by using *heterodyne receivers*. In this case, the incoming signal from the sky with frequency ν_{sky} is superposed with a signal of the local oscillator with frequency ν_{LO}, which differs only by a few GHz from the sky frequency. This effectively leads to a downsampling of the signal to an intermediate frequency $\nu_{\mathrm{IF}} = \nu_{\mathrm{sky}} - \nu_{\mathrm{LO}}$, a frequency which can easily be amplified by contemporary low-noise electronics. The signal is then sent to the backend, e.g., spectrometers, which further process the data, before it is delivered to the user.

Beam Characteristics

Due to its finite spatial extent, a telescope never observes a single point, but it is rather sensitive to a larger area on the sky. This directional dependence is described by the telescope power pattern $P(\theta, \phi)$, which is the received power in dependence on the direction of the sky. Very often, astronomers also use the normalised beam power pattern $P_{\mathrm{n}}(\theta, \phi) = P(\theta, \phi)/P_{\mathrm{max}}$ to characterise a telescope. The *beam solid angle* Ω_{A} of the antenna is given by

$$\Omega_{\mathrm{A}} = \int_{4\pi} P_{\mathrm{n}}\, \mathrm{d}\Omega, \tag{2.20}$$

which should be more seen as a theoretical quantity, as it conforms to a beam pattern of $P_{\mathrm{n}} = 1$ within Ω_{A}, and $P_{\mathrm{n}} = 0$ outside.

The true beam pattern, i.e., the instrumental response to a point source (commonly known as *point spread function*), is given by diffraction theory. A simple approach to get the beam power pattern is to define the aperture illumination by a grading function $g(x)$, which is related to the power pattern via

$$P(\theta) = \mathrm{FT}[g(x)] \times \mathrm{FT}^{*}[g(x)] \tag{2.21}$$

where FT and FT* are the Fourier transform, and the complex conjugate of the Fourier transform of $g(x)$, respectively. A few simple examples are shown in Figure 2.6. For a circular aperture, the grading would simply be a step function, which then results in the well-known Airy function as the beam power pattern. The resolution, i.e., the position of the first null, is given by

$$\theta = 1.22\,\frac{\lambda}{D}, \tag{2.22}$$

where D is the aperture diameter and λ the wavelength. Another measure for the resolution is also the FWHM of the central maximum, which is in the case of the Airy pattern given by

$$\theta_{\mathrm{FWHM}} = 1.02\,\frac{\lambda}{D}. \tag{2.23}$$

Notable for the power pattern is the presence of secondary maxima, which are certainly not a desired effect. One can reduce this effect by tapering the edges of the aperture, i.e., lowering down their relative sensitivity (Figure 2.6, second row). One can see that their relative intensity goes down, but also that the beam broadens to some extent, which in turn means a lower resolution. In the case of a Gaussian taper, which is depicted in the third row, the power pattern is also a Gaussian, and the sidelobes disappear completely. In general, one has to find a compromise between sidelobe suppression, and loss of resolving power.

To get an estimate of the resolution power of a telescope, it is convenient to approximate the central maximum with a normalised Gaussian power pattern of the form

$$P_{\mathrm{n}} = \exp\left(-2.77\,\frac{\theta}{\theta^{2}_{\mathrm{FWHM}}}\right). \tag{2.24}$$

The beamsize is then given, according to Equation (2.20) by

$$\Omega_{\mathrm{A}} = 1.133\,\theta^{2}_{\mathrm{FWHM}} \tag{2.25}$$

Due to the presence of the sidelobes, a telescope does not simply receive signal from the pointing direction, but also from other parts of the sky (Figure 2.7). Generally one describes the central maximum as main lobe, and secondary maxima as sidelobes and rear lobes (depending on their orientation on the sky). Most of the received power is received by the main beam with an angular size of

$$\Omega_{\mathrm{mb}} = \int_{\theta_{\mathrm{mb}}} P_{\mathrm{n}}\,\mathrm{d}\Omega, \tag{2.26}$$

where we now only integrate between the first nulls of the power pattern. The fractional power in the main lobe gives the *beam efficiency*

$$B_{\mathrm{eff}} = \frac{\Omega_{\mathrm{mb}}}{\Omega_{\mathrm{A}}}. \tag{2.27}$$

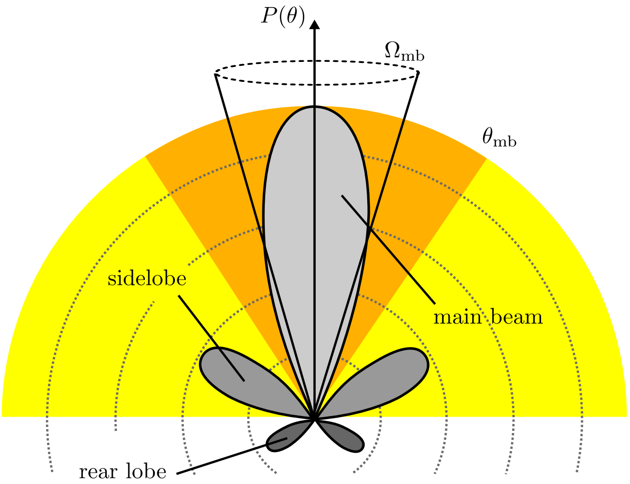

Figure 2.7.: Polar plot of a simplified beam pattern of a radio telescope. The *forward efficiency* F_{eff} is the fractional power received from forward direction, the *main beam efficiency* B_{eff} accordingly the fractional power between the first null at θ_{mb}.

In analogy, one can also define the fraction of power which comes from forward direction, the so-called *forward efficiency*

$$F_{\mathrm{eff}} = \frac{\int_{2\pi} P_{\mathrm{n}}\, \mathrm{d}\Omega}{\Omega_{\mathrm{A}}}. \tag{2.28}$$

As an example for true telescope characteristics, Table A.4 in the Appendix gives some values for the IRAM-30m telescope. In general, the FWHM of a telescope beam cannot be simply given by Equation (2.23), but must be measured and are usually provided on the telescope webpages. For the IRAM-30m telescope, the beam size can approximated by

$$\theta_{\mathrm{FWHM}}^{30\mathrm{m}} = 1.166\, \frac{\lambda}{D}, \tag{2.29}$$

which closely resembles Equation (2.22).

Observational parameters

From a point source with flux density S_ν a telescope will receive the monochromatic power

$$p_\nu = \frac{1}{2} A_{\mathrm{eff}}\, S_\nu \tag{2.30}$$

where A_{eff} is the effective antenna aperture, S_ν is the observed flux density of the source, and the factor of 0.5 is due to the fact that only one polarisation can be measured at a time.

The effective antenna aperture A_{eff} is given by the relation

$$A_{\mathrm{eff}} = \eta_{\mathrm{A}}\, A \tag{2.31}$$

where A is the geometric size of the telescope, and η_{A} is the antenna efficiency factor with many different contributions (e.g., surface inaccuracies, shading by structure, etc.), with $\eta_{\mathrm{A}} < 1$.

The observed flux density S_ν depends both on the intensity of the source and the beam pattern, and is given by

$$S_\nu = \int_{4\pi} I_\nu \, P_\mathrm{n} \, \mathrm{d}\Omega. \tag{2.32}$$

In radio astronomy it is very common to express the intensity I_ν in terms of temperature. In case of thermal processes, this temperature then conforms to the source temperature, and is directly related to the Planck function (Equation 2.14). However, this scheme turned out to be so useful, that even nonthermal processes are described by a corresponding temperature. This so called *brightness temperature* T_b then conforms to the theoretical temperature, which a blackbody would have to yield the same specific intensity. The *effective source temperature* $J(\nu, T)$ is given by

$$J(\nu, T_\mathrm{b}) = \frac{T_0}{\exp(-T_0/T_\mathrm{b}) - 1}, \tag{2.33}$$

with $T_0 = h\nu/k_\mathrm{B}$, and the Planck function is then

$$B_\nu = \frac{2\,k_\mathrm{B}\,\nu^2}{c^2}\,J(\nu, T). \tag{2.34}$$

In the case of $h\nu \ll k_\mathrm{B}T$, the exponential function can be Taylor expanded, and $J(\nu, T) \rightarrow T$. This is the so called *Rayleigh-Jeans law*

$$B_{\nu,\mathrm{RJ}} = \frac{2\,\nu^2\,k_\mathrm{B}}{c^2}\,T_\mathrm{RJ}, \tag{2.35}$$

where the temperature is now denoted as the Rayleigh-Jeans temperature T_RJ. From the condition to express the Planck function as the Rayleigh-Jeans law we see, that

$$T\,[\mathrm{K}] \gg \frac{\nu\,[\mathrm{GHz}]}{20} \tag{2.36}$$

must be fulfilled for Equation (2.35) to be true. Therefore, for objects at $T = 10\,\mathrm{K}$, the observing frequency must be way below 200 GHz ($\lambda \gg 1.5\,\mathrm{mm}$).

Observation and Calibration

However, one has to bear in mind that at (sub)mm wavelengths the signal from the source of interest is almost negligibly small compared to other emitters, e.g., the atmosphere, the ground, and the telescope structure. The total signal, which is received by the antenna, is called *antenna temperature*. For a pointing at the source it is given by

$$T_\mathrm{A} = F_\mathrm{eff}\,[\,T_\mathrm{b}\,\mathrm{e}^{-\tau} + (1 - \mathrm{e}^{-\tau})\,T_\mathrm{atm}\,] + (1 - F_\mathrm{eff})\,T_\mathrm{g} + T_\mathrm{rx}, \tag{2.37}$$

where T_b is the brightness temperature of the source, T_atm is the temperature and τ the optical depth of the atmosphere, T_g the temperature of the ground and telescope structure, and T_rx an additional contribution by the receiver. The unit of interest is the brightness temperature T_b, which can be extracted by various different methods. A commonly used strategy is the so-called *position switching*, where in an alternating sequence the source (the *on* position) and a nearby, empty region of the sky (the *off* position) are observed. Subtraction will then immediately give the antenna temperature of the source. Other methods (e.g., frequency switching) exist, but will not be discussed any further in this context.

For spectrometers, the relative spectral response of the spectrometers are obtained by observing sources which are known to have a flat spectrum in the desired wavelength range. For this purpose, quasars have turned out to be very useful, and a list of good calibration sources can be found online at the webpages of respective telescopes.

In most cases, heterodyne instruments are – differently from bolometer arrays – single pixel instruments. Maps were until recently obtained by pointing the telescope at the different positions on the sky. This was a tedious task, as one had to move the telescope to every single grid point. Nowadays, large-scale maps can easily be obtained via the so-called *on-the-fly* (OTF) mapping scheme. With this method the telescope scans a strip on the sky at a speed of a few arcseconds per second, with a typical read out of a spectrum in intervals of a few seconds. A map is then built up by subsequent scanning of strips in both right ascension and declination direction, with repeated measurements at the *off* position between the scans. Every single spectrum has a low signal-to-noise, but with this technique easily a few thousand spectra are obtained. These are then averaged on a regular grid, which then allows astronomers to obtain a decent signal-to-noise ratio.

Sensitivity

The sensitivity of a radio telescope is directly linked to a quantity called *system temperature* $T_{\text{sys}} = \sum T_i$, which summarises all noise contributions from the source, the sky, the atmosphere, the receiver, the ground, etc. The *radiometer formula* then gives the noise

$$\sigma = \frac{K\,T_{\text{sys}}}{\sqrt{\Delta\nu\,t}}, \tag{2.38}$$

where K is a sensitivity constant and of the order of unity, $\Delta\nu$ is the observed bandwidth and t the integration time.

Temperature Scales

In the previous parts of this section, we already got a hold of the antenna temperature of a source. The antenna temperature T_{A} can be seen as a radiation resistance. If a resistor would replace the antenna feedhorn, then it would have to have the temperature T_{A} to emit the same monochromatic power p_ν as the radio source. However, the antenna temperature does not take into account the attenuation of the atmosphere $\mathrm{e}^{-\tau}$. Therefore, we introduce the

$$T'_{\text{A}} = T_{\text{A}}\,\mathrm{e}^{\tau}, \tag{2.39}$$

which conforms to the antenna temperature, which a telescope would measure outside the atmosphere. The source brightness and antenna temperature can be related with the aid of

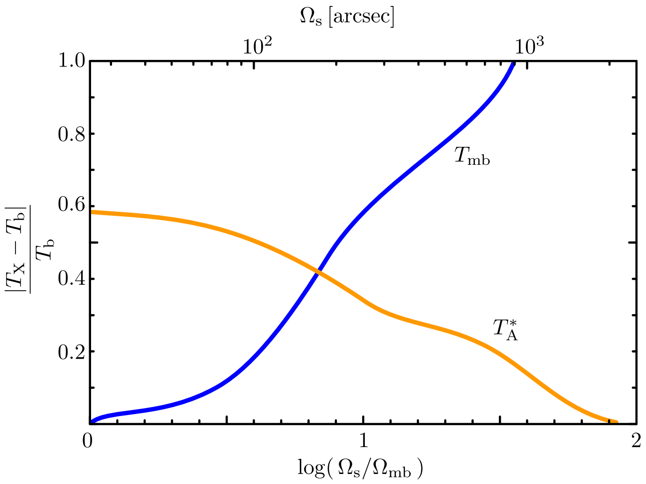

Figure 2.8.: Deviations of the antenna temperature T_A^* and main beam temperature T_{mb} from the true brightness temperature T_b in dependence of the source size Ω_s for IRAM-30m observations at $\lambda = 1.3$ mm (Hily-Blant, 2008).

Equation (2.30), which then yields

$$\frac{1}{2} S_\nu A_{eff} = k_B T'_A \tag{2.40}$$

It is, however, not convenient to express the temperatures in terms of the antenna temperature T'_A, as it is not a measure, which depends solely on the source.

Taking into account only emission from forward direction yields a new quantity, the so-called *corrected antenna temperature*

$$T_A^* = \frac{T'_A}{F_{eff}}. \tag{2.41}$$

Considering only emission from inside the main beam gives the *main beam temperature*

$$\begin{aligned} T_{mb} &= \frac{T'_A}{B_{eff}} \\ &= \frac{F_{eff}}{B_{eff}} T_A^* \end{aligned} \tag{2.42}$$

To determine, which temperature scale is an accurate representation of the true brightness temperature T_b, one has to know the size of the source (Figure 2.8):

- $\mathbf{\Omega_s = 2\pi}$: If a source spans the whole hemisphere, then T_A^* represents the brightness temperature T_b. The rear lobes are not taken into account, as T_A^* is already corrected by the forward efficiency. The main beam temperature exceeds the brightness temperature ($T_{mb} > T_b$), as erroneously the energy, which is spread out over the whole hemisphere, is assumed to come only from the area of the main beam Ω_{mb}.
- $\mathbf{\Omega_{mb} < \Omega_s < 2\pi}$: If the source size is somewhat inbetween the main beam size and 2π, we consequently get $T_{mb} > T_b > T_A^*$.
- $\mathbf{\Omega_s = \Omega_{mb}}$: In this case, the main beam temperature scale correctly represents the brightness temperature $T_{mb} = T_b$, as the sidelobes are devoid of any emission.

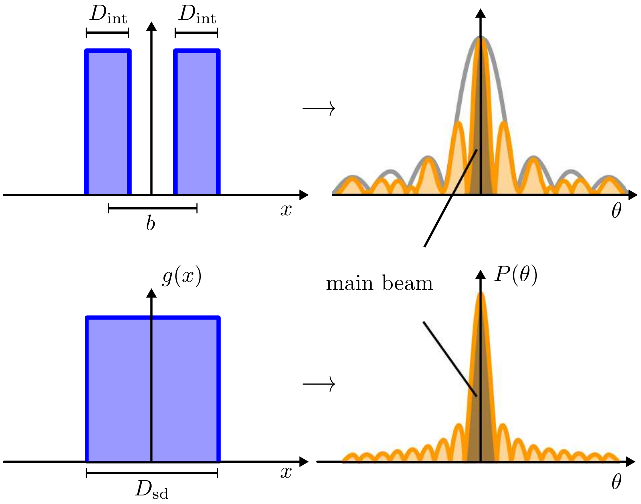

Figure 2.9.: Power pattern for a two element interferometer with a baseline b, and a single dish telescope. The grey line represents the Airy pattern of a single dish telescope with D_{int}.

- $\mathbf{\Omega_s < \Omega_{mb}}$: For sources smaller than the beam size the main beam brightness temperature underestimates the true brightness temperature. This effect is called *beam dilution*, as the beam efficiency B_{eff} "undercorrects" the antenna temperature. The relation between the temperature scales is then given by

$$T_{\text{mb}} = T_{\text{b}} \frac{\Omega_{\text{s}}}{\Omega_{\text{mb}}} \tag{2.43}$$

2.3.3. Radio Astronomy – Interferometry

Recalling Equation (2.22), the resolution of an imaging device is given by $\sim \lambda/D$. To achieve the resolution of a 10 m class telescope at 1 μm, a telescope, which observes at mm-wavelengths, needs to have a size of $\sim$ 10 km. To build a single dish telescope of this size is technologically impossible. However, by combining the signal of two (or more) smaller telescopes, which are placed far away from each other at distance D, one can achieve the same resolution. The principles of this so-called *interferometry* will be discussed in more detail in the following section.

Angular Resolution

To a simple extent, the angular resolution of an interferometer can be obtained by applying the same formalism as was made for single dish telescopes. In Figure 2.9 the grading function $g(x)$ and the power pattern of a simple two-element interferometer with two telescopes of diameter D_{int} placed at distance b (the so-called *baseline*) are shown and compared to a single dish telescope. The envelope of the power pattern follows the beam pattern of a single dish telescope with the diameter D_{int}. The resolution, i.e., the size of the main beam, on the other hand is the same as for a telescope with diameter D_{sd}, which resembles the longest extent of the two-element interferometer. This shows in a very simple way that it is possible to achieve high resolutions without the need of filled aperture telescopes, at the cost of stronger sidelobes. Enlarging the baseline will further increase

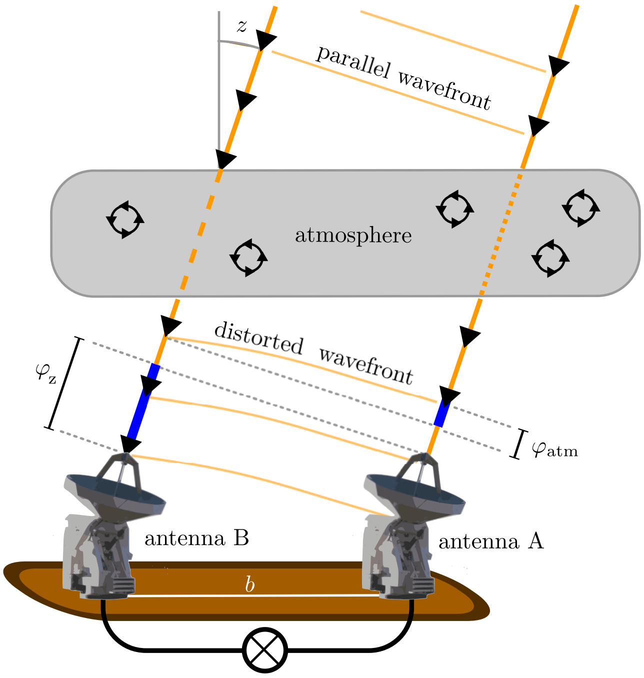

Figure 2.10.: Schematic setup of a two-element interferometer with baseline b. The light from the source will reach the telescopes at different times. This induces a phase offset between the two electromagnetic waves, which consists of the geometric phase shift φ_z (which depends on the zenith distance z and the baseline b), and the atmospheric shift φ_{atm}, when the two rays of light pass through parts of the atmosphere, which are affected by different turbulent cells. These effects have to be compensated before cross-correlating the two signals.

the resolution by effectively decreasing the extent of the central maximum. However, the envelope function will always resemble the Airy pattern of the single dish telescopes.

It should be noted, that an interferometer is, however, not a classical imaging device, but does rather recover the Fourier components (amplitude A and phase φ) by cross-correlating the incident radiation of two telescopes. Its mode of operation is essentially analogous to the double-slit experiment, and the distance between the telescopes conforms to the slit separation. In the case of a two-element interferometer (Figure 2.10), the effective telescope separation is given by

$$b^* = b\,\cos(z), \tag{2.44}$$

where b is the baseline length, and z is the zenith angle of the pointing centre (α_0, δ_0). For various reasons, the light from the source reaches the two telescopes at a different time, which causes a phase shift. This is on one hand caused by the geometric delay φ_z, and on the other hand by wavefront distortions in the atmosphere φ_{atm}. Using a proper calibration strategy, these phase shifts have to be compensated to obtain the intrinsic phase φ. A point source at the pointing centre (α_0, δ_0) would have a phase of $\varphi = 0$. However, a source with an angular offset would cause an optical path difference and thus a phase $\varphi \neq 0$. The fact, that the spatial information is stored in the phase is demonstrated in Figure 2.11 by a simple experiment using two arbitrary images, which are converted via a Fourier transform. Exchanging amplitude $A_{1,2}$ and phase $\varphi_{1,2}$ information, and performing the backward transformation will result in two images, where one can still recognise the image with retained phase information, whereas the amplitude information does have surprisingly low influence.

To be applicable for real observations, the simple formalism of the two-element interferometer in Figure 2.10 has to be extended (although the formalism itself is still

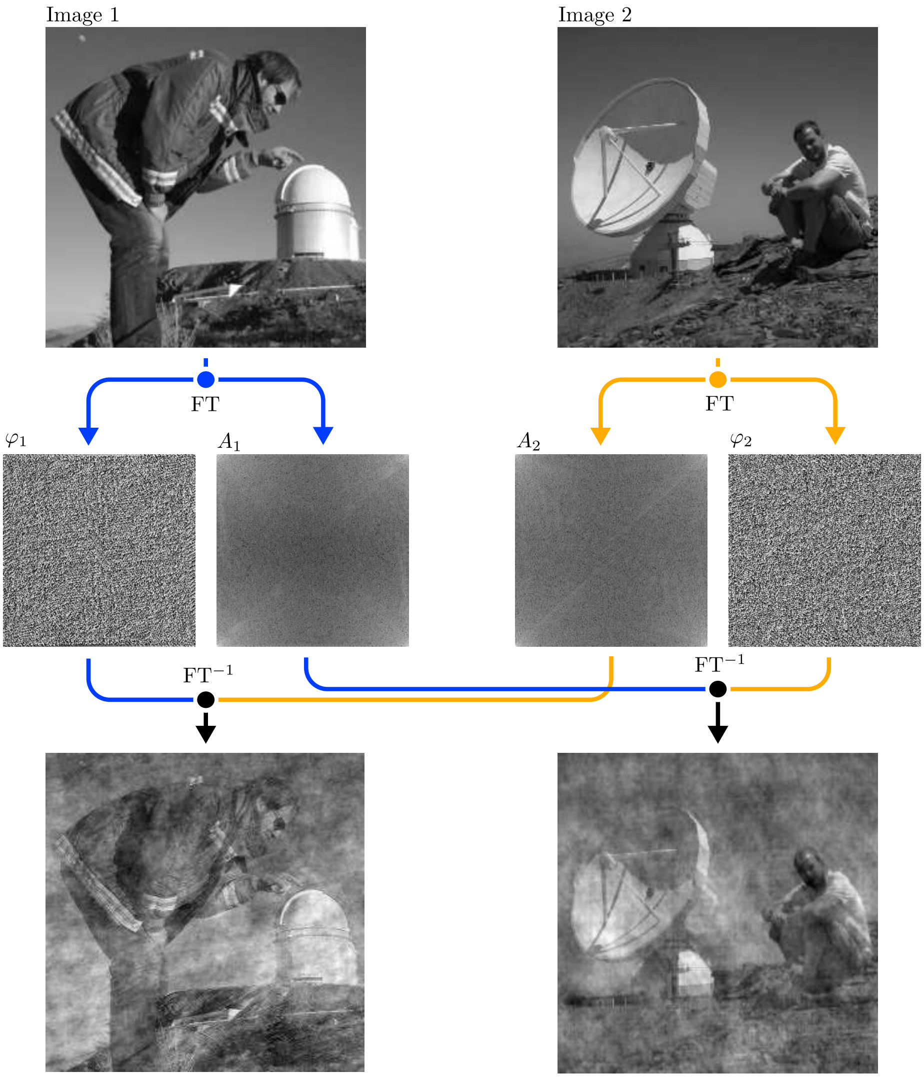

Figure 2.11.: The spatial information in the Fourier transform lies within the phase φ. This is demonstrated for two images, where after the Fourier transform the amplitudes are swapped, and the images are restored. One can still clearly see the image, of which the phase information has been retained.

valid), as the source will generally not be aligned with the antennas. To derive the projected baseline b^* for this case, a new coordinate system is needed, namely the (u, v, w)-system. This coordinate system has its origin in the observed position (α_0, δ_0), with $\vec{e}_u$ in right ascension direction, $\vec{e}_v$ pointing towards the celestial pole (in declination direction) and $\vec{e}_w$ radially out of the celestial sphere. The projected baseline is then given by projecting the baseline b of the local coordinate system ($\vec{e}_x$ to the South, $\vec{e}_y$ to the East, and $\vec{e}_z$ towards the zenith) into the so-called uv-plane (i.e., the plane of the sky) of the new coordinate system, and we obtain $\vec{b}^* = (u, v)$.

From the double-slit experiment it is known, that the slit separation and the resolution are inversely related (which is obvious, as they are directly related via a Fourier transform). Long baselines resolve the small spatial scales, and short baselines recover the large-scale structure. However, a double-slit is not capable of recovering other spatial scales than the one, which is governed by the slit separation. Furthermore, the sampling of only a few spatial scales causes sidelobes of considerable strength (Figure 2.9). Therefore, astronomers are interested to get a good sampling of the *uv*-plane, and several strategies exist to achieve this goal:

- Building more telescopes will increase the number of simultaneously sampled baselines manifold. Cross-correlating the light of $N_{\rm ant}$ single dish antennas will increase the number of baselines to

$$N_{\rm base} = \frac{N_{\rm ant}(N_{\rm ant}-1)}{2}. \tag{2.45}$$

- During the diurnal motion of the source across the sky, a source will exhibit different projected baselines (u, v). Therefore, over the course of a celestial passage of the source, one can sample many different baselines from the same pair of telescopes. The principle of this so-called *aperture synthesis* is illustrated in Figure 2.12, where the *uv*-coverage and the resulting beam power pattern of the six 10 m-antenna array ($N_{\rm base} = 15$) of CARMA is shown, which is achieved after a simple snapshot, 2 and 12 hours of observations. As the source moves across the sky, the projected baselines start to fill the *uv*-plane (panels in the top row), which then gradually improves the shape of the beam (bottom row). Due to the nature of the Fourier transform, every baseline conforms to two points, namely (u, v) and $(-u, -v)$ in the *uv*-plane, which are indicated as blue and red dots, respectively.
- Interferometers with many telescopes, and aperture synthesis provide a good sampling of the *uv*-plane. However, as the source always follows the same path across the sky, an interferometer would repeatedly sample the same baselines. Thus, interferometers typically switch between a few different antenna configurations every few months, to change their sensitivity to different spatial scales.

Observations and Calibration

In interferometry, a considerable amount of time is spent on calibration. The absolute flux scale is determined by observations of either unresolved quasars with well known flux density, or preferentially planets, where the flux density can be modelled by taking into account their distance and illumination by the sun. For spectrometric observations, it is furthermore necessary to observe a source with a flat spectrum (usually quasars), which then allows to derive the relative spectral response of each channel.

As mentioned earlier, the phase φ for two baselines will change with both the position of the source on the sky ($\varphi_{\rm z}$), and the atmosphere ($\varphi_{\rm atm}$). The geometric phase delay $\varphi_{\rm z}$ can be derived by simple trigonometry, whereas the determination of $\varphi_{\rm atm}$ involves observations of a so-called gain calibrator, which is conveniently an unresolved quasar close to the observed source. It is necessary, that the calibrator is unresolved and at the pointing centre to ensure, that the measured phase (after correction for the geometric delay $\varphi_{\rm z}$) can be completely

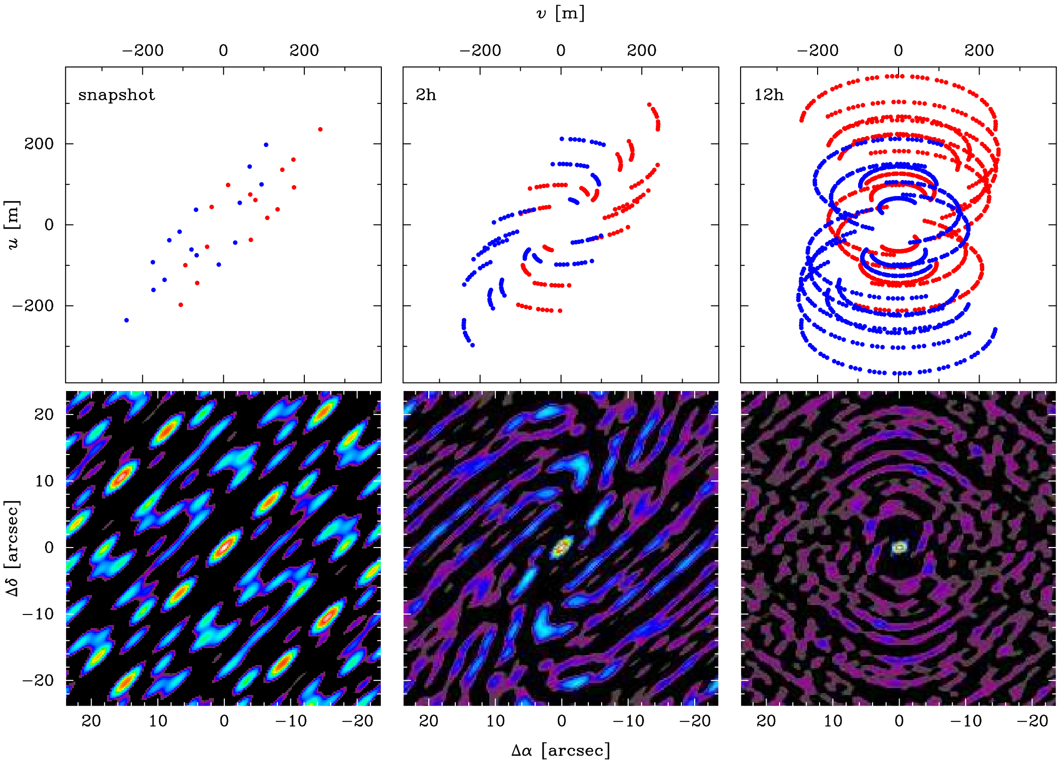

Figure 2.12.: Improvement of the shape of the beam due to aperture synthesis. These simulations show the beam for observations with the 10m-array of CARMA for a simple snapshot (left column), after 2 hours (centre column) and 12 hours (right column) of observations. One can see the reduction of the sidelobes in the beam power pattern (lower row, peak values normalised to unity) with increasing *uv*-coverage (upper row).

attributed to the atmosphere $\varphi = \varphi_{\text{atm}}$. Furthermore, the gain calibrator is used to correct for the varying attenuation of the incoming radiation in dependence on the airmass. As the phase-shifts, which are induced by the atmosphere, are relatively stable on timescales of a few 10 minutes, the scientific observations are usually interrupted for the observations of the calibrator in intervals of the order of 15 minutes.

For an interferometer it is not as easy as for a single dish telescope to cover large regions on the sky with an OTF mapping scheme. Interferometers can only do pointed observations, with the advantage of getting more than only one resolution element per pointing. As it can be seen in Figure 2.9 the interferometer is most sensitive to emission from a region, which is defined by the primary beam of the single dish telescopes with diameter D_{int}. Therefore, the field-of-view (FOV) of an interferometer is usually defined as the FWHM of the single dish primary beam. Larger areas can be mapped by pointing towards different regions on the sky, which are usually are separated by half a primary beam.

Image Analysis

In order to obtain an astronomical image, one effectively has to perform a Fourier transform of the amplitude $A(u, v)$ and phase $\varphi(u, v)$. Generally this so-called *dirty image*, will not allow a clear look on what is going on in your science object, as it is effectively the true brightness distribution convolved with the interferometric beam (or *dirty beam*). Due to the incomplete sampling of the *uv*-plane, strong sidelobes lead to a distorted image, which first has to be deconvolved to allow a good data analysis.

Several deconvolution techniques have been developed, of which the most commonly used is called CLEAN. It is an iterative procedure with the following steps:

1. Search for the emission peak (α, δ) in the dirty map.
2. Subtract a dirty beam (which is usually scaled to 10% of the emission peak) centred at (α, δ) from the dirty map (which then gives the *residual map*).
3. Mark the position (α, δ) in a separate map, the so-called *clean component map*.
4. Repeat steps 1-3 on the residual map, until all emission lies below a threshold, which is generally dictated by the noise.

The clean-component map, which now is effectively a map with δ-functions at the positions of emission is in the next step convolved with the *clean beam*, which is a Gaussian fit to the central maximum of the dirty beam. By doing this, the spatial resolution of the interferometric image is retained, but the sidelobes are effectively removed. The residual dirty map is then added to the convolved image, which then gives the *clean map* as the final result.

Short Spacings

As mentioned earlier, an interferometer cross-correlates the incident radiation of two different antennas at different separations. It cannot sample baselines $b^* < D_{\rm int}$, as in this case the background antenna is shaded by the one standing in front of it. This limits the recovery of large-scale structure by interferometers. That effect is illustrated in Figure 2.13, which shows how a complex, artificial brightness distribution (left panel) is seen by an interferometer (central panel) and a single dish telescope (right panel). The latter one is able to recover the total flux and the large-scale structure, whereas the small scale structure is completely smoothed out by the large beam size. The interferometer, on the other hand, is capable of recovering the small scales, whereas the large-scale variation of the background is completely lost. Furthermore, the absolute flux scale is unknown[†].

Therefore, if one has to deal with extended objects, the general strategy is to get both single dish and interferometric data, and merge these two datasets to fill the central gap in the *uv*-plane. The magic is then, to first convert the single dish data into Fourier space and downweight it (due to the relatively higher sampling) before the combination. As an interferometer measures flux density and not temperatures, one has to convert from the Kelvin to Jansky per beam scale with the aid of Equation (2.40). Due to the dependence on

---

[†] The total flux is given by the Fourier component at $(u, v) = 0$, which is not sampled by interferometers. Only if the source is not resolved, the total flux is also recovered at longer baselines.

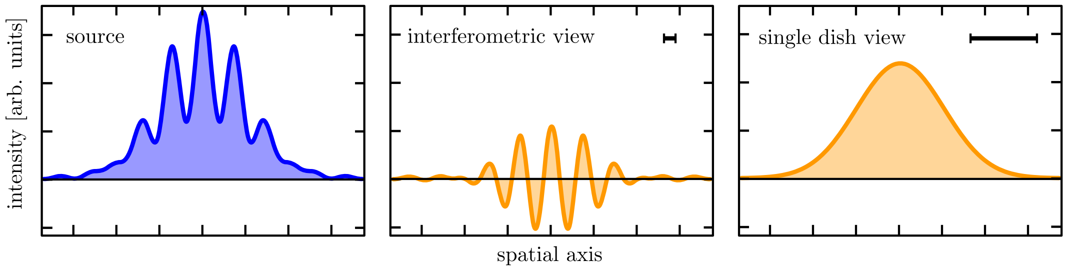

Figure 2.13.: Schematic sketch how a source with a complex brightness distribution (left panel) is recovered by an interferometer (central panel) and a single dish telescope (right panel). The resolution of the respective instrument is indicated in the upper right corner by the scale bar.

effective aperture, this conversion factor is different for different telescopes and frequencies. Values for the IRAM-30m telescope are listed in Table A.4. Furthermore, as the Jansky is not a measure of surface brightness, one has to divide by the beam size. One generally uses the approximation of a Gaussian beam, which is $\Omega_\mathrm{A} = 1.133\,\theta^2_\mathrm{FWHM}$. The merged data set can then be converted an cleaned following the procedure introduced in the previous paragraph. Due to the lower level of the sidelobes the CLEAN algorithm will work more accurately, compared to interferometry data only.

2.4. Cosmic Dust

After giving a short introduction into radiative transfer basics, and *how* astronomers measure the light coming from outer space, I will now explain the basics of *why* we can observe both dust and molecules (of which the latter one will be explained in more detail in the subsequent section).

To talk about the observability of dust grains, let us recall that the optical thickness is defined as $\mathrm{d}\tau = -\rho\,\kappa_\nu\,\mathrm{d}s$. Integration along the line of sight then yields

$$\begin{aligned}\tau_\nu &= -\int_{s_0}^{0} \rho\,\kappa_\nu\,\mathrm{d}s \\ &= m_\mathrm{dust}\,N_\mathrm{dust}\,\kappa_\nu \\ &= \frac{m_\mathrm{H}\,N_\mathrm{H}}{R_\mathrm{g/d}}\,\kappa_\nu. \end{aligned} \tag{2.46}$$

In Equation (2.46) the dust mass, which is given by $m_\mathrm{dust}N_\mathrm{dust}$, is expressed via the hydrogen mass m_H. The ratio $R_\mathrm{g/d}$ is the so-called *hydrogen gas-to-dust mass ratio*, which is not easy to determine. A commonly used value is $R_\mathrm{g/d} = 110$ (Sodroski et al., 1997), which will also be used throughout this work. It is convenient to incorporate the $R_\mathrm{g/d}$ directly into the dust opacity, which then gives the corrected value

$$\kappa^*_\nu = \frac{\kappa_\nu}{R_\mathrm{g/d}}, \tag{2.47}$$

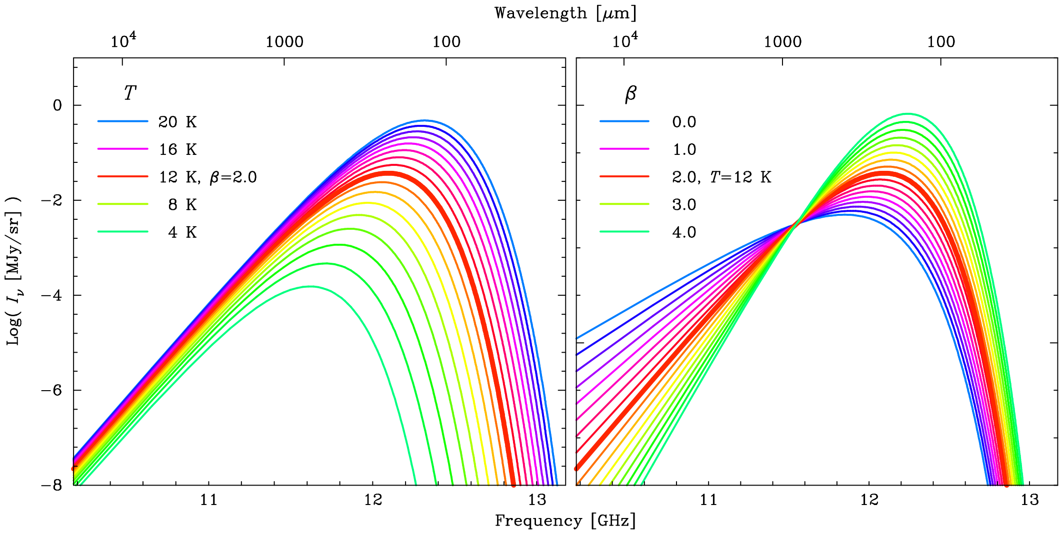

Figure 2.14.: Modified blackbody curves for $\beta = 2.0$ with temperatures $T = 4\ldots20\,\mathrm{K}$ (left panel), and $T = 12\,\mathrm{K}$ with dust opacities $\beta = 0.0\ldots4.0$ (right panel). All curves assume a hydrogen column density of $N_\mathrm{H} = 10^{22}\,\mathrm{cm}^{-2}$, and a fixed dust opacity of $\kappa = 1.0\,\mathrm{cm}^2\mathrm{g}^{-1}$ at λ=850 μm. The thick red lines in both panels conform to the curve with $T = 12\,\mathrm{K}$ and $\beta = 2.0$. For all configurations we obtain $\tau \ll 1$, and therefore the curves are not affected by optical depth effects.

and Equation (2.46) turns into

$$\tau_\nu = m_\mathrm{H}\, N_\mathrm{H}\, \kappa_\nu^*. \tag{2.48}$$

Not only $R_{\mathrm{g/d}}$ is hard to constrain, but also the dust opacity κ_ν is part of many investigations, and it varies from dust model to dust model. At millimetre and sub-mm wavelengths, the dust opacity is usually parametrised by a power law of the form

$$\kappa_\nu \propto \lambda^{-\beta}, \tag{2.49}$$

where β is the so-called dust opacity index. However, for a larger wavelength range this simplification breaks down, and one has to make a more elaborate analysis of the dust and its properties. A commonly used dust model for pre- and protostellar cores is that of Ossenkopf and Henning (1994). These authors computed dust opacities κ_ν for grains with an initial grain size distribution from MRN, and considered various effects like coagulation and/or ice coatings of different thickness. Opacity curves for some configurations are shown in Figure 1.3 (Chapter 1).

2.4.1. FIR/Millimetre Wavelengths

As mentioned earlier molecular clouds are one of the coldest places in the universe with temperatures of only a few 10 K above absolute zero. At these temperatures, the peak of the thermal emission, which is described by the Planck function $B_\nu(T)$, lies well at FIR and millimetre wavelengths. In the optically thick case, the position of the maximum can be calculated from Wien's displacement law, which also serves as a good approximation for the optically thin case[†]. For typical column densities of the order of $N_{\mathrm{H}} \sim 10^{22}\,\mathrm{cm}^{-2}$ the emission is seldomly optically thick, but is of the order of $\tau_\nu \sim 10^{-2} \ldots 10^{-5}$. In fact, $\tau_\nu \ll 1$ is a great advantage, as it allowed scientists to get an estimate on the column density and/or other parameters. Recalling Equation (2.16),

$$\begin{aligned} I_\nu &= \tau_\nu\, B_\nu(T) \\ &= m_{\mathrm{H}}\, N_{\mathrm{H}}\, \kappa_\nu^*\, B_\nu(T). \end{aligned} \tag{2.50}$$

The estimate of the column density, therefore, relies on an accurate knowledge of the dust opacity and temperature. With the advent of the *Herschel Space Observatory*, observers are now able to obtain measurements not from a single wavelength, but from multiple ones following the shape of the SED. As the shape of the curve mainly depends on the opacity κ_ν, and therefore the opacity index β, one can then get also better constraints on the dust model.

Some examples of theoretical curves are shown in Figure 2.14, where the temperatures vary from $T = 4 \ldots 20\,\mathrm{K}$, and dust opacity indices from $\beta = 0.0 \ldots 4.0$. Not surprisingly, a rise in temperature shifts the maximum of the emission towards shorter wavelength. More interestingly, however, is the change of the dust opacity index at constant temperature, which not only shifts the maximum towards shorter wavelength, but also considerably narrows down the overall curve.

2.4.2. Optical/NIR Wavelengths

In contrast to millimetre wavelengths, where we can directly measure the dust emission, there is not much to see – in the literal sense – at optical and NIR wavelengths. Cold material does not emit considerably at wavelengths of the order of $10^{-6}\,\mathrm{m}$. However, as the optical depths rise considerably above unity, one can use the obscuring nature of dust to constrain its amount in the molecular cloud. This technique depends on the presence of background stars, which shine through the molecular cloud. According to Equation (2.18), these stars appear systematically dimmer by a factor, which is described by the extinction A_ν. If the extinction is considerably strong, molecular clouds appear as dark(er) patches on the sky, which also lead to their detection. First, scientists believed to observe *holes in the sky*, but now it is known that the light of background stars was simply too dim to be observed by these ancient observers. Figure 2.15 shows the famous example of the dense core B 68. In the left panel one can clearly see the cloud as a black area, because the light of background stars cannot pass through.

One could measure the extinction of a molecular cloud, from Equation (2.18)

$$m_{\nu,\tau} = m_\nu + A_\nu. \tag{2.51}$$

However, this needs the knowledge of the true apparent magnitude of the star m_ν, which in the general case is not known as for most of the background stars it is impossible to

---

[†] In the optically thin case, the maximum of the dust emission can be calculated from Wien's displacement law only in the case of $\beta = 0$. For $\beta \neq 0$ the peak position will slightly change (Figure 2.14)

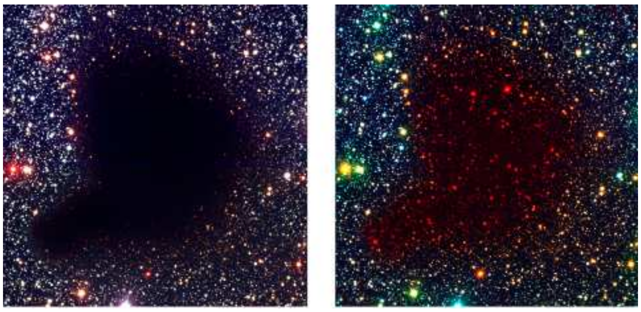
B, V, I B, I, K

Figure 2.15.: Observations of the Barnard Dark Cloud B 68 at optical and NIR wavelengths reveal the dependency of extinction on wavelength, which leads to the "reddening" of background stars (Image Credits: ESO)

determine its absolute magnitude and the distance. This information, however, would be necessary to compute the apparent magnitude with the aid of stellar evolution models. Therefore, different methods were developed to constrain the extinction through molecular clouds.

Background Star Counts

One way to derive the amount of dust is from counting the number of background stars. This technique, however, strongly depends on an accurate assumption of the stellar luminosity function, and the distribution of background stars. Obviously, the latter strongly varies both with galactic latitude and longitude. Nevertheless, this technique allowed Dobashi et al. (2005) to compile an all-sky extinction map from optical images of the Digital All-Sky Survey (DSS) with a resolution of the order of a few arcminutes.

However, the relatively high opacity at optical wavelengths sets an obvious limit to this technique. In the absence of background stars, one can only give an upper limit to the extinction, which emphasises the need for deep observations. As these are time-consuming and, thus, not feasible, observations at NIR wavelengths seem to be more promising, where the extinction is by an order of magnitude lower, and more background stars can shine through the molecular cloud and still be detected.

NIR Colour Excess

Having again a look at B 68 in Figure 2.15, one can see in the right panel, how many more stars shine through the dark cloud, when one replaces the V-band (0.55 μm) with a K-band image (2.2 μm). Furthermore, the stars behind the cloud appear considerably redder (which of course in this case is caused by the choice of filters for the false-colour image, but is in general seen as the trend of dominance of longer wavelengths). This so-called *reddening* is quantified by the NIR extinction law. Table 2.1 lists the relative extinctions of some commonly filters with respect to V and K_s from Rieke and Lebofsky (1985), and one sees that at 2.2 μm we have only about 10% of the extinction compared to wavelengths visible to the human eye, thus giving the stars in Figure 2.15, which shine *through* a molecular cloud a redder colour in comparison to nearby stars, which are not affected by the dust.

Table 2.1.: Extinction conversion factors (Rieke and Lebofsky, 1985)

Band	**Wavelength [μm]**	A_λ/A_V	$A_\lambda/A_{\mathrm{K_s}}$
U	0.36	1.53	13.7
B	0.44	1.32	11.8
V	0.55	1.0	8.93
J	1.2	0.282	2.52
H	1.6	0.175	1.56
K_s	2.2	0.112	1.0

Because of its independence on distance, it is convenient to consider the colour of an object. The reddening of an object can be quantified by the so-called *colour excess* $E(\nu_1-\nu_2)$, which is defined as the difference between the observed and the true intrinsic colour of an object

$$\begin{aligned} E(\nu_1-\nu_2) &= [(m_{\nu_1}+A_{\nu_1})-(m_{\nu_2}+A_{\nu_2})]-(m_{\nu_1}-m_{\nu_2}) \\ &= A_{\nu_1}-A_{\nu_2}, \qquad (2.52) \end{aligned}$$

Further substitution then leads to

$$\begin{aligned} E(\nu_1-\nu_2) &= A_{\nu_1}-A_{\nu_2} \qquad (2.53) \\ &= 1.086\,(\tau_{\nu_1}-\tau_{\nu_2}) \\ &\sim m_\mathrm{H}\,N_\mathrm{H}\,(\kappa^*_{\nu_1}-\kappa^*_{\nu_2}), \qquad (2.54) \end{aligned}$$

Therefore, the colour excess allows, under the assumption of known dust opacities, to estimate the hydrogen column density. However, to measure the colour excess, it is necessary to know the true intrinsic colour of a background object.

Lada et al. (1994) were the first ones that derived extinction maps by using the fact, that the colours of Main Sequence stars spread over a very narrow range in colour[†] $(H-K)$ of $\lesssim$ 0.1 mag. Plotting the colour $(H-K)$ already gives a very good estimate of the spatial distribution of dust, as it is – apart from a constant offset – effectively the colour excess. Such a map is shown in Figure 2.16, which depicts the filament L 1495 of the Taurus Molecular Cloud. Not by chance, this plot is of the region that will be investigated further in Chapter 3. One can clearly see the filamentary structure with pronounced regions of relatively high values of $(H-K)$. In the colour-magnitude diagram in the left panel of Figure 2.16, the background stars (which make up most of the stars) can be found at relatively low values of $(H-K)\sim 0.15$ mag (with an increased scatter towards lower magnitudes due to higher photometric errors). But one can also clearly see a considerable amount of stars with strong reddening. These are mainly located behind the filamentary structure, where the relatively high dust content then causes these red colours.

[†] For reasons of brevity, H and K depict not only the filters, but also correspond to their respective magnitudes. H_0 and K_0 then correspond to the true magnitude, without any extinction.

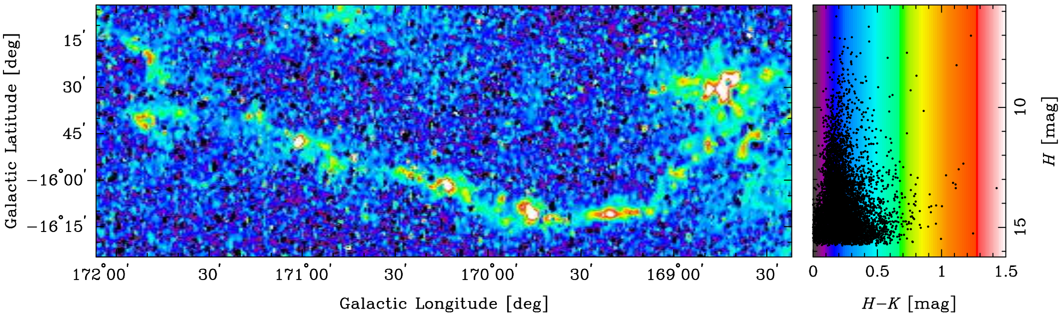

Figure 2.16.: *left panel:* 2MASS ($H - K_\mathrm{s}$) colour map of the Filament L 1495 in the Taurus Molecular Cloud. – *right panel:* The colour-magnitude diagram with stars from the same region exhibits a very narrow distribution in its colour ($H - K_\mathrm{s}$). The colour coding in the background corresponds to the map on the left panel.

An extinction map is then obtained averaging angularly close stars. Under the assumption of the reddening law of Rieke and Lebofsky (1985), the average extinction A_V towards a region on the sky can be estimated by

$$A_\mathrm{V} = 15.87 \left[\frac{1}{N} \sum_{n=1}^{N} (H - K_\mathrm{s})_i - (H - K_\mathrm{s})_0 \right], \tag{2.55}$$

where the intrinsic colour $(H - K_\mathrm{s})_0$ is usually estimated from stars in nearby empty regions on the sky. This technique was simply called NICE, which is short for **N**ear-**I**nfrared **C**olour **E**xcess.

The tool of Lada et al. (1994) was later refined by Lombardi and Alves (2001), who developed a tool called NICER (NICE **R**evisited). They further take into account a third filter, namely the J band at 1.2 μm, to derive a more accurate estimate of the extinction with the aid of a maximum likelihood technique, which is illustrated in Figure 2.17. Observations of an unreddened control field provide an estimate of the intrinsic colour and scatter of the population of Main Sequence stars. The covariance for these stars is indicated as a blue ellipse. Note, that the almost vertical alignment of the ellipse, i.e., the small dependence on colour ($H - K_\mathrm{s}$) for unreddened stars was the basis of NICE. The NICER algorithm then searches for the most likely reddening of a star by taking into account both the covariance of the control field, and the covariance of the star, which is given by its photometric errors.

The extinction map is then again obtained by spatially smoothing the individual extinctions on a regular grid. This can be again done by giving each data point a weight of unity (Equation 2.55), or by assigning a suitable weight w_i, i.e.,

$$A_\mathrm{V} = \frac{\sum_{i=1}^{N} w_i \, A_{\mathrm{V},i}}{\sum_{i=1}^{N} w_i}, \tag{2.56}$$

The weight term generally consists of a spatial term (i.e., the distance of a star with respect to the centre of the regular grid cell) and an error term, i.e., $\propto 1/\mathrm{Var}(A_\mathrm{V})$. Stars with intrinsically different colours (e.g., YSOs, evolved stars, etc.), can be effectively removed via σ-clipping. In doing so, extinction estimates from all stars, which are considered for the smoothing on a certain grid point, are compared, and extinction outliers are chopped.

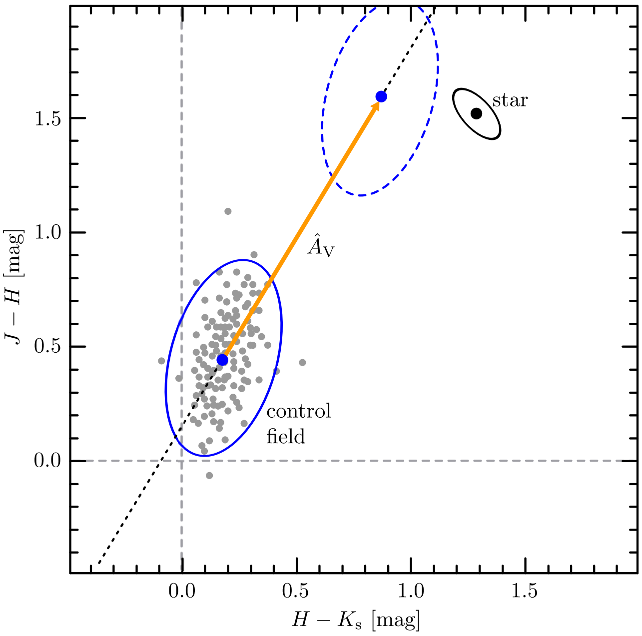

Figure 2.17.: Schematic sketch of the principle of NICER. A star under the influence of extinction will exhibit a displacement in the colour-colour diagram. Shifting the control field, which represents the locus of intrinsic colours of Main Sequence stars, along the reddening vector will, under consideration of both the covariance of the control field (blue ellipse) and the star (black ellipse), yield the extinction A_V.

A tool like NICER is ideal for the Two-Micron All-Sky Survey (2MASS, Skrutskie et al., 2006). It has an excellent spatial coverage, but is on the other hand still quite shallow. Deep observations of 4m size telescope towards selected positions on the sky easily have limiting magnitudes of up to 5 mag deeper. Of course, the number of background stars rises, but one then also recovers a considerable amount of background galaxies. These do have intrinsically different colours $(J - H)$ and $(H - K_s)$, and galaxies found in 2MASS are usually removed from the analysis by the σ-clipping method introduced in the previous paragraph. However, with the recovery of a significant number of background galaxies, one can also obtain information about their reddening, as galaxies also tend to group at a certain position in the colour-colour diagram. Foster et al. (2008) developed a method named GNICER (**G**alaxy NICER), which has to deal with several new problems. For example, as bright galaxies tend to have blue colours, a relatively larger fraction of blue galaxies is recovered, which effectively would then result in an underestimation of the extinction. Appropriate consideration of effects like this, then leads to a considerable noise reduction in low- and intermediate extinction regions. Towards the densest regions, the number of detected galaxies will effectively be zero, and therefore these regions will remain just as dark as before.

2.5. Molecules in Space

In the previous section I gave a quick introduction into observations of dust. Although they are very powerful, there are still some disadvantages (e.g., the unability of dust to recover the velocity structure, or temperature). One also has to consider, that only 1% of the total mass is made up by dust, whereas the other 99% consist of gas (and most of it in molecular form). By now more than 150 interstellar molecules are already identified, and most of their properties can be looked up online in databases like, e.g., in the *Cologne Database for Molecular Spectroscopy (CDMS)*[†]. However, one does not have to know all of these molecules to fully understand star formation, but it is rather important to pick a few with the right properties.

2.5.1. Molecular Structure

A molecule is, in general, a group of at least two atoms, which are held together by chemical bonds. The molecule as a quantum-mechanical system can be described by the Schrödinger equation. Due to the complexity of molecules compared to a simple hydrogen atom, this equation will also reach a certain level of complexity, but nevertheless a transition from one state into another is only possible at discrete energy levels. However, one does not have to treat all terms of the equation simultaneously, but can analyse different processes independently. This so called *Born-Oppenheimer approximation* then allows us to distinguish between three cases of molecular transitions at different energies W:

- *electronic transitions* with transition lines in the optical and UV,
- *vibrational transitions* of nuclei with transition lines in the infrared,
- *rotational transitions* of nuclei with transition lines in the millimetre and centimetre wavelength.

The total energy is then simply the sum of all these contributions

$$W_{\mathrm{tot}} = W_{\mathrm{el}} + W_{\mathrm{vib}} + W_{\mathrm{rot}} \tag{2.57}$$

and the resulting wavefunction is then a product of the electronic, vibrational and rotational wavefunctions.

The molecular line transitions I was working on during my PhD thesis were exclusively rotational transitions, which is why I will restrict myself to a quick introduction of this type of transition only.

Rotational Transition

The rotational energy of a quantum-mechanical system is described by its Hamiltonian operator

$$H_{\mathrm{rot}} = \frac{\Theta\,\omega^2}{2} = \frac{\vec{J}^2}{2\,\Theta} \tag{2.58}$$

where Θ is the molecular moment of inertia, ω the angular frequency, and $\vec{J}$ is the angular momentum. In the simple case of a linear molecule, application of this operator to the wavefunction gives the eigenvalues of the rotational energy

$$E_{\mathrm{J}} = \frac{\hbar^2}{2\,\Theta}\,J(J+1) \tag{2.59}$$

[†] `http://www.astro.uni-koeln.de/cdms`

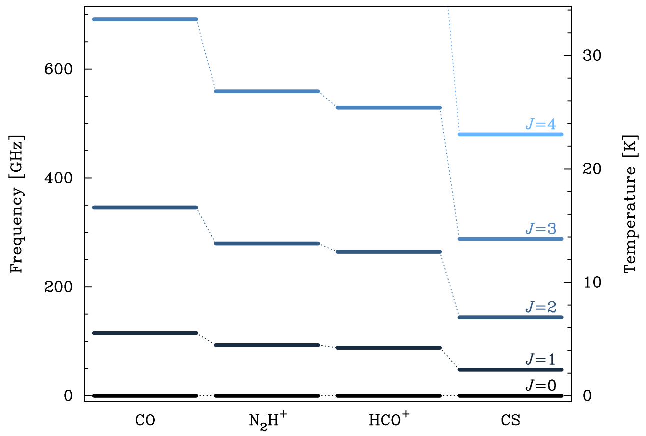

Figure 2.18.: Rotational energies (expressed in terms of frequency and temperature) for the levels $J = 0, 1, 2, \ldots$ of some selected molecules, which were used in the course of this PhD thesis.

where J is now the quantum number of the angular momentum, which has to be a natural number ($J = 0, 1, 2\ldots$). For reasons of convenience one can define the *rotational constant* $B = \hbar^2/4\pi\,\Theta$, and rewrite Equation (2.59)

$$E_\mathrm{J} = h\,B\,J(J+1). \tag{2.60}$$

These energies can of course also be expressed in terms of temperature ($T = E_\mathrm{J}/k_\mathrm{B}$) or frequency ($\nu = E_\mathrm{J}/h$). Rotational energies of a small selection of molecules, which were used in this thesis, are shown in Figure 2.18.

Transitions between two such energy levels are subject to some exclusion rules. In the case of dipolar transitions this means that only transitions between two neighbouring energy levels are possible ($\Delta J = \pm 1$), as the parity of the initial and final state must be opposite. This allows us to calculate the energies, if one assumes that J is the quantum number of the lower state

$$\begin{aligned}\Delta E &= E_\mathrm{J+1} - E_\mathrm{J}\\ &= h\,B\,(J+1)(J+2) - h\,B\,J(J+1)\\ &= 2\,h\,B(J+1).\end{aligned} \tag{2.61}$$

From Equation (2.61) it is obvious, why one often speaks of the *rotational ladder*, as the energy scales linearly with the quantum number.

Knowing the energies of the different levels and the energies involved in transitions between them, however, does not answer the question of how strongly different levels are populated.

2.5.2. Level Population

The relative occupancy of the upper n_u and lower level n_l in a two-level system can be described by the Boltzmann relation

$$\frac{n_\mathrm{u}}{n_\mathrm{l}} = \frac{g_\mathrm{u}}{g_\mathrm{l}}\,\exp\left(-\frac{\Delta E}{k_\mathrm{B}T_\mathrm{ex}}\right) \tag{2.62}$$

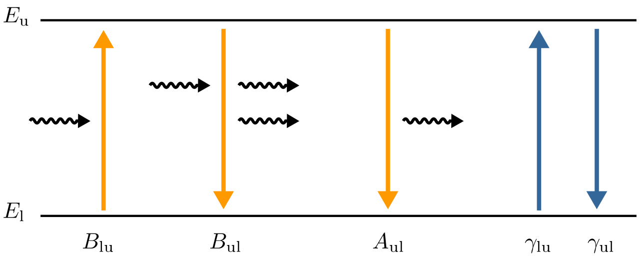

Figure 2.19.: A two-level system with radiative (yellow) and collisional transitions (blue).

where $g_{u,l}$ are the relative weights of the different levels, ΔE is the energy separation, k_B is the Boltzmann constant, and T_{ex} is the so called *excitation temperature*, which is not necessarily a temperature in the physical sense, but rather a parameter to quantify the level population. For all molecules which were used in this work, the relative weights are given by the simple relation

$$g_J = 2J + 1. \tag{2.63}$$

Figure 2.19 illustrates the processes, that lead to population and de-population of one or the other level. One can distinguish between two different types of transitions, namely the radiative and the collisional transitions.

Radiative transitions are characterised by the Einstein coefficients $B_{lu,ul}$, and A_{ul}. B_{lu} describes the transition from the lower level to the upper level by *absorption* of an incident photon with $\nu = \Delta E/h$. B_{ul} describes the case of *stimulated emission*, where an incident photon causes a downward transition, and a subsequent emission of a second photon. However, this stimulated emission is not the only effect that leads to a depopulation of the upper level. This can also happen due to *spontaneous emission*, which is described by A_{ul}.

On the other hand, collisions can also trigger transitions between two levels. These are described by coefficients $\gamma_{ul,lu}$. They can be calculated by taking into account the cross sections of the collisional partners, and also the velocity distribution (and thus they depend also on the temperature of the system).

All the aforementioned effects, of course, depend on the number density of the upper and lower level respectively. However, the rates for stimulated emission and absorption obviously depend also on the the average intensity of the incident radiation $\overline{I}$. For collisional transitions, the total number density has to be taken into account, as all present particles can serve as collisional partners.

In a steady state system the rate of depopulation and population equal each other, and one gets the rate equation

$$n_l\,(B_{lu}\,\overline{I} + \gamma_{lu}\,n_{tot}) = n_u\,(B_{ul}\,\overline{I} + A_{ul} + \gamma_{ul}\,n_{tot}). \tag{2.64}$$

Collisional Transitions

In a first approach we will only take a look at the regime, where transitions are completely dominated by collisions. We can therefore neglect the radiative transitions, and from

Equations (2.62) and (2.64) we then obtain

$$\frac{\gamma_{\mathrm{lu}}}{\gamma_{\mathrm{ul}}} = \frac{n_{\mathrm{u}}}{n_{\mathrm{l}}} = \frac{g_{\mathrm{u}}}{g_{\mathrm{l}}} \exp\left(-\frac{\Delta E}{k_{\mathrm{B}}\, T_{\mathrm{kin}}}\right), \tag{2.65}$$

where T_{ex} is in this case given by the kinetic temperature T_{kin} of the molecules. From the collisional coefficients $\gamma_{\mathrm{ul,lu}}$ and the number of collisional partners n_{tot} one can calculate the collisional rates $C_{\mathrm{ul,lu}}$ from

$$\begin{aligned} C_{\mathrm{ul,lu}} &= n_{\mathrm{tot}}\, \gamma_{\mathrm{ul,lu}} \\ &= n_{\mathrm{tot}} \langle \sigma_{\mathrm{ul,lu}}\, v \rangle \end{aligned} \tag{2.66}$$

where $\sigma_{\mathrm{ul,lu}}$ is the collisional cross-section for up- and downward transitions respectively, and v is the velocity of the collisional partner. Hereby, the fact that the colliding particles follow a velocity distribution is reflected by the average $\langle \ldots \rangle$ of the product of the cross-section and the velocity. The temperature dependence of the velocity distribution then also contributes to the collisional rate, which is therefore not only dependent on the number density of collisional partners.

The determination of the collisional coefficients γ_{ul} for different molecules is not a simple thing, and many different working groups try to constrain these parameters. A comprehensive list of many commonly used molecular parameters can be, e.g., found in the *Leiden Atomic and Molecular Database* (LAMDA[†]).

Radiative Transitions

However, in the opposite case of dominating radiation one can neglect collisional transitions and, again with the aid of Equation (2.62), one therefore obtains

$$B_{\mathrm{lu}}\, \bar{I}\, n_{\mathrm{l}} = B_{\mathrm{ul}}\, \bar{I}\, n_{\mathrm{u}} + A_{\mathrm{ul}}\, n_{\mathrm{u}} \tag{2.67}$$

$$\bar{I} = \frac{A_{\mathrm{ul}}/B_{\mathrm{ul}}}{g_{\mathrm{u}} B_{\mathrm{ul}}/g_{\mathrm{l}} B_{\mathrm{lu}}\, \exp\left(-\Delta E/k_{\mathrm{B}}\, T_{\mathrm{rad}}\right) - 1} \tag{2.68}$$

where in this case the excitation temperature T_{ex} conforms to the radiation temperature T_{rad} of the system. In the case of LTE, the average specific intensity in case of an isotropic illumination is given by the Planck function

$$\bar{I} = \frac{2\, h\, \nu_0^3/c^2}{\exp\left(-\Delta E/k_{\mathrm{B}}\, T_{\mathrm{rad}}\right) - 1}. \tag{2.69}$$

Comparison of Equations (2.68) and (2.69) yields the relation between the Einstein coefficients, which is

$$A_{\mathrm{ul}} = \frac{2\, h\nu_0^3}{c^2}\, B_{\mathrm{ul}} \tag{2.70}$$

$$g_{\mathrm{u}}\, B_{\mathrm{ul}} = g_{\mathrm{l}}\, B_{\mathrm{lu}} \tag{2.71}$$

[†] `http://www.strw.leidenuniv.nl/~moldata/`

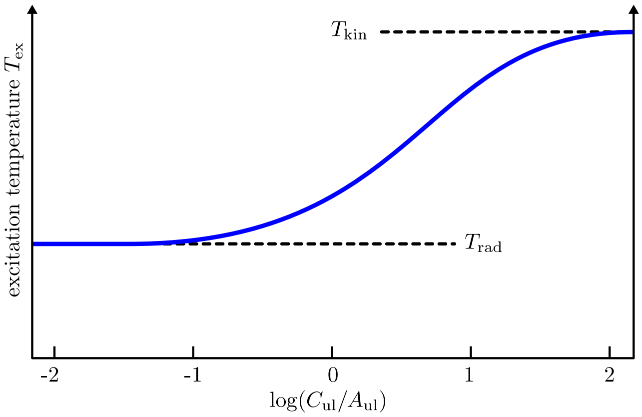

Figure 2.20.: Excitation temperature $T_{\rm ex}$ of a molecule in dependence on the ratio of collisional to radiative downward transitions $C_{\rm ul}/A_{\rm ul}$.

Both Types of Transitions

In the intermediate regime with a mix of both collisional and radiative transitions, the excitation temperature $T_{\rm ex}$ is also given by a mix of the radiation temperature $T_{\rm rad}$ and kinetic temperature $T_{\rm kin}$. For its calculation, we can use the Equation (2.64) and derive after some tedious calculations, and the use of Equations (2.65), (2.69), (2.70), and (2.71)

$$\frac{n_{\rm u}}{n_{\rm l}} = \frac{g_{\rm u}}{g_{\rm l}} \exp(-T_0/T_{\rm rad}) \frac{A_{\rm ul} + C_{\rm ul} \exp(-T_0/T_{\rm kin}) \left[\exp(T_0/T_{\rm rad}) - 1 \right]}{A_{\rm ul} + C_{\rm ul} \left[1 - \exp(-T_0/T_{\rm rad}) \right]} \tag{2.72}$$

where $T_0 \equiv \Delta E/k_{\rm B}$. Comparing this result with the definition of the excitation temperature $T_{\rm ex}$ in Equation (2.62) then gives us, together with the assumption that $T_{\rm rad}$, $T_{\rm kin}$ and $T_{\rm ex} \gg T_0$

$$T_{\rm ex} = T_{\rm kin} \frac{T_{\rm rad}\, A_{\rm ul}/C_{\rm ul} \; + \; T_0}{T_{\rm kin}\, A_{\rm ul}/C_{\rm ul} \; + \; T_0}. \tag{2.73}$$

This equation is shown in Figure 2.20, which shows the smooth transition in this intermediate regime from $T_{\rm rad}$ towards $T_{\rm kin}$. For dominance of radiative transitions $A_{\rm ul}/C_{\rm ul} \gg 1$ it is $T_{\rm ex} \rightarrow T_{\rm rad}$, whereas in the case of dominating collisions we have the case of $A_{\rm ul}/C_{\rm ul} \ll 1$ and $T_{\rm ex} \rightarrow T_{\rm kin}$. It should be noted, however, that Figure 2.20 has the ratio $C_{\rm ul}/A_{\rm ul}$ on the abscissa, as it then scales directly with the number density due to the proportionality $C_{\rm ul} \propto n_{\rm tot}$, and is therefore more intuitive.

As the collisional transition rate $C_{\rm ul}$ exhibits a dependence on the number density of the collisional partners, one can derive the so-called *critical density* for the case of $C_{\rm ul} = A_{\rm ul}$, that separates the radiative and the collisional regime, which is then simply given by

$$n_{\rm crit} = \frac{A_{\rm ul}}{\gamma_{\rm ul}}. \tag{2.74}$$

The critical density plays a crucial role for the quantitative analysis of the molecular line radiative transfer, which will be described in more detail in the following section.

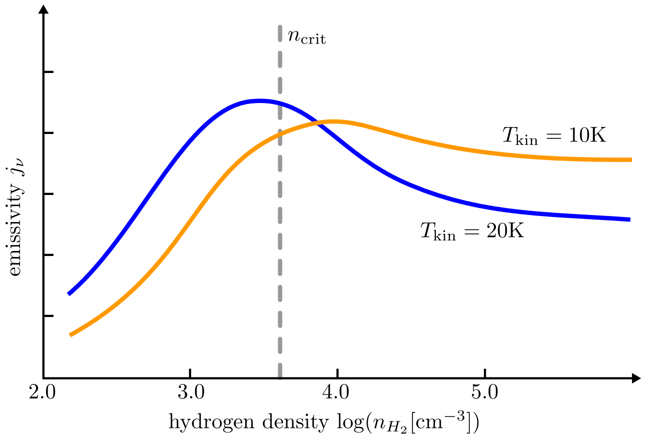

Figure 2.21.: Emissivity for CO(1-0) as obtained from numerical simulations (Stahler and Palla, 2005). The CO(1-0) critical density of $n_{\rm crit} \sim 3 \times 10^3\,\mathrm{cm}^{-3}$ is indicated as dashed vertical line.

2.5.3. Molecular Line Emission

Recalling Equation (2.13), the intensity of the Planck function is given by $B_\nu = j_\nu/\alpha_\nu$. In the case of molecular line transitions, the emissivity j_ν is directly related to the rate of spontaneous emission $A_{\rm ul}$, and is given by

$$j_\nu = \frac{h\nu_0}{4\pi}\, n_{\rm u}\, A_{\rm ul}\, \phi(\nu). \tag{2.75}$$

$\phi(\nu)$ is the line profile function with the condition

$$\int_0^\infty \phi(\nu)\mathrm{d}\nu = 1, \tag{2.76}$$

which is most conveniently defined by a Normal distribution.

As it was shown in Figure 2.20, the excitation temperature rises with increasing density. This then directly causes a higher population of the upper level $n_{\rm u}$, and thus a higher emissivity. For $C_{\rm ul}/A_{\rm ul} \gg 1$ the emissivity then levels off and reaches a constant value, according to $T_{\rm ex} = T_{\rm kin}$.

This is, however, only true in the simple two-level approximation. In the case of a real molecule, e.g., CO, the whole rotational ladder will be populated according to the excitation temperature. This then leads to a substantial depopulation of the upper level into even higher states at $n_{\rm H_2} \gg n_{\rm crit}$. The emissivity for such a real system is shown in Figure 2.21. At low densities ($n_{\rm H_2} \ll n_{\rm crit}$) every collisionally excited molecule will emit a photon before the next collision, as the relation $C_{\rm ul} \ll A_{\rm ul}$ holds. The excitation temperature is $T_{\rm ex} < T_{\rm kin}$, and therefore the line is said to be subthermally excited. The emissivity will rise with increasing number density $n_{\rm H_2}$, before it then reaches its maximum and drops off towards lower emissivity due to the depopulation of the upper level. This peak, as a rule of thumb, occurs approximately at the critical density $n_{\rm crit}$.

2.5.4. Column Density Derivation

The optical depth τ_ν, which is directly proportional to the column density, can be derived from the absorption coefficient α_ν, which in the case of line radiative transfer is given by

$$\begin{aligned}\alpha_\nu &= \frac{h\nu_0}{4\pi}\,(n_\mathrm{l}\,B_\mathrm{lu} - n_\mathrm{u}\,B_\mathrm{ul})\,\phi(\nu)\\ &= \frac{h\nu_0}{4\pi}\,n_\mathrm{l}\,B_\mathrm{lu}\left(1 - \frac{n_\mathrm{u}\,B_\mathrm{ul}}{n_\mathrm{l}\,B_\mathrm{lu}}\right)\phi(\nu).\end{aligned} \tag{2.77}$$

Using Equations (2.62), (2.70) and (2.71) we can further rewrite this, and then obtain

$$\alpha_\nu = \frac{c^2}{8\pi\,\nu_0^2}\,n_\mathrm{l}\,\frac{g_\mathrm{u}}{g_\mathrm{l}}\,A_\mathrm{ul}\left[1 - \exp\left(-\frac{h\nu_0}{k_\mathrm{B}T_\mathrm{ex}}\right)\right]\phi(\nu) \tag{2.78}$$

from which we can derive the optical depth by integration along the line of sight, which then yields

$$\tau_\nu = \frac{c^2}{8\pi\,\nu_0^2}\,\frac{g_\mathrm{u}}{g_\mathrm{l}}\,A_\mathrm{ul}\left[1 - \exp\left(-\frac{h\nu_0}{k_\mathrm{B}T_\mathrm{ex}}\right)\right]\phi(\nu)\int_0^{s_0} n_\mathrm{l}\,\mathrm{d}s \tag{2.79}$$

where the integral is the column density of molecules in the lower state N_l. Rewriting Equation (2.79) then gives

$$N_\mathrm{l} = \frac{8\pi\,\tau\,\Delta\nu}{A_\mathrm{ul}}\,\frac{\nu_0^3}{c^3}\,\frac{g_\mathrm{l}}{g_\mathrm{u}}\left[1 - \exp\left(-\frac{h\nu_0}{k_\mathrm{B}T_\mathrm{ex}}\right)\right]^{-1}, \tag{2.80}$$

where we now focus on the line centre at ν_0, and the profile function is substituted by $\phi(\nu_0) \sim 1/\Delta\nu = c/(\nu_0\Delta v)$. From the column density in one state, as it is given in Equation (2.80), one can now derive the total column density in all states by acknowledging that only a fraction of all molecules is found in this lower level. This fraction of molecules is given by

$$\frac{N_\mathrm{l}}{N_\mathrm{tot}} = \frac{g_\mathrm{l}\,\exp(-E_\mathrm{J}/k_\mathrm{B}T_\mathrm{ex})}{Z} \tag{2.81}$$

where E_J is the energy level of this state, which is given by Equation (2.60), and Z is the partition function of this system, which is simply the sum over all states, and therefore is

$$Z = \sum_{J=0}^{\infty} g_\mathrm{J}\,\exp\left(-\frac{E_\mathrm{J}}{k_\mathrm{B}T_\mathrm{ex}}\right) \tag{2.82}$$

From Equation (2.81) one can then derive the total column density of a molecule, which is then

$$N_\mathrm{tot} = \frac{8\pi\,\tau\,\Delta v}{A_\mathrm{ul}}\,\frac{\nu_0^3}{c^3}\,\frac{g_\mathrm{l}}{g_\mathrm{u}}\left[1 - \exp\left(-\frac{h\nu_0}{k_\mathrm{B}T_\mathrm{ex}}\right)\right]^{-1}\frac{Z}{g_\mathrm{l}}\,\exp\left(\frac{h\,B\,J(J+1)}{k_\mathrm{B}T_\mathrm{ex}}\right). \tag{2.83}$$

Although Equation (2.83) looks intriguingly simple, it still contains a lot of unknown quantities, namely the optical depth τ and the excitation temperature T_{ex}, which cannot be obtained from single line observations.

However, one can utilise simultaneous observations of two isotopic molecules, and the textbook example is in many cases ^{12}CO and ^{13}CO, of which the first one is usually optically thick in molecular clouds, whereas the latter one is in most cases optically thin. If this second condition is not met, one can extend this analysis to other, even rarer isotopes of CO (C^{18}O, C^{17}O, …).

In order to derive the column density of a molecular species, some conditions have to be met:

1. All molecules from both isotopes along the line-of-sight can be described by the same excitation temperature T_{ex}.
2. The optically thick component is $\tau \gg 1$, and the optical thin component must have $\tau \ll 1$.
3. The two isotopes have a constant abundance ratio.

Of course, the conditions are not always met. In these cases, the following analysis then should be seen as a low-order estimate of the column density.

Before starting the analysis, the equation of radiative transfer has to be modified. For analysis of molecular lines, in the first step the baseline is subtracted. Therefore, Equation (2.15) has to be expanded, and when it is rewritten in terms of temperature it reads

$$T_{\mathrm{b}} = T_0 \left[f(T_{\mathrm{ex}}) - f(T_{\mathrm{bg}}) \right] (1 - \mathrm{e}^{-\tau}), \tag{2.84}$$

where T_{bg} is the background temperature (which is generally set to 2.7 K to match the temperature of the cosmic microwave background), $T_0 = h\nu/k_{\mathrm{B}}$, and we have introduced the abbreviation $f(T) = [\exp(T_0/T) - 1]^{-1}$. It immediately becomes obvious that from the optical thick line (i.e., $1 - \mathrm{e}^{-\tau} \sim 1$) one can directly derive the excitation temperature T_{ex} by rewriting Equation (2.84)

$$T_{\mathrm{ex}} = \frac{T_0}{\ln\left(1 + \left[T_{\mathrm{thick}}/T_0 + f(T_{\mathrm{bg}})\right]^{-1}\right)}, \tag{2.85}$$

where T_{thick} is the peak temperature of the optically thick component. Using assumption (1), we can then derive the optical depth of the optically thin line from Equation (2.84)

$$\tau_{\mathrm{thin}} = -\ln\left(1 - \frac{T_{\mathrm{thin}}}{T_0\,[f(T_{\mathrm{ex}}) - f(T_{\mathrm{bg}})]}\right). \tag{2.86}$$

Knowledge of both the optical depth τ_{thin} and the excitation temperature T_{ex}, alongside with the molecular constants then can be fed into Equation (2.83) to derive the column density of the optically thin line. In case the abundance ratio is known, this can then further be converted into the column density of the optically thick component.

3

Star Formation in the Taurus Filament L 1495: From Dense Cores to Stars

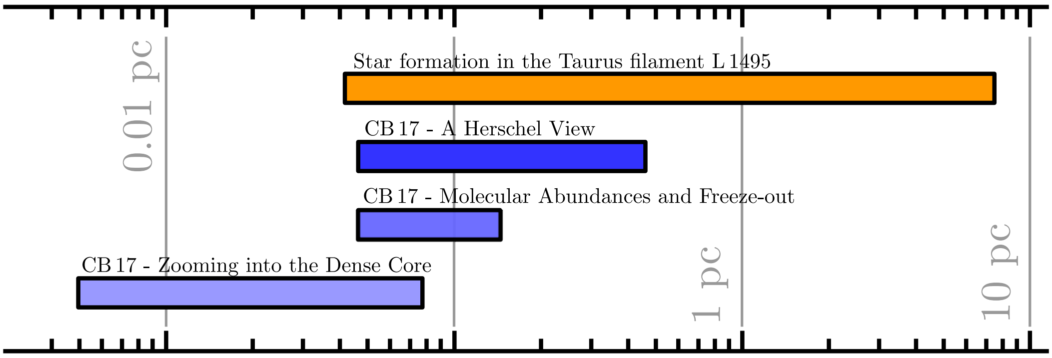

> Whoopee! Man, that may have been a small one for Neil, but that's a long one for me.
>
> — *Pete Conrad, Apollo 12, 3rd man on the Moon*

OUTLINE:

This chapter is based on a paper, which is published in the Astrophysical Journal (Schmalzl et al., 2010). §3.1 gives a quick introduction into the scientific field, and in §3.2 we give an overview of the observations and data reduction. In §3.3 we present our NIR extinction map of unprecedented depth and resolution, and derive the dense core population, which is discussed in section §3.4. Finally, the conclusions and summary follow in §3.5.

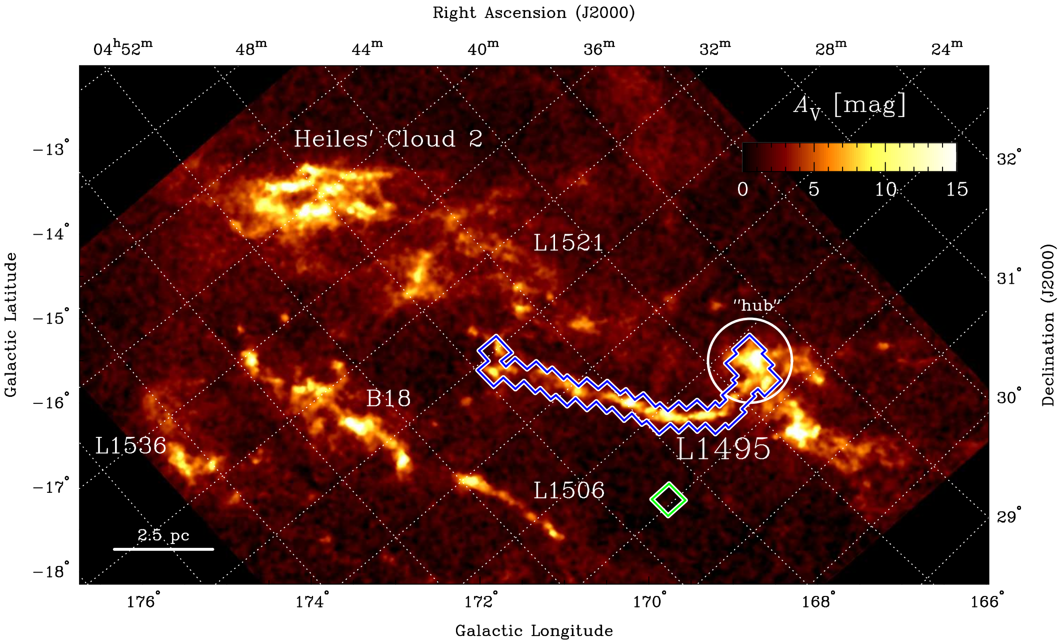

Figure 3.1.: Extinction map of the Taurus Molecular Cloud (Kainulainen et al., 2009) derived from 2MASS data. The circle marks the centre of the *hub-filament* system in L 1495 (Myers, 2009) with three filaments emanating towards the east, south-west and west. The solid blue line marks the region of our Omega2000 observations in L 1495, and the green line indicates the position of the control field to the south of it.

3.1. Introduction

Filaments appear to be common structural features in both quiescent and star-forming molecular clouds. In particular, recent observations of molecular clouds with *Herschel* (Pilbratt et al., 2010) have signified the role of filaments as a momentous, perhaps even dominant mode of star formation (e.g., Henning et al., 2010; Molinari et al., 2010; Men'shchikov et al., 2010). However, their formation and small scale structure is still not well understood and under debate (see, e.g., Myers, 2009, and references therein). Schneider and Elmegreen (1979) noted that filaments tend to fragment into equally spaced condensations of sizes $\sim 10^0$ pc. These clumps, in turn, consist of even smaller, gravitationally bound entities, namely cores, of sizes $\sim 10^{-1}$ pc, which is of the order of the local Jeans length. These cores are then believed to be the direct precursors of stars and binary systems (see review by Bergin and Tafalla, 2007).

Such a hierarchical structure can also be found in the Taurus Molecular Cloud (Figure 3.1), which is one of the closest star-forming regions at a distance of only 137 ± 10 pc (Torres et al., 2007), and therefore an excellent testbed to study the small scale structure of filaments. Large scale surveys in CO (Mizuno et al., 1995; Onishi et al., 1998; Narayanan et al., 2008) and mid-infrared dust emission (Rebull et al., 2010), alongside with dust extinction maps (Dobashi et al., 2005; Kainulainen et al., 2009; Lombardi et al., 2010) have built a detailed view of a complex network of filaments in Taurus, which are known to be the birth sites of stars (see reviews about star formation in Taurus by, e.g., Palla and Stahler, 2002; Kenyon et al., 2008). These filament are composed of clumps (Barnard et al., 1927; Lynds, 1962; Lee and Myers, 1999) with sizes of $\sim$ 1 pc, which host a plethora of cores with typical sizes of $\sim$ 0.1 pc. These have been detected, e.g., via molecular line observations tracing cold and dense gas with volume densities of $n_{\mathrm{H}_2} \gtrsim 10^5\,\mathrm{cm}^{-3}$, such as NH_3 (Jijina et al., 1999) and $\mathrm{H}^{13}\mathrm{CO}^+$ (Onishi et al., 2002, hereafter OMK02). Further down in this hierarchical structure, from dust continuum observations Sadavoy et al. (2010) found a population of pre- and protostellar cores, supposedly representing the scale of direct core-protostar connection. The Taurus Molecular Cloud is known to host $\gtrsim$ 250 Young Stellar Objects (YSOs, Rebull et al., 2010), and their distribution shows a strong correlation to the filamentary structures, i.e., their birth sites (Hartmann, 2002; Kenyon et al., 2008).

To further understand the connection between filamentary structures and star formation, it is essential to characterize the filament in high spatial resolution over a wide dynamic range. Molecular line species can be used as probes for column densities, but typically rather exhibit a narrow dynamical range. Larger dynamical range can be achieved by thermal dust emission observations, which are used to trace intermediate to high column densities, and dust extinction mapping, which is more sensitive at low to intermediate column density range (see, e.g., Pineda et al., 2008; Goodman et al., 2009; Vasyunina et al., 2009, for a comparison of different methods). The aforementioned observations allow to determine the structure of the low density clumps on one hand, and the core population detected by dense gas tracers on the other hand. However, to make a direct connection between the diffuse envelope structure and the denser cores, one preferably needs a single tracer with a uniform calibration, which covers both these regimes.

Therefore, the aim of this work is to create a column density map of L 1495 (Lynds, 1962) with unprecedented dynamical range and resolution with the aid of near-infrared (NIR) dust extinction mapping. NIR colors of stars in the background of clouds provide hundreds to thousands of pencil beam measurements of reddening, which can be smoothed out to construct maps of column density along a molecular cloud. This is the basis of NIR excess technique NICE and its derivatives (Lada et al., 1994; Lombardi and Alves, 2001; Foster et al., 2008; Lombardi, 2009), which obtain extinction measurements by correlating the observations from the science field with a nearby control field. The color excess with respect to this control field is then completely attributed to be caused by the molecular cloud. These methods typically probe extinctions $A_\mathrm{V} \sim 0.5\ldots50$ mag (e.g., Lombardi and Alves, 2001; Kainulainen et al., 2006, 2007; Román-Zúñiga et al., 2009), allowing us to examine both the detailed fragmentation of the filament into dense cores, and the envelopes surrounding them. Thus, the observations presented in this chapter will provide the most complete census of the small scale structures in the Taurus filament so far, and shed more light on the link between filaments and star-forming cores.

3.2. Observations and Data Reduction

We carried out NIR observations of the Taurus filament L 1495 with the Omega2000 camera at the Calar Alto 3.5m telescope. The camera is equipped with a HAWAII2

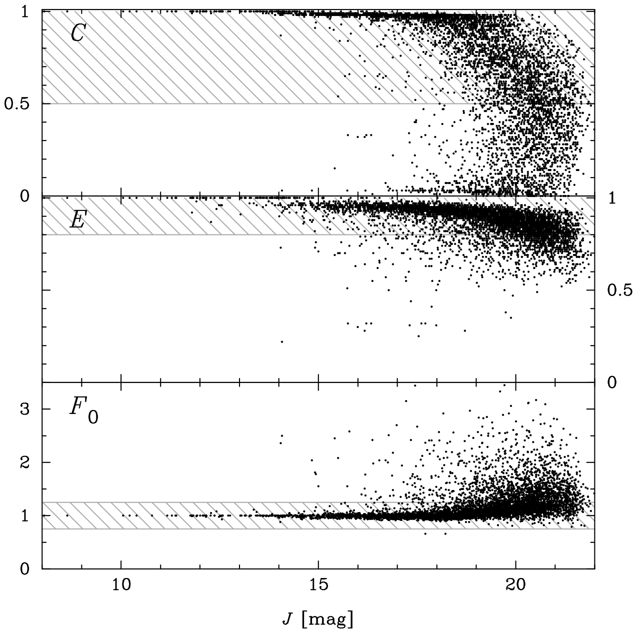

Figure 3.2.: Our star-galaxy separation is based on the stellarity index C, elongation E and its normalized FWHM F_0. The hatched areas indicate the regions populated by stars. Due to illustrative reasons, only a small part of our final catalog is shown.

HgCdTe detector that offers 2048×2048 pixels with a pixel scale of 0.45″ and a field of view of $15.4 \times 15.4'$. Observations were carried out during two observing periods from October 2004 to December 2005 (Quanz et al., 2010) and January to March 2009. In total, 21 science fields and 1 control field were observed in J, H, and K_s bands (1.2 μm, 1.6 μm, and 2.2 μm, respectively). The locations of the observed frames are shown in Figure 3.1.

The observations of a single Omega2000 field consisted of 30 dithered exposures, each having an integration time of 60 s. This resulted in total exposure times of 30 minutes per filter per field. We performed a standard NIR data reduction with the Omega2000 pipeline (Fassbender, 2003), including flatfield, dark, and bad pixel corrections, sky subtraction, and image registering. The world coordinate system (WCS) was appended to the frames with `koords` (Gooch, 1996) by matching the positions of at least 10 stars per frame to matching stars from the corresponding 2MASS image. This resulted to the rms accuracy of 0.1 px (or 0.045″) in all frames.

In addition to stars, a significant amount of background galaxies was expected to be detected in the frames. In order to disentangle these two types of sources from each other, we performed photometry using Sextractor (Bertin and Arnouts, 1996), which provides an automatic source classification via the so-called *stellarity index* (`CLASS_STAR`). In particular, photometry was run in a fully automated two-pass mode. First, Sextractor was run for the brightest stars only, in order to get an accurate estimate of the seeing, which is a crucial input parameter to get reliable measures of the stellarity index, and furthermore determined our choice of aperture size. Second, the actual photometry was performed, resulting in instrumental magnitude and uncertainty, position, the stellarity index C, elongation E (the inverse of the aspect ratio) and the parameter F_0, which is a source's FWHM normalized by the seeing.

Each source was classified as either star or galaxy following the classification scheme from Cantiello et al. (2005). In this scheme, a source is regarded as a *star* if it fulfills two out of

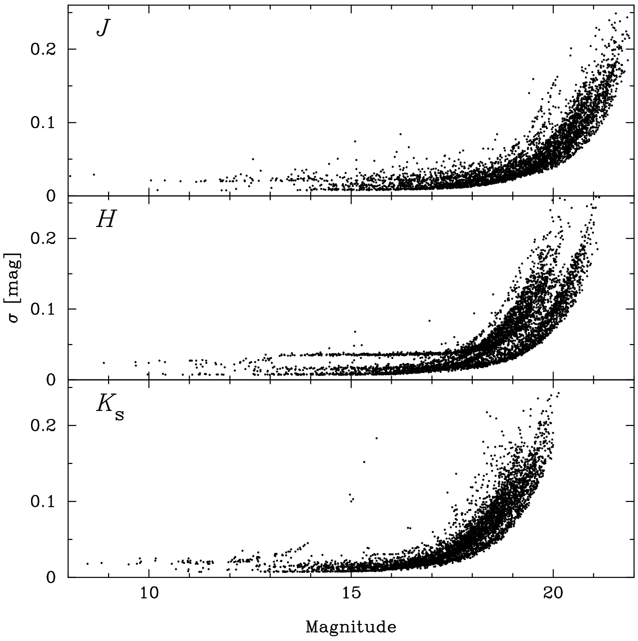

Figure 3.3.: Photometric uncertainties for our sources in the different filters. They contain contributions from the photometric error and the uncertainty of their individual photometric zero-point. This figure clearly shows the contributions from different frames, which differ in terms of sensitivity due to varying observing conditions. Due to illustrative reasons, only a small part of our final catalog is shown.

the three following conditions:

- $C > 0.5$
- $E > 0.8$
- $0.75 < F_0 < 1.25$

which are indicated as hatched regions in in Figure 3.2.

The photometric calibration was done for each frame separately by matching sources within the frame with stars from the 2MASS catalog, and determining photometric zero-points and color corrections using those stars. These catalogs in J, H and K_s were then merged, and sources with a detection in only one filter were rejected. Saturated stars were replaced by their 2MASS counterparts. The final catalog of L 1495 contains ~33,000 sources, of which 63% are classified as stars, according to our classification scheme. Photometric uncertainties for an excerpt from this catalog are shown in Figure 3.3. The median magnitudes for which $\sigma = 0.1$ mag are at $J = 20.6$ mag, $H = 19.4$ mag and $K_s = 18.8$ mag, which is on average 4 mag deeper than 2MASS, and emphasizes the depth of our observations.

3.3. Results

3.3.1. Dust Extinction in the Taurus Filament

We used the JHK_s photometry of the detected sources to derive dust extinction through the Taurus filament L 1495. In the following, we first shortly describe the adopted technique and then present the results.

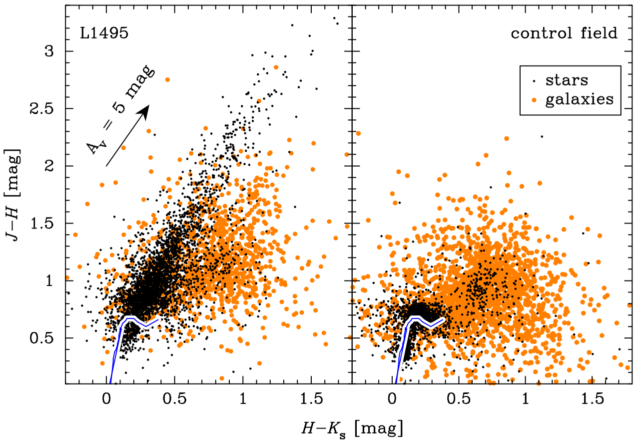

Figure 3.4.: NIR color-color diagram of the science (*left*) and the control field (*right*). A shift caused by an extinction of $A_V = 5$ mag (assuming the reddening law of Rieke and Lebofsky, 1985) is indicated by the arrow in the left panel. The continuous line shows an unreddened Zero-Age Main-Sequence (Siess et al., 2000) for comparison.

As mentioned earlier, in addition to stars there is a significant number of background galaxies among detected sources. The intrinsic colors of galaxies are very different from those of stars, and therefore theses two classes need to be treated separately in deriving extinction towards them. This difference is illustrated in Figure 3.4, which shows color-color diagrams of our reference (right panel) and one science field (left panel). Especially in the reference field, one can clearly see the different color distribution of stars and galaxies, as it is unaffected by the dust extinction from the molecular cloud. We note that there is a concentration of stars at $[H - K_S, J - H] = [0.7, 1.0]$ that is clearly outside the Zero-Age Main-Sequence (ZAMS) of stars. These sources could be YSOs, brown dwarfs, or even point like distant galaxies and or quasars.

Recently, Foster et al. (2008) presented a NIR color-excess mapping technique tailored specifically for inclusion of galaxies. In this technique, the *colors of stars* behind the cloud are compared to the intrinsic colors of stars in the reference field. In addition, the *magnitude dependent colors* of *galaxies* are compared to those in the reference field. This comparison yields a pencil-beam-like extinction value towards each source (for further details we refer to Foster et al., 2008). From these values we then generate a uniformly gridded extinction map by smoothing the data using a Gaussian kernel. Sigma-clipping removes sources with outliers in extinction, which might be caused by intrinsically different colors (e.g., YSOs, brown dwarfs, etc). For our map, we chose a resolution of $0.9'$ as a compromise between resolving the small scale structures in the filament and having low noise over the dynamical range covering most of the map. In this resolution, the map covered the dynamical range of $A_V = 1.5 \ldots 35$ mag. The noise of the final map depends on extinction, being $\sigma = 0.5$ mag at $A_V = 0$ mag and $\sigma = 2$ mag at $A_V = 35$ mag.

Figure 3.5 shows the resulting extinction map, with blow-ups of different regions of it shown in Figure 3.6. The map reveals, on one hand, a remarkably well defined, high aspect ratio filamentary structure, and on the other hand complex clumpy substructures within this filament. We note that within the mapped region we find six Barnard objects, namely the clumps B 211, B 213, B 216, B 217, and B 218 (which represent the *filament*), and B 10 (which forms the *hub*).

Within the filament, the lowest completely mapped iso-contour is at $A_V = 5$ mag. The total mass within this region is $280 \pm 19\,\mathrm{M}_{\odot}$, yielding a mass surface density of

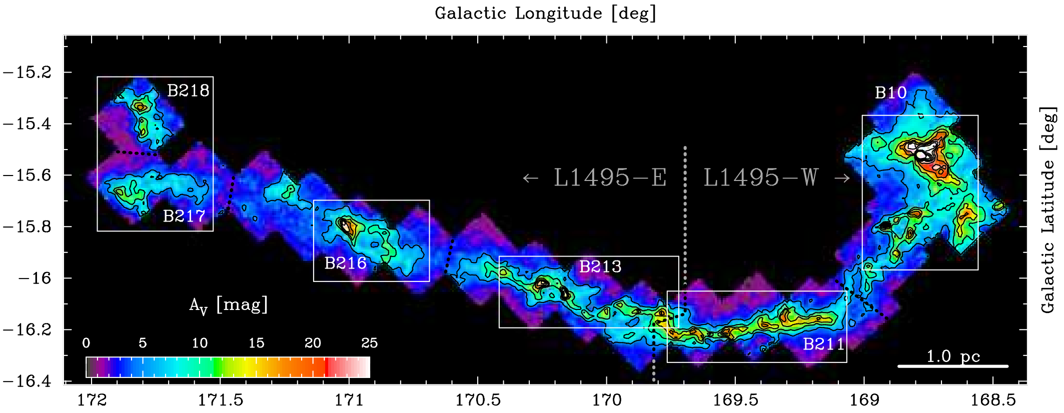

Figure 3.5.: Extinction map of the Filament L 1495 with a resolution of 0.9′ derived from deep NIR observations with Omega2000. Contours are plotted in steps of $A_V = 5$ mag. We separate the filament into different subregions, which conform to Barnard's Dark Objects (Barnard, 1927). The boxes indicate the positions of the zoom-ins shown in Figure 3.6.

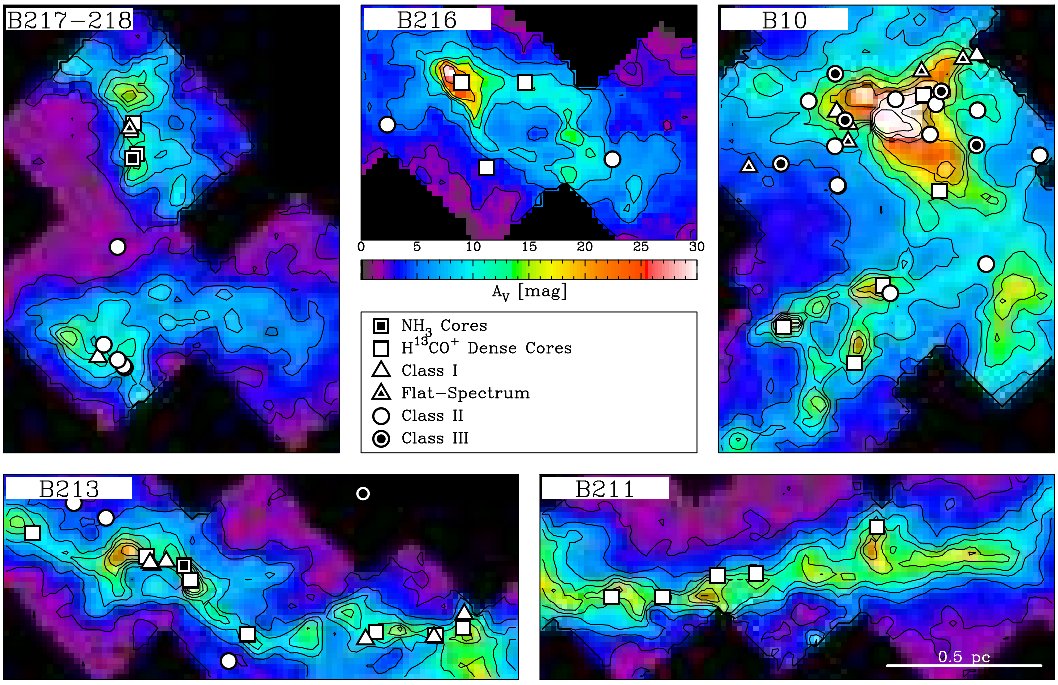

Figure 3.6.: Zoom-ins into the extinction map. The scale bar indicated in the bottom panel is common to all sub-plots. Contours are plotted in steps of 5σ each. The positions of dense cores mapped in NH_3 (Jijina et al., 1999), and $H^{13}CO^+$ (OMK02) are overplotted alongside YSOs (Rebull et al., 2010).

Table 3.1.: Barnard Objects in the L 1495 filament

Region	Mass [$M_\odot$]	Area [pc^2]	Σ_M [$M_\odot$ pc^{-2}]
B 211	84 ± 5	0.40 ± 0.06	210.7 ± 14.8
B 213	87 ± 6	0.48 ± 0.07	180.3 ± 12.6
B 216	57 ± 4	0.34 ± 0.05	169.8 ± 11.9
B 217	29 ± 2	0.19 ± 0.03	154.8 ± 10.8
B 218	22 ± 1	0.13 ± 0.02	174.8 ± 12.2
Total	280 ± 19	1.54 ± 0.22	182.3 ± 12.8

$\Sigma_M = 182 \pm 13\,M_\odot\,\mathrm{pc}^{-2}$. Table 3.1 lists these parameters also separately for the subregions. The mass was estimated from the extinction map by assuming all hydrogen in molecular form and the standard conversion factor of $N_{H_2}/A_V = 0.94\,10^{21}\,\mathrm{cm}^{-2}\mathrm{mag}^{-1}$ (Bohlin et al., 1978; Rieke and Lebofsky, 1985), which then yields the total hydrogen mass

$$\frac{M_H}{M_\odot} = 4.89\,10^{-3}\left(\frac{D}{137\,\mathrm{pc}}\right)^2\left(\frac{\theta}{0.45\,'}\right)^2\sum_i\left(\frac{A_{V,i}}{1\,\mathrm{mag}}\right) \tag{3.1}$$

where D is the distance to the cloud, θ is the pixel scale of the map, and $A_{V,i}$ are the extinction values of the individual pixels. Using a standard cloud composition of 63% hydrogen, 36% helium and 1% dust (Lombardi et al., 2006) one can assume the total mass from Equation (3.1) to be

$$M_{tot} = 1.37\,M_H. \tag{3.2}$$

The blow-ups shown in Figure 3.6 reveal numerous dense fragments with peak extinction values of $A_V \gtrsim 15$ mag. This population of *dense cores*[†] will be investigated in more detail in the following section. The main filament is strongly meandering along almost its entire length of 8 pc, and sometimes forms even ring-like structures (e.g., B 216, B 10). However, B 211 is different in that it exhibits a linear, narrow *bar* with a length of 1.5 pc and a median FWHM of only 0.11 pc. The inter-core regions also show considerably higher extinction values of $A_V \gtrsim 10$ mag in contrast to the other parts of the filament, where cores seem to be rather isolated.

3.3.2. The Dense Core Population

Identification and characterization of small-scale structures, such as cores, from 2D data (e.g., extinction maps or continuum observations) is a long-lasting, non-trivial problem, and several methods exist (e.g., Stutzki and Guesten, 1990; Williams et al., 1994). We adopted a two-step approach, which consisted of background removal and 2D thresholding.

[†] Our analysis (§3.4.2) shows that these are indeed dense cores, i.e. gravitationally bound entities with densities of $n_{H_2} \sim 10^4\,\mathrm{cm}^{-3}$. Therefore, we already introduce this term here, for reasons of consistency.

In the first step, we performed a subtraction of large-scale structures from the map using wavelet filtering. This resulted in a map describing structures only at spatial scales smaller than 0.14 pc ("cores-only" map, c.f. Alves et al. 2007). In the second step, we used the 2-dimensional thresholding algorithm Clumpfind2D (Williams et al., 1994) to identify a population of dense cores from the cores-only map. The algorithm works by first contouring the data (usually these levels are defined by a detection threshold, and subsequent contours with separations of multiples of the rms noise of the observations), and then searches for peaks of emission, which mark the cores. It then follows these down to lower intensities, assigning every pixel to a certain core (if any). Obviously, such an algorithm works best for isolated cores. Pineda et al. (2009) pointed out that for observations, where one has to deal with blending of cores, Clumpfind2D is very sensitive to the choice of input parameters. Therefore, we ran a set of calculations with different values of detection thresholds and level separations. We performed various tests, which included visual verification of the positions, sizes and shapes of the cores. A detection threshold and a level separation of 3σ was chosen to yield a representative core distribution. This is in agreement with the simulations by Kainulainen et al. (2009), in which such parameters resulted in an acceptable core identification.

However, the narrow *bar* in B 211 was not removed by the wavelet filter, eventually not allowing a look at the "naked cores". This prohibited a reliable recovery of the dense cores and their properties in B 211. We believe that this is caused by its different structure, which is discussed in more detail in § 3.4.1. Therefore, we did not consider this region in the following investigation. Furthermore, we also did not take into account B 10 because of its cluster-like nature and very high extinction, that does not allow to break the structure into separate cores (Kainulainen et al., 2009). Follow-up analysis using *dendrograms* (Rosolowsky et al., 2008) on 3D position-position-velocity molecular line data might allow us to also disentangle the dense core population in these two regions in the western part (L 1495–W). In this chapter, however, due to the limitations of 2D data we restrict our analysis to the dense core population in the eastern part (L 1495–E), which consists of regions B 213, B 216, B 217, and B 218.

In total 39 cores were detected in L 1495–E (Figure 3.7, Table 3.2). We calculated the core orientation together with the zeroth, first and second moment, which after suitable conversions conformed to the core mass, position and FWHM along the minor and major axis. Furthermore, we defined the effective radius as $r_{\rm eff} = (A/\pi)^{1/2}$, assuming spherical symmetry. We note that the mass is quite insensitive for the choice of the threshold level, changing on average only 15% when going from 3σ to 6σ. A few cores (#23, #29 and #35) extended beyond our mapped region. We used data from the 2MASS catalog to extend the map to cover these cores completely.

The nearest neighbor separation of the cores exhibits a strong peak at 0.13 pc with a dispersion of 0.04 pc, and all cores had at least one neighbor within 0.25 pc. Another approach to quantify the "clustering" is to measure the two-point correlation function (e.g., Johnstone et al., 2000; Hartmann, 2002), where the number of core pairs N with separations in the interval $[\log(r), \log(r) + {\rm d}\log(r)]$ is compared to the number N_0 in a sample, where cores were randomly distributed over the whole region. The two-point correlation function

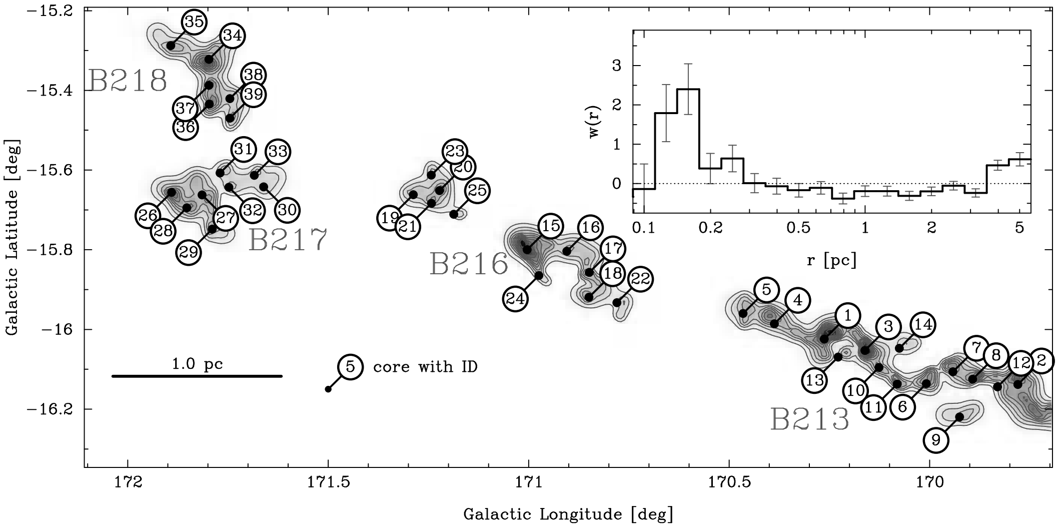

Figure 3.7.: The distribution of cores in L 1495–E. The core-IDs can be found in Table 3.2. In the top right corner, the inset depicts the two-point correlation function $w(r)$.

is then

$$w(r) = \frac{N}{N_0} - 1.$$

Applying this to our sample of cores, strong correlations, i.e., $w(r) > 0$, on separations of $r \sim 0.15$ pc and $r \sim 5$ pc are evident (Figure 3.7). The latter, large separation derives from small clusters of dense cores at both ends of L 1495–E, whereas the first one represents the separation between the individual cores inside these clusters. At our pixel scale of the map, a separation of 0.15 pc corresponds to $\sim$ 7 px, and is, therefore, well above the resolution limit.

Core masses range from $M_{\rm core} = 0.4 \ldots 10\,{\rm M}_\odot$. The total mass found in cores is $104 \pm 16\,{\rm M}_\odot$, which makes up ~50% of the total mass in L 1495–E (as defined by the $A_{\rm V} = 5$ mag contour). We derived mean core densities $\rho = 3\,M_{\rm core}/(4\,r_{\rm eff}^3)$, and hydrogen

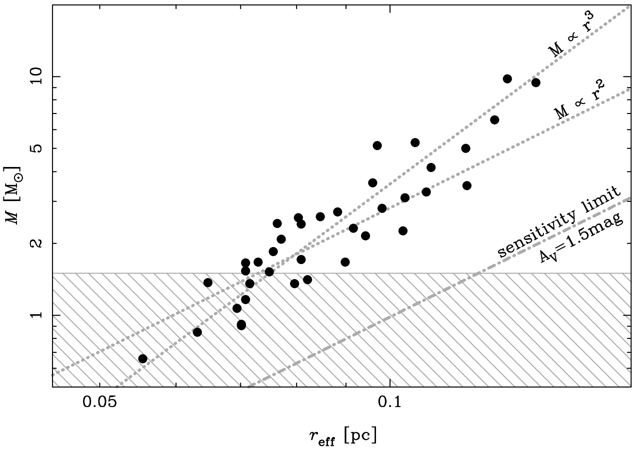

Figure 3.8.: Mass-size relation for our cores. The hatched area marks the region of incompleteness. The dotted lines represent the cases of constant volume density $M \propto r^3$ and column density $M \propto r^2$.

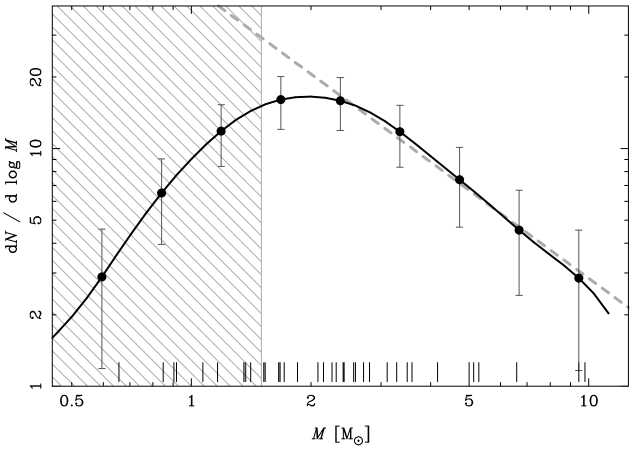

Figure 3.9.: The Dense Core Mass Function (DCMF) of L 1495–E, which was obtained by smoothing the core masses (indicated as vertical dashes along the abscissa) with a Gaussian kernel with FWHM = 0.3 dex. Points with error bars are plotted in separations of 50% of the FWHM. The dashed line shows the power law fit with slope $\Gamma = 1.2 \pm 0.2$ for $M > 2.0\,\mathrm{M}_\odot$. The hatched area indicates the region of incompleteness.

number densities $n_{\mathrm{H}_2} = \rho/(\mu\, m_{\mathrm{H}})$, where m_{H} is the proton mass and $\mu = 2.34$ the mean molecular weight per hydrogen molecule, assuming a molecular cloud with standard composition (Lada et al., 2008). The frequency distribution of the derived number densities closely follows a Gaussian distribution with $n_{\mathrm{H}_2} = 14.3\,10^3\,\mathrm{cm}^{-3}$ and a dispersion of $4.1\,10^3\,\mathrm{cm}^{-3}$.

Table 3.2.: Dense Cores in L 1495–E

ID #	l [deg]	b [deg]	M_{core} [$M_\odot$]	r_{eff} [pc]	n_{H_2} [$10^4\,\mathrm{cm}^{-3}$]	Aspect Ratio R
	B 213					
1	170.26	-16.02	9.4	0.14	1.4	1.6
2	169.78	-16.14	5.3	0.11	1.8	1.2
3	170.16	-16.05	5.1	0.10	2.3	1.5
4	170.39	-15.99	5.0	0.12	1.2	1.7
5	170.47	-15.96	3.1	0.10	1.2	1.1
6	170.01	-16.14	2.7	0.09	1.6	1.2
7	169.94	-16.11	2.6	0.08	1.8	1.1
8	169.89	-16.12	2.4	0.08	1.9	1.2
9	169.93	-16.22	2.3	0.10	0.9	2.1
10	170.13	-16.10	1.8	0.08	1.8	1.3
11	170.08	-16.14	1.7	0.07	1.8	1.7
12	169.83	-16.14	1.5	0.07	1.8	2.1
13	170.23	-16.07	1.4	0.08	1.1	2.6
14	170.08	-16.05	0.9	0.07	1.1	1.2
	B 216					
15	171.00	-15.80	9.8	0.13	1.7	1.3
16	170.90	-15.80	3.3	0.11	1.0	1.7
17	170.85	-15.86	2.8	0.10	1.2	1.6
18	170.85	-15.92	2.3	0.09	1.2	1.6

Table 3.2.: Dense Cores in L 1495–E

ID #	l [deg]	b [deg]	$M_{\rm core}$ [$M_\odot$]	$r_{\rm eff}$ [pc]	$n_{\rm H_2}$ [10^4 cm^{-3}]	Aspect Ratio R
19	171.29	-15.66	1.7	0.08	1.3	1.2
20	171.22	-15.65	1.7	0.07	1.9	1.2
21	171.24	-15.68	1.4	0.06	2.1	1.3
22	170.78	-15.93	0.9	0.07	1.1	1.6
23	171.24	-15.61	0.8	0.06	1.4	1.3
24	170.97	-15.86	0.7	0.06	1.6	1.4
25	171.19	-15.71	0.4	0.05	1.5	2.1
	B 217					
26	171.89	-15.66	4.2	0.11	1.3	1.2
27	171.81	-15.66	3.6	0.10	1.7	2.4
28	171.85	-15.69	2.6	0.08	2.0	1.3
29	171.79	-15.75	2.2	0.09	1.1	1.5
30	171.66	-15.64	1.7	0.09	1.0	1.8
31	171.77	-15.61	1.4	0.08	1.1	2.0
32	171.75	-15.64	1.2	0.07	1.4	1.7
33	171.68	-15.61	1.1	0.07	1.3	2.5
	B 218					
34	171.80	-15.32	6.6	0.13	1.3	1.6
35	171.89	-15.29	3.5	0.12	0.8	2.1
36	171.80	-15.43	2.4	0.08	2.2	1.1
37	171.80	-15.39	2.1	0.08	1.9	1.3
38	171.75	-15.42	1.5	0.07	1.5	1.4
39	171.75	-15.47	1.4	0.07	1.5	1.3

In Fig. 3.8, we show the mass-size relation of the cores in our sample. For reference, the figure also shows the sensitivity limit of $A_{\rm V} = 1.5\,$mag for an isolated, flat and spherical core. Lada et al. (2008) derived a slope of of $M \propto r_{\rm eff}^{2.6}$ for the dense cores of the Pipe Nebula. Due to the low number of cores and the strong influence of the completeness limit on the fit, we rather show representative relations with constant column density ($M \propto r_{\rm eff}^2$), which would be predicted for clouds obeying Larson's laws (Larson, 1981), and constant volume density ($M \propto r_{\rm eff}^3$), which would be expected in case of constant thermal pressure and kinetic temperature. However, with the data at hand we cannot rule out one or the other model.

The Dense Core Mass Function (DCMF), which is the number of cores per logarithmic mass interval $\mathrm{d}N/\mathrm{d}\log(m) \propto m^{-\Gamma}$, exhibits its maximum at $\sim 2.0\,\mathrm{M}_\odot$, and falls off to both the low-mass and high-mass ends (Figure 3.9). This peak could be either true, or simply be caused due to incompleteness. However, estimating the completeness and accuracy of the DCMF is not a trivial task (see e.g., Kainulainen et al., 2009; Pineda et al., 2009). This is

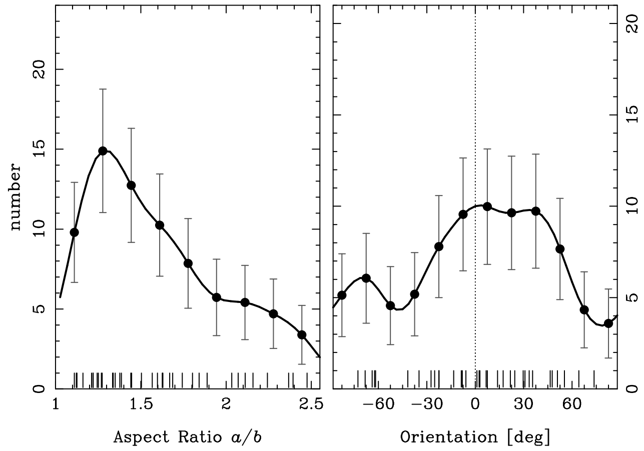

Figure 3.10.: *left panel:* Distribution of aspect ratios *R*, which was obtained by smoothing the data points (indicated as vertical dashes on the abscissa) with a Gaussian kernel of FWHM = 0.3. Data points are plotted in steps of 50% of the FWHM. — *right panel:* Distribution of core orientations with respect to the filament. The FWHM for the Gaussian kernel was chosen to be 30 °.

partly due to the inability of the adopted algorithm to detect cores from the variable, more extended column density component. Partly it is also due to the noise in the map, which makes mass determination of low-mass cores significantly less accurate than for high-mass cores. In an analysis similar to this paper, Kainulainen et al. (2009) analyzed the accuracy derived for the cores in the Pipe Nebula, and concluded the DCMF to be accurate above about $1.2\,M_\odot$. By comparing the noise levels within these two maps we roughly estimate the DCMF to be accurate for $M_{\rm core} \geq 1.5\,M_\odot$. A power-law fit to the DCMF above this completeness limit yields an exponent $\Gamma = 1.2 \pm 0.2$. This slope agrees with the results of OMK02, which found $\Gamma = 1.5 \pm 0.3$ for $3 < M/M_\odot < 20$. Slopes of $\Gamma \sim 1.2$ are also commonly observed in other star-forming regions (e.g. Motte et al., 1998; Rathborne et al., 2009; André et al., 2010).

The distribution of aspect ratios *R*, which is defined as the ratio of the major vs. the minor axis a/b, is strongly skewed. The mode of the distribution is found to be $R = 1.3$, whereas the mean aspect ratio is found to be $R = 1.5$, with a dispersion of 0.4 (Figure 3.10, *left panel*). Within the region of our observations, we find five cores from the sample of optically selected cores from Lee and Myers (1999). Three of these cores were classified as round ($R = 1$), and the remaining two had only moderate aspect ratios of $R \sim 1.8$. Compared to the all-sky sample of 406 cores from Lee and Myers (1999) with $R = 2.4 \pm 0.1$, the cores in Taurus are therefore only moderately elongated.

We also considered the orientation of the cores with respect to the filament. Due to its meandering nature, this is not a trivial task. Therefore, we first defined the baseline of the filament by setting points along its path, and then interpolated between these points using a cubic spline function. The orientation angle of the core with respect to this baseline was then obtained, and we find that the 39 cores seem to have a slight tendency to align with the filament. However, a KS-test results in a probability of $p = 0.46$ that this distribution is drawn from a uniform distribution. Given the large error bars on the individual orientations, which come along with the small aspect ratios, we can therefore not draw any secure conclusions about preferential or random core alignment in this filament.

3.3.3. Reddening Law

Algorithms like GNICER obtain the excess extinction of a source by comparing its position in the color-color diagram with respect to a control field. It is crucial for a proper estimation of extinction values to assume a reddening law (e.g., Rieke and Lebofsky, 1985; Indebetouw et al., 2005). For observations in JHK_s the ratio of the colour excesses

$$\alpha = \frac{E(J-H)}{E(H-K_\mathrm{s})} \tag{3.3}$$

is constant, and defines the direction of the displacement of a source in the color-color diagram when it is subject to extinction. Therefore, the colors $(J-H)$ and $(H-K_\mathrm{s})$ are connected by the linear relation

$$(J-H) = \alpha\,(H-K_\mathrm{s}) + \beta. \tag{3.4}$$

As unreddened ZAMS stars occupy only a small region of the color-color-diagram, the slope α could be simply obtained by fitting Equation (3.4) for all stars simultaneously. This, however, would give the high number of low-extinction stars too much weight compared to the low number of high-extinction stars. Therefore, we followed a procedure similar to Lombardi et al. (2006).

The first step was to obtain visual extinctions A_V of every star by converting color excesses $E(J-H)$ and $E(H-K_\mathrm{s})$ assuming the reddening law of Indebetouw et al. (2005). Stars are then binned in the color-color diagram according to their extinction A_V. These data points are then fitted according to Equation (3.4) to obtain a corrected slope. With the aid of this new slope, corrected extinction values A_V are then computed. This procedure is repeated until the slope α converges, which generally happened after 3-6 iterations. In order to decrease dependence on the bin size, we repeated this procedure for bin sizes ranging from $\Delta A_\mathrm{V} = 0.5\,\mathrm{mag} \ldots 1.5\,\mathrm{mag}$ in steps of 0.2 mag. The best fit slope α was then the variance weighted mean from all runs with different bin sizes.

For this analysis we considered only sources classified as stars without any photometry flags. The best fit slope was found to be $\alpha = 1.82 \pm 0.08$. This value is in very good agreement to the reddening laws of Lombardi et al. (2006, $\alpha = 1.82 \pm 0.03$) and Indebetouw et al. (2005, $\alpha = 1.78 \pm 0.15$).

3.4. Discussion

3.4.1. Star Formation in the Filament

Due to its proximity, the Taurus Molecular Cloud is an excellent target to study the connection between filamentary structure and star formation. In this chapter we present a new, high-resolution view of the L 1495 filament, allowing characterization of its density structure down to tenth-of-a-parsec scales. Indeed, as illustrated in Figures 3.5-3.7, L 1495 shows a highly fragmented small-scale structure and in some places extinctions, which are higher than can be traced by the chosen technique (i.e., $A_\mathrm{V} \gtrsim 35\,\mathrm{mag}$).

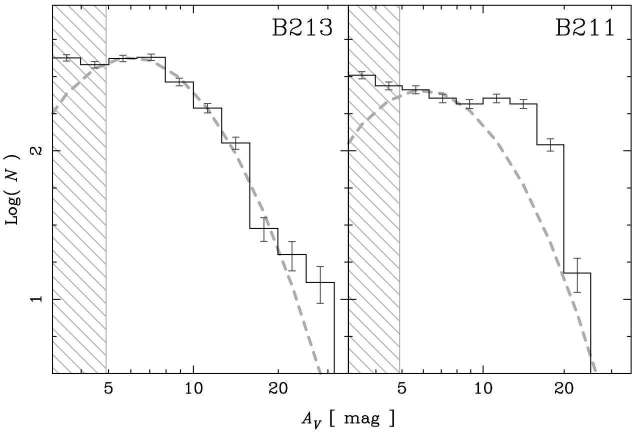

Figure 3.11.: Column density distribution of B 213 and B 211. Our observations do not completely cover regions with $A_V < 5$ mag (hatched area). The dashed line is the log-normal fit to B 213, which is shown as a scaled-down version in the right panel.

To estimate the star-forming potential of the filament, we calculated the mass-per-length $M_{\rm line}$. For an undisturbed filament, filaments with a mass exceeding the critical value of $M_{\rm line}^{\rm crit} = 15\,{\rm M_\odot\,pc^{-1}}$ are prone to filamentary fragmentation and collapse (Ostriker, 1964; Inutsuka and Miyama, 1997). In presence of magnetic fields, this critical value can be increased by a factor of 2 (Fiege and Pudritz, 2000a). Due to the presence of dense cores, L 1495 does not really fulfill the requirement of being an undisturbed filament. However, considering only the large-scale structure, which was filtered out in the wavelet transform, we derived a value of $M_{\rm line} = 16.8 \pm 0.2\,{\rm M_\odot\,pc^{-1}}$ for the whole filament. As this must be seen as a lower limit, as some of the mass is already bound in the dense cores, this value underlines the star-forming potential of the filament.

In Figure 3.6 we show the previously known YSOs[†]. Interestingly, while YSOs are generally found close to dense cores in the filament, the bar-like B 211 is completely devoid of them (Goldsmith et al., 2008). Given that the mass-per-length value in this particular region is also high ($M_{\rm line} = 15\,{\rm M_\odot\,pc^{-1}}$), and that it also harbors several $H^{13}CO^+$ cores signifying the presence of high density gas ($n_{\rm crit} = 10^5\,{\rm cm^{-3}}$), it can be argued to be well underway towards star formation.

More insight into the assembly of material in the non-star-forming part of the filament can be gained by examining the distribution of column densities. Therefore, in Figure 3.11 we compare the quiescent B 211 with B 213, in which star formation has already occurred. The column density distribution of B 213 shows a continuous decline towards higher extinctions. In contrast, B 211 shows a flat plateau at intermediate extinctions, falling steeply at extinctions higher than $A_V \sim 13$ mag. This excess with respect to the column density distribution of B 213 can be related particularly to *inter-core* regions. This is illustrated in Figure 3.12, which shows the contour of $A_V = 11$ mag for both B 211 and B 213. Clearly, in B 213 such extinction range is related to cores, while in B 211 it is more continuous and related to the material *surrounding* the cores. Therefore, we suggest that B 211 is not at all devoid of star-forming capability, but in an early stage of its evolution where the filament is fragmenting and the inter-core regions have not yet been cleared from material by accretion towards the cores. Given the high mass reservoir in the filament, such

---

[†] Rebull et al. (2010) separate YSOs into Class I, Flat-Spectrum, Class II and Class III. We include all YSOs, which were classified as *confirmed*, *probable*, and *possible* Taurus members in their paper.

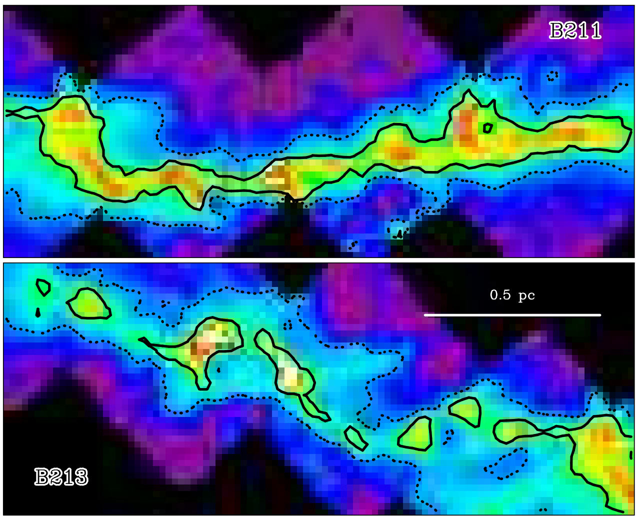

Figure 3.12.: Zoom-ins into the regions B 211 and B 213 with contours at $A_V = 5$ mag (dotted lines) and $A_V = 11$ mag (solid).

fragmentation is inevitably leading to star formation in B 211.

In L 1495–E, the star-forming part of the filament, we investigated the spatial distribution of YSOs with respect to the filament. Class I and Flat-Spectrum sources are found at extinctions of $A_V = 8.2 \pm 3.0$ mag, which is higher compared to the extinctions at the positions of Class II and III ($A_V = 5.2 \pm 2.6$ mag). The mean spatial separation of Class I and Flat-Spectrum sources from the filament was found to be only 0.06 pc, whereas older sources showed considerably larger mean distances. To verify whether this could be a pure evolutionary effect, we performed a simple Monte Carlo simulation to model the time dependence of the spatial distribution of sources. We distributed 10,000 test sources with a 3D velocity dispersion of $0.2\,\mathrm{km\,s^{-1}} \sim 0.2\,\mathrm{pc\,Myr^{-1}}$ along the baseline of the filament (defined in §3.3.2). The mean distance of sources from the filament was then measured as a function of time. The test sources started to show larger mean distances than Class I and Flat-Spectrum sources after ~ 1 Myr. A mean distance similar to that of Class II and Class III objects was reached after ~ 3.5 Myr, which is in good agreement with the evolutionary timescale of these sources (Luhman et al., 2003, 2009).

3.4.2. The Nature of the Dense Cores

In §3.3.2, we defined and examined the dense core population in L 1495–E. To test whether these cores are gravitationally bound entities, one can estimate the Bonnor-Ebert critical mass (Lada et al., 2008)

$$M_{\mathrm{BE}} \sim 1.82 \left(\frac{n_{\mathrm{H_2}}}{10^4\,\mathrm{cm^{-3}}}\right)^{-1/2} \left(\frac{T}{10\,\mathrm{K}}\right)^{3/2} M_{\odot}.$$

Within this framework, in cores with $M_{\mathrm{core}} > M_{\mathrm{BE}}$ thermal motions do not provide enough support against gravity, and in the absence of other forces they inevitably collapse and form protostars. With a mean density of $n_{\mathrm{H_2}} = 1.5\,10^4\,\mathrm{cm^{-3}}$ and a temperature of $T = 10\,\mathrm{K}$ (Terebey et al., 2010), we obtain $M_{\mathrm{BE}} = 1.5\,\mathrm{M_{\odot}}$. Calculating the Bonnor-Ebert critical mass for all cores allowed us to analyze the stability of each core separately (Figure 3.13).

Figure 3.13.: Ratio of core masses $M_{\rm core}$ to the Bonnor-Ebert critical mass $M_{\rm BE}$ plotted against core mass. $M_{\rm BE}$ was calculated individually for every core, assuming its respective density and a temperature of $T = 10\,{\rm K}$. Open circles represent cores which have a counterpart from the dense core sample of OMK02.

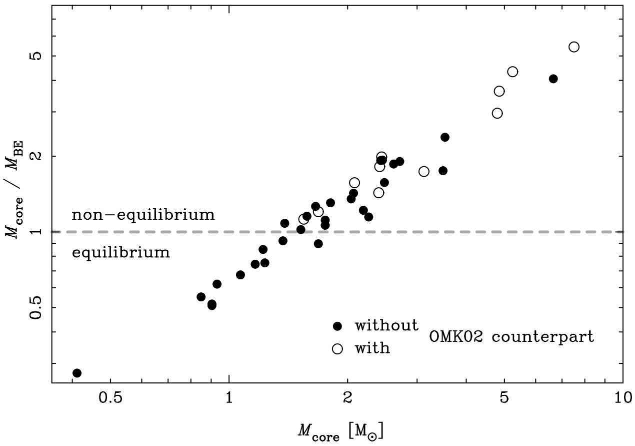

As a result we find that in L 1495–E, the majority of cores is prone to collapse. Without exception, all cores that coincide with a dense $H^{13}CO^+$ core (OMK02) exhibit $M_{\rm core} > M_{\rm BE}$. Apparently, in these cores the collapse has already led to a density enhancement, which can be traced by $H^{13}CO^+$ with its critical density of $n_{\rm crit} \sim 10^5\ {\rm cm}^{-3}$.

Compared, e.g., to the starless core population in the Pipe Nebula ($n_{\rm H_2} = 7.3\,10^3\ {\rm cm}^{-3}$, Lada et al. 2008), the cores in the Taurus filament are clearly denser by a factor of 2. For the cores in the Pipe Nebula, the Bonnor-Ebert critical mass is $\sim 2\,M_\odot$ (assuming $T = 10\,{\rm K}$), and only a few cores exceed this value and are prone to collapse. Cores in Taurus are also considerably more clustered than those in the Pipe Nebula. The nearest neighbor separation and two-point correlation function (Figure 3.7) show a clear peak at separations of the order of 0.13 pc, whereas cores in the Pipe Nebula show separations of 0.38 pc (Rathborne et al., 2009). Fragmentation in Taurus happens mainly only on a very distinct spatial scale. In the case of thermal fragmentation, such a preferential length scale would be determined by the Jeans length

$$\lambda_J = c_s \left(\frac{\pi}{G\rho}\right)^{1/2}, \tag{3.5}$$

where c_s is the local sound speed, G the gravitational constant, and ρ the mass density. Assuming $c_s = 0.19\,{\rm km\,s^{-1}}$ ($T = 10\,{\rm K}$) and the mean mass density of our sample of cores ($\rho = 5.8\,10^{-26}\,{\rm g\,cm^{-3}}$) we derive $\lambda_J = 0.18\,{\rm pc}$, which is only slightly larger than the peak in the nearest neighbor distribution of 0.13 pc. This is in contrast to the Pipe Nebula with a separation of 0.38 pc (Rathborne et al., 2009), which exceeds its local Jeans length ($\lambda_J \sim 0.25\,{\rm pc}$).

We note that due to the unknown inclination angle i we can only derive the *projected* nearest neighbor separation, but the true separation between cores remains unclear. For $i \sim 45°$ the true nearest neighbor separation would match the local Jeans length. VLBA observations allow accurate distance measurements of selected stars in the Taurus Molecular Cloud exist (Loinard et al., 2007; Torres et al., 2007, 2009), but do not allow to estimate of the true spatial orientation of the filament.

We note, that non-zero inclination angles would not only affect the derived nearest neighbor separation, but also the aspect ratio. Randomly oriented cores would yield the observed mean aspect ratio of $R = 1.5$, if the true aspect ratio is $R_{\mathrm{true}} \sim 1.7$ in the case of prolate, and $R_{\mathrm{true}} \sim 2.2$ for oblate cores, respectively (Myers et al., 1991). However, from a large set of dense cores and Bok globules, Ryden (1996) argues that cores are generally rather prolate than oblate. This shape is furthermore supported by theoretical simulations (Fiege and Pudritz, 2000b), where helical magnetic fields are able to produce a population of prolate dense cores through filamentary fragmentation. The aspect ratios of these cores are in good agreement with the sample of Ryden (1996), who finds $R = 2.0 \ldots 2.5$. Therefore, under the assumption of prolate cores, we find cores, which are slightly more spherical ($R_{\mathrm{true}} \sim 1.7$). The same trend is visible, when comparing the Taurus cores from the sample of Lee and Myers (1999) to their galactic average. Whether this is truly the case, or simply a projectional effect cannot be determined. Due to the core formation in the filament, we do not expect our sample of cores to be oriented randomly, but rather inheriting some preferential direction. However, the meandering nature of the filament does not allow to determine a common inclination angle. Considering these limitations, the elongation of our cores agrees reasonably well with theoretical predictions and other observations.

3.5. Summary

In this chapter, we study the star formation in the Taurus filament L 1495. In particular we present a NIR extinction map of this filament with unprecedented dynamical range ($A_V \sim 1.5 \ldots 35$ mag) and resolution ($0.9'$). The main results of our paper are as follows:

1. The extinction map of L 1495 reveals the highly fragmented nature of the filament, harboring a population of dense cores preferentially separated by the local Jeans length. The mass-per-length in the filament is $M_{\mathrm{line}} = 17\,\mathrm{M}_{\odot}\,\mathrm{pc}^{-1}$, indicative of its star-forming potential. We find, that the part of the filament that harbors no YSOs, namely B 211, shows an internal structure different from that of the rest of the filament. We argue, that B 211 is still younger than other parts of the filament, being still in process of filament fragmentation. Given its high mass reservoir, star formation will inevitably ensue.
2. The dense core population in L 1495–E was investigated in detail. A total of 39 dense cores with masses between $M_{\mathrm{core}} = 0.4 \ldots 10\,\mathrm{M}_{\odot}$ and densities of $n_{\mathrm{H}_2} = 1.5\,10^4\,\mathrm{cm}^{-3}$ were found. The majority of these cores exceeds the critical mass for collapse M_{BE}, and is therefore prone to collapse. The high-mass tail of the DCMF can be fitted with a power-law with an exponent $\Gamma = 1.2 \pm 0.2$, a form commonly observed also in other star-forming regions.

Acknowledgements

We thank Calar Alto Observatory for allocation of director's discretionary time to this programme. This publication makes use of data products from the Two Micron All Sky Survey (Skrutskie et al., 2006), which is a joint project of the University of Massachusetts and the Infrared Processing and Analysis Center/California Institute of Technology, funded by the National Aeronautics and Space Administration and the National Science

Foundation. We furthermore acknowledge the use of NASA's SkyView facility[†] located at NASA Goddard Space Flight Center (McGlynn et al., 1998) and the ViZier database located at CDS in Strasbourg, France (Ochsenbein et al., 2000).

[†] `http://skyview.gsfc.nasa.gov`

4

CB 17 – A Herschel View

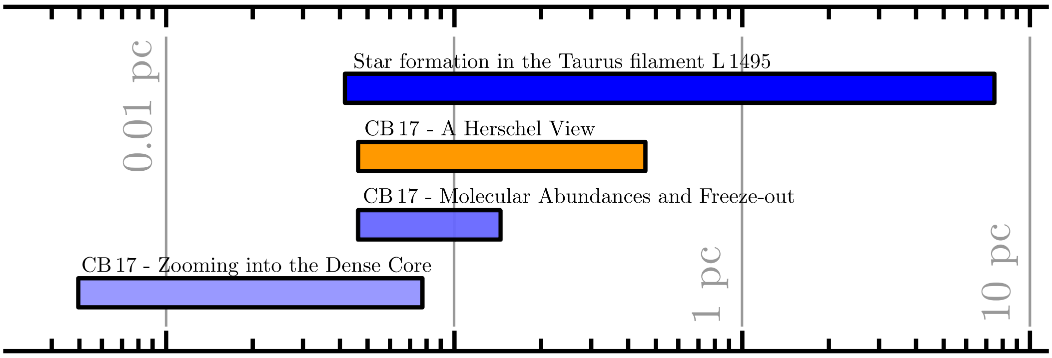

> Al is on the surface. And it's been a long way, but we're here.
>
> — *Alan Shepard, Apollo 14, 5th man on the Moon*

OUTLINE:

After the general study of the dense core population in Taurus in the previous chapter, I will now for the rest of the thesis focus on a single, isolated prestellar core, namely CB 17. In this chapter, I will first give a quick overview of it in §4.1. This chapter then focuses on the large-scale column density and temperature distribution in CB 17. The NIR and FIR observations are described and presented in §4.2 and §4.3, respectively. The results are then discussed in §4.4, and a summary follows in §4.5.

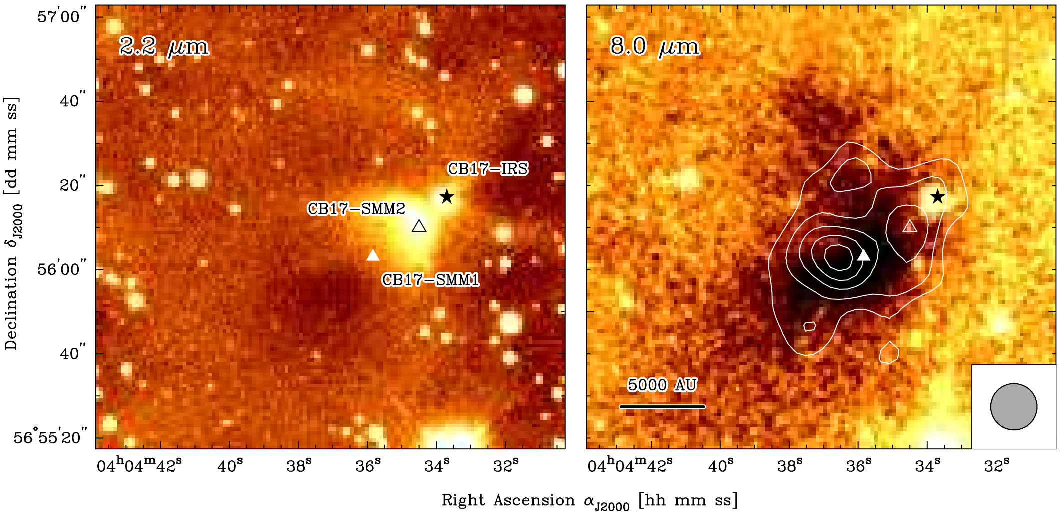

Figure 4.1.: The isolated prestellar core CB 17 as seen at 2.2 μm (*left panel*) and 8.0 μm (*right panel*). The symbols mark the sources CB 17-IRS (★), CB 17-SMM1 (▲) and CB 17-SMM2 (△) from Launhardt et al. (2010). An outflow of CB 17-IRS (X. Chen, private communication) causes the bright NIR reflection nebula at 2.2 μm. The right panel shows as contours the IRAM-30m 1.3 mm continuum, of which the beamsize is indicated in the bottom right corner.

4.1. Introduction

CB 17 (Clemens and Barvainis, 1988), also known as LDN 1389 (Lynds, 1962), is a small and slightly cometary-shaped globule (Figure 4.1). Launhardt et al. (2010) found that it hosts a prestellar core (CB 17-SMM1+2) and a Class I source (CB 17-IRS) at a projected distance of 22″. The original distance estimate of 600 pc from Clemens and Barvainis (1988), which was determined to be the mean distance to their sample of 248 cores, was revised by Launhardt and Henning (1997). These authors associated the globule with the Lindblad ring (Lindblad et al., 1973), which towards CB 17 is assumed to have a distance of 300 pc (Dame et al., 1987). HD 25347, a bright G5 III star at a distance of 210 ± 40 pc (F. van Leeuwen, 2007), is located about 11′ (0.65 pc at 210 pc) south of CB 17 and could be responsible for the cometary shape and diffuse cloudshine from the rim and tail of CB 17. Combining the possible associations of CB 17 with both the Lindblad Ring and HD 25347, we adopt a distance of 250 ± 50 pc for CB 17, which will be used throughout this work. In this case, the projected distance between the CB 17-SMM1 and CB 17-IRS conforms to ~ 5500 AU.

The roundish cloud core of CB 17 is associated with an IRAS point source (IRAS 04005+5647) that is detected only at 60 and 100 μm (F_{100} = 5.78 Jy, F_{60} = 0.91 Jy). Recently, it was also detected by the AKARI Infrared Satellite in all its four bands (F_{65} = 0.28 Jy, F_{90} = 0.96 Jy, F_{140} = 5.02 Jy, F_{160} = 1.37 Jy).

CB 17 has been studied extensively by various authors using different mm molecular line transitions. The core CB 17-SMM1 was found to have a mean kinetic gas temperature of $T_{\rm kin} \sim 10$ K (Lemme et al., 1996). Pavlyuchenkov et al. (2006, herafter PWLH06) compared a number of different molecular line maps of CB 17 with chemodynamical models. They derive a chemical age of 2 Myr, as well as the relative rotational, thermal, and turbulent energies, concluding that the core will most likely fragment. Indications for such fragmentation into two sources (CB 17-SMM1 and CB 17-SMM2) was found by Launhardt et al. (2010) in a 1.3 mm continuum map, which is shown in the right panel of Figure 4.1 as contours. CB 17 is thus one of those globules that contain two, or maybe even more, sources of different evolutionary stage within a few thousand AU. However, the nature of CB 17-SMM2 is more than unclear, as it is located in the centre of a NIR reflection nebula, but also coincides with a NIR, and a faint Spitzer IRAC point source.

However, there remains a plethora of open questions for CB 17, which we will try to answer in the next three chapters. In this chapter we will present maps of the temperature and density distribution derived from dust emission maps at sub(mm) wavelengths, and analyse the dust emission properties of CB 17. In the following chapters we will present a kinematic analysis, and an analysis of the variation of molecular abundances (Chapter 5) in comparison to the dust emission maps. Chapter 6 will then be dedicated to the dense core CB 17-SMM1, where we analyse its nature and small scale velocity structure with the aid of interferometric molecular line observations.

4.2. Observations and Data Reduction

4.2.1. Herschel Space Observatory

CB 17 was observed as part of the Herschel Guaranteed Time Key Programme "Earliest Phases of Star Formation" (EPoS; P.I. O. Krause) with the PACS (Poglitsch et al., 2010) and SPIRE (Griffin et al., 2010) instruments on board the Herschel Space Observatory (Pilbratt et al., 2010).

PACS 100 and 160 μm observations were performed on 23 February, 2010. We obtained two orthogonal scan maps with scan leg length of $\sim 7'$, using a scan speed of $20'' \mathrm{s}^{-1}$, with 30 repetitions each. The data were processed in a way similar to Stutz et al. (2010). The data were processed using the HIPE software package and highpass-filtering, using a large median filter filter window width of 104 samples (418″), to remove the effects of bolometer temperature drifts during the map acquisition. Furthermore, we mask out the bright central source before computing the high-pass mask. The SPIRE 250 μm standard processing L2 image flux level of 0.05 Jy beam^{-1} was used for the PACS 100 and 160 μm region mask, ensuring that the highpass median subtraction minimizes over-subtraction of source flux.

The SPIRE 250, 350 and 500 μm data were obtained on 13 February, 2010. A scan and cross-scan were obtained, for a total for total scan leg length of 9′ each, at the nominal scan speed of $30'' \mathrm{s}^{-1}$. The data have been processed within HIPE with the standard photometer script up to level 1. During baseline removal, we masked out the high-emission area in the centre of the field. We have used the Bendo et al. (2010) de-striping scheme to mitigate the effect of striping in the data.

To account for the unknown background flux level all images were zeroed by subtracting a constant offset from the images. This offset was calculated from two different control fields

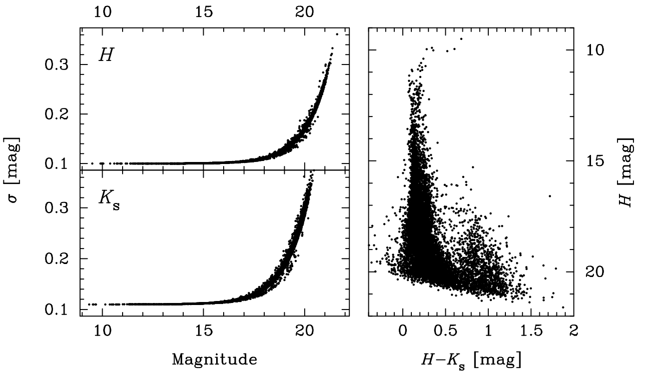

Figure 4.2.: Photometric uncertainties (*left row*) and colour-magnitude diagram (*right panel*).

to the south and to the west of the globule. Both regions exhibited the same background level in all images. Therefore, the final Herschel image contained only the excess emission of the globule above the local interstellar radiation field at each wavelength.

4.2.2. (Sub)mm Maps

In addition to the Herschel observations, we also included available sub(mm) data into our analysis. These are a SCUBA 850 μm map (which was obtained from the SCUBA Data archive), and a 1.3 mm continuum map, obtained with the MPIfR 7-channel bolometer at the IRAM-30m telescope. A more detailed description of these observations can be found in Launhardt et al. (2010).

4.2.3. NIR observations

CB 17 was also observed with the Omega2000 camera at the Calar Alto 3.5m telescope, which is equipped with a HAWAII2 HgCdTe detector, and offering 2048×2048 pixels with a pixel scale of 0.45″ and a field of view of 15.4′ × 15.4′. The observations in H, and K_s bands (1.6 μm, and 2.2 μm, respectively) were carried out on 31 January 2010, and due to the large field of view, a single pointing was sufficient.

In both filters the observations consisted of 60 dithered exposures, each having an integration time of 60 s. This resulted in total exposure times of 60 minutes per filter per field. A standard NIR data reduction was performed with the aid of the Omega2000 pipeline (Fassbender, 2003), which included dark, flatfield, and bad pixel corrections, sky subtraction, and image registering. The world coordinate system (WCS) was appended to the frames with `koords` (Gooch, 1996) by matching the positions of 10 stars per frame to matching stars from the corresponding 2MASS image. This resulted to the rms accuracy of 0.1 px (or 0.045″) in all frames.

As CB 17 is located at galactic latitude of only $b \sim 3°$, the stars are considerably crowded. Therefore, source extraction and photometry were performed with the IDL tool *starfinder* (Diolaiti et al., 2000). The PSF was extracted by modelling ten isolated, non-saturated point sources. The photometric zero-points were obtained by matching stars in our field to their 2MASS counterparts. As the H and K_s filters of Omega2000 and 2MASS coincide, no colour-correction was applied. Only sources with detections in both bands were considered for the final catalogue, which contained ~10,000 sources. The colour-magnitude diagram and the photometric uncertainties are shown in Figure 4.2. One can see the almost vertical line of main sequence stars, which are found at a relatively constant intrinsic colour $(H - K_s)_0 \sim 0.15$ mag. The population of faint sources with $H \gtrsim 17$ mag and $(H - K_s) \sim 1$ mag are most likely background galaxies, but could also be YSOs or evolved stars.

4.3. Results

4.3.1. NIR Extinction Map

From our deep NIR observations we obtained a dust extinction map of the dense core CB 17. Following Lada et al. (1994), the extinction along pencil-beams towards the background stars is directly estimated from the colour excess $E(H-K)$, which is calculated by assuming a constant intrinsic colour $(H - K)_0$ for Main Sequence stars. For the conversion of colour-excess to extinction A_K we used the extinction law of Rieke and Lebofsky (1985). These pencil-beam extinctions were then smoothed into a continuous map by convolving the data with a Gaussian beam of FWHM = 36.9″, which was chosen to match the beamsize of Herschel at 500 μm. However, one has to take into account that not all sources are Main Sequence stars, and therefore might have intrinsically different colour $(H-K)$, which is the case for YSOs, evolved stars, or galaxies. In order to exclude these sources, a σ-clipping was performed before averaging the extinction values to derive the mean extinction A_K.

The final dust extinction map is shown in the top right corner of Figure 4.3. The dense core is clearly visible and exhibits an almost spherical shape. The peak extinction is $A_K = 1.4$ mag, which conforms to an optical extinction of $A_V = 13$ mag. Extinction measurements towards single stars at the column density peak reveal even higher extinction values of $A_V \gtrsim 20$ mag. CB 17-SMM1 can be clearly associated with the regions of highest column densities, whereas CB 17-IRS is slightly offset.

4.3.2. Dust Emission Maps

Herschel PACS and SPIRE bands nicely cover the peak of the spectral energy distribution (SED) for objects at very low temperatures. Therefore, they can be used to get accurate maps of physical parameters like column density N_H, dust temperature, and dust properties by fitting SEDs for each pixel individually[†]. In order to do this all Herschel maps were convolved to a common resolution, which was set by the map with the coarsest resolution. This is in our case the Herschel 500 μm map with FWHM = 36.9″. For the Herschel images, convolution kernels from Gordon et al. (2008) were used, which are also provided online[†]. The SCUBA 850 μm and IRAM-30m 1.3 mm data, which were convolved with a

---

[†] Strictly speaking, the SED is νS_ν vs. ν, whereas we will generally fit, and also plot the S_ν vs. ν.

[†] `http://dirty.as.arizona.edu/~kgordon/mips/conv_psfs/conv_psfs.html`

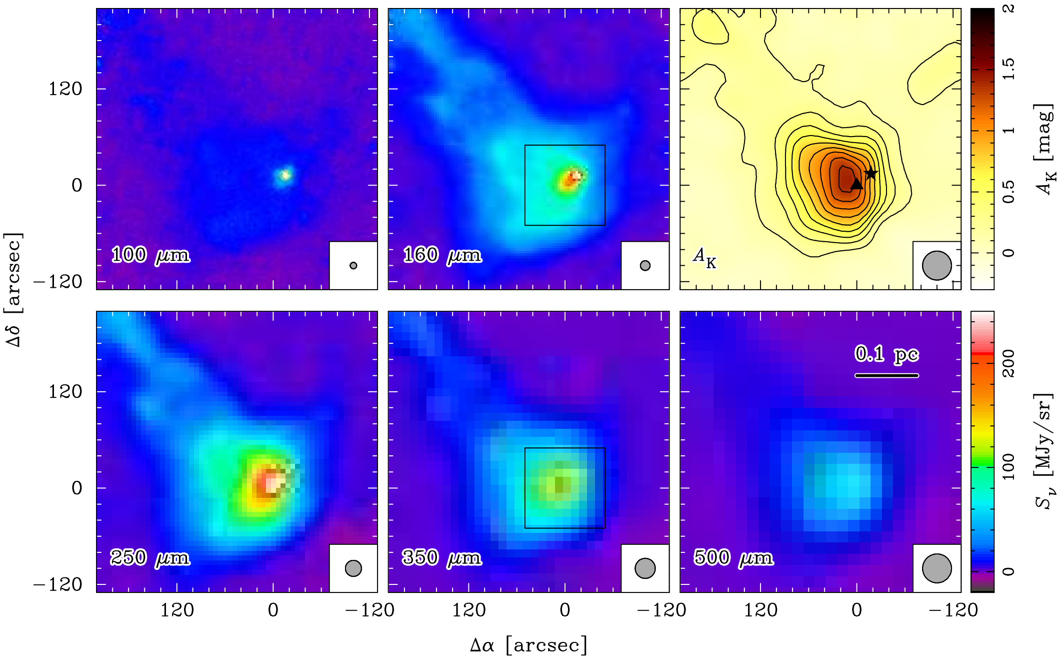

Figure 4.3.: Herschel dust emission maps at 100 μm, 160 μm, 250 μm, 350 μm, and 500 μm. The top right panel shows the NIR A_K dust extinction map with contours in steps of $3\sigma = 0.15$ mag. The respective beam sizes are indicated in the bottom right corner. Zoom-ins into the areas indicated as black boxes are shown in Figure 4.4.

Gaussian function of FWHM

$$\theta = \sqrt{(36.9'')^2 - (\theta_{\mathrm{instr}})^2}, \tag{4.1}$$

where θ_{instr} is the original instrumental FWHM of 14.9″ for SCUBA, and 11″ for IRAM-30m. The noise levels in the convolved maps were derived, and served as basis to define emission thresholds. In total we had measurements from seven different wavelengths at hand. Additional data from Spitzer IRAC bands (3.6 – 8.0 μm) was not taken into account, as for wavelengths considerably shorter than ∼ 50 – 100 μm emission starts to be strongly affected by non-thermal processes. Furthermore, Spitzer MIPS (24 – 160 μm) observations with its resolution and artefacts pose significant obstacles for this sort of spatially resolved analysis of extended emission. For all Herschel wavelengths we assumed the calibration to be accurate to 15%, whereas SCUBA and IRAM-30m data was downweighted by setting the uncertainty to 50%.

In addition, the Herschel data at 100 μm and 160 μm had to be colour corrected, as the SED for temperatures of the order of 10 K falls off very steeply in the PACS bands. Due to their extended bandwidth, the measured intensity does not correspond to the true intensity at the designated band centres of 100 μm and 160 μm, respectively. However, with the knowledge of the spectral response function of these filters one can obtain a model for the

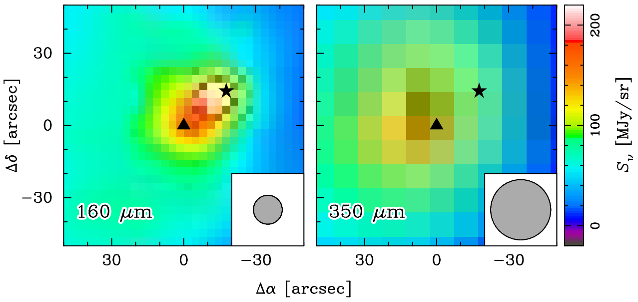

Figure 4.4.: Zoom-ins into 160 μm and 350 μm emission maps. The symbols mark the positions of CB 17-IRS (★) and CB 17-SMM1 (▲).

colour-correction. This is given by

$$S_{\nu,\mathrm{corr}} = \frac{S_\nu}{a + \left(\frac{20-T\,[\mathrm{K}]}{b}\right)^c}, \tag{4.2}$$

where S_ν is the measured specific intensity, and a, b, c are filter-dependent correction constants (Table 4.1). As the temperature is unknown, one can derive it iteratively by first fitting the temperature without colour-correction, before using this first estimate as input for the colour-corrected subsequent fits.

Table 4.1.: Colour-correction factors for the PACS filters.

Filter	a	b	c
PACS 100	1.04	11.8	2.4
PACS 160	0.94	16.5	3.0

Modified Blackbody Fit

In a first approach every pixel in the map was fitted independently by a modified blackbody (MBB), under the condition that at least 5/7 maps had an emission above the emission threshold. Due to our reduction scheme, i.e., the modelling of only the excess emission of the globule, the background emission had to be subtracted from Equation (2.15). Therefore, it corrects to

$$I_\nu = [B_\nu(T_\mathrm{los}) - B_\nu(T_\mathrm{bg})]\,(1 - \mathrm{e}^{-\tau_\nu}), \tag{4.3}$$

where T_los is the average line-of-sight (LOS) temperature, and T_bg is the temperature of the background emission, which is assumed to be the the cosmic microwave background ($T_\mathrm{bg} = 2.7\,\mathrm{K}$). The optical depth along the line-of-sight is given by

$$\tau_\nu = \frac{m_\mathrm{H}\, N_\mathrm{H}\, \kappa_\nu}{R_\mathrm{g/d}}, \tag{4.4}$$

where m_H is the proton mass, N_H is the hydrogen column density, κ_ν is the dust opacity, and $R_\mathrm{g/d} = 110$ (Sodroski et al., 1997) is the hydrogen-to-dust mass ratio. The drawback

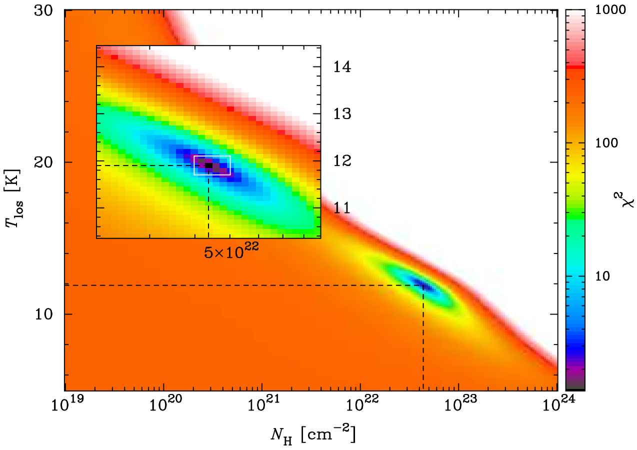

Figure 4.5.: χ^2 distribution map in parameter space. The inset depicts a zoom into the region around the minimum, which is indicated by the dashed lines. The white box indicates the uncertainty estimate.

of this procedure is, that we cannot account for any temperature variations along the line-of-sight, but rather derive an average line-of-sight temperature $T_{\rm los}$. One also has to bear in mind that $T_{\rm los}$ is furthermore affected by optical depth effects. This means that first of all, regions of relatively higher density will contribute more. Furthermore, for $\tau \gtrsim 1$ the derived temperature will be dominated by the near side of the cloud. Nevertheless, the MBB fitting allows us to get reasonable estimates of some cloud parameters like column density or size.

In a first step, we searched for the best fit pairs of column density $N_{\rm H}$ and temperature $T_{\rm los}$. Throughout this chapter, we always use the dust model of Ossenkopf and Henning (1994, OH94), unless noted differently. In particular, we used the configuration with a classical particle size distribution of Mathis et al. (1977, MRN), no coagulation and thin ice mantles. We fitted the parameter space within the range $N_{\rm H} = 10^{19} \ldots 10^{24}\,{\rm cm}^{-2}$ and $T_{\rm los} = 1 \ldots 30\,{\rm K}$ with resolutions of $\Delta N_{\rm H} = 0.02\,{\rm dex}$ and $\Delta T_{\rm los} = 0.1\,{\rm K}$.

The intensities I_ν for all possible combinations of $N_{\rm H}$ and $T_{\rm los}$ of the parameter space were calculated from Equation (4.3). The best fit parameters were determined by minimising χ^2, which is given by

$$\chi^2(N_{\rm H}, T_{\rm los}) = \sum_{i=1}^{N} \frac{[S_{\nu,{\rm i}} - I_{\nu,{\rm i}}(N_{\rm H}, T_{\rm los})]^2}{\sigma_i^2}, \tag{4.5}$$

where the index i indicates all measurements, which are above the emission threshold. An example for a χ^2 map of a region close to the column density maximum is shown in Figure 4.5, which is in its general shape similar to all other regions. Important for the interpretation of the results is the presence of a single minimum. Therefore, we do not have to deal with the possibility of multiple minima, which would add additional complexity to this problem. Under the assumption of Gaussian error distribution, the 1σ uncertainties for the individual parameters are defined by the maximum extent of the region in the parameter space, for which the relation

$$\chi^2 \leq \min(\chi^2) + 1 \tag{4.6}$$

holds. However, we find that in general we do find χ^2 values which are lower than expected for Gaussian error distribution. This might have its reason in the fact that the

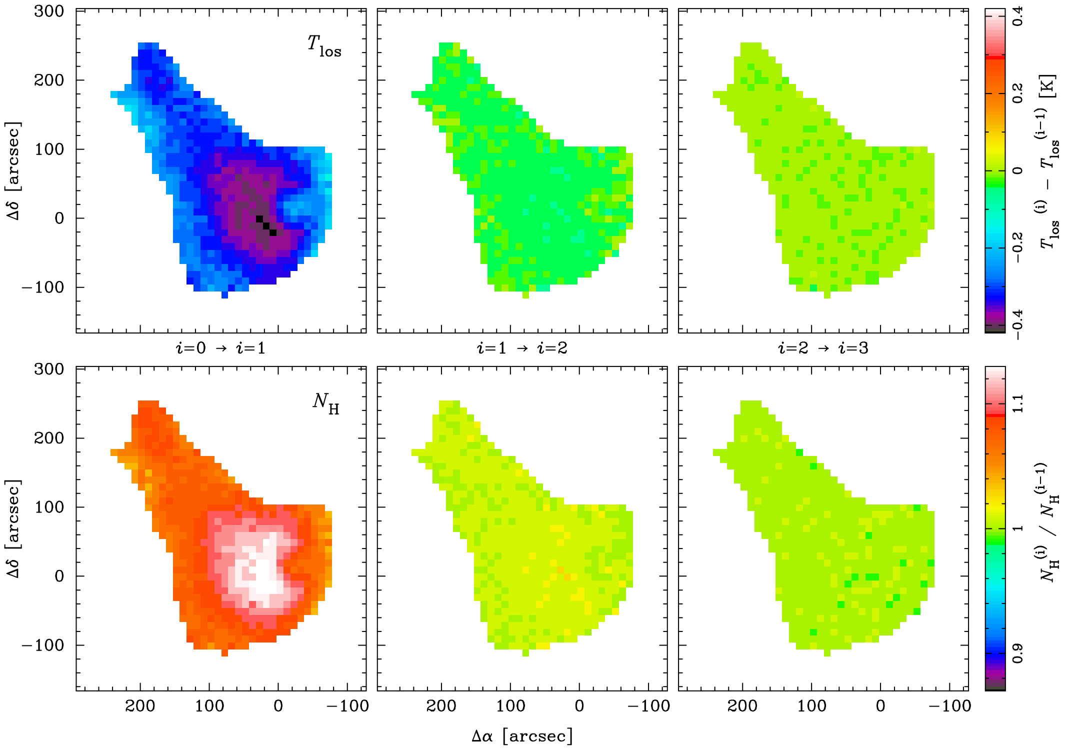

Figure 4.6.: Changes of temperature (*top row*) and column density (*bottom row*) between subsequent iterations for the colour-correction.

15% calibration uncertainty for the Herschel data does not only describe a Gaussian scatter around the true value, but includes also systematic uncertainties (e.g., calibrational offsets). The derived uncertainties were generally of the order of 10% for column densities, and $\sigma T \sim 0.2\,\mathrm{K}$ for the temperatures.

Using this χ^2 minimisation procedure, we were then able to obtain a dust temperature map which served as input for the colour correction. The quick convergence towards a constant value with iterative colour corrections is shown in Figure 4.6, and makes it clear that already a single colour correction step is already sufficient.

The best fit results for the temperature and column density are shown in Figure 4.7. One can see that both the core, and the cometary tail towards the north-east exhibit considerable emission, and fulfil the criterion of 5 of 7 measurements above the emission threshold. The column density map shows an almost circular structure with an aspect ratio of $R = 1.1$. The profile along the emission region, which is shown in the inset of Figure 4.7 shows a column density enhancement by a factor of $\gtrsim 10$ with respect to the cometary tail. The emission profile also clearly shows that the peak is not centred, but rather shifted towards the south-western part of the globule. The general shape of the column density distribution is also reproduced by the temperature map. One can see the clear anti-correlation, which only brakes down around CB 17-IRS, where the central heating of the Class I source strongly influences the fit. Due to the effect of a large beam, the temperature minimum and maximum do not correspond to to the locations of the cold core (CB 17-SMM1) and protostar (CB 17-

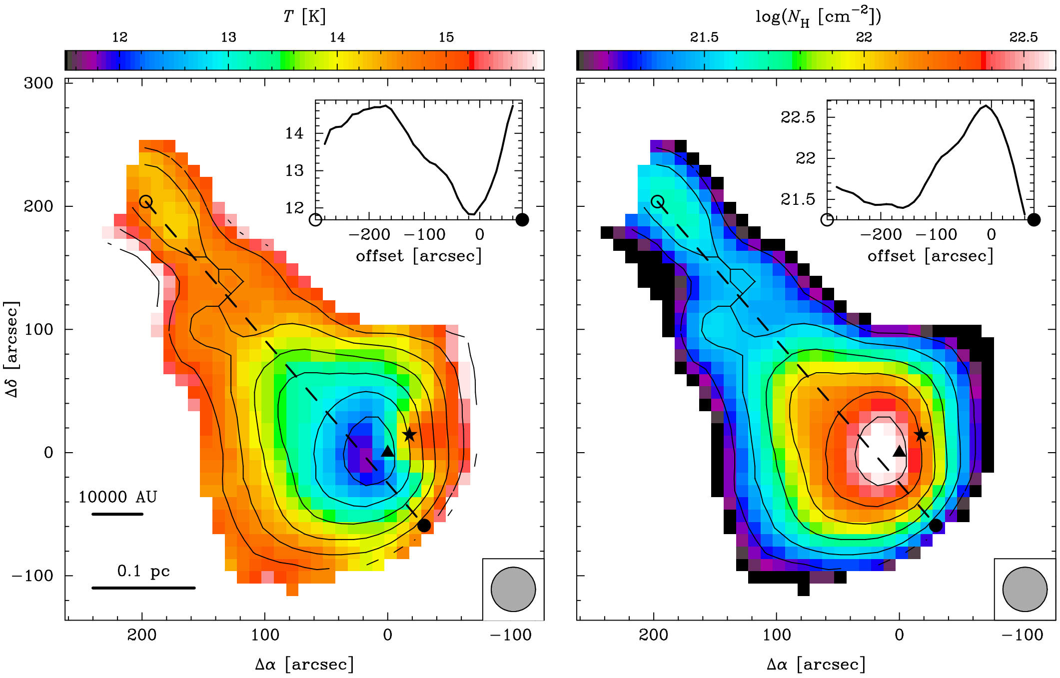

Figure 4.7.: Temperature (*left panel*) and hydrogen column density (*right panel*) maps as derived from the **modified blackbody fits**. The contours represent the hydrogen column density from $\log(N_\mathrm{H}) = 22.50$ downwards in steps of $\Delta N_\mathrm{H} = 0.25$ dex. The insets represent the profiles between the open and the closed circle along the dashed line.

IRS). Conversion of the column density to hydrogen mass, and assuming $M_\mathrm{tot} = 1.37 M_\mathrm{H}$ (Lombardi et al., 2006) then yields a total mass of $M_\mathrm{tot} = 5.3 \pm 0.5\,\mathrm{M}_\odot$ in regions beyond $N_\mathrm{H} = 4\,10^{21}\,\mathrm{cm}^{-2}$ (or $A_\mathrm{V} > 2$ mag, Bohlin et al. 1978).

Beta Fitting

In a more elaborate approach, we did not only fit column density and temperature, but we furthermore also fitted the dust model by varying the dust opacity index β. In general, the dust opacity is expressed by

$$\frac{\kappa}{\kappa_0} = \left(\frac{\lambda}{\lambda_0}\right)^{-\beta} = \left(\frac{\nu}{\nu_0}\right)^{\beta}, \tag{4.7}$$

where κ_0 is a normalisation constant, which is set to match the model of OH94 at $\lambda_0 = 850\,\mu$m. The dust opacity index β changes the overall shape of the spectral energy distribution. In the Rayleigh-Jeans limit, the dust opacity index can be directly estimated from the slope of the SED

$$I_\nu \propto \nu^{2+\beta}\, T_\mathrm{RJ}. \tag{4.8}$$

In order to get an estimate on the best dust model, we extended the parameter space by fitting $\beta = -1 \ldots 5$ in steps of $\Delta\beta = 0.025$. For the column density and temperatures, we

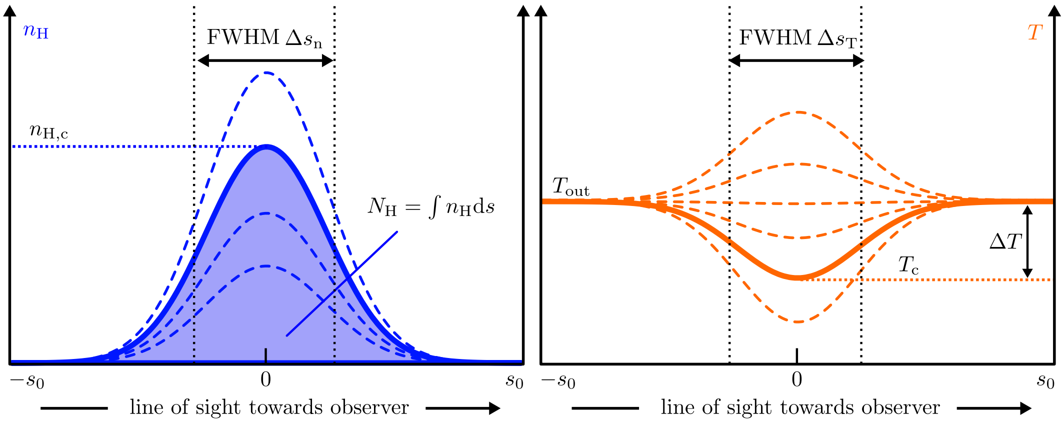

Figure 4.8.: Illustrative sketch of the raytracing model, which finds the best fit parameters for the column density $N_\mathrm{H} = \int n_\mathrm{H} \mathrm{d}s$ and the central temperature T_c. Gaussian distributions with a given FWHM Δs_n and Δs_T for both the volume density $n_\mathrm{H}(s)$ and temperature $T(s)$ are assumed. The intensity $I_\nu(s_0)$ is calculated for all different configurations of the parameter space (indicated as dashed curves). The best fit (solid line) is determined by the minimum $\chi^2(N_\mathrm{H}, T_\mathrm{c}$.

used the same specifications as for the previous fit. Again, the emission at all wavelengths was calculated for all possible combinations in the parameter space, and the best fit parameters were determined by the minimum χ^2. Due to the presence of a heating source at CB 17-IRS, the β fit breaks down in regions which are affected by this source. In regions of column density $N_\mathrm{H} > 10^{21}\,\mathrm{cm}^{-2}$, which are not affected by CB 17-IRS, we derived a dust opacity index of $\beta = 2.0 \pm 0.2$.

Raytracing Fit

From Figure 4.7 we see that the average line-of-sight temperature drops towards the hydrogen column density peak by $\sim 2.5\,\mathrm{K}$, which rejects the hypothesis of an isothermal globule. In order to estimate the temperature in the core, one has to apply a more elaborate model than the modified blackbody fit of the previous section. T_los only gives the average temperature along the line-of-sight, which is strongly influenced by warmer regions in front and behind the core, and therefore does not allow an estimate of the central temperature.

In order to get an idea of the 3D temperature and number density distribution we ran a simple raytracing code along the LOS for each individual pixel of the map. As we only do have a minimum of 5 (and a maximum of 7) measurements available, we had to make some reasonable assumptions in order to keep the number of degrees of freedom as small as possible:

1. Both the temperature $T(s)$ and number density $n_\mathrm{H}(s)$ distribution are Gaussian

functions (Figure 4.8) of the form

$$T(s) = T_{\rm out} + \Delta T \, \exp\left(-2.77 \, \frac{s^2}{\Delta s_{\rm T}^2}\right) \tag{4.9}$$

$$n_{\rm H}(s) = n_{\rm H,c} \, \exp\left(-2.77 \, \frac{s^2}{\Delta s_{\rm n}^2}\right) \tag{4.10}$$

Their respective FWHM $\Delta s_{\rm T} = 0.11\,{\rm pc}$ and $\Delta s_{\rm n} = 0.08\,{\rm pc}$ were estimated by approximating the temperature and column density profiles of the MBB fit (Figure 4.7) with Gaussian curves, assuming a distance of 250 pc, and that the extent of the core along the line of sight coincides with the extent in the plane of the sky. Gaussian curves are a very convenient way to define density profiles, as they do exhibit some advantages. Most notably, the FWHM of a Gaussian number density distribution exhibits the same FWHM, when converting it into the observable column density. Secondly, cuts through a core with a Gaussian distribution at arbitrary radial offset from the core centre will again yield a Gaussian shape with the same FWHM. The use of other density profiles is discussed in more detail in §4.4.

2. We also used the MBB temperature map for an estimate of the external temperature, which was set to $T_{\rm out} = 14.5\,{\rm K}$. This value conformed to the temperature in the cometary tail, which is a region of moderate to low column density.
3. The central number density $n_{\rm H,c}$ is directly related to the column density $N_{\rm H}$ via the integral of the number density distribution along the line-of-sight, which is in the case of Gaussian curves

$$n_{\rm H,c} = \frac{N_{\rm H}}{1.07\,\Delta s_{\rm n}} \tag{4.11}$$

$$= 2.8\,10^{-18}\,N_{\rm H}. \tag{4.12}$$

For the raytracing we separated each ray along the line-of-sight into 50 cells, and calculated in the region $\pm 2\Delta s_{\rm n}$ around the peak of the Gaussian to ensure that the relative contribution at the core edges is negligible. For this configuration, the total length of the ray was 0.32 pc, and the extent of a single cell conformed to a size of $6.4\,10^{-3}$ pc, or $1.3\,10^{3}$ AU. The choice of 50 cells was the result of a compromise between coarse resolution and computational tractability.

Again, the emission at each individual pixel was calculated for all possible combinations of the parameter space. Column densities were again varied between $\log(N_{\rm H}\,[{\rm cm}^{-2}]) = 19\ldots24$ at a resolution of $\Delta N_{\rm H} = 0.02\,{\rm dex}$. The second parameter was the central temperature, which was varied in the range $T_{\rm c} = 2\ldots30\,{\rm K}$ at a resolution of $\Delta T_{\rm c} = 0.1\,{\rm K}$. The position of the minimum χ^2 again determined the best fit parameters. Figure 4.9 shows the SEDs for the two positions of maximum and minimum temperature $T_{\rm c}$, alongside with the best fit curve. One can clearly see the change in overall shape for different temperatures.

The full temperature and column density maps are presented in Figure 4.10. The overall morphology of both maps closely resembles the results from the modified blackbody fit,

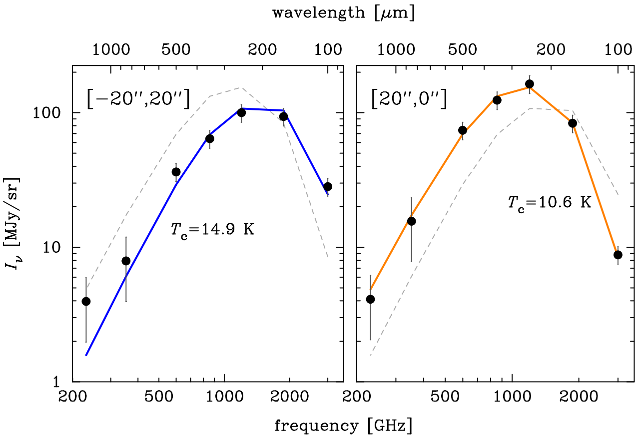

Figure 4.9.: Spectral energy distribution towards two different positions. The solid coloured lines represent the best fit model as obtained from the **raytracing fit**. As a reference, the best fit model of the neighbouring panel is shown as a dashed line.

and the extinction map. The column density maximum of $N_H = 5.8\,10^{22}\,\mathrm{cm}^{-2}$ translates to a central number density of $2.2\,10^5\,\mathrm{cm}^{-2}$, and it is reached at [20″, 0″] slightly to the east of CB 17-SMM1. In regions exceeding column densities of $A_V = 2$ mag we find a total mass of $M_{\mathrm{tot}} = 5.5 \pm 0.5\,\mathrm{M}_\odot$, which is in very good agreement with the estimate from the modified blackbody fit ($M_{\mathrm{tot}} = 5.3 \pm 0.5\,\mathrm{M}_\odot$).

4.4. Discussion

4.4.1. Modified Blackbody vs. Raytracing

In §4.3 we presented temperature and column density maps, which were derived by applying a modified blackbody (MBB) and a raytracing (RT) fitting model. The latter model shows slight variations in column density and temperature. Comparison of these two models reveals that the largest changes can be seen towards the centre of the core (Figure 4.11). In the envelope, i.e., along the cometary tail, the raytracing fit yields almost no temperature variation along the LOS, i.e., $T_c \sim T_{\mathrm{out}} \sim T_{\mathrm{los}}$. Therefore, the differences between the modified blackbody fit and the raytracing fit are small. The situation changes when we have a look at the densest regions. The RT fit yields minimum temperatures of the order of 10.5 K, whereas we find $T_{\mathrm{los}} = 12$ K. A similar, however less pronounced, effect is observed for the column densities which are by up to a factor of ~1.1 higher in the case of the RT fit. Therefore we conclude, that the average line-of-sight temperature T_{los} is not a suitable parameter to describe the physics of the densest regions.

The relatively higher temperature towards the centre in the case of MBB fitting is compensated by a lower column density to reach the same flux level. However, one cannot oversimplify this picture. The strong non-linearity of the Planck function causes that regions with relatively low column densities but marginally higher temperatures, are the main contributors to the the measured signal. This is depicted in Figure 4.12, where we calculated the contribution function along the line of sight for an isothermal core (dashed line), and for a core with a Gaussian temperature profile (solid line). We assumed a wavelength of 100 μm, a Gaussian density profile for the core, and $\tau \ll 1$

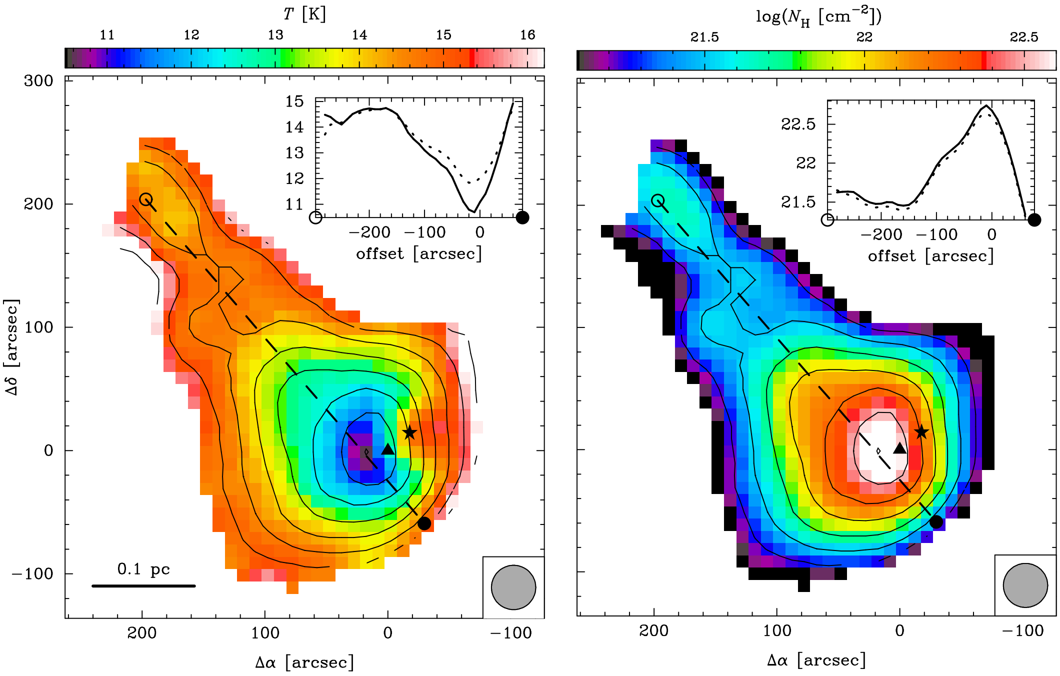

Figure 4.10.: Temperature (*left panel*) and hydrogen column density (*right panel*) maps as derived from the **raytracing fits**. The contours represent the hydrogen column density from $\log(N_\mathrm{H}\,[\mathrm{cm}^{-2}]) = 22.5$ downwards in steps of $\Delta N_\mathrm{H} = 0.25$ dex. The insets represent the profiles between the open and the closed circle along the dashed line. The dotted lines in these insets are the results from the modified blackbody fit (Figure 4.7).

In the case of an isothermal core, the contribution function to the total emission obviously is directly related to the Gaussian density profile. In the case of a Gaussian temperature distribution, which is defined by the outside T_out and the central temperature T_c, the contribution function does not follow the Gaussian density distribution, but the strongest contribution emerges from the less dense envelope with its relatively higher temperature. The two temperature profiles in Figure 4.12 are chosen to give the same specific intensity, and are therefore not distinguishable for the outside observer. An outside temperature of $T_\mathrm{out} = 14.5$ K and a central temperature of $T_\mathrm{c} = 8.0$ K would be reproduced by an average line-of-sight temperature of $T_\mathrm{los} = 10.3$ K. Lowering the central temperature by 5 K down to $T_\mathrm{c} = 5.0$ K would result in a relative change of T_los of less than 1 K. This therefore explains the relatively shallow curve of T_los (Figure 4.7), and supports the idea that the central temperatures T_c are indeed lower than the isothermal estimate T_los.

Due to the strong non-linearity of the Planck function, at 100 μm a temperature change from 10 K to 11 K results in 4 times stronger thermal emission. At longer wavelengths towards the Rayleigh-Jeans (RJ) limit, this effect decreases to a linear relation $I_\nu \propto T$. At 850 μm, the two profiles with $T_\mathrm{c} = 8.0$ K and $T_\mathrm{c} = 5.0$ K are reproduced by $T_\mathrm{los} = 9.1$ K and $T_\mathrm{los} = 6.8$ K, respectively. These values do come considerably closer to the estimate of the Gaussian temperature profile. However, as these values for T_los differ from the ones, which were derived for 100 μm it already becomes clear that the full spectrum cannot be characterised by a single temperature T_los.

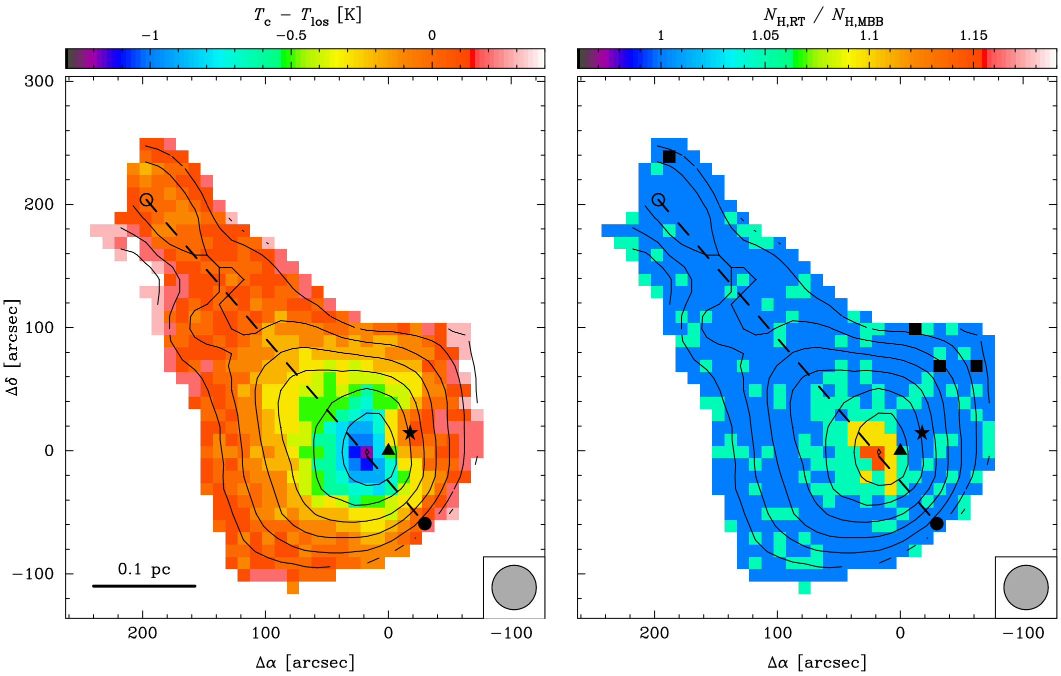

Figure 4.11.: Temperature difference and column density ratio of the modified blackbody (MBB) and the raytracing (RT) model. The contours represent the hydrogen column density from the RT fit, and are drawn from $\log(N_H\,[\mathrm{cm}^{-2}]) = 22.5$ downwards in steps of $\Delta N_H = 0.25$ dex.

Therefore, we investigated the influence of temperature gradients on the general shape of the SED by modelling different temperature distributions along the line-of-sight with constant T_{out}, but varying temperature T_c. All models were calculated with the same Gaussian density distribution with $\Delta s_n = 0.1$ pc, and a column density of $N_H = 10^{22}$ cm^{-2}. The temperature distribution was also assumed to be Gaussian with $T_{out} = 14.5$ K and a distribution width of $\Delta s_T = 1.4\,\Delta s_n$, which conformed to the finding in §4.3. We then varied the central temperature in the range $T_c = 4.5 \ldots 14.5$ K in steps of 1 K. Figure 4.13 shows the synthetic SEDs, which were calculated by using the RT algorithm, and These spectra were then fitted with the modified blackbody routine (4.3.2), and the best fit lines are indicated in Figure 4.13 as the dashed lines. It immediately becomes obvious that the general line shape can only poorly be approximated by a modified blackbody curve in the case of strong temperature variations along the line of sight.

The difference between the central temperature T_c, which was put into the model, and the recovered average LOS temperature T_{los} is shown in the right panel of Figure 4.13. In the presence of strong temperature gradients, the contributions of the “luke-warm” core envelope inhibit an accurate recovery of the true central temperature by the modified blackbody fit. Figure 4.13 also shows the MBB best-fit column density N_H, which is in the case of a temperature gradient of $\Delta T = 10$ K by a factor of 5 lower than the input value of 10^{22} cm^{-2}. The higher temperature, and therefore relatively strong emissivity in the dense regions have to be compensated by decreasing the column density significantly.

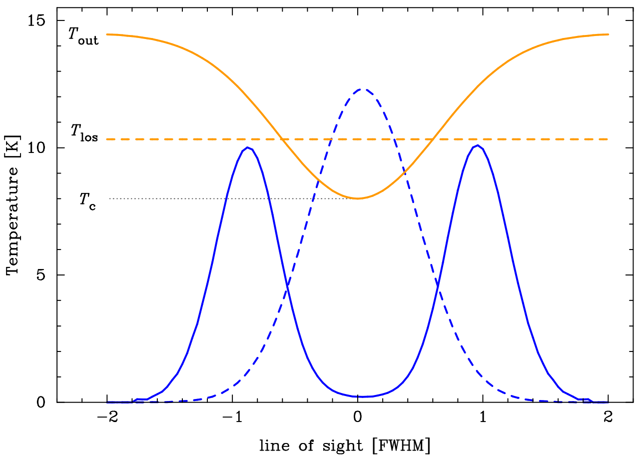

Figure 4.12.: Relative contributions (blue) along the line of sight in dependence on the temperature (orange) for a Gaussian number density distribution. The integral of the relative contributions (i.e.,, the observable intensity I_ν) of the two temperature profiles are the same, but different parts of the cloud contribute to it. The dashed line represents T_{los}, the solid line the raytracing model with T_{out} and T_c.

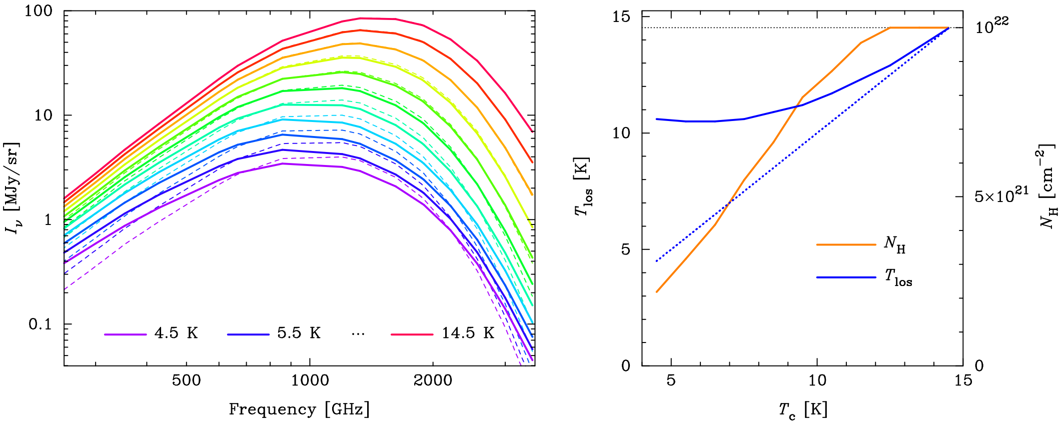

Figure 4.13.: *Left panel:* Spectral energy distributions for models with different central temperatures $T_c = 4.5\ldots14.5$ K in steps of $\Delta T_c = 1$ K (solid lines). The outside temperature is constant at $T_{out} = 14.5$ K, and the column density is set to $N_H = 10^{22}$ cm^{-2} for all models. The dashed lines represent the best fits for a modified blackbody model. *Right panel:* Best fit parameters for the modified blackbody model in dependence on the central temperature T_c. The blue dotted line represents the relation $T_c = T_{los}$.

As already mentioned above, the general line shape cannot be approximated by a single temperature MBB model, as the SED significantly broadens in the presence of temperature gradients. The reason can be found in what was just discussed above: Towards the RJ limit, temperature and emissivity are related via a linear relation, whereas towards shorter wavelengths, this relation follows an exponential law (Wien's law). Therefore, the spectrum is strongly skewed towards shorter wavelengths due to the relatively stronger contribution of the envelopes at high frequencies.

However, it should be noted that most commonly a broadening of the SED is attributed to a change of the dust opacity index β towards lower values (Figure 2.14 in Chapter 2). Therefore, temperature gradients along the LOS do not only inhibit an accurate recovery of the true column density, but also mimic variations of β, which could be misinterpreted as a result of dust growth. To quantify the error in the estimate of β, we performed a second

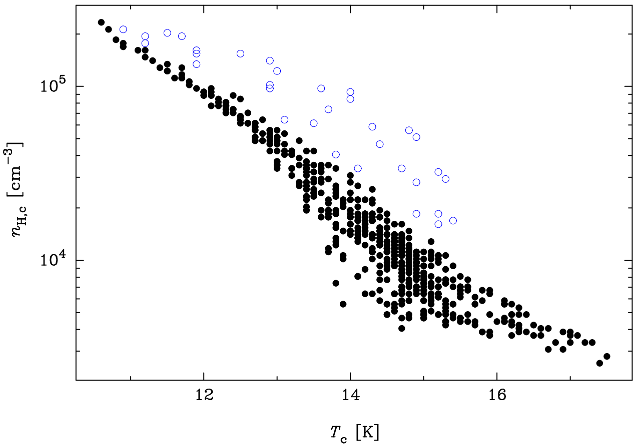

Figure 4.14.: Central hydrogen density $n_{\rm H,c}$ vs. central temperature $T_{\rm c}$. The open circles all correspond to pixels, which are affected by CB 17-IRS.

set of measurements where we also fitted the dust opacity index. The general shape of the SEDs was accurately reproduced by the artificial broadening due to lower β-values. For small temperature gradients of the order of $\lesssim 4$ K, the recovered dust opacities showed only small deviations from the input value of $\beta = 1.8$. Larger temperature gradients then lead to a considerable decrease in β down to values of $\beta = 1.0$ at $T_{\rm c} = 6$ K. In the case of CB 17, however, we do not see evidence for strong variations of the derived column density from the modified blackbody and raytracing fits. Therefore, the temperature gradients seem to be reasonably moderate, and we expect a quite accurate recovery of the dust opacity index, which was found to be $\beta = 2.0 \pm 0.2$.

4.4.2. Temperature and Density Distribution

From the raytracing model we cannot only derive a column density $N_{\rm H}$, but due to the a-priori assumption of a density and temperature profile, we can derive the full 3D core structure. For the densest regions we obtained values of $n_{\rm H,c} = 2.2\,10^5\,{\rm cm}^{-3}$, which is in good agreement for other cores of this evolutionary age (Stamatellos et al., 2007). Plotting the central density vs. the central temperature $T_{\rm c}$ reveals a clear anti-correlation (Figure 4.14). The map regions, which are affected by the heating of CB 17-IRS (open circles) do not follow the trend, but rather exhibit excess heat. The coldest regions are clearly associated with the regions of highest central density. As these regions are efficiently shielded from heating through the interstellar radiation field by the envelope, they can cool quite efficiently. As the linear trend can be followed even down to the highest densities and coldest temperature, we see no evidence for a heating source in the centre of CB 17-SMM1. However, the possibility of the presence of such a *first core* will be discussed in more detail in Chapter 6.

The results of our RT model strongly depends on the choice of profile shapes and profile widths. In our model, we used Gaussian distributions for both temperature and density with $\Delta s_{\rm T} = 1.4 \Delta s_{\rm n}$, which was estimated from 2D temperature and column density profiles (Figure 4.7) and assumed the same extent along the LOS as in the plane of the sky. Although this seems to be a reasonable assumption, this remains a possible source of systematic errors. Therefore, we investigated the influence of different model parameters on the best-fit results.

Considering the relative contribution of different regions along the line of sight (Figure 4.12), a narrower temperature distribution with $\Delta s_{\mathrm{T}} = \Delta s_{\mathrm{n}}$ would result in a larger contribution from the envelope. Therefore, a lower central temperature would be needed to compensate this effect. Performing a RT fit with such a configuration would yield a minimum temperature of $T_{\mathrm{c}} = 8.6\,\mathrm{K}$, in contrast to $T_{\mathrm{c}} = 10.5\,\mathrm{K}$ for the broader temperature profile. However, in the presence of strong temperature gradients, the χ^2 map exhibits a strong degeneracy for T_{c} and N_{H}, which makes the derived best fit parameters less reliable.

But not only the relative width of the distributions would change the general picture, but also the density distribution itself. In our case, we chose Gaussian curves because of the various advantages they offer. A more realistic approach, however, is to define a power-law density profile (e.g., Tafalla et al., 2002) of the form

$$n_{\mathrm{H}}(r) = \frac{n_{\mathrm{H,c}}}{1 + (r/r_0)^{\alpha}} \tag{4.13}$$

which exhibits a relatively flat region towards the centre, and falls off with the slope α at radii $r \gtrsim r_0$. Such a power-law exhibits considerably stronger wings than a Gaussian function, and thus a relatively strong contribution of the envelopes.

A Gaussian density profile offers various advantages: The FWHM of the density profile is also regained for density profiles along lines-of-sight with nonzero impact parameter, and is also reproduced by the observable column density. The power-law profile, however, does not exhibit such a simple relation between all these parameters. For nonzero impact parameters, the profiles broaden considerably, and also the column density profile does not show a simple one-to-one relation to the radial profile, but rather broadens by a factor $\gtrsim 2$. To test the case of a power-law profile, we performed a RT fit at the peak position of the column density map, to ensure that the power-law profile is a valid estimate of the LOS density distribution. We used a Gaussian temperature distribution, and a power-law density distribution with $r_0 = 0.02\,\mathrm{pc}$ and $\alpha = 2$. The best fit density profile is shown in the left panel of Figure 4.15. With a central density of $n_{\mathrm{H,c}} = 3.6\,10^5\,\mathrm{cm}^{-3}$ it is by a factor of 1.5 denser than the Gaussian profile, and is also shown in the plot. The column density N_{H} values were higher in the case of a power-law profile by a factor of 1.2, whereas the best fit central temperature T_{c} remained essentially the same.

The central temperature of 10.5 K is in reasonable agreement with estimates for other prestellar cores. Stamatellos et al. (2007) modelled cores in the ρOph cloud using a 3D radiative transfer model. Their model cores consist of an outer envelope of constant density with pristine MRN particle size distribution, and an embedded core with coagulated grains with thin ice mantles. Heating is provided by the interstellar radiation field. The envelope temperatures are of the order of $13 - 30\,\mathrm{K}$, and are therefore in reasonable agreement with our finding for CB 17. Core temperatures, however, are in general slightly lower, and of the order of 7 K. Due to the relative uncertainty in the determination of the temperature profile for our case, we cannot exclude such temperatures for CB 17.

We can get a rough estimate of the stability of both core configurations (power-law and Gaussian) under the assumption of the Gaussian temperature profile with $T_{\mathrm{out}} = 14.5\,\mathrm{K}$,

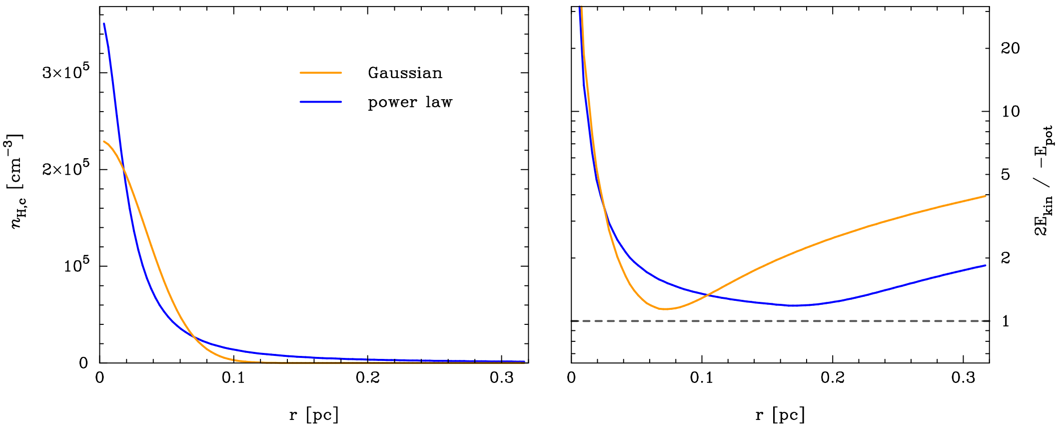

Figure 4.15.: *Left panel:* Best fit density profiles for both the Gaussian (blue) and power-law (orange) profile. Right panel: Jeans stability criterion for spherical regions inside radius r.

and $T_c = 10.5\,\mathrm{K}$ by using the Jeans criterion for stability

$$2E_{\mathrm{kin}} + E_{\mathrm{pot}} > 0. \tag{4.14}$$

We obtained E_{kin} and E_{pot} by numerical integration, and analysed the thermal stability individually for regions inside a certain radius r. In both configurations, the core appears to be marginally stable, even without further support, e.g., via magnetic fields or turbulence. The fact to find CB 17 in a marginally stable state is, however, not surprising, as the prestellar core is in a quasi-static phase, and does therefore neither collapse due to gravitational collapse, nor disperse thermally.

4.4.3. Dust Properties

With both the NIR dust extinction and the FIR dust emission maps at hand, we have two independent measurements of the dust, and therefore the hydrogen column density. Of particular interest, however, is the question of the relation between the dust opacities κ_ν of these two regimes, as different dust models predict different ratios of, e.g., $\kappa_{2.2}/\kappa_{500}$. Figure 4.16 shows commonly used dust models of Draine and Lee (1984, DL84), and OH94 (using different ice covers and coagulation).

Recalling that the optical depth τ_ν is related to the dust opacity κ_ν via

$$\tau_\nu = \frac{m_{\mathrm{H}}\, N_{\mathrm{H}}\, \kappa_\nu}{R_{\mathrm{g/d}}}, \tag{4.15}$$

where m_{H} is the proton mass, and $R_{\mathrm{g/d}} = 110$ is the hydrogen-to-dust mass ratio, then gives

$$\frac{\kappa_{2.2}}{\kappa_{500}} = \frac{\tau_{2.2}}{\tau_{500}}. \tag{4.16}$$

In order to be able to compare the dust models, we also performed a RT fit using the model of DL84. Due to the difference of absolute values ($\kappa_{500}^{\mathrm{DL84}} = 1.89\,\mathrm{cm^2 g^{-1}}$, $\kappa_{500}^{\mathrm{OH94}} =$

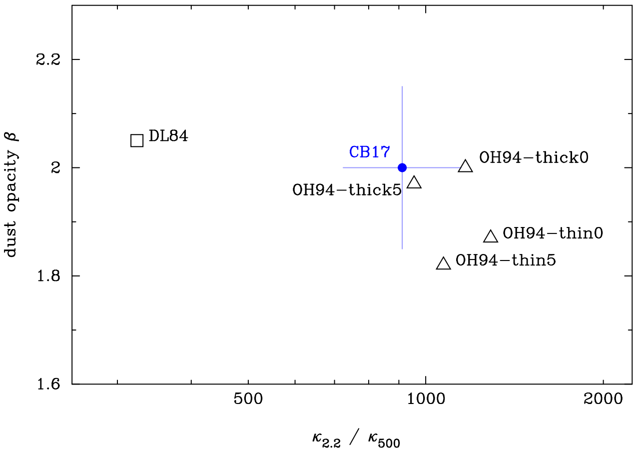

Figure 4.16.: Dust opacity index β in dependence on the κ-ratio. Additional data points are from the dust models of Ossenkopf and Henning (1994) and Draine and Lee (1984).

$2.9\,\mathrm{cm^2 g^{-1}}$) the derived column densities N_H of the DL84 model were higher by factors of 1.7, but the optical depths agreed reasonably well. The extinction $A_{2.2}$ is related to the optical depth via

$$A_{2.2} = 1.086\,\tau_{2.2}. \tag{4.17}$$

The $\kappa_{2.2}/\kappa_{500}$-ratio is then calculated for each pixel of the map. Taking into account only regions with $N_\mathrm{H} \geq 10^{21}\,\mathrm{cm^{-2}}$, which are not affected by CB 17-SMM1, we get a ratio of $\kappa_{2.2}/\kappa_{500} = (0.94 \pm 0.22)\,10^3$. Figure 4.16 puts this in context with some theoretical dust models of DL84 and OH94 (included are the models with thin or thick ice mantles, no coagulation or coagulation at $10^5\,\mathrm{cm^{-3}}$). We see a reasonable agreement of the dust models of OH94 with our data, whereas the ISM model of DL84 can be ruled out. Therefore, CB 17 seems to be in a stage where dust grains already have undergone some processing by dust coagulation.

4.5. Summary and Outlook

In this chapter we present a column density and temperature map of the prestellar core CB 17, which were derived from dust emission maps obtained with Herschel Space Observatory ($100 - 500\,\mu$m), SCUBA ($850\,\mu$m), and IRAM-30m (1.3 mm). We applied two models to derive the column density and temperature, namely a modified blackbody (MBB) and a raytracing (RT) algorithm.

The MBB fit allowed us to derive the average line-of-sight temperature T_los and column density N_H by using a χ^2 minimisation technique. T_los varied between $14 - 16$ K at the core edges and 12 K in the core centre. The column density ranged up to values of $N_\mathrm{H} \sim 6\,10^{22}\,\mathrm{cm^{-3}}$, and dropped towards the core edges, following a Gaussian distribution with FWHM = 0.08 pc. From this profile we approximated a density profile, which served as the basis for a RT fit. As a temperature drop is expected towards the core centre, we also modelled the temperature distribution along the line-of-sight with a Gaussian function. From the MBB temperature map we estimated a temperature profile, which was a factor of 1.4 wider than the density distribution. These profiles served as input for the RT algorithm, which allowed us to derive a central density $n_{\mathrm{H,c}}$, and also get an estimate of the central temperature T_{c}. The column density remained similar for the two fitting methods. In the dense core the best fit values gave central density of $n_{\mathrm{H}} = 2\,10^{5}\,\mathrm{cm}^{-3}$, and a temperature of $T_{\mathrm{c}} = 10.5\,\mathrm{K}$. The total mass of CB 17 was estimated to be $M_{\mathrm{tot}} = 5.5\,\mathrm{M}_{\odot}$. A stability analysis using the Jeans criterion assuming both Gaussian and power-law radial density and temperature distribution lead to the conclusion that CB 17 is in an only marginally stable phase.

Together with a NIR extinction map, which was derived from observations with the Omega2000 camera at the CAHA-3.5m telescope, we were able to constrain the dust model. Comparison of the NIR to FIR dust opacities, namely the $\kappa_{2.2}/\kappa_{500}$-ratio, showed us that the dust model of OH94 exhibits better agreement with the data than the ISM dust model of DL84. Therefore, the dust already was processed and reformed by freeze-out of molecular species on its surface and/or coagulation.

Outlook

Further studies will involve the study of a sample of 14 low-mass cores, which were all observed within the framework of the Herschel EPoS key project. This will allow us to get a broader overview on dust properties, column density, number density and temperature structure of these earliest stage of low-mass star formation. The RT fitting algorithms are continuously improved, and the use of more realistic temperature and density profiles will further improve the quality of our results.

5

CB 17 – Molecular Abundances and Freeze-out

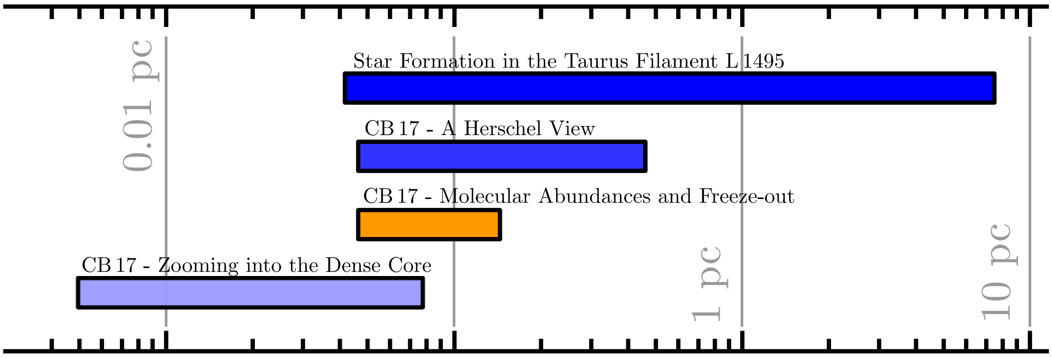

> As I stand out here in the wonders of the unknown at Hadley, I sort of realize there's a fundamental truth to our nature, Man must explore. . . and this is exploration at its greatest.
>
> — *Dave Scott, Apollo 15, 7th man on the moon*

OUTLINE:

After the study of dust emission and extinction, I will focus on the kinematics and molecular abundances of different types of molecules. A general introduction about molecular line observations is given in §5.1. In §5.2 the observations are presented. The derived molecular abundances and velocity maps are shown in §5.3. In §5.4 follows an analysis and discussion of the radial structure of CB 17, the freeze-out and velocities. This chapter then concludes with a summary and outlook in §5.5.

5.1. Introduction

Observations of molecular line transitions are a powerful tool to obtain information about various cloud parameters. Specifically, optically thin lines, e.g., allow estimates of the velocity structure along the line of sight by modelling velocity centroid and linewidth (e.g., Goodman et al., 1993; Kane and Clemens, 1997). On the other hand, optically thick lines can be used to trace infall motions, which can produce a skewed self-absorption line profile (e.g., Lee et al., 1999). The general influence of infall motions and/or rotation on the shapes of optically thick lines was recently modelled by Pavlyuchenkov et al. (2008).

However, the velocity structure is not the only core property probed by molecular line emission, but they also allow to draw conclusions about density, mass or temperature distribution. Combined analysis of optically thin and thick molecular isotopes allows to derive the optical depth τ, the excitation temperature T_{ex}, and with the aid of these parameters also the molecular column density N_{mol} along the line of sight.

Emission of molecular lines depends on various factors. Chemical reactions provide replenishment or depletion of certain molecules from the gas phase, but also freeze-out of certain molecular species onto dust grains in the centre of dense cores change the relative molecular abundances (e.g., Bergin and Tafalla, 2007). Furthermore, the emission of molecular lines depends strongly on excitation conditions. Because of the complex interplay of these effects, there is not a single molecule which allows for a unique characterisation of all the relevant physical parameters at once. It is rather the combined analysis of a set of well chosen molecular line transitions and species, which allows us to form a more complete picture of the conditions in the globule.

In this chapter, we present our analysis of the molecular properties of CO, CS, HCO^+, and N_2H^+ in CB 17. The reason for the selection of these molecules was their ability, to trace different environments. CO(2-1), CS(2-1), HCO^+(1-0), and N_2H^+(1-0) trace gradually denser material (in that order). This is on one hand caused by their different critical densities, on the other hand on the freeze-out and depletion of carbonaceous molecules at high densities, and the subsequent presence of N_2H^+ in the dense core (e.g., Bergin et al., 2002). Therefore, with these molecules we can probe the abundances and velocity structure at all scales – from the envelope at low to intermediate densities down to the dense core.

5.2. Observations and Data Reduction

5.2.1. IRAM-30m

Alongside the FIR and NIR observations, which were already introduced in Chapter 4, we have obtained observations of various molecular transition lines. In order to estimate the column densities, and therefore quantify the freeze-out of CO, CS, and HCO^+, we observed for each of these molecules an optically thick and thin line transition. Furthermore, we also observed N_2H^+(1-0), which also allows to estimate its column density by a direct analysis of its seven hyperfine structure (HFS) components. For all carbonaceous species we used pointed observations in a regular grid with a spacing of $7''$, whereas for N_2H^+ an on-the-

Table 5.1.: Molecular line transitions, rest frequency, map size and observing date.

Line	Frequency [GHz]	map size	date
$H^{13}CO^+$(1-0)	86.754288	$2' \times 2'$	3 Oct 1996
HCO^+(1-0)	89.188526	$2' \times 2'$	2 Oct 1996
N_2H^+(1-0)	93.171621	$2' \times 2'$	12 Jul 2004
$C^{34}S$(2-1)	96.412950	$1' \times 1'$	4,5 Oct 1996
CS(2-1)	97.980953	$2' \times 2'$	3 Oct 1996
$C^{18}O$(2-1)	219.560358	$1' \times 1'$	4 Oct 1996
^{13}CO(2-1)	220.398681	$2' \times 2'$	2 Oct 1996
CO(2-1)	230.538000	$2' \times 2'$	2 Oct 1996

fly mapping scheme was used. The pointing centre for all observations was chosen to be α_{J2000}=04:04:35.8, δ_{J2000}=56:56:03.1.

All observations were carried out with the IRAM-30m telescope, and are listed in Table 5.1. The data reduction was performed with the *GILDAS* package. Rest Frequencies were updated according to the *NIST Recommended Rest Frequencies*[†]. All data cubes were convolved to a final resolution of FWHM = 36.9$''$, to match the resolution of the hydrogen column density map (Chapter 4), and regridded to a spacing of 15$''$.

5.3. Results

5.3.1. Molecular Column Density

To get an estimate of the column density of molecular species, we obtained maps of size $2' \times 2'$ for CO(2-1), ^{13}CO(2-1), HCO^+(1-0), $H^{13}CO^+$(1-0), CS(2-1), and N_2H^+(1-0), together with smaller maps of size $1' \times 1'$ for $C^{34}S$(2-1), and $C^{18}O$(2-1). Figure 5.1 shows both the optically thin (black) and optically thick (blue) spectra towards CB 17-SMM1 of CO, CS and HCO^+. The optically thin lines can be well represented by a Gaussian shape. Optically thick lines show some considerable deviations from this shape, which are most apparent in the case of HCO^+(1-0). The double peaked profile is caused by self-absorption due to excitation temperature gradients along the line of sight (e.g., Evans, 1999).

The approach to derive the column density is briefly introduced here, but described in more detail in §2.5. The peak temperature of the optically thick line can be used to estimate the excitation temperature T_{ex}. Assuming the same excitation temperature for the optically thin and thick component, the optical depth τ of the optically thin line can be derived. For N_2H^+ it is possible to obtain the optical depth τ and excitation temperature T_{ex} from the fit of the hyperfine structure. This was done with the standard fitting routine provided by CLASS.

[†] http://pml.nist.gov/cgi-bin/micro/table5/start.pl

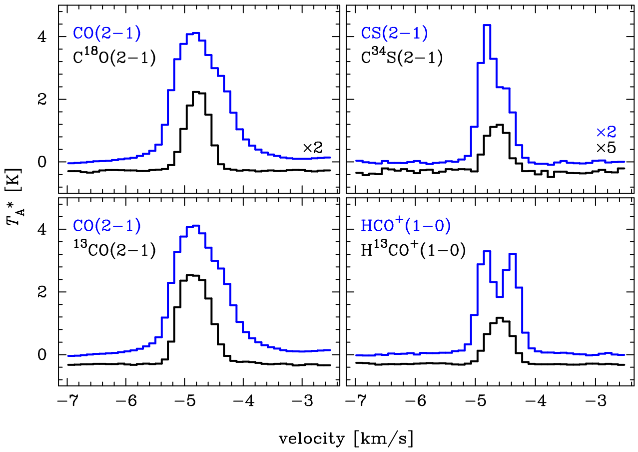

Figure 5.1.: Optically thick (blue) and thin (black, offset by $T_A^* = -0.2$ K for reasons of clarity) components for CO, CS, HCO^+.

The column density can then be estimated from Equation (2.83)

$$N_{\rm tot} = \frac{8\pi\,\tau\,\Delta v}{A_{\rm ul}}\,\frac{\nu_0^3}{c^3}\,\frac{g_{\rm l}}{g_{\rm u}}\left[1-\exp\left(-\frac{h\nu_0}{k_{\rm B}T_{\rm ex}}\right)\right]^{-1}\frac{Z}{g_{\rm l}}\,\exp\left(\frac{h\,B\,J(J+1)}{k_{\rm B}T_{\rm ex}}\right), \tag{5.1}$$

where Δv is the linewidth, $A_{\rm ul}$ is the Einstein coefficient, ν_0 is the molecular rest frequency, c is the speed of light, $g_{\rm u,l}$ are the relative statistical weights of the upper and lower level, Z is the partition function, B is the rotational constant, and J is the quantum number of the lower state. The derived parameters for our sample of molecules are shown in Table 5.2. Column density maps for the molecules with a coverage of $2' \times 2'$ (^{13}CO, HCO^+, N_2H^+) are shown in Figure 5.2.

Table 5.2.: Derived optical depth, excitation temperature and column density ranges for the molecules in our sample.

Molecule	τ	$T_{\rm ex}$ [K]	$N_{\rm mol}$ [cm^{-2}]
$H^{13}CO^+$	0.2 . . . 0.8	3.5 . . . 6.5	(1.9 . . . 10.9) 10^{11}
N_2H^+	3 . . . 10	3.0 . . . 5.2	(1.4 . . . 8.4) 10^{12}
$C^{34}S$	0.1 . . . 0.2	4.1 . . . 5.2	(1.3 . . . 2.2) 10^{12}
$C^{18}O$	0.3 . . . 0.5	8.0 . . . 9.2	(3.4 . . . 7.2) 10^{14}
^{13}CO	0.9 . . . 1.7	7.4 . . . 9.2	(1.7 . . . 3.2) 10^{15}

The column density map of ^{13}CO does not show an strongly peaked nature, but rather small variations by a factor of ∼ 2 from north-west to south. Furthermore, we do not note a correlation with the hydrogen column density. $H^{13}CO^+$ is most abundant around CB 17-SMM1, but is slightly elongated towards CB 17-IRS. This might indicate a possible connection between these two sources.

N_2H^+ on the other hand, is only found around CB 17-SMM1, but shows no association with CB 17-IRS. The 50% contour, which is usually used to define the dense core (e.g., Caselli et al., 2002), shows after deconvolution an extent of only $38'' \times 28''$, which

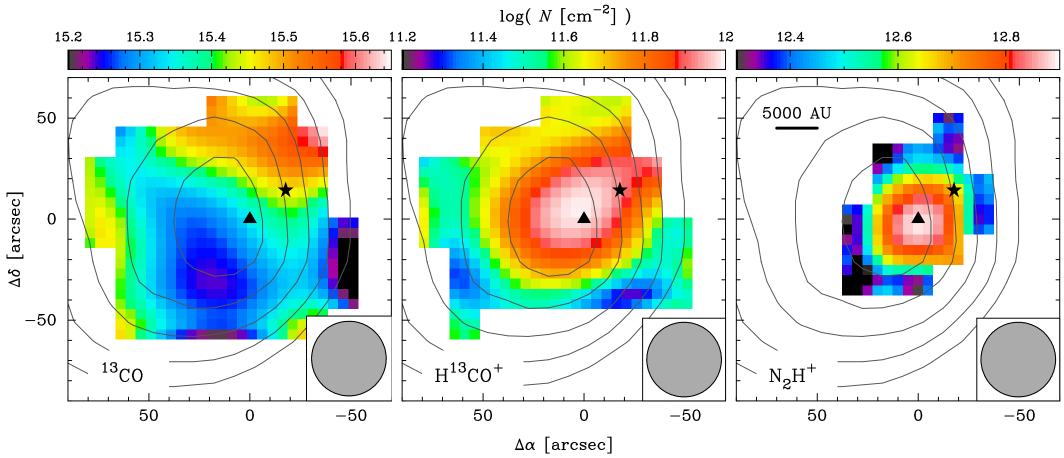

Figure 5.2.: Column density maps of $H^{13}CO^+$, N_2H^+, and ^{13}CO. Contours show hydrogen column densities from $\log(N_\mathrm{H}\,[\mathrm{cm}^{-2}]) = 22.5$ downwards in steps of $\Delta N_\mathrm{H} = 0.25$ dex. The positions of CB 17-SMM1 (▲) and CB 17-IRS (★) are marked.

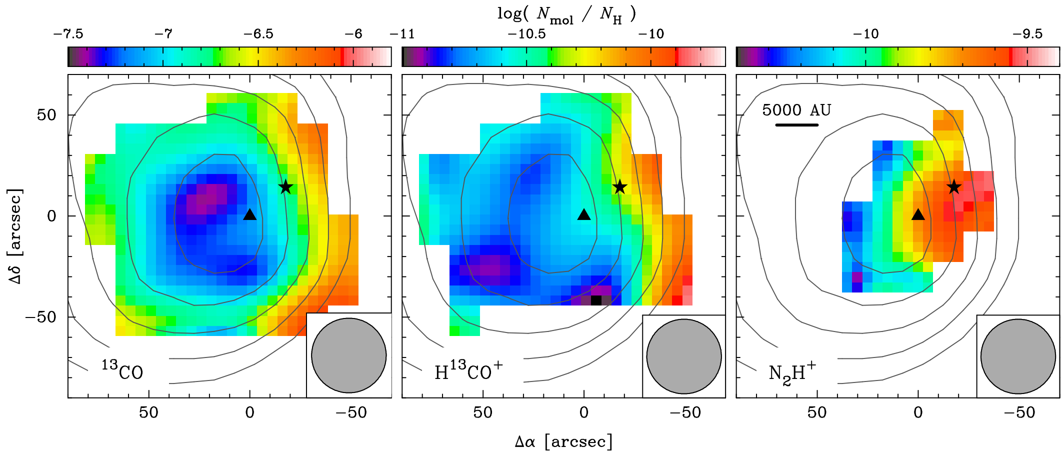

Figure 5.3.: Fractional abundance of ^{13}CO, $H^{13}CO^+$, and N_2H^+ compared to the hydrogen column density. Contours show hydrogen column densities from $\log(N_\mathrm{H}\,[\mathrm{cm}^{-2}]) = 22.5$ downwards in steps of $\Delta N_\mathrm{H} = 0.25$ dex. The positions of CB 17-SMM1 (▲) and CB 17-IRS (★) are marked.

conforms to a size of 9500 AU × 7000 AU at a distance of 250 pc. Interestingly, the dense core is slightly offset from the peak of the dust column density[†]. Various authors (e.g., Bergin et al., 2002; Friesen et al., 2010) observed similar offsets of N_2H^+ column density from continuum emission peaks. It is known that CO is one of the key players in the destruction of N_2H^+, and therefore one would expect a spatial coincidence of the N_2H^+ and CO depletion peaks. Possible explanations of this will be discussed in more detail in §5.4.

[†] For reasons of clarity, the term "dense core" in this work always relates to the region of N_2H^+ emission, although the results from Chapter 4 indicate, that the densest region is located ~ 20″ further the East.

Selective Freeze-Out

CO is known to freeze-out onto the surface of dust grains at low temperatures (e.g., Redman et al., 2002), and can be even used as a tracer for the evolutionary stage of a core (Jørgensen et al., 2005). Freeze-out occurs in the centres of dense cores, where collisions are likely due to high dust particle densities, and the desorption back into the gas phase is inhibited by very low temperatures. Figure 5.3 shows the fractional abundance of ^{13}CO, H^{13}CO$^+$ and N$_2$H$^+$ with respect to the hydrogen column density (derived in Chapter 4). Towards the region of highest column densities, CO shows a by a factor of $\gtrsim 10$ lower fractional abundance with respect to the outer regions, whereas for HCO$^+$ the situation is less conclusive. Plotting the fractional abundances of all carbonaceous species vs. effective radius[†] $r_{\rm eff}$ exhibits systematic underabundances towards the core centre. However, the relative small molecular column density maps do not allow to immediately derive the depletion factor f (Bacmann et al., 2002), which is defined by

$$f = \frac{(N_{\rm mol}/N_{\rm H})_{\rm can}}{N_{\rm mol}/N_{\rm H}}, \tag{5.2}$$

where $(N_{\rm mol}/N_{\rm H})_{\rm can}$ is the canonical abundance, which is is most accurately measured in the cloud regions, which are not affected by depletion.

It is interesting to note, that the CO column density ratio varies between ^{13}CO/C^{18}O= 6 towards the centre and a value of 3 outside, which is in contrast to the predicted ratio of ~ 9 (Wilson and Rood, 1994; Schöier et al., 2002). This could be caused by the fact, that ^{13}CO is marginally optically thick, which thus leads to an underestimation of the true column density. The relatively better agreement with the theoretical abundance towards the centre is likely due to the relatively lower optical depth $\tau \sim 0.8$. At larger radii we find $\tau \gtrsim 1$, and thus a stronger deviation.

5.3.2. Velocity Structure

From optically thin lines one can easily obtain information about the general velocity structure. By fitting Gaussian profiles to H^{13}CO$^+$(1-0), ^{13}CO(2-1), and applying the HFS fitting analysis to N$_2$H$^+$(1-0), we were able to derive maps of the central velocity $v_{\rm LSR}$ (Figure 5.5) and linewidth Δv (Figure 5.6). H^{13}CO$^+$ and N$_2$H$^+$, show a well ordered velocity pattern with clearly defined velocity gradients. We fitted these according to Kane and Clemens (1997) with a solid body rotation model

$$v_{\rm LSR} = v_0 + g_\alpha \Delta\alpha + g_\delta \Delta\delta \tag{5.3}$$

where v_0 is the rest velocity of the globule, $g_{\alpha,\delta}$ are the right ascension and declination components of the velocity gradient, and $\Delta\alpha, \Delta\delta$ are the offsets in right ascension and declination. For H^{13}CO$^+$(1-0) we derived a gradient of $\mathscr{G} = 1.6\,{\rm km\,s^{-1}\,pc^{-1}}$ and a rotational axis with P.A. = 82° east of north. N$_2$H$^+$(1-0) exhibits a velocity gradient of

---

[†] The $r_{\rm eff}$ is defined as the distance from the peak of the column density, which is corrected for the elliptical shape of the column density distribution. For CB 17 the aspect ratio of the column density distribution was only $R = 1.1$, resulting in only a small correction.

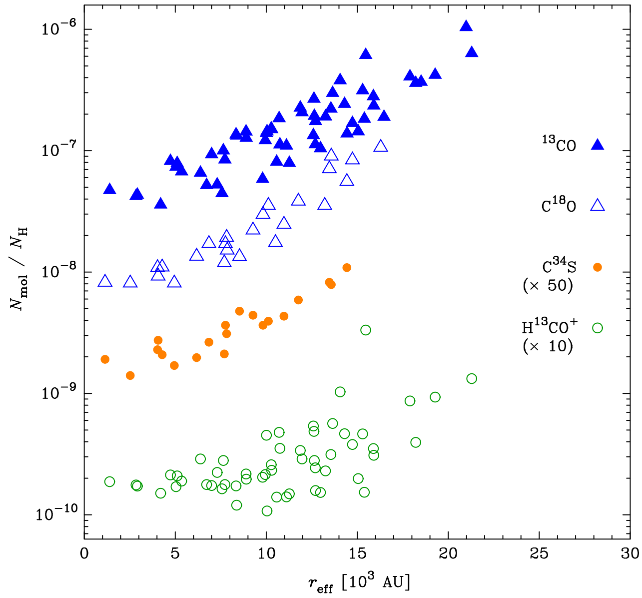

Figure 5.4.: Relative abundances with respect to hydrogen of ^{13}CO, C^{18}O, C^{34}S and H^{13}CO$^+$ (from top to bottom).

$\mathscr{G}$ = 2.1 km s^{-1} pc^{-1}, and a rotational axis with P.A. = 53°. Therefore, the envelope and the dense core seem to be slightly decoupled. In their systematic study of dense cores in dark clouds (Myers et al., 1983), Goodman et al. (1993) used NH$_3$ data, and found significant velocity gradients towards 29 out of 43 clouds with 0.3 km s^{-1} pc^{-1} $\gtrsim \mathscr{G} \gtrsim$ 2.5 km s^{-1} pc^{-1}. In a more recent study, Caselli et al. (2002) used N$_2$H$^+$ as a tracer and found similar results. Following Goodman et al. (1993) we can estimate the ratio of rotational to gravitational energy for a sphere with constant density ρ_0

$$\beta = \frac{1}{4\pi G\rho_0}\,\frac{\mathscr{G}^2}{\sin^2(i)}, \tag{5.4}$$

where G is the gravitational constant, and i the inclination angle. As the derived velocity gradient appears to be very strong, we can assume for the sake of simplicity to see the core edge-on (i = 90°). Assuming a mean density of $n_{\rm H} \sim 5\,10^4$ cm^{-3}, which was derived from the density distribution in Chapter 4 we obtain β = 0.06. Rotational support is found to be higher as in the sample of Caselli et al. (2002), but nevertheless shows no significant support to stabilise CB 17. The specific angular momentum j of the dense core in CB 17 is

$$j = 0.4\,r\,\Omega, \tag{5.5}$$

where $\Omega = \mathscr{G}/\sin(i) \sim \mathscr{G}$ is the angular velocity , r is the radius of the dense core, and the factor of 0.4 originates from the assumption of a sphere with constant density (e.g., Dib et al., 2010). Taking the 50% contour as an estimate for the radius ($r = 4\,10^3$ AU), the specific angular momentum of the dense core is found to be $j = 1\,10^{20}$ cm^2 s^{-1}.

The linewidth of H^{13}CO$^+$(1-0) of $\Delta v \sim$ 0.45 km s^{-1} remains relatively constant in the regions of strongest abundance around CB 17-SMM1 and CB 17-IRS. N$_2$H$^+$(1-0) exhibits typical linewidths of $\Delta v \sim$ 0.3 km s^{-1}, but it shows a non-linear variation from south-east to north-west. An in-depth analysis of this pattern will be presented in Chapter 6, where interferometric observations provide a factor of ~ 10 higher resolution. The linewidth,

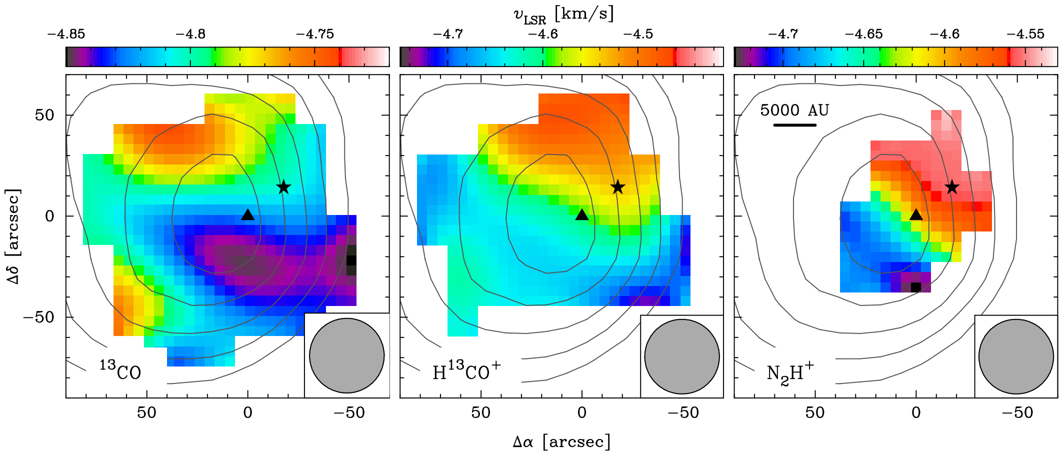

Figure 5.5.: Velocity $v_{\rm LSR}$ maps for optically thin lines ^{13}CO(2-1), H^{13}CO$^+$(1-0), and N_2H^+(1-0). The positions of CB 17-SMM1 (▲) and CB 17-IRS (★) are marked. Contours show hydrogen column densities from $\log(N_{\rm H}\,[{\rm cm}^{-2}]) = 22.5$ downwards in steps of $\Delta N_{\rm H} = 0.25$ dex.

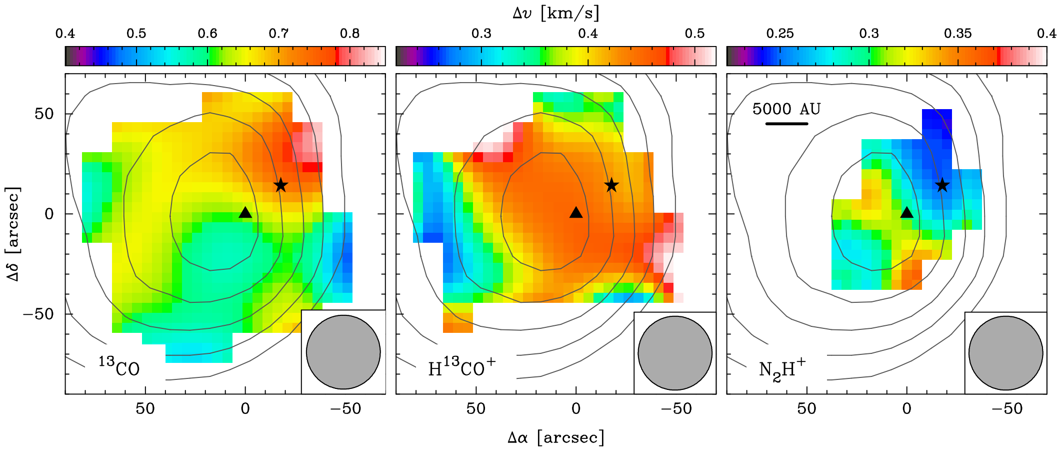

Figure 5.6.: Linewidth Δv maps for optically thin lines ^{13}CO(2-1), H^{13}CO$^+$(1-0), and N_2H^+(1-0). The positions of CB 17-SMM1 (▲) and CB 17-IRS (★) are marked. Contours show hydrogen column densities from $\log(N_{\rm H}\,[{\rm cm}^{-2}]) = 22.5$ downwards in steps of $\Delta N_{\rm H} = 0.25$ dex.

together with the size allow us to estimate the virial mass of the dense core. Following Caselli et al. (2002), this is given by

$$M_{\rm vir} = 210 \left(\frac{r}{1\,{\rm pc}}\right) \left(\frac{\Delta v_{\rm m}}{1\,{\rm km\,s^{-1}}}\right)^2 M_\odot, \tag{5.6}$$

where r is the radius. $\Delta v_{\rm m}$ is the linewidth of typical molecule of the dense core with $\mu = 2.34$ (Lada et al., 2008), which is given by

$$\Delta v_{\rm m} = \sqrt{\Delta v_{\rm T}^2 + \Delta v_{\rm NT}^2}, \tag{5.7}$$

where $v_{\mathrm{T,NT}}$ are the thermal and nonthermal linewidths, respectively. The thermal linewidth is given by

$$\Delta v_{\mathrm{T}} = \sqrt{\frac{8\ln(2)\, k_{\mathrm{B}} T}{\mu\, m_{\mathrm{H}}}}, \tag{5.8}$$

where T is the gas temperature. The nonthermal component can be derived from the observations of N_2H^+

$$\Delta v_{\mathrm{NT}} = \sqrt{\Delta v^2 - \frac{8\ln(2)\, k_{\mathrm{B}} T}{29\, m_{\mathrm{H}}}}, \tag{5.9}$$

where $\mu = 29$ is the atomic weight of the N_2H^+ molecule. Assuming $r = 4\,10^3$ AU and an average linewidth of $\Delta v = 0.3\,\mathrm{km\,s^{-1}}$ yields a virial mass of $M_{\mathrm{vir}} = 0.4\,\mathrm{M}_{\odot}$. This result differs from the finding of Caselli et al. (2002), which estimated $M_{\mathrm{vir}} = 5.7\,\mathrm{M}_{\odot}$, which was determined under the assumption of a distance of $D = 600\,\mathrm{pc}$, and a different linewidth.

In contrast to these well structured velocity gradients, the velocity field of ^{13}CO is completely different, as it cannot be described with a simple solid body rotation model. Towards the north and east the linewidths exhibit velocity maxima, whereas towards the centre there is a velocity minimum. In a large-scale ^{13}CO map with a coverage of $5' \times 5'$, Kane and Clemens (1997) saw a continuation of this velocity pattern with redshifted velocities of up to 0.7 km/s with respect to the core centre. This was interpreted as being the result of some sheering motion, implying that the low density envelope is blown away from the observer. Interestingly, the velocity shows a strong 6σ correlation with the column density, and a moderate 4σ correlation with linewidth.

It is also noteworthy that the velocities for ^{13}CO (and also C^{18}O, of which the velocity map is not shown here due to the relatively small spatial coverage) are shifted by $-0.2\,\mathrm{km\,s^{-1}}$ with respect to HCO$^+$, C^{34}S (also not shown), and N_2H^+. Therefore, one might expect relative motions of the envelope, which is traced by CO(2-1) ($n_{\mathrm{crit}} \sim 10^4\,\mathrm{cm^{-3}}$), and the core with relatively higher densities, which is traced by the other molecules with critical densities of $n_{\mathrm{crit}} \sim 10^5\,\mathrm{cm^{-3}}$. The implications of this, and possible solutions, are discussed in more detail in the subsequent section.

5.4. Discussion

5.4.1. Molecular Abundances

Carbonaceous Molecules

From our observations of optically thin and thick isotopes of CO, CS, and HCO$^+$, we are able to derive the respective molecular column densities. Figure 5.4 shows that the molecular abundance with respect to hydrogen is not constant, but strongly correlates with radius. This effect is most likely driven by freeze-out of molecules onto dust grain, and chemical reactions.

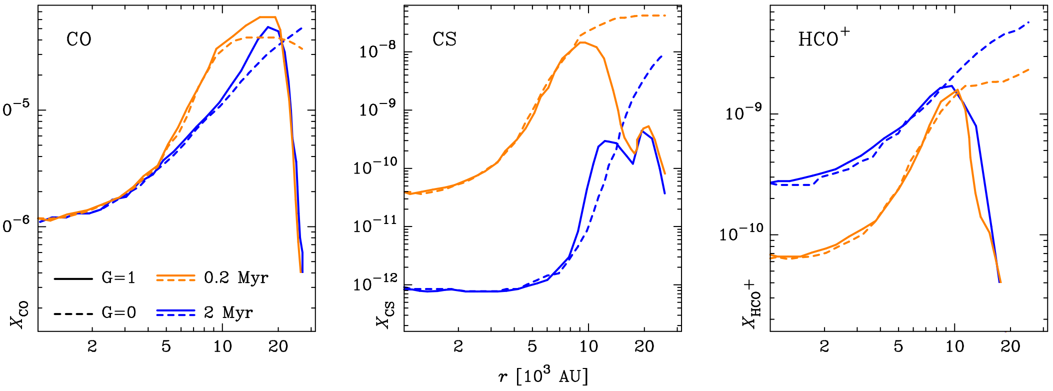

Figure 5.7.: Radial abundance profiles $X_{\mathrm{mol}}(r)$ from PWLH06 for CO, CS, HCO$^+$ in the case of strong UV field ($G = 1$), and no UV field ($G = 0$) for cores at an age of 0.2 Myr and 2 Myr.

Both of these effects are taken into account in chemical networks (Wiebe et al., 2003; Semenov et al., 2004), which were used by PWLH06 in their study of the dynamical history of CB 17. Using a radiative transfer code, these authors found best agreement of the molecular line profiles for a low UV field of $0.1G$, a sticking coefficient of $S = 0.3$, and a chemical age of 2 Myr.

We derive the best fit parameters independently by quantifying the radial dependence of the molecular freeze-out of carbonaceous molecules. As a starting point we used the radial molecular abundance profiles (Figure 5 in PWLH06)

$$X_{\mathrm{mol}}(r) = \frac{n_{\mathrm{mol}}(r)}{n_{\mathrm{H_2}}(r)}, \tag{5.10}$$

which were calculated for various ages and UV field strengths. In particular we focused on the cases of strong and no UV field ($G = 1$ and $G = 0$, respectively), and ages of $t_0 = 0.2$ Myr and $t_0 = 2$ Myr (Figure 5.7). For all models, we assumed a sticking coefficient of $S = 0.5$.

We included three different hydrogen density profiles in our analysis:

- a Gaussian profile (G0) with a width of $\Delta s_{\mathrm{n}} = 0.08$ pc and a central density of $n_{\mathrm{H,c}} = 2.2\,10^5$ cm^{-3},
- a power law profile (P0) with $n_{\mathrm{H,c}} = 3.6\,10^5$ cm^{-3}, $r_0 = 0.02$ pc, and fixed slope of $\alpha = 2.0$,
- and a power law profile from PWLH06 (PP), which is parametrised by $n_{\mathrm{H,c}} = 1.1\,10^6$ cm^{-3}, $r_0 = 0.016$ pc, and a slope $\alpha = 2.2$.

The molecular radial densities $n_{\mathrm{mol}}(r)$ were calculated, which was then converted into the observable molecular column density $N_{\mathrm{mol}}(r)$ and normalised by the hydrogen column density $N_{\mathrm{H}}(r)$. To convert the abundances of CO, CS and HCO$^+$ from PWLH06 into the abundances for the isotopic molecules, we used standard conversion factors of CO/^{13}CO=HCO$^+$/H^{13}CO$^+$=60 (Schöier et al., 2002), CO/C^{18}O=560, and CS/C^{34}S=22 (Wilson and Rood, 1994).

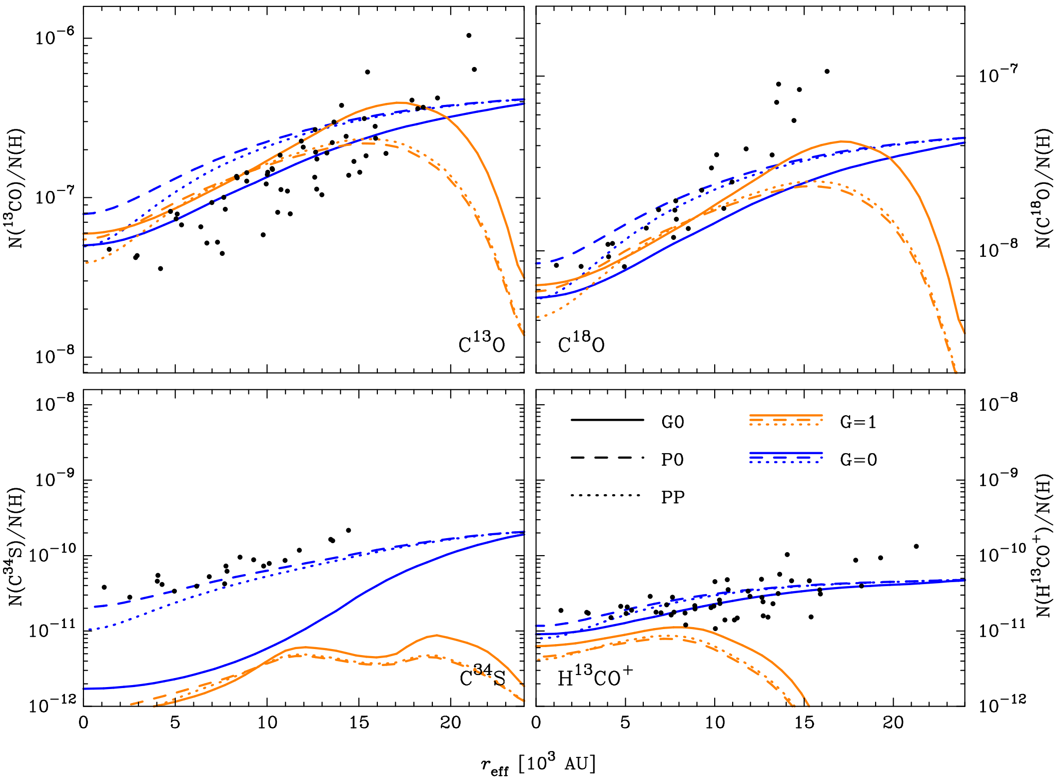

Figure 5.8.: Column density ratios in comparison with the models of PWLH06 with sticking coefficient $S = 0.5$ and evolutionary time $t_0 = 2$ Myr for different UV field strength $G = 1$ (orange) and $G = 0$ (blue). The theoretical curves are calculated for the Gaussian (G0, solid line) and power law (P0, dashed line) density distributions from this work (Chapter 4), and the power law distribution from PWLH06 (PP, dotted line).

From the derived fractional abundances of H^{13}CO$^+$ and C^{34}S, we can obtain good constraints the UV field (Figure 5.8). Both of these molecules are easily destroyed in the envelope in the presence of UV radiation, whereas they can persists towards the centre, which is shielded from the interstellar radiation field (Figure 5.7). High fractional abundances even at large radii therefore contradict the presence of a strong UV field. A constraint on the age is given by CS, which shows a gradual freeze-out with time (Figure 5.9). The relatively low fractional abundance therefore suggests an age of 2 Myr. Furthermore, CS also allows to draw conclusions about the shape of the density distribution. Power law profiles exhibit relatively strong line wings with respect to Gaussian density distributions, where most material is found relatively close to the centre. As the molecular abundance $X_{\rm CS}$ in the case of $t_0 = 2$ Myr, and $G = 0$ steeply drops by almost four orders of magnitudes from $X_{\rm CS} \sim 10^{-8}$ at $r = 2\,10^4$ AU to $X_{\rm CS} \sim 10^{-12}$ at $r = 10^4$ AU, most of the CS in the case of a Gaussian line profile is predicted to be frozen out, whereas in the case of a Power law profile a considerable amount can persist in the envelope. This explains the strong deviation for the predicted fractional abundances of CS in Figures 5.8 and 5.9, and leads to the conclusion that the density profile cannot be assumed to be a Gaussian.

The CO data, in contrast to CS and HCO$^+$, does not strongly constrain one or the other

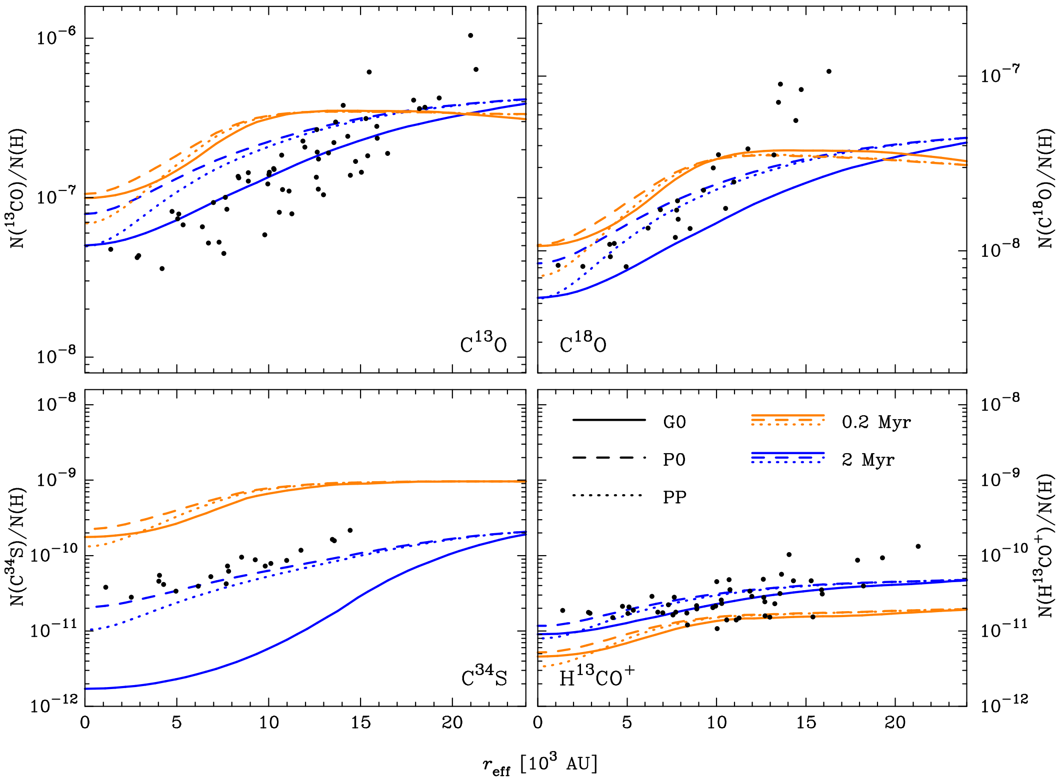

Figure 5.9.: Column density ratios in comparison with the models of PWLH06 with sticking coefficient $S = 0.5$ and UV field strength $G = 0.0$ at evolutionary times $t_0 = 0.2\,\mathrm{Myr}$ (orange) and $t_0 = 2\,\mathrm{Myr}$ (blue). The theoretical curves are calculated for the Gaussian (G0, solid line) and power law (P0, dashed line) density distributions from this work (Chapter 4), and the power law distribution from PWLH06 (PP, dotted line).

models. This is on one hand caused by the fact, that CO quickly freezes out, and is in addition hardly influenced by the UV radiation at $r < 2\,10^4$ AU, which is the maximum size of our map. Furthermore, due to the presence of a second source (CB 17-IRS), our assumption of spherical symmetry breaks down, and prevents an accurate determination of the true abundance.

Diazenulium

In the previous section, we discussed the molecular abundance of the carbonaceous molecules. In this section we focus on the abundance of diazenulium, N_2H^+, the only nitrogen bearing molecule in our dataset. It is known to be a good tracer for the densest and coldest parts of a molecular cloud, as it can only exist in the absence of carbonaceous species. Therefore, it is surprising to see a clear, distinct offset of the N_2H^+ column density peak relative to the centre of the hydrogen column density. Bergin et al. (2002) found a similar offset in B 68, and Friesen et al. (2010) for some cores in ρOph, which was in both cases interpreted it with freeze-out of even N_2H^+.

Another possibility for the observed offset between the hydrogen and N_2H^+ column density peak could be the fact, that N_2H^+ is a so-called *late-type molecule*, i.e., it needs considerable time to form (Bergin et al., 1995). If the dense and cold core towards the column density peak only formed recently, CO could already be frozen out due to its relatively quick freeze-out time (Figure 5.7), but N_2H^+ would still need time to form.

More light on the true structure of CB 17 could be shed by observations of H_2D^+, which is known to remain in the gas phase even in the most extreme environments. This molecule was first observed in L 1544 by Caselli et al. (2003), and Vastel et al. (2006) found a strong anticorrelation between the abundance of H_2D^+ and the CO depletion factor. With the fact that H_2D^+ can only be present in the densest and coldest parts, without the possibility of freeze-out, its observations would then allow us to find the "true" dense core in CB 17, as the data at hand are inconclusive.

5.4.2. Velocity Structure

In §5.3, we presented maps of the velocity structure of CB 17. The excitation conditions, together with the expected molecular abundances allow us to trace different regions of the cloud with the aid of different molecules. ^{13}CO(2-1) and C^{18}O(2-1) with critical densities of $n_{\rm crit} \sim 9\,10^3\,{\rm cm}^{-3}$ are excellent tracers for the low to intermediate density regions. C^{34}S(2-1) and H^{13}CO$^+$(1-0) with $n_{\rm crit} > 10^5\,{\rm cm}^{-3}$ trace the velocity field of denser gas, but freeze-out towards the denser regions. The velocity structure of these regions can then be obtained by N_2H^+, which freezes out only under very extreme conditions, but we do not see any evidence for such a freeze-out to occur.

Distribution of Angular Momentum

From our observations of N_2H^+ we found a size of the dense core of FWHM $\sim 8\,10^3$ AU, and a velocity gradient of $\mathscr{G} = 2.1\,{\rm km\,s^{-1}\,pc^{-1}}$. The rotational support against gravitational collapse is $\beta = 0.06$. These findings are in good agreement with findings for other dense cores in N_2H^+ (e.g. Caselli et al., 2002; Chen et al., 2007). The specific angular momentum for the dense core is $j = 1\,10^{20}\,{\rm cm^2\,s^{-1}}$. PWLH06 find $j = 1.6\,10^{21}\,{\rm cm^2\,s^{-1}}$ for CB 17, including the envelope with radii out to $r \sim 2.5\,10^4$ AU by using optically thin and thick lines of HCO$^+$, CS and CO. These two values fit reasonably well into the distribution of specific angular momentum, which can be modelled for dense cores by the relation

$$j \propto r^{\xi}, \tag{5.11}$$

where Goodman et al. (1993) find $\xi = 1.6 \pm 0.2$, and Chen et al. (2007) find $\xi = 1.7 \pm 0.1$. Comparison of the specific angular momentum of the envelope, as derived by PWLH06, and the dense core yields $\xi \sim 1.5$, which therefore follows the evolutionary trend.

Velocity Structure

As mentioned in §5.3, we observe considerable differences in the velocity centroids $v_{\rm LSR}$ for the different molecules (Figure 5.10). Tracers for dense regions exhibit a clear trend

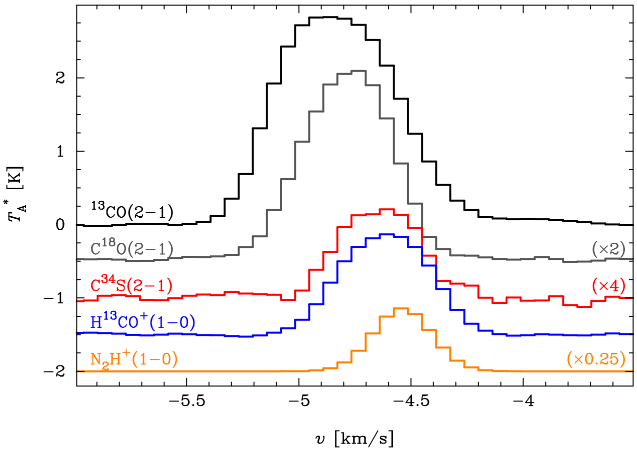

Figure 5.10.: Optically thin line spectra towards CB 17-SMM1. The N_2H^+(1-0) is an ideal representation of the best fit values v_{LSR} and Δv for the seven HFS components.

towards higher velocities. We note, that it is possible that a relative shift of the centroid velocity could be caused by the uncertainty in the rest frequency of molecules: at 100 GHz, an assumed rest frequency which is offset from the intrinsic frequency by 0.1 MHz, would cause the observed shift of ∼ 0.2 m s^{-1}. For higher frequencies the frequency offset has to be even larger to result in the observed velocity shift. However, rest frequencies (especially for optically thin lines) are accurate to a factor, which is much smaller than the observed offset.

This leads to the conclusion, that the dense core moves with respect to the less dense envelope, and exhibits a relatively redshifted velocity. On the other hand, Kane and Clemens (1997) found redshifted velocities also for the envelope, which they interpreted as the less dense envelope further outward being blown away. This apparent contradiction, that both the dense core and the envelope exhibit a relative redshift to each other, is only a contradiction at first sight, but could be a motion of the dense core inside the globule, which is simultaneously stripped off its low density envelope. This internal motion could be caused by interaction of CB 17-SMM1 with CB 17-IRS, and be part of some global rotation. However, the true nature cannot be solved with contemporary data. A NIR spectrum of the Class I source CB 17-IRS would not only reveal its true velocity, and therefore help to interpret the velocity structure. Beyond that, it could also allow to confirm or disprove its nature as a Class I source, which is by now only a tentative classification (Launhardt et al., 2010).

The cometary shape of CB 17 could be caused by HD 25347, which is a G5 III star at a distance of 210 pc (Perryman et al., 1997). It is located at a projected distance of ∼ 0.65 pc to the south (Figure 5.11). The fact that the cometary tail is not pointing towards the giant star could be caused by a relative motion of of the globule with respect to the star. A proper motion of $\mu_\alpha = 20$ mas yr^{-1} and $\mu_\delta = -31$ mas yr^{-1} was measured for HD 25347 from Hipparcos (Perryman et al., 1997), whereas the proper motion of the globule is unknown. The position of the giant star 10^4 yr into the past is indicated in Figure 5.11 by the white star symbol. Proper motion considerations, therefore, do not contradict the theory, that the cometary tail is indeed caused by HD 25347. Duflot et al. (1995) measured a radial velocity of $v_{LSR} = 15$ km s^{-1}, which conforms to a speed of 15 pc Myr^{-1}. As CB 17 exhibits a speed of $v_{LSR} \sim -4.7$ km s^{-1}, these two sources are not gravitationally bound. Therefore, they

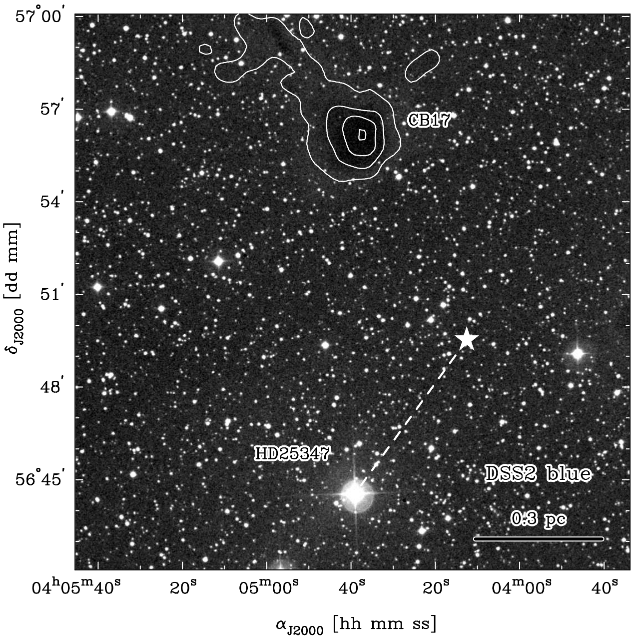

Figure 5.11.: DSS2 blue image of HD 25347 and CB 17. The contours show the NIR extinction map to highlight the cometary shape of CB 17. The dashed line indicates the proper motion of the star within the last 10^4 yr.

will be passing each other, leaving only a relatively short time for interaction.

5.5. Summary and Outlook

In this section we analysed the molecular abundances of selected molecular species with respect to the hydrogen column density derived in Chapter 4. The column density peak of N_2H^+ was found to show a small offset from the hydrogen column density peak, which is also coincident with the strongest CO freeze-out. Similar results were found by Bergin et al. (2002) in B 68, or Friesen et al. (2010) in ρOph, who interpreted this as freeze-out of N_2H^+. However, we do not see any indication, that this is also the case in CB 17. A possible solution could be, that the N_2H^+ in its nature as late-type molecule, could not yet form in all parts of CB 17. Further observations with dense gas tracers, e.g., H_2D^+, could shed more light on the true nature of the dense core. One can even speculate, that the collapse of the CB 17-SMM1 is triggered by the influence of CB 17-IRS, and CB 17 might form the simplest case of triggered star formation.

Molecular abundances for all carbonaceous species in our dataset were modelled by PWLH06. Comparison of the abundances along the line-of-sight showed good agreement for the age ($t_0 = 2\,\mathrm{Myr}$) and the UV field strength ($G = 0.1$) in their paper, which they derived by comparing line shapes and line strength. Molecular line data was only available for the central $\sim 10^4$ AU, and within this limited area, the observations of CO could not give strong arguments for one or the other models. However, CS proved to be a very good tracer for the age, and both CS and HCO^+ strongly constrained the strength of the UV field. Furthermore, the observations of CS do not support radial density profiles with a Gaussian shape, but rather indicate that the density distribution follows a power law.

From optically thin lines we were able to derive the velocity structure of CB 17. We found a significant velocity difference between CO (which traces the envelope material), and the dense gas tracers. We interpreted this as a motion of the dense core with respect to the ambient globule. From N_2H^+ observations, we found that the dense core rotates around an axis with P.A. $\sim 53^\circ$ at a rate of $2.1\,\mathrm{km\,s^{-1}\,pc^{-1}}$, whereas the envelope (which is traced by $H^{13}CO^+$) rotates around an axis with P.A. $= 82^\circ$ at a rate of $1.6\,\mathrm{km\,s^{-1}\,pc^{-1}}$. This is seen as an indicator, that the dense core is decoupled from the surrounding envelope. The specific angular momentum of the dense core was found to be $j = 10^{20}\,\mathrm{cm^2\,s^{-1}}$, which was in good agreement with theoretical predictions (e.g., Goodman et al., 1993; Chen et al., 2007). Rotational support for CB 17 is negligible, as the ratio of rotational to gravitational energy was found to be $\beta = 0.06$, which is similar to what is found for other prestellar cores at this stage (Goodman et al., 1993; Caselli et al., 2002; Chen et al., 2007).

Outlook

The key to understand the structure of CB 17 could be to find a consistent model of the complex velocity structure. The presence of the Class I source CB 17-IRS, which is known to harbour a low-velocity outflow, and the possible presence of a third source (CB 17-SMM2) add a degree of complexity to this problem, which still leaves enough space for speculations.

The analysis of CB 17, as one core of the EPoS sample, might serve as a template for the chemical analysis of other low-mass cores. Peculiar findings in the velocity structure might not be solely the case for CB 17, but might also be found in a larger sample. This could help to find a consistent model for the origin of such structures. Furthermore, the influence of multiple sources, which are embedded in the same globule, can only be further investigated by the joint analysis of other targets at similar evolutionary stages. For CB 130, we already have a similar dataset available, with a large set of optically thin and thick molecular line tracers, and FIR observations from Herschel. Analysis is performed as we speak, and will also have possible influence on the interpretation of CB 17.

6

CB 17 – Zooming into the Dense Core

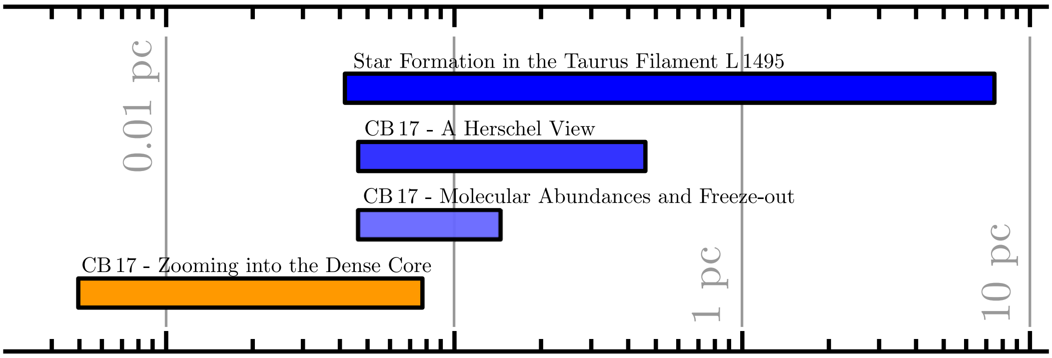

> There you are, mysterious and unknown Descartes highland plains. Apollo 16 is gonna change your image. . . . I'm sure glad they got ol' Brer Rabbit here, back in the briar patch where he belongs.
>
> — *John Young, Apollo 16, 9th man on the Moon*

OUTLINE:

The analysis of CB 17 in the previous chapters was performed at the relatively low resolution of more than half an arcminute, which inhibits an individual analysis of the two sources CB 17-SMM1 and CB 17-IRS, which are separated by only 22″. With the interferometric observations, which are introduced in §6.1 and §6.2 we achieve resolutions, which are high enough to do that. The velocity structure around the two sources is presented in §6.3. In §6.4 we discuss various hypotheses which could explain the various features we find. A summary of this chapter then follows in §6.5.

6.1. Introduction

In Chapters 4 and 5 we made an elaborate analysis of CB 17 with the aid of NIR, FIR and sub(mm), and molecular line observations. However, all these investigations focused on the large scale structure at a relatively moderate resolution of 37″, which was dictated by the Herschel SPIRE 500 μm map. We accepted the fact, that we would not be able to resolve the two sources CB 17-SMM1 and CB 17-IRS, which are only separated by only 22″. Therefore, in this last chapter we will focus on the small scale structure of CB 17 with the aid of interferometric studies at resolutions of the order of 5″.

Our tracers, namely N_2H^+(1-0), HCO^+(1-0), and CS(2-1), were selected because of their ability to trace all different regions of CB 17 – from the outer envelope with CS(2-1) and HCO^+(1-0) down to the dense core with N_2H^+(1-0). A higher resolution is obviously necessary to derive the velocity structure in and around the dense core, as from the single dish observations it is known to have a size of ∼ 40″, and is therefore barely resolved by the single dish observations from Chapter 5.

6.2. Observations and Data Reduction

In order to obtain information about the structure of the dense core and its envelope, we observed several molecular line transitions. The pointing centre for all these observations was chosen to be α_{J2000}=04:04:35.8, δ_{J2000}=56:56:03.1.

6.2.1. Formylium (HCO^+)

The HCO^+(1-0) transition line at 89.17 GHz was observed with the *Owens Valley Radio Observatory* (OVRO). In total 3.5 tracks were observed in configurations C (22 May 2000, 1 track), L (4 October 1995, 1 track) and H (14 and 24 December 1995, 1.5 tracks). The spectral band which contained the signal of the HCO^+ observations had a bandwidth of 1.5 MHz (5.0 km s^{-1}) and 71 channels with a channel width of 20 kHz (0.07 km s^{-1}) each. Calibrators were 0355+508 for the gain, and 3C27 for the bandpass. Flux calibration was performed with 0355+508 by using the flux-monitoring database[†]. The calibration of interferometric data was performed with MIRIAD.

In addition to the high resolution interferometric data, we also obtained HCO^+(1-0) single dish data with the IRAM-30m antenna, which has a resolution of 29″. A spectral map was obtained by pointed observations in a regular grid with a spacing of 7″. The single dish data reduction was performed with the CLASS, which is part of the GILDAS software package. The combination of the two datasets was done in MIRIAD, and included spectral regridding, conversion into *uv*-space, primary beam attenuation, and downsampling of the single dish data to make the two datasets compatible. A conversion factor of $S_\nu/T_{\mathrm{A}} = 6.1\,\mathrm{Jy\,K^{-1}}$ was used. Both the interferometric and the combined dataset were

---

[†] Quasars like 0355+508 were regularly flux-calibrated with the aid of planets, and the results were written into a database. This allowed then to interpolate the flux scale, which was more reliable than a single calibration measurement.

then reduced by using standard MIRIAD tasks INVERT, CLEAN and RESTOR. For the OVRO data we used a map size of twice the primary beam (FWHM = 81″), and a robust value of 2 to decrease the weight of long baselines. For the combined data, a robust value of 0.5 was used. Cleaning was performed down to 2σ in the area of the FWHM of the OVRO primary beam. The resulting image had synthesised beam sizes of $5.8'' \times 5.5''$ (OVRO) and $8.6'' \times 7.2''$ (OVRO+IRAM-30m). All images were corrected for primary beam attenuation, and regions outside the 50% level of the primary beam were masked.

6.2.2. Dyazenulium (N_2H^+)

Observations of the N_2H^+(1-0) hyperfine structure (HFS) complex at 93.171 GHz were obtained from the *Plateau de Bure Interferometer* (PdBI) on 2 and 8 April 2009 in configurations 6Cq and 6Dq, respectively. 3C84 served as bandpass and flux calibrator, whereas 0444+634 and 0355+508 served as gain calibrators. The spectrometer was setup to have a bandwidth of 20 MHz, with each of its 512 channels having a width of 39 kHz. At the frequency of the N_2H^+(1-0) transition of 93.17 GHz the bandwidth then conforms to a velocity of 64 $\mathrm{km\,s^{-1}}$ at a channel separation of 0.13 $\mathrm{km\,s^{-1}}$. Therefore, we were easily able to capture the full extent of the HFS complex, which stretches out over 15 $\mathrm{km\,s^{-1}}$.

In addition to the interferometric observations, we used single dish data to account for the missing short spacings. This data was obtained with the IRAM-30m antenna with the aid of an On-the Fly (OTF) mapping scheme on 12 July 2004. The data was remapped to match the pointing centre of the PdBI observations, and then merged. Calibration, data reduction and combination of single dish and interferometric data was all performed by using the tools CLIC and MAPPING, which are provided in the GILDAS package. The final map had a synthesised beam size of $4.5'' \times 3.7''$.

6.2.3. Carbon Monosulphide (CS)

The CS(2-1) transition line at 97.98 GHz was observed during one track with the D-configuration of the *Combined Array for Research in Millimeter-wave Astronomy* (CARMA) on 26 August 2009. The calibrators were Uranus for the flux, and 3C84 for the bandpass. As a gain calibrator we used 0359+509, which was alternately observed with CB 17 in 20 min intervals. The 3 spectral bands of the CARMA correlator were setup in two different configurations. Observations of the science target, CB 17, were made at high resolution with a bandwidth of 2 MHz, where each of its 63 channels then conformed to a width of 31 kHz. This translates to a bandwidth of 6.1 $\mathrm{km\,s^{-1}}$, and a channel separation of 0.09 $\mathrm{km\,s^{-1}}$ at the frequency of the CS(2-1) transition. To improve the signal-to-noise ratio we observed the gain calibrator in wideband mode at a bandwidth of 500 MHz. To account for the phase offset, which is caused by the change of the observational setup, the bandpass calibrator at the beginning of the observational run was observed in both configurations, which then allowed us to determine the phase offset, and transfer it correctly from the wideband gain calibrator to the narrowband observations of CB 17. All steps of the calibration and data reduction were performed by MIRIAD.

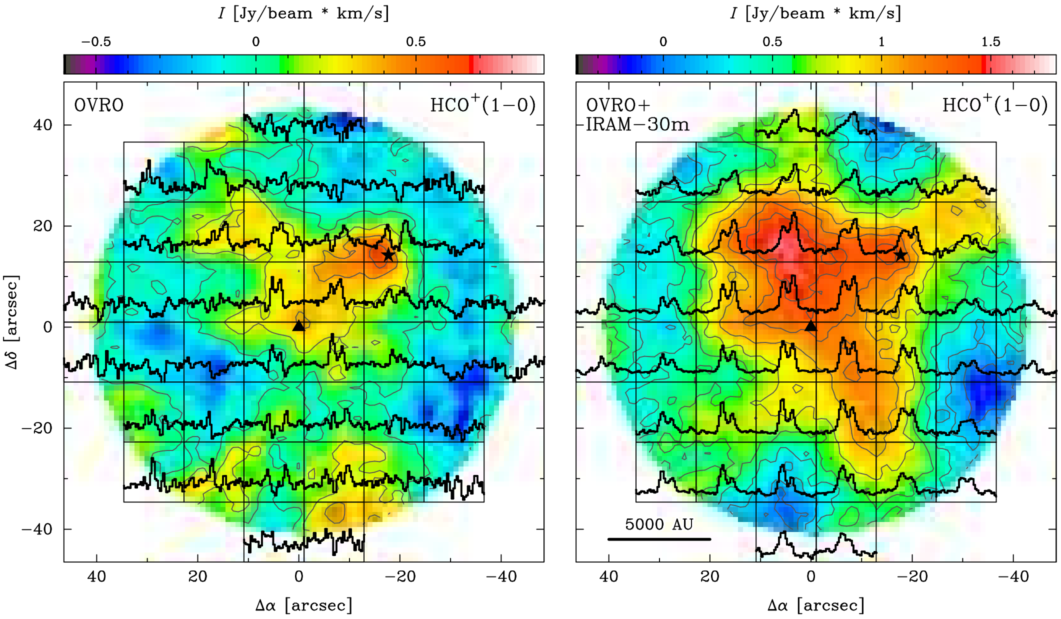

Figure 6.1.: Spectral Maps of the HCO$^+$(1-0) transition from OVRO (*left panel*) and with included short spacings from IRAM-30m telescope (*right panel*), with synthesised beam sizes of 5.8″ × 5.5″ and 7.8″ × 7.3″, which are indicated in the bottom-right corners. The spectra are plotted in the velocity range −6.0 . . . − 3.4 km/s, and the intensity range is −0.3 . . . 0.7 Jy/beam and −0.5 . . . 2.5 Jy/beam in the left and right panel, respectively. The symbols mark CB 17-SMM1 (▲) and CB 17-IRS (★). The colour-map in the background represents the primary beam corrected integrated spectral line intensity.

For the inversion from the *uv*-plane, several weighting schemes were used, and the noise limit was generally at ∼ 0.14 Jy/beam. However, the CS(2-1) line could not be detected. As the CS(2-1) is considerably strong in the single dish data, this can only be caused by a lack of small-scale structure. In §5.4 we see a strong CS freeze-out towards the centre, which could lead to a flat density profile that is resolved out by the interferometer. Therefore, we will not further include CS(2-1) it in our analysis.

6.3. Results

6.3.1. Formylium

In §5.4 we saw, that HCO$^+$(1-0) is depleted in the cold dense core, but with its critical density of 10^5 cm^{-3} is, therefore, an excellent tracer for the dense core envelope. In CB 17, it is a textbook example for what it means to resolve out the large-scale structure with interferometers. The left panel in Figure 6.1 shows a spectral map overplotted on a map of the integrated intensity of the interferometric HCO$^+$(1-0) observations. The strongest emission at the small scales is found around CB 17-IRS, whereas other parts of the map only show moderate or no emission. This picture changes drastically when inserting short spacing information in the right panel. CB 17-IRS does still exhibit a local maximum, but

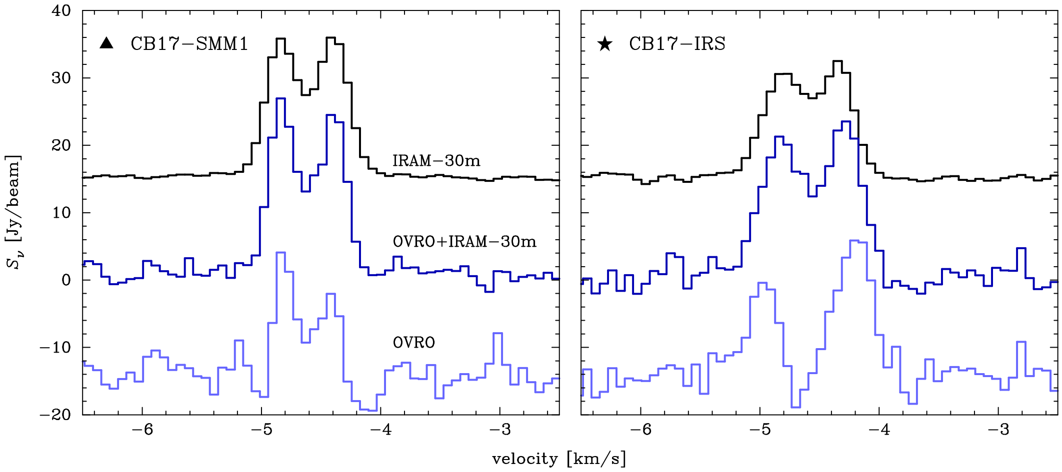

Figure 6.2.: Spectra of HCO$^+$(1-0) at the position of CB 17-SMM1 (*left panel*) and CB 17-IRS (*right panel*). The three spectra represent the observations of IRAM-30m telescope (*top*, shifted by +10 Jy/beam), and OVRO+IRAM-30m (*centre*), and OVRO (*bottom*, shifted by −10 Jy/beam). The intensity of the spectra was normalised to the beam size of the single dish data (29″).

most of the emission now comes from a region ~ 30″ to the east. Using different weighting schemes in the INVERT task, and decreasing or increasing the number of single dish points in the combined dataset, showed a gradual evolution from the interferometry-only (with basically only CB 17-IRS as a point source) to the single-dish-only picture (with its large-scale emission region).

Adding the short-spacing information, however, does not only recover more flux, but is also important when considering a more elaborate analysis by having a look at the line shape. HCO$^+$(1-0) is in general optically thick, and in the presence of excitation temperature gradients along the line-of-sight the line profile then exhibits a typical double-peaked profile with a self-absorption feature at the line centre (e.g., Pavlyuchenkov et al., 2008).

Figure 6.2 shows spectra towards CB 17-IRS and CB 17-SMM1 for single dish (top), combined (centre) and interferometric (bottom) observations. All spectra were normalised to the beam size of the single dish antenna (FWHM = 29″). The most obvious feature in the CB 17-SMM1 spectra is the absence of line wings in the OVRO spectrum, and an asymmetry of the intensities of the blue and red peak, respectively. This skewness in the profile is already greatly reduced in the combined dataset, and completely vanishes in the single dish data. Also the line wings are fully recovered in the case of included short spacings.

The change in line shape is also very prominent in the spectra towards CB 17-IRS. In the interferometric observations one can see a very strong self-absorption feature, which gets smaller and smaller with increasing sensitivity to short spacings. One should also note that in the OVRO spectrum, the intensity was dominated by the redshifted peak, whereas in the merged dataset the blue peak starts to grow in relative intensity, and more notably in width. The strong dip in the interferometer-only spectrum could be caused by self-absorption in

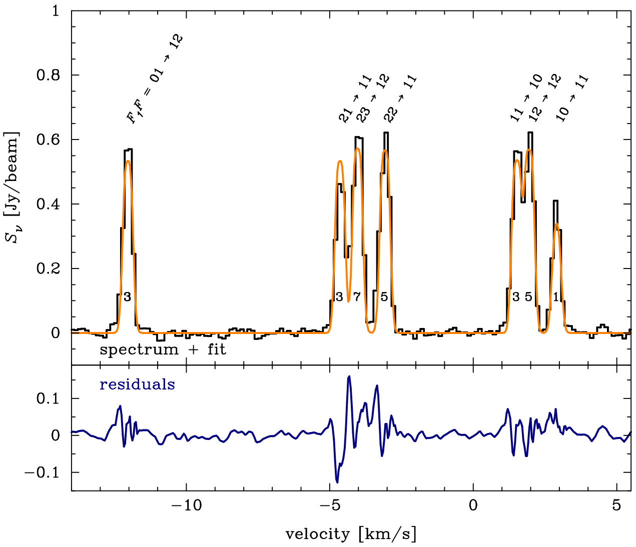

Figure 6.3.: Hyperfine structure complex of the N_2H^+(1-0) transition line towards the position of CB 17-SMM1. The yellow line indicates the best fit, which was obtained by simultaneously fitting all seven HFS line components. Each component is labelled with its quantum numbers F_1F (above), and the theoretical relative intensities (below).

the large-scale envelope, which is itself resolved out by the interferometer, and is therefore only evident in the spectra with recovered short spacings. The fact, that towards CB 17-IRS the interferometric spectrum appears to be stronger can be explained with the relatively compact nature of the emission around the Class I source, and the large single dish beam is affected by beam dilution. In CB 17-SMM1 the situation is not as evident, as the emission is rather extended.

6.3.2. Diazenulium

N_2H^+(1-0) with its hyperfine structure complex offers the big advantage of obtaining a multitude of parameters like optical depth τ or excitation temperature T_{ex} with a single observation, for which usually observations of optically thin and thick isotopes would be necessary. Furthermore, the simultaneous fit of all HFS satellites allows to determine the systemic velocity v_{LSR} and line FWHM Δv with much higher precision than for a single line, and also allows an accurate determination of the above mentioned parameters for data with moderate to low SNR.

The HFS complex was fitted with the according routine provided by CLASS, which needs the data to be present in units of antenna temperature. Therefore, we converted the data according to the Rayleigh-Jeans relation

$$S_\nu = 8.2\,10^{-3}\,\mathrm{Jy}\left(\frac{\nu}{100\,\mathrm{GHz}}\right)^2\left(\frac{\theta}{1''}\right)^2\left(\frac{T}{1\,\mathrm{K}}\right), \tag{6.1}$$

where ν is the frequency, and θ the beam FWHM. Figure 6.3 shows as an example the spectrum, the best fit and the residuals towards the position of CB 17-SMM1. One can see that the fitting routine is able to accurately reproduce the HFS line complex, although the noise gets larger at the position of the HFS satellites. The disagreement of the fit and the data can be caused by, e.g, anomalous excitation conditions (Caselli et al., 1995), but will not be discussed any further in this context, as the deviations are generally small. We only included

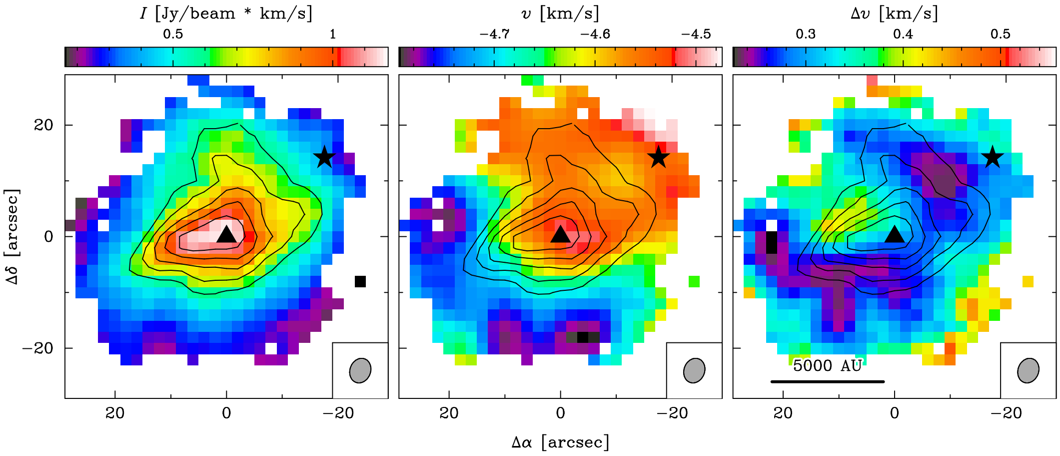

Figure 6.4.: Integrated intensity (*left panel*), velocity $v_{\rm LSR}$ (*centre panel*) and linewidth Δv (*right panel*) of N_2H^+(1-0). Contours in all three panels show the integrated intensity, and are plotted from 50% of the peak value upwards in steps of 10%. The symbols mark CB 17-SMM1 (▲) and CB 17-IRS (★). The synthesised beam with a size of $4.5'' \times 3.7''$ is indicated in the bottom-right corners.

spectra, where the isolated HFS component ($F_1F = 01 \rightarrow 12$) exhibited SNR ≥ 5. From the example spectrum one can clearly see the effect of optical depth. The small numbers on top of HFS components indicate their theoretical relative intensities in the case of optically thin lines. For optically thick lines, the line intensity is not any more proportional to the optical thickness, but converges towards the Planck function (Equation 2.16). In the case of the spectrum towards CB 17-SMM1, the total optical depth of all seven HFS is $\tau = 25$, where each of the lines contributes according to its theoretical relative intensity.

Maps of the fitted integrated line intensity I, the mean velocity $v_{\rm LSR}$ and linewidth Δv are shown in Figure 6.4. Clearly, N_2H^+(1-0) emission is only coming from CB 17-SMM1, whereas CB 17-IRS is completely devoid of it. The dense core shows a slight elongation with an aspect ratio of $R = 1.4$. The 50% intensity contour can be approximated by an ellipse of $28'' \times 23''$ at P.A. = 130° (north of east), which conforms to a size of $7.1\,10^3$ AU × $5.2\,10^3$ AU.

CB 17 exhibits a velocity gradient along the major axis of the dense core. Therefore, the rotation axis of CB 17 is perpendicular to the ellipse, which defines the 50% contour, and thus bears a position angle of P.A. = 40° (north of east). The global velocity gradient is clearly visible, but the small-scale velocity structure is quite complex, and will be discussed in more detail in §6.4. Just like the velocity profile, the line width map also reveals unexpected structure. Large parts of the dense core exhibit a relatively constant line width of the order of $\Delta v \sim 0.25$ km/s. Interestingly, from CB 17-SMM1 a cone-like region with $\Delta v \sim 0.45$ km/s emanates towards the north-east. The rise in linewidth is not spatially coincident with any features from the velocity or intensity map, and its possible origin will be discussed in the following section.

6.4. Discussion

CB 17 is one a few sources from the sample of EPoS cores, which contains two (or more) sources at different evolutionary stages. The interferometric observations of N_2H^+(1-0) and HCO^+(1-0), which were presented in §6.3, allow to further constrain this picture.

On on hand, there is CB 17-IRS, which is tentatively classified as a Class I source (Launhardt et al., 2010), which hosts a low-velocity outflow. It exhibits strong compact emission of HCO^+(1-0), and a considerably broader line, which could be caused by increased velocities in a disk around the Class I source CB 17-IRS. The fact, that these broad lines are also recovered in the small-scale interferometry map support the idea of rotational broadening.

On the other hand, CB 17-SMM1 shows a completely different morphology. Its most prominent feature is a compact N_2H^+(1-0) emission, indicative of the presence of a dense core (its virial mass was determined to be $M_{\mathrm{vir}} = 0.4\,\mathrm{M}_\odot$ in Chapter 5). There was not found evidence for a centrally embedded source, although there are some indicators of early activity, which will be discussed in this section.

Although these findings were quite clear, there remained a couple of open questions, which will be discussed in more detail in the following paragraphs.

6.4.1. Envelope Structure

Optically thick HCO^+(1-0) with its critical density of $n_c \sim 10^5\,\mathrm{cm}^{-3}$ and depletion towards the core centre is an excellent tracer to study core envelopes. Its double-peaked profile, which is caused by self-absorption along the line-of-sight, allows to draw conclusions about the velocity structure from the blue to red peak intensity asymmetry. Infall causes a stronger blue peak, whereas rotation is identified by a change in the blue to red asymmetry when analysing spectra along the plane of the rotation. Rotation and infall are revealed by a mixture of both these effects (Pavlyuchenkov et al., 2008).

Figure 6.5 shows position-velocity cuts at P.A. = $0\ldots150°$ in steps of 30°. One can see a very prominent change in the red-blue asymmetry at P.A. = 0°, and a velocity gradient of $\mathscr{G} \sim 2\,\mathrm{km\,s^{-1}\,pc^{-1}}$ along the profile cut. Towards the north, the red peak dominates, whereas in the south the spectrum is inverted. This pattern gradually changes, and completely vanishes for P.A. = 90°, where the relative intensities remain constant along the profile cut, and no obvious velocity gradient can be seen. All this is indicative of core rotation around an axis with P.A. ~ 90°. This can also be seen in the channel map in Figure 6.6, where the emission in the South appears at lower velocities, but vanishes towards higher velocities, when emission from the North is still clearly detectable. In the case of infall, the position-velocity cut at P.A. = 90°, which is thus not affected by rotational motion, should therefore exhibit a stronger blue peak. However, such a structure is not seen, and therefore infall motions in CB 17 are not evident.

To further constrain the velocity structure of CB 17, we used the `hill5` model of the analytic infall fitting routine of De Vries and Myers (2005), which models the self-absorption profile to search for infall motions. Differently a the simple two-layer model,

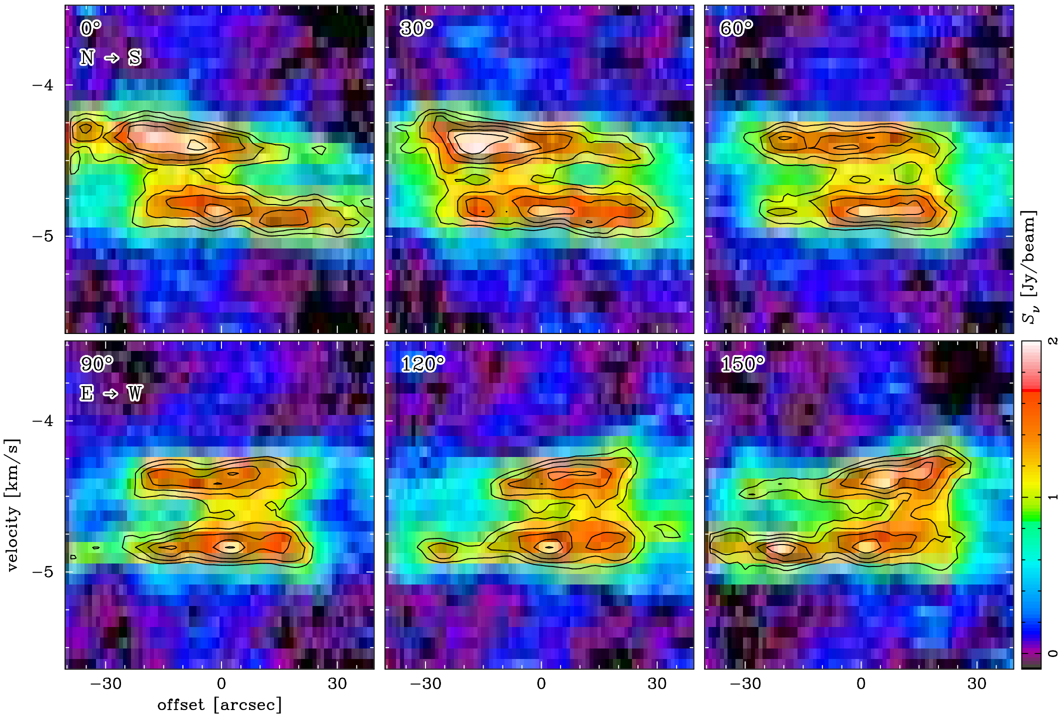

Figure 6.5.: Position-velocity diagrams at different angles (east of north) through CB 17-SMM1. Contours are plotted from 1.0 . . . 2.0 mJy/beam in steps of 0.25 mJy/beam.

where the emission is caused by a rear layer with an excitation temperature T_r and the self-absorption dip by a front layer with excitation temperature $T_\mathrm{f} < T_\mathrm{r}$, the `hill5` model assumes a linear excitation temperature gradient towards the centre. The temperature at the core boundaries is assumed to be the temperature of the cosmic microwave background $T_\mathrm{bg} = 2.7\,\mathrm{K}$. Infall occurs from both sides of the core towards the centre at a constant speed v_in.

From this model, we obtained maps of the infall velocity v_in and the systemic velocity v_LSR of CB 17. The latter one showed a clear velocity gradient along north-south direction, which was fitted by a solid body rotation model according to Kane and Clemens (1997), where the rotation at each position is determined by

$$v_\mathrm{LSR} = v_0 + g_\alpha \Delta\alpha + g_\delta \Delta\delta \tag{6.2}$$

where v_0 is the rest velocity of the globule, $g_{\alpha,\delta}$ are the right ascension and declination components of the velocity gradient, and $\Delta\alpha, \Delta\delta$ are the offsets in right ascension and declination. According to this model, CB 17 exhibits a velocity gradient of $\mathscr{G} = 1.9\,\mathrm{km\,s^{-1}\,pc^{-1}}$, and rotates around an axis with P.A. = 91° north of east. These findings confirm the qualitative finding from above. The infall velocity map, however, exhibits a similar north-south gradient with infall speeds of the order of $v_\mathrm{in} = 0.05\,\mathrm{km\,s^{-1}}$ in the south and $v_\mathrm{in} = -0.10\,\mathrm{km\,s^{-1}}$ in the north. The position-velocity cut along the rotational axis, i.e., where the influence of the rotation on the spectrum vanishes, the deduced infall velocity is small ($v_\mathrm{in} \sim 0.01\,\mathrm{km\,s^{-1}}$).

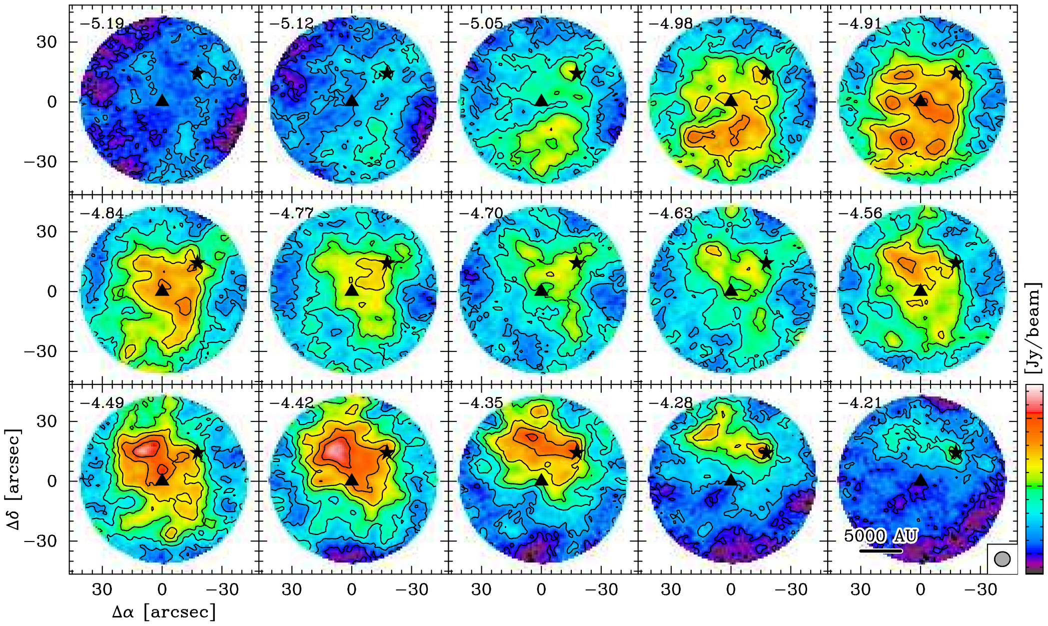

Figure 6.6.: Channel Maps of the HCO$^+$(1-0) transition. The channel velocities are indicated in the top left corner. The symbols mark CB 17-SMM1 (▲) and CB 17-IRS (★). The synthesised beam with a size of 7.8″ × 7.3″ is indicated in the bottom-right corner.

The presence of inward ($v_{\rm in} > 0$) and outward ($v_{\rm in} < 0$) motion could be indicative of a pulsation mode. Some authors claim to have found such pulsation modes in prestellar cores (e.g., Lada et al., 2003; Aguti et al., 2007), but whether this is truly the case for CB 17 remains questionable. Spectra from the south of CB 17-SMM1 exhibit blueshifted $v_{\rm LSR}$ and infall motion, whereas spectra from the north have higher $v_{\rm LSR}$ and outward motion. This direct correlation is puzzling, but can be explained by the weakness of the analytic infall model, which cannot correctly take into account rotation. In order to support this statement, one has to recall which velocity pattern cause a certain phenomenology (Pavlyuchenkov et al., 2008). Spectra towards the side of a rotating core, which moves towards the observer (for now simply called the “blue side”) exhibits the same profile shape as a static core with infall – except for a small blueshift of the whole line in the case of rotation. The `hill5` model therefore fits spectra from the blue side with a velocity shift and infall. Accordingly, the red side is modelled by “outfall” motion to account for the stronger red peak. Therefore, the analytic infall model can correctly recover the global rotation pattern, but the derived infall velocities (except for spectra along the rotational axis) are more than questionable. Therefore, we can reject the model of the globular pulsation in CB 17, and question results for other sources, in which rotation was not properly accounted for.

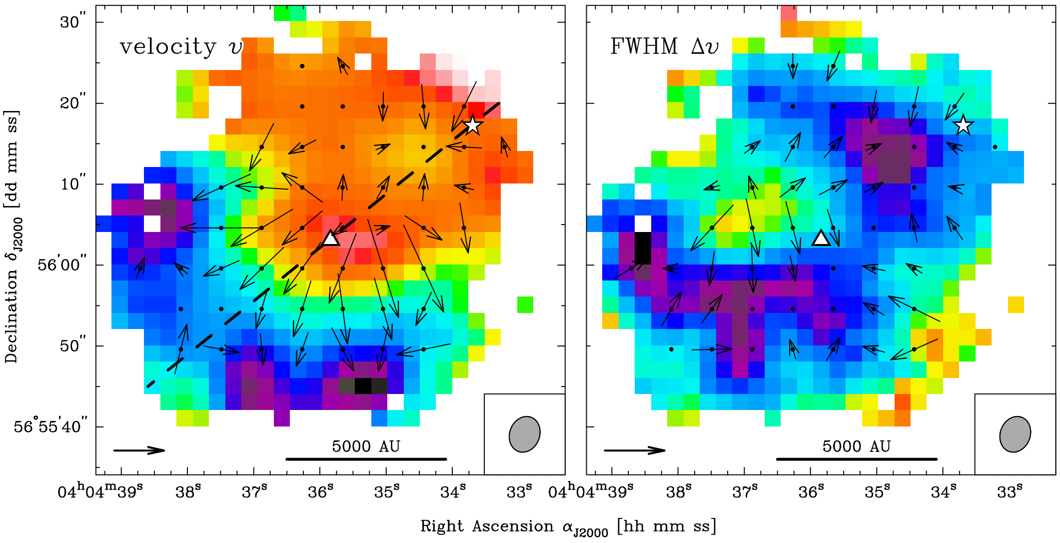

Figure 6.7.: N_2H^+(1-0) velocity v and linewidth Δv maps with overplotted local velocity and linewidth gradients, respectively. The length of the arrows in the bottom left corners conforms to gradients of 5 km s^{-1} pc^{-1} (velocity) and 0.05 km $s^{-1}/10^3$AU (linewidth). The dashed line in the left panel indicates the profile cut, which is shown in Figure 6.8.

6.4.2. Structure of the Dense Core

HCO^+ is an excellent tracer to study the kinematics in the core envelope, but in the cold and dense core centre is is depleted. On the other hand, nitrogen-bearing molecules like N_2H^+ can remain in the gas phase, even in this extreme environment, and therefore serve as better tracer to study the structure in the core centres.

Despite its simple structure in the integrated intensity map, the velocity and linewidth of N_2H^+(1-0) reveal an unexpected level of complexity (Figure 6.4). This is made particularly clear by maps of the local velocity and linewidth gradients (Figure 6.7), which were calculated from Equation (6.2) by taking into account all pixels within one beam size from the local reference position. It is evident, that the local velocity structure in the dense core in general cannot be explained with only global rotation. CB 17-SMM1 is found to be at a local maximum of the velocity, and exhibits particularly strong velocity gradients towards all directions of up to 15 km s^{-1} pc^{-1} over a region which corresponds to a beam size. This sinusoidal shape of the velocity field can be even more clearly see in the position velocity cut through CB 17-SMM1 and CB 17-IRS (indicated as dashed line in Figure 6.7), which are interestingly almost aligned in the plane of the global rotation (Figure 6.8).

Similarly to the velocity, also the linewidth map exhibits some prominent features. Figure 6.9 shows the linewidth vs. effective radius (assuming an aspect ratio of $R = 1.4$ and P.A. = 130°). In general, the dense core exhibits small linewidths of the order of $\Delta v = 0.25 - 0.30$ km s^{-1} at intermediate radii, and somewhat larger linewidths towards the core boundaries. The open circles depict data points, which spatially coincide with the cone-like region of elevated linewidth towards the north-east of CB 17-SMM1 (Figure 6.4). The origin of this will be discussed in more detail later. For now, we will first

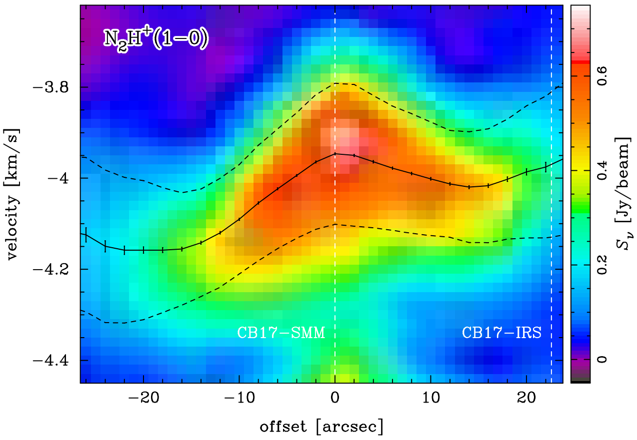

Figure 6.8.: Position-velocity cut through CB 17-SMM1 and CB 17-IRS along the dashed line in Figure 6.7 from SE to NW. The abscissa offset is measured with respect to CB 17-SMM1. The plot shows only the main component ($F_1F = 23 \rightarrow 12$) of the HFS complex, with the fitted velocity (solid line, shifted to match the HFS line) and line width (dashed line) overplotted.

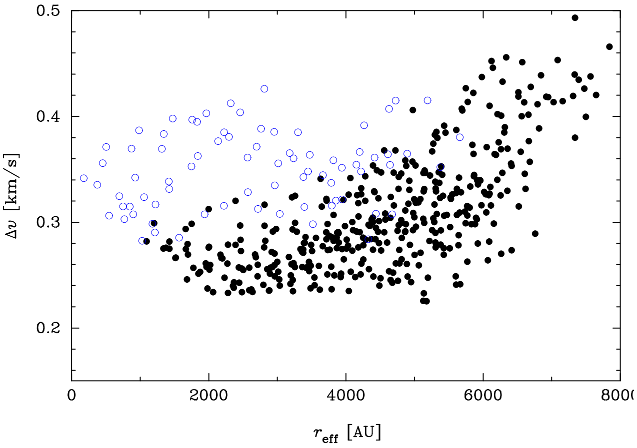

Figure 6.9.: N_2H^+(1-0) linewidth vs. effective radius. The open circles coincide spatially with the cone-like region of eleveated linewidth towards the north-east of CB 17-SMM1 (Figure 6.4).

focus on the relatively constant linewidth at intermediate distances, which could be what Barranco and Goodman (1998) and Goodman et al. (1998) called “transition to coherence”, i.e., the centres of dense cores are regions of constant linewidth. The nonthermal component of the linewidth is given by

$$\Delta v_{\rm NT} = \sqrt{\Delta v^2 - \frac{8 \ln(2)\, k_{\rm B} T}{m_{\rm H}\, \mu}}, \tag{6.3}$$

where $\mu = 29$ amu is the atomic weight of the N_2H^+ molecule, and the temperature was assumed to be 10.5 K (Chapter 4). From Equation (6.3) we calculate $\Delta v_{\rm NT} = 0.22\,{\rm km\,s^{-1}}$, which is therefore of the order of the local sound speed at this temperature, which is $c_{\rm s} \sim 0.19\,{\rm km\,s^{-1}}$ for a molecular cloud with standard composition $\mu = 2.34$ (Lada et al., 2008). However, the N_2H^+ emission is not very extended, and therefore we do not get a good coverage of the transition region from the envelope to coherence in the centre like, e.g., Pineda et al. (2010). These authors used NH_3, which is less prone to destruction by CO, and therefore allows to trace the velocity field at larger distances.

Support against gravitational collapse can be given by thermal and non-thermal processes. Thermal pressure is given by (Tafalla et al., 2004)

$$P_{\rm T} = n\, k_{\rm B}\, T, \tag{6.4}$$

where n is the gas density, k_B is the Boltzmann constant, and T the kinetic temperature. Non-thermal pressure is given by

$$P_{NT} = \mu\, m_H\, n\, \sigma_{NT}^2, \tag{6.5}$$

where $\mu = 2.34$ is again the mean molecular weight, and $\sigma_{NT} = \Delta v_{NT}/2.355$ is the non-thermal velocity dispersion. Assuming a temperature of $T = 10.5\,\mathrm{K}$ throughout the whole dense core, the ratio of non-thermal to thermal pressure is generally of the order of $P_{NT}/P_T \sim 0.3$ in the regions of low linewidth, and $P_{NT}/P_T \sim 0.8$ in the cone-like part of elevated linewidth towards the north-east of CB 17-SMM1. In general, however, non-thermal support is small, but cannot be neglected completely.

In the following, we will present different scenarios, which could explain both the velocity and linewidth morphology, and discuss their pros, the assumptions which are necessary, and the cons.

Optical Depth Effects

As mentioned earlier, the total optical depth towards CB 17-SMM1 is found to be $\tau = 25$, which is distributed among the 7 HFS components. The main component ($F_1F = 23 \rightarrow 12$) with a theoretical relative intensity of $7/27 = 0.25$ therefore exhibits an optical depth of $\tau = 6.5$, whereas the smallest component does not even reach an optical depth of unity. Therefore, in regions of high optical depths, the different HFS components trace different regions along the line of sight. Optically thick lines only observe the near side of the globule, whereas the full column density contributes to optically thin components.

To investigate the influence of optical depth effects on the velocity v_{LSR} and linewidth Δv we masked the spectra, and performed a fit of only the smallest HFS component $F_1F = 10 \rightarrow 11$. With a statistical weight of only $1/27$, this line is never optically thick in our observations. Apart from a larger noise, which is expected, the best fit results for intensity, velocity and linewidth represent exactly the findings of the HFS fit. Therefore, we reject the hypothesis, that optical depths effects play any role in the complex velocity and linewidth structure around CB 17-SMM1.

Decelerated Rotation

In the *Deceleration Scenario*, the velocity minimum between CB 17-SMM1 and CB 17-IRS is caused by the low-velocity outflow of CB 17-IRS, which was detected in CO(2-1) emission (X. Chen, private communication) at the SMA. In the left panel of Figure 6.10, the red ($v = -1 \ldots -3.7\,\mathrm{km\,s^{-1}}$) and blue lobe $v = -5.7 \ldots 8.5\,\mathrm{km\,s^{-1}}$ are overplotted on the N_2H^+(1-0) velocity map. With CB 17-IRS located *behind* the dense core, the blue outflow lobe would blow into the red side of the rotating dense core. The deceleration scenario would therefore yield a simple explanation, why there is only a small, almost circular region which exhibits lower velocity than the surrounding regions. However, it is particularly intriguing, that this velocity minimum coincides with a region of low linewidth. If the outflow causes a local deceleration of the global rotation motion, one would expect that at least some level of turbulence in the velocity field is induced, which would lead

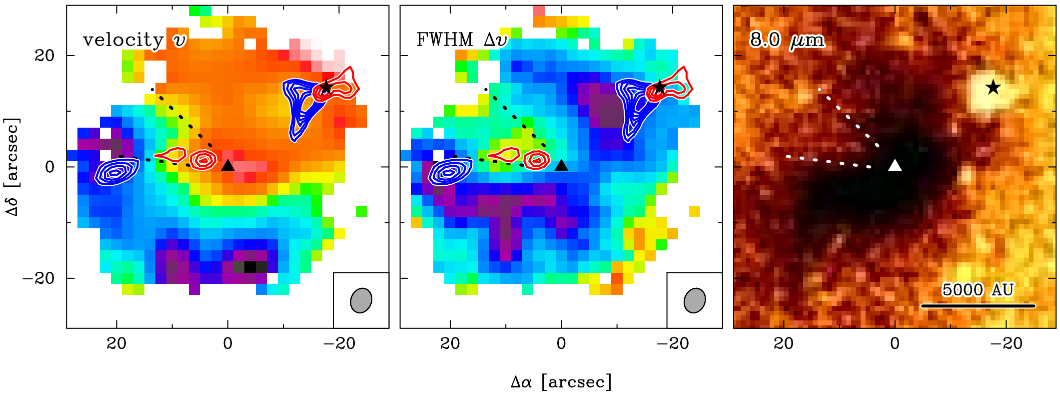

Figure 6.10.: Comparison of N_2H^+(1-0) velocity (*left panel*), linewidth (*central panel*), and Spitzer 8.0 μm. The blue and red lobe of the CO(2-1) emission (X. Chen, private comm.) are overplotted on the N_2H^+ maps from 3σ in steps of 1σ. In each panel, the cone-like region of enhanced linewidth is indicated by the dotted line.

to an increased linewidth. Assuming, that the velocity gradient of $\sim$ 10 km s^{-1} pc^{-1}, which is measured between offsets of $-20''$ and $0''$, continues towards CB 17-IRS, the outflow would have to cause a deceleration by 0.3 km s^{-1}, but leave the line width constant (Figure 6.8), which is not a reasonable assumption.

Bullet

The *Bullet Scenario* is a catchphrase, which in general describes relative bulk motions of the dense core in the centre with respect to the envelope. Hints for such a scenario were already found in Chapter 5. When the dense core traverses the envelope, the outer layers would be stripped off the core, and therefore would show systematically different velocities. This scenario is supported by the fact that the radial velocities, which are found for N_2H^+(1-0) in the dense core are by 0.15 km s^{-1} higher than for the envelope (as traced by HCO^+). CB 17-SMM1 is found at the maximum velocity, and at different impact parameters from the centre of the dense core, the velocities (traced by N_2H^+) are somewhat lower, and therefore closer to the value found in the envelope.

In this scenario, the cone-like region of elevated linewidth towards the north-east could be caused by the motion of the dense core in the plane of the sky from north-east towards south-west. As it is impossible to get hold of the proper motion, we assumed a velocity equal to the radial velocity. Then, the dense core would cover a distance of 3000 AU (which is the minimum extent of the region of elevated linewidth) in 0.1 Myr, which is shorter than the presumed lifetime of such a core. The strongest velocity gradients are found towards the “head side”, which would be expected in the bullet scenario, as the relative velocities between the ambient medium and the core are relatively high compared to the velocities, which are expected in the wake.

Further support for this theory could be given by observations with *Spitzer* (AOR: 4912384, PI: C. Lawrence). At 8.0 μm, CB 17-SMM1 shows a prominent absorption towards the dense core, apart from a region which spatially coincides with the region of elevated linewidth (right panel, Figure 6.10). In this region, the absorption is less prominent, which might indicate a cavity, which is indicated by the dotted lines, that could be caused by the dense core "ploughing" through the envelope.

The reason for such a bulk motion could be an induced motion under the influence of CB 17-IRS. However, due the unknown relative constellation, masses, and velocities of the involved objects, the hypothesis of CB 17-IRS being responsible for this, remains in the realm of speculations.

Front Side Infall - Scenario

In the *Front Side Infall Scenario*, the sinusoidal velocity variation, which is seen along the profile cut through CB 17-SMM1 (Figure 6.8), is caused by radial infall motion towards the core centre at a speed of $v_{\mathrm{in}} \sim 0.1\,\mathrm{km\,s^{-1}}$, which is superposed on a larger velocity gradient of $\mathscr{G} \sim 2\,\mathrm{km\,s^{-1}\,pc^{-1}}$.

However, infalling material from the backside would emit a blueshifted line and therefore lead to line broadening instead of a line shift. Therefore, we propose a scenario with decreased abundance of N_2H^+ at the core backside, which could be for various reasons:

- the core exhibits a cavity towards the backside,
- there is considerable destruction of N_2H^+ in that region,
- or a mixture of both.

It is known that CO is a key player in the destruction of N_2H^+, and the CB 17-IRS outflow could provide the necessary carbonaceous material for this reaction.

However, it could also be CB 17-SMM1 itself, which could have already launched its own, low-velocity outflow. Indicators for such an outflow could be a detection of a red CO lobe towards the north-east of CB 17-SMM1. Whether this outflow can also be responsible for the elevated linewidth, and the cavity towards the north-east with a length of ∼ 3000 AU remains more than questionable. Low-velocity outflows are known to already launch in such an early stage of evolution, but reach only sizes of a few hundred AU (Machida et al., 2008). Although this scenario cannot explain all observational results, the size of the tentative detection of a red outflow lobe would conform to theoretical results from simulations.

6.4.3. CB 17-SMM1 – A First Core?

A driver for such an outflow would be a so-called *first hydrostatic core* (FHSC; Larson, 1969; Boss and Yorke, 1995), which is the first, hydrostatically stable phase during the collapse phase of the molecular cloud. Due to their relatively short lifetimes of only a few 10^3 yr (Boss and Yorke, 1995), only a low number of FHSC is expected. Another limiting factor, apart from their rareness, is their small size of only a few hundred solar radii. Due to their high temperatures of $10^2 - 10^3$ K they would be easily detectable at NIR and even optical wavelengths, if not the dense envelope would absorb the emission and re-radiate it at longer wavelengths. In Chapter 4 we introduced a method to obtain the dust temperature

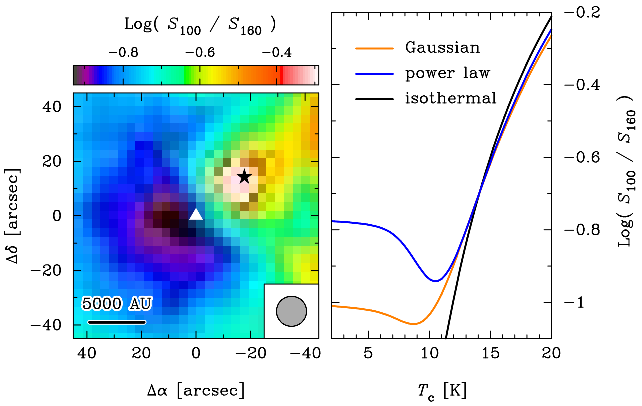

Figure 6.11.: *Left panel:* S_{100}/S_{160} flux ratio map with the positions of CB 17-IRS (★) and CB 17-SMM1 (▲). *Right panel:* Flux ratio predictions for an isothermal core (black), a Gaussian (orange) and a power-law (blue) distribution with the best fit parameters for CB 17 (Chapter 4).

by fitting spectral energy distributions around the emission peak at very low temperatures. However, we could not reveal any evidence of central heating towards the column density maximum. This could be caused by the relatively low resolution of only 36.9″ in that study, which was dictated by the map with the lowest resolution (in our case the SPIRE 500 μm map).

To get temperature estimates with higher resolution, one can calculate the flux ratios of only the maps with the highest resolutions. From flux ratios of ISO 170 μm and 200 μm images, Ward-Thompson et al. (2002) found evidence that dense cores are colder than their environment. In the case of simple isothermal structure, the flux ratios can be determined from Planck law, and reduces in the optically thin case to

$$\frac{S_{\nu_1}}{S_{\nu_2}} = \left(\frac{\kappa_{\nu_1}}{\kappa_{\nu_2}}\right)\left(\frac{\nu_1}{\nu_2}\right)^3 \frac{\exp(h\nu_2/k_B T) - 1}{\exp(h\nu_1/k_B T) - 1}. \tag{6.6}$$

Interestingly, the column density cancels out in the isothermal case. Only upon introduction of temperature gradients, the density profile does play a role.

In the left panel of Figure 6.11, the flux ratio map for PACS 100 μm and 160 μm is shown. The 100 μm map was convolved with the kernel provided by Gordon et al. (2008) to match the resolution at 160 μm. The differences between CB 17-SMM1 and CB 17-IRS are clearly visible in this map. Although the resolution in this map is higher by a factor of 3 compared to the dust emission map in Chapter 4, the influence of CB 17-IRS is still evident. In the right panel of Figure 6.11, theoretical flux ratios in dependence on the central temperatures are calculated for the different configurations, which were found in Chapter 4. These were the power law core profile ($r_0 = 0.02$ pc, $n_{H,c} = 3.6\,10^5$ cm^{-3}), and a Gaussian density profile ($\Delta s_n = 0.08$ pc, $n_{H,c} = 2.2\,10^5$ cm^{-3}). Both these models assumed Gaussian temperature profile with $\Delta s_T = 0.11$ pc, and an outside temperature of $T_{out} = 14.5$ K. Additionally, we calculated the flux ratio for an isothermal core.

The lowest flux ratios are found to be of the order of $\log(S_{100}/S_{160}) = -0.95$. This is consistent with an average line-of-sight temperature of $T_{los} = 12.5$ K. Assuming a density gradient towards the core-centre, one would find central temperatures of $T_c = 10.5$ K. All these values are consistent with the previous findings from Chapter 4, and are therefore not indicative of central heating, even at higher spatial resolution.

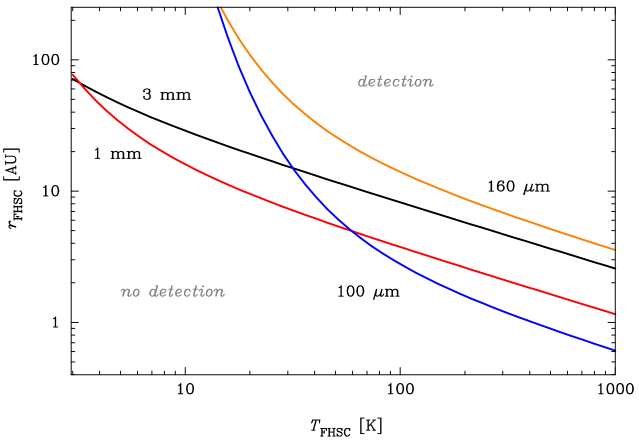

Figure 6.12.: Detection thresholds for 1 mm continuum (red), 3 mm continuum (black), 100 μm (blue) and 160 μm (orange) for different radii and temperatures of a possible first hydrostatic core.

However, the influence of CB 17-IRS might still disguise any signal from the FHSC, and from a simple model, we set upper limits to the detectability by assuming a spherical FHSC at distance D, with a radius r_{FHSC} and a constant temperature T_{FHSC}. The flux from such a source can be computed by integrating the Planck function over the source size

$$F_\nu = B_\nu(T_{\mathrm{FHSC}})\,\Omega_{\mathrm{s}} \tag{6.7}$$

$$= B_\nu(T_{\mathrm{FHSC}})\,\frac{r_{\mathrm{FHSC}}^2\pi}{D^2}. \tag{6.8}$$

At 100 μm and 160 μm we do see some non-zero, extended emission coming from the position of CB 17-SMM1, which could also be attributed to CB 17-IRS. However, we used this emission value as the detection threshold, and converted the surface brightness to flux by integrating over the respective beamsizes. Furthermore, we used the continuum data available from the OVRO and PdBI observations of $\mathrm{HCO^+}$(1-0) and $\mathrm{N_2H^+}$(1-0), respectively, and combined the tracks to obtain a 3 mm continuum map (CS observations at CARMA did not contain any wideband observations of CB 17). Analysis in the *uv*-plane did not reveal any point source, but the 3σ noise level served as the estimate of an upper limit for temperature and size of the FHSC, in order to be still not detected. From these limits we calculated the radius in dependence on the temperature of a FHSC at the respective detection thresholds with

$$r_{\mathrm{FHSC}} = D\,\sqrt{\frac{\tilde{F}_\nu}{\pi\,B_\nu(T_{\mathrm{FHSC}})}}, \tag{6.9}$$

where r_{FHSC} and T_{FHSC} are the radius and temperature of a possible FHSC, $\tilde{F}_\nu$ is the flux detection threshold, and $B_\nu(T)$ the Planck function. The detection limits are shown in Figure 6.12. The PACS 100 μm observations put the strongest constraint on a possible finding (or non-finding) of a FHSC.

Theoretical work on the formation of FHSC yields typical sizes of $r_{\mathrm{FHSC}} = 0.5\ldots2.5$ AU and temperatures of the order of $T_{\mathrm{FHSC}} \sim 10^2$ K. Therefore, we are just slightly cutting the edge of detectability, and especially the 100 μm sets a strong limit on the temperature. The possible outflow of CB 17-SMM1 appears as an almost pointlike source, which would conform to the general theory. Current outflow models predict sizes of a few 10^2 AU and velocities of the order of $2\,\mathrm{km\,s^{-1}}$.

6.5. Summary

With the aid of interferometric observations of HCO^+(1-0), N_2H^+(1-0) and CS(2-1) we analysed the kinematic structure of CB 17. CS(2-1) could not be detected, as there is apparently no small scale structure present, whereas the large-scale structure is resolved out.

From HCO^+(1-0), we could derive that the envelope rotates with a rate of $\mathscr{G} \sim 2\,\mathrm{km\,s^{-1}\,pc^{-1}}$ at a P.A. $\sim 90^\circ$. There is no evidence for strong infall motions, as from the spectra along the rotational axis (which do not exhibit any influence from the rotational pattern) we deduced $v_{\mathrm{in}} \sim 0.01\,\mathrm{km/s}$. Away from the rotational axis, line shapes indicating infall and rotation blend together, and cannot be disentangled by our analytic model.

The structure of the dense core was analysed with the aid of N_2H^+(1-0) observations. We find a global rotation pattern around an axis with P.A. $= 40^\circ$, and therefore assume that the core is decoupled from the rotation of the envelope structure. However, the small scale structure of the velocity field is rather complex, and there are many assumptions necessary to explain all the observations. The main issues – but therefore also the keys to get insight into the structure of CB 17 – are the enhanced linewidth towards the north-east (Figure 6.4), and the sinusoidal velocity pattern (Figure 6.7). We tested several hypotheses, but could not fully exclude all of them. Following the principle of Occam's razor, the *bullet scenario*, i.e., bulk motion of the dense core with respect to the surrounding envelope, seems to be the most plausible. However, we do not see the smoking gun, which would prove this theory correct.

Furthermore we investigated the presence of a first hydrostatic core. Continuum observations at 1 mm and 3 mm, and observations with Herschel at $100\,\mu$m and $160\,\mu$m did not yield a detection, but we could put upper limits on the possible temperature and size of such a first core. Comparison to theoretical models then showed us that under certain circumstances, a first core could have formed and would still be undetected.

The observations of CB 17-SMM1 gave rise to more new question, than were answered so far. Especially the observations of the dense core with N_2H^+ and its complex velocity structure do not yet form a consistent picture. One has to take into account excitation, depletion/destruction, bulk motion, and rotation, and furthermore consider the possible influence of the already evolved, nearby source CB 17-IRS.

Obviously, there are still a lot of open questions to be answered for CB 17. Observations like the ones presented in this chapter, however, help us to rephrase our questions, so that we know what we are looking for.

A

Appendices

As we leave the Moon at Taurus-Littrow, we leave as we came, and God willing, as we shall return, with peace and hope for all mankind. As I take these last steps from the surface for some time to come, I'd just like to record that America's challenge of today has forged man's destiny of tomorrow.

— *Gene Cernan, Apollo 17, Last man on the moon*

A.1. Molecular Line Parameters

Molecule	**Transition**	A_{ul} [s^{-1}]	f [GHz]	T_{u} [K]	γ_{ul} [$\mathrm{cm}^3\mathrm{s}^{-1}$]	n_{crit} [cm^{-3}]
CO	1-0	7.20E-08	115.27	5.53	2.80E-11	2.57E+03
	2-1	6.91E-07	230.54	16.60	7.00E-11	9.87E+03
	3-2	2.50E-06	345.80	33.19	8.20E-11	3.05E+04
^{13}CO	1-0	6.29E-08	110.20	5.29	2.80E-11	2.25E+03
	2-1	6.04E-07	220.40	15.87	7.00E-11	8.63E+03
	3-2	2.18E-06	330.59	31.73	8.20E-11	2.66E+04
C^{18}O	1-0	6.27E-08	109.78	5.27	2.80E-11	2.24E+03
	2-1	6.01E-07	219.56	15.81	7.00E-11	8.59E+03
	3-2	2.17E-06	329.33	31.61	8.20E-11	2.65E+04
CS	1-0	1.75E-06	48.99	2.35	3.70E-11	4.73E+04
	2-1	1.68E-05	97.98	7.05	5.30E-11	3.17E+05
	3-2	6.07E-05	146.97	14.11	4.80E-11	1.26E+06
C^{34}S	1-0	1.67E-06	48.21	2.31	3.70E-11	4.50E+04
	2-1	1.60E-05	96.41	6.94	5.30E-11	3.02E+05
	3-2	5.78E-05	144.62	13.88	4.80E-11	1.21E+06
HCO$^+$	1-0	4.25E-05	89.19	4.28	2.60E-10	1.64E+05
	2-1	4.08E-04	178.38	12.84	3.80E-10	1.07E+06
	3-2	1.48E-03	267.56	25.68	4.30E-10	3.43E+06
H^{13}CO$^+$	1-0	3.85E-05	86.75	4.16	2.60E-10	1.48E+05
	2-1	3.70E-04	173.51	12.49	3.80E-10	9.73E+05
	3-2	1.34E-03	260.26	24.98	4.30E-10	3.11E+06
N$_2$H$^+$	1-0	3.63E-05	93.17	4.47	2.60E-10	1.40E+05
	2-1	3.48E-04	186.34	13.41	3.80E-10	9.16E+05
	3-2	1.26E-03	279.51	26.83	4.30E-10	2.93E+06

Table A.2.: Einstein coefficients A_{ul}, rest frequencies f, energies of the upper level (expressed in units of temperature T_{u}), collisional coefficients γ_{ul} at $T_{\mathrm{kin}} = 10\,\mathrm{K}$, and critical densities n_{crit} for commonly used molecular species.

A.2. IRAM-30m Telescope Efficiencies

f [GHz]	θ_{FWHM} [$''$]	F_{eff} [%]	B_{eff} [%]	η_{A} [%]	S_ν/T_{A}^* [Jy/K]
86	29	95	81	63	5.9
145	16	93	74	57	6.4
210	11	94	63	49	7.5
260	9	88	53	41	8.4

Table A.4.: IRAM-30m telescope efficiencies (beam FWHM θ_{FWHM}, forward efficiency F_{eff}, beam efficiency B_{eff}, antenna efficiency η_{A}, and flux conversion factor S_ν/T_{A}^*) as measured with the new receiver system EMIR in 2009.

Bibliography

Aguti, E. D., C. J. Lada, E. A. Bergin, J. F. Alves, and M. Birkinshaw (2007, August). The Dynamical State of the Starless Dense Core FeSt 1-457: A Pulsating Globule? ApJ *665*, 457–465.

Alves, J., M. Lombardi, and C. J. Lada (2007, January). The mass function of dense molecular cores and the origin of the IMF. A&A *462*, L17–L21.

André, P., A. Men'shchikov, S. Bontemps, V. Könyves, F. Motte, N. Schneider, P. Didelon, V. Minier, P. Saraceno, D. Ward-Thompson, J. di Francesco, G. White, S. Molinari, L. Testi, A. Abergel, M. Griffin, T. Henning, P. Royer, B. Merín, R. Vavrek, M. Attard, D. Arzoumanian, C. D. Wilson, P. Ade, H. Aussel, J. Baluteau, M. Benedettini, J. Bernard, J. A. D. L. Blommaert, L. Cambrésy, P. Cox, A. di Giorgio, P. Hargrave, M. Hennemann, M. Huang, J. Kirk, O. Krause, R. Launhardt, S. Leeks, J. Le Pennec, J. Z. Li, P. G. Martin, A. Maury, G. Olofsson, A. Omont, N. Peretto, S. Pezzuto, T. Prusti, H. Roussel, D. Russeil, M. Sauvage, B. Sibthorpe, A. Sicilia-Aguilar, L. Spinoglio, C. Waelkens, A. Woodcraft, and A. Zavagno (2010, July). From filamentary clouds to prestellar cores to the stellar IMF: Initial highlights from the Herschel Gould Belt Survey. A&A *518*, L102+.

Bacmann, A., B. Lefloch, C. Ceccarelli, A. Castets, J. Steinacker, and L. Loinard (2002, July). The degree of CO depletion in pre-stellar cores. A&A *389*, L6–L10.

Barnard, E. E. (1927). *Catalogue of 349 dark objects in the sky*.

Barnard, E. E., E. B. Frost, and M. R. Calvert (1927). *A photographic atlas of selected regions of the Milky way*.

Barranco, J. A. and A. A. Goodman (1998, September). Coherent Dense Cores. I. NH 3 Observations. ApJ *504*, 207–+.

Bendo, G. J., C. D. Wilson, M. Pohlen, M. Sauvage, R. Auld, M. Baes, M. J. Barlow, J. J. Bock, A. Boselli, M. Bradford, V. Buat, N. Castro-Rodriguez, P. Chanial, S. Charlot, L. Ciesla, D. L. Clements, A. Cooray, D. Cormier, L. Cortese, J. I. Davies, E. Dwek, S. A. Eales, D. Elbaz, M. Galametz, F. Galliano, W. K. Gear, J. Glenn, H. L. Gomez, M. Griffin, S. Hony, K. G. Isaak, L. R. Levenson, N. Lu, S. Madden, B. O'Halloran, K. Okumura, S. Oliver, M. J. Page, P. Panuzzo, A. Papageorgiou, T. J. Parkin, I. Perez-Fournon, N. Rangwala, E. E. Rigby, H. Roussel, A. Rykala, N. Sacchi, B. Schulz, M. R. P. Schirm, M. W. L. Smith, L. Spinoglio, J. A. Stevens, S. Sundar, M. Symeonidis, M. Trichas, M. Vaccari, L. Vigroux, H. Wozniak, G. S. Wright, and W. W. Zeilinger (2010, July). The Herschel Space Observatory view of dust in M81. A&A *518*, L65+.

Benson, P. J., P. Caselli, and P. C. Myers (1998, October). Dense Cores in Dark Clouds. XI. A Survey for N_2Hˆ+, C_3H_2, and CCS. ApJ *506*, 743–757.

Benson, P. J. and P. C. Myers (1983, July). Dense cores in dark clouds. IV - HC5N observations. ApJ *270*, 589–604.

Bergin, E. A., J. Alves, T. Huard, and C. J. Lada (2002, May). N_2H^+ and $C^{18}O$ Depletion in a Cold Dark Cloud. ApJ *570*, L101–L104.

Bergin, E. A., D. R. Ciardi, C. J. Lada, J. Alves, and E. A. Lada (2001, August). Molecular Excitation and Differential Gas-Phase Depletions in the IC 5146 Dark Cloud. ApJ *557*, 209–225.

Bergin, E. A., W. D. Langer, and P. F. Goldsmith (1995, March). Gas-phase chemistry in dense interstellar clouds including grain surface molecular depletion and desorption. ApJ *441*, 222–243.

Bergin, E. A. and M. Tafalla (2007, September). Cold Dark Clouds: The Initial Conditions for Star Formation. ARA&A *45*, 339–396.

Bertin, E. and S. Arnouts (1996, June). SExtractor: Software for source extraction. A&AS *117*, 393–404.

Bohlin, R. C., B. D. Savage, and J. F. Drake (1978, August). A survey of interstellar H I from L-alpha absorption measurements. II. ApJ *224*, 132–142.

Bok, B. J. and E. F. Reilly (1947, March). Small Dark Nebulae. ApJ *105*, 255–+.

Boss, A. P. and H. W. Yorke (1995, February). Spectral energy of first protostellar cores: Detecting 'class -I' protostars with ISO and SIRTF. ApJ *439*, L55–L58.

Cantiello, M., J. P. Blakeslee, G. Raimondo, S. Mei, E. Brocato, and M. Capaccioli (2005, November). Detection of Radial Surface Brightness Fluctuations and Color Gradients in Elliptical Galaxies with the Advanced Camera for Surveys. ApJ *634*, 239–257.

Carroll, B. W. and D. A. Ostlie (2006, July). *An introduction to modern astrophysics and cosmology*.

Caselli, P., P. J. Benson, P. C. Myers, and M. Tafalla (2002, June). Dense Cores in Dark Clouds. XIV. N_2H^+ (1-0) Maps of Dense Cloud Cores. ApJ *572*, 238–263.

Caselli, P., P. C. Myers, and P. Thaddeus (1995, December). Radio-astronomical Spectroscopy of the Hyperfine Structure of N 2H +. ApJ *455*, L77+.

Caselli, P., F. F. S. van der Tak, C. Ceccarelli, and A. Bacmann (2003, May). Abundant H_2D^+ in the pre-stellar core L1544. A&A *403*, L37–L41.

Chen, X., H. G. Arce, Q. Zhang, T. L. Bourke, R. Launhardt, M. Schmalzl, and T. Henning (2010, June). L1448 IRS2E: A Candidate First Hydrostatic Core. ApJ *715*, 1344–1351.

Chen, X., R. Launhardt, and T. Henning (2007, November). OVRO N_2H^+ Observations of Class 0 Protostars: Constraints on the Formation of Binary Stars. ApJ *669*, 1058–1071.

Clemens, D. P. and R. Barvainis (1988, October). A catalog of small, optically selected molecular clouds - Optical, infrared, and millimeter properties. ApJS *68*, 257–286.

Dame, T. M., H. Ungerechts, R. S. Cohen, E. J. de Geus, I. A. Grenier, J. May, D. C. Murphy, L. Nyman, and P. Thaddeus (1987, November). A composite CO survey of the entire Milky Way. ApJ *322*, 706–720.

De Vries, C. H. and P. C. Myers (2005, February). Molecular Line Profile Fitting with Analytic Radiative Transfer Models. ApJ *620*, 800–815.

Dib, S., P. Hennebelle, J. E. Pineda, T. Csengeri, S. Bontemps, E. Audit, and A. A. Goodman (2010, November). The Angular Momentum of Magnetized Molecular Cloud Cores: A Two-dimensional-Three-dimensional Comparison. ApJ *723*, 425–439.

Diolaiti, E., O. Bendinelli, D. Bonaccini, L. M. Close, D. G. Currie, and G. Parmeggiani (2000, July). StarFinder: an IDL GUI-based code to analyze crowded fields with isoplanatic correcting PSF fitting. In P. L. Wizinowich (Ed.), *Society of Photo-Optical Instrumentation Engineers (SPIE) Conference Series*, Volume 4007 of *Society of Photo-Optical Instrumentation Engineers (SPIE) Conference Series*, pp. 879–888.

Dobashi, K., H. Uehara, R. Kandori, T. Sakurai, M. Kaiden, T. Umemoto, and F. Sato (2005, February). Atlas and Catalog of Dark Clouds Based on Digitized Sky Survey I. PASJ *57*, 1–+.

Draine, B. T. and H. M. Lee (1984, October). Optical properties of interstellar graphite and silicate grains. ApJ *285*, 89–108.

Duflot, M., C. Fehrenbach, C. Mannone, R. Burnage, and V. Genty (1995, April). Mesures de vitesses radiales. VII. Accompagnement AU sol DU programme d'observation DU satellite Hipparcos. Radial velocities. VII. Ground based measurements for Hipparcos. A&AS *110*, 177–+.

Enoch, M. L., J. Lee, P. Harvey, M. M. Dunham, and S. Schnee (2010, October). A Candidate Detection of the First Hydrostatic Core. ApJ *722*, L33–L38.

Evans, II, N. J. (1999). Physical Conditions in Regions of Star Formation. ARA&A *37*, 311–362.

F. van Leeuwen (Ed.) (2007). *Hipparcos, the New Reduction of the Raw Data*, Volume 350 of *Astrophysics and Space Science Library*.

Fassbender, R. (2003). Commissioning of the near IR camera OMEGA2000 and development of a pipeline reduction system.

Fiege, J. D. and R. E. Pudritz (2000a, January). Helical fields and filamentary molecular clouds - I. MNRAS *311*, 85–104.

Fiege, J. D. and R. E. Pudritz (2000b, May). Prolate Cores in Filamentary Molecular Clouds. ApJ *534*, 291–308.

Foster, J. B., C. G. Román-Zúñiga, A. A. Goodman, E. A. Lada, and J. Alves (2008, February). Hunting Galaxies to (and for) Extinction. ApJ *674*, 831–845.

Friesen, R. K., J. Di Francesco, Y. Shimajiri, and S. Takakuwa (2010, January). The Initial Conditions of Clustered Star Formation. II. N_2H^+ Observations of the Ophiuchus B Core. ApJ *708*, 1002–1024.

Fuller, G. A. and P. C. Myers (1992, January). Dense cores in dark clouds. VII - Line width-size relations. ApJ *384*, 523–527.

Goldsmith, P. F., M. Heyer, G. Narayanan, R. Snell, D. Li, and C. Brunt (2008, June). Large-Scale Structure of the Molecular Gas in Taurus Revealed by High Linear Dynamic Range Spectral Line Mapping. ApJ *680*, 428–445.

Gooch, R. (1996). Karma: a Visualization Test-Bed. In G. H. Jacoby & J. Barnes (Ed.), *Astronomical Data Analysis Software and Systems V*, Volume 101 of *Astronomical Society of the Pacific Conference Series*, pp. 80–+.

Goodman, A. A., J. A. Barranco, D. J. Wilner, and M. H. Heyer (1998, September). Coherence in Dense Cores. II. The Transition to Coherence. ApJ *504*, 223–+.

Goodman, A. A., P. J. Benson, G. A. Fuller, and P. C. Myers (1993, April). Dense cores in dark clouds. VIII - Velocity gradients. ApJ *406*, 528–547.

Goodman, A. A., J. E. Pineda, and S. L. Schnee (2009, February). The ”True” Column Density Distribution in Star-Forming Molecular Clouds. ApJ *692*, 91–103.

Gordon, K. D., C. W. Engelbracht, G. H. Rieke, K. A. Misselt, J. Smith, and R. C. Kennicutt, Jr. (2008, July). The Behavior of the Aromatic Features in M101 H II Regions: Evidence for Dust Processing. ApJ *682*, 336–354.

Gould, R. J. and E. E. Salpeter (1963, August). The Interstellar Abundance of the Hydrogen Molecule. I. Basic Processes. ApJ *138*, 393–+.

Griffin, M. J., A. Abergel, A. Abreu, P. A. R. Ade, P. André, J. Augueres, T. Babbedge, Y. Bae, T. Baillie, J. Baluteau, M. J. Barlow, G. Bendo, D. Benielli, J. J. Bock, P. Bonhomme, D. Brisbin, C. Brockley-Blatt, M. Caldwell, C. Cara, N. Castro-Rodriguez, R. Cerulli, P. Chanial, S. Chen, E. Clark, D. L. Clements, L. Clerc, J. Coker, D. Communal, L. Conversi, P. Cox, D. Crumb, C. Cunningham, F. Daly, G. R. Davis, P. de Antoni, J. Delderfield, N. Devin, A. di Giorgio, I. Didschuns, K. Dohlen, M. Donati, A. Dowell, C. D. Dowell, L. Duband, L. Dumaye, R. J. Emery, M. Ferlet, D. Ferrand, J. Fontignie, M. Fox, A. Franceschini, M. Frerking, T. Fulton, J. Garcia, R. Gastaud, W. K. Gear, J. Glenn, A. Goizel, D. K. Griffin, T. Grundy, S. Guest, L. Guillemet, P. C. Hargrave, M. Harwit, P. Hastings, E. Hatziminaoglou, M. Herman, B. Hinde, V. Hristov, M. Huang, P. Imhof, K. J. Isaak, U. Israelsson, R. J. Ivison, D. Jennings, B. Kiernan, K. J. King, A. E. Lange, W. Latter, G. Laurent, P. Laurent, S. J. Leeks, E. Lellouch, L. Levenson, B. Li, J. Li, J. Lilienthal, T. Lim, S. J. Liu, N. Lu, S. Madden, G. Mainetti, P. Marliani, D. McKay, K. Mercier, S. Molinari, H. Morris, H. Moseley, J. Mulder, M. Mur, D. A. Naylor, H. Nguyen, B. O’Halloran, S. Oliver, G. Olofsson,

H. Olofsson, R. Orfei, M. J. Page, I. Pain, P. Panuzzo, A. Papageorgiou, G. Parks, P. Parr-Burman, A. Pearce, C. Pearson, I. Pérez-Fournon, F. Pinsard, G. Pisano, J. Podosek, M. Pohlen, E. T. Polehampton, D. Pouliquen, D. Rigopoulou, D. Rizzo, I. G. Roseboom, H. Roussel, M. Rowan-Robinson, B. Rownd, P. Saraceno, M. Sauvage, R. Savage, G. Savini, E. Sawyer, C. Scharmberg, D. Schmitt, N. Schneider, B. Schulz, A. Schwartz, R. Shafer, D. L. Shupe, B. Sibthorpe, S. Sidher, A. Smith, A. J. Smith, D. Smith, L. Spencer, B. Stobie, R. Sudiwala, K. Sukhatme, C. Surace, J. A. Stevens, B. M. Swinyard, M. Trichas, T. Tourette, H. Triou, S. Tseng, C. Tucker, A. Turner, M. Vaccari, I. Valtchanov, L. Vigroux, E. Virique, G. Voellmer, H. Walker, R. Ward, T. Waskett, M. Weilert, R. Wesson, G. J. White, N. Whitehouse, C. D. Wilson, B. Winter, A. L. Woodcraft, G. S. Wright, C. K. Xu, A. Zavagno, M. Zemcov, L. Zhang, and E. Zonca (2010, July). The Herschel-SPIRE instrument and its in-flight performance. A&A *518*, L3+.

Hartley, M., S. B. Tritton, R. N. Manchester, R. M. Smith, and W. M. Goss (1986, January). A catalogue of southern dark clouds. A&AS *63*, 27–48.

Hartmann, L. (2002, October). Flows, Fragmentation, and Star Formation. I. Low-Mass Stars in Taurus. ApJ *578*, 914–924.

Heitsch, F., M. Mac Low, and R. S. Klessen (2001, January). Gravitational Collapse in Turbulent Molecular Clouds. II. Magnetohydrodynamical Turbulence. ApJ *547*, 280–291.

Henning, T., H. Linz, O. Krause, S. Ragan, H. Beuther, R. Launhardt, M. Nielbock, and T. Vasyunina (2010, July). The seeds of star formation in the filamentary infrared-dark cloud G011.11-0.12. A&A *518*, L95+.

Herschel, W. (1800, January). Investigation of the Powers of the Prismatic Colours to Heat and Illuminate Objects; With Remarks, That Prove the Different Refrangibility of Radiant Heat. To Which is Added, an Inquiry into the Method of Viewing the Sun Advantageously, with Telescopes of Large Apertures and High Magnifying Powers. *Phil. Trans. R. Soc. Lond. 90*, 255–283.

Hily-Blant, P. (2008, October). Single-dish antenna at radio wavelength. Sixth IRAM Millimeter Interferometry School.

Houghton, H. E. (1942, January). Sir William Herschel's "Hole in the Sky". *Monthly Notes of the Astronomical Society of South Africa 1*, 107–+.

Indebetouw, R., J. S. Mathis, B. L. Babler, M. R. Meade, C. Watson, B. A. Whitney, M. J. Wolff, M. G. Wolfire, M. Cohen, T. M. Bania, R. A. Benjamin, D. P. Clemens, J. M. Dickey, J. M. Jackson, H. A. Kobulnicky, A. P. Marston, E. P. Mercer, J. R. Stauffer, S. R. Stolovy, and E. Churchwell (2005, February). The Wavelength Dependence of Interstellar Extinction from 1.25 to 8.0 μm Using GLIMPSE Data. ApJ *619*, 931–938.

Inutsuka, S. and S. M. Miyama (1997, May). A Production Mechanism for Clusters of Dense Cores. ApJ *480*, 681–+.

Jijina, J., P. C. Myers, and F. C. Adams (1999, November). Dense Cores Mapped in Ammonia: A Database. ApJS *125*, 161–236.

Johnstone, D., C. D. Wilson, G. Moriarty-Schieven, G. Joncas, G. Smith, E. Gregersen, and M. Fich (2000, December). Large-Area Mapping at 850 Microns. II. Analysis of the Clump Distribution in the ρ Ophiuchi Molecular Cloud. ApJ *545*, 327–339.

Jørgensen, J. K., F. L. Schöier, and E. F. van Dishoeck (2005, May). Molecular freeze-out as a tracer of the thermal and dynamical evolution of pre- and protostellar cores. A&A *435*, 177–182.

Kainulainen, J., H. Beuther, T. Henning, and R. Plume (2009, December). Probing the evolution of molecular cloud structure. From quiescence to birth. A&A *508*, L35–L38.

Kainulainen, J., C. J. Lada, J. M. Rathborne, and J. F. Alves (2009, April). The fidelity of the core mass functions derived from dust column density data. A&A *497*, 399–407.

Kainulainen, J., K. Lehtinen, and J. Harju (2006, February). The ratio of N(C^{18}O) and A$_V$ in Chamaeleon I and III-B. Using 2MASS and SEST. A&A *447*, 597–607.

Kainulainen, J., K. Lehtinen, P. Väisänen, L. Bronfman, and J. Knude (2007, March). A comparison of density structures of a star forming and a non-star-forming globule. ¡ASTROBJ¿DCld303.8-14.2¡/ASTROBJ¿ and ¡ASTROBJ¿Thumbprint nebula¡/ASTROBJ¿. A&A *463*, 1029–1037.

Kane, B. D. and D. P. Clemens (1997, May). Rotation of Starless BOK Globules. AJ *113*, 1799–1814.

Kenyon, S. J., M. Gómez, and B. A. Whitney (2008, December). *Low Mass Star Formation in the Taurus-Auriga Clouds*, pp. 405–+.

Klessen, R. S., J. Ballesteros-Paredes, Y. Li, and M. Mac Low (2004, December). Gravoturbulent Star Cluster Formation. In H. J. G. L. M. Lamers, L. J. Smith, & A. Nota (Ed.), *The Formation and Evolution of Massive Young Star Clusters*, Volume 322 of *Astronomical Society of the Pacific Conference Series*, pp. 299–+.

Klessen, R. S., F. Heitsch, and M. Mac Low (2000, June). Gravitational Collapse in Turbulent Molecular Clouds. I. Gasdynamical Turbulence. ApJ *535*, 887–906.

Kroupa, P. (2002, January). The Initial Mass Function of Stars: Evidence for Uniformity in Variable Systems. *Science 295*, 82–91.

Lada, C. J., E. A. Bergin, J. F. Alves, and T. L. Huard (2003, March). The Dynamical State of Barnard 68: A Thermally Supported, Pulsating Dark Cloud. ApJ *586*, 286–295.

Lada, C. J. and E. A. Lada (2003). Embedded Clusters in Molecular Clouds. ARA&A *41*, 57–115.

Lada, C. J., E. A. Lada, D. P. Clemens, and J. Bally (1994, July). Dust extinction and molecular gas in the dark cloud IC 5146. ApJ *429*, 694–709.

Lada, C. J., A. A. Muench, J. Rathborne, J. F. Alves, and M. Lombardi (2008, January). The Nature of the Dense Core Population in the Pipe Nebula: Thermal Cores Under Pressure. ApJ *672*, 410–422.

Larson, R. B. (1969). Numerical calculations of the dynamics of collapsing proto-star. MNRAS *145*, 271–+.

Larson, R. B. (1981, March). Turbulence and star formation in molecular clouds. MNRAS *194*, 809–826.

Launhardt, R. and T. Henning (1997, October). Millimetre dust emission from northern BOK globules. A&A *326*, 329–346.

Launhardt, R., D. Nutter, D. Ward-Thompson, T. L. Bourke, T. Henning, T. Khanzadyan, M. Schmalzl, S. Wolf, and R. Zylka (2010, May). Looking Into the Hearts of Bok Globules: Millimeter and Submillimeter Continuum Images of Isolated Star-forming Cores. ApJS *188*, 139–177.

Lee, C. W. and P. C. Myers (1999, July). A Catalog of Optically Selected Cores. ApJS *123*, 233–250.

Lee, C. W., P. C. Myers, and M. Tafalla (1999, December). A Survey of Infall Motions toward Starless Cores. I. CS (2-1) and N_2H^+ (1-0) Observations. ApJ *526*, 788–805.

Lemme, C., T. L. Wilson, A. R. Tieftrunk, and C. Henkel (1996, August). Ammonia and $C^{18}O$ in globules. A&A *312*, 585–598.

Lindblad, P. O., K. Grape, A. Sandqvist, and J. Schober (1973, April). On the kinematics of a local component of the interstellar hydrogen gas possibly related to Gould's Belt. A&A *24*, 309–312.

Loinard, L., R. M. Torres, A. J. Mioduszewski, L. F. Rodríguez, R. A. González-Lópezlira, R. Lachaume, V. Vázquez, and E. González (2007, December). VLBA Determination of the Distance to Nearby Star-forming Regions. I. The Distance to T Tauri with 0.4% Accuracy. ApJ *671*, 546–554.

Lombardi, M. (2009, January). nicest, a near-infrared color excess method tailored to small-scale structures. A&A *493*, 735–745.

Lombardi, M. and J. Alves (2001, October). Mapping the interstellar dust with near-infrared observations: An optimized multi-band technique. A&A *377*, 1023–1034.

Lombardi, M., J. Alves, and C. J. Lada (2006, August). 2MASS wide field extinction maps. I. The Pipe nebula. A&A *454*, 781–796.

Lombardi, M., C. J. Lada, and J. Alves (2010, March). 2MASS wide field extinction maps. III. The Taurus, Perseus, and California cloud complexes. A&A *512*, A67+.

Luhman, K. L., C. Briceño, J. R. Stauffer, L. Hartmann, D. Barrado y Navascués, and N. Caldwell (2003, June). New Low-Mass Members of the Taurus Star-forming Region. ApJ *590*, 348–356.

Luhman, K. L., E. E. Mamajek, P. R. Allen, and K. L. Cruz (2009, September). An Infrared/X-Ray Survey for New Members of the Taurus Star-Forming Region. ApJ *703*, 399–419.

Lynds, B. T. (1962, May). Catalogue of Dark Nebulae. ApJS *7*, 1–+.

Machida, M. N., S. Inutsuka, and T. Matsumoto (2008, April). High- and Low-Velocity Magnetized Outflows in the Star Formation Process in a Gravitationally Collapsing Cloud. ApJ *676*, 1088–1108.

Mathis, J. S., W. Rumpl, and K. H. Nordsieck (1977, October). The size distribution of interstellar grains. ApJ *217*, 425–433.

McGlynn, T., K. Scollick, and N. White (1998). SKYVIEW:The Multi-Wavelength Sky on the Internet. In B. J. McLean, D. A. Golombek, J. J. E. Hayes, & H. E. Payne (Ed.), *New Horizons from Multi-Wavelength Sky Surveys*, Volume 179 of *IAU Symposium*, pp. 465–+.

Men'shchikov, A., P. André, P. Didelon, V. Könyves, N. Schneider, F. Motte, S. Bontemps, D. Arzoumanian, M. Attard, A. Abergel, J. Baluteau, J. Bernard, L. Cambrésy, P. Cox, J. di Francesco, A. M. di Giorgio, M. Griffin, P. Hargrave, M. Huang, J. Kirk, J. Z. Li, P. Martin, V. Minier, M. Miville-Deschênes, S. Molinari, G. Olofsson, S. Pezzuto, H. Roussel, D. Russeil, P. Saraceno, M. Sauvage, B. Sibthorpe, L. Spinoglio, L. Testi, D. Ward-Thompson, G. White, C. D. Wilson, A. Woodcraft, and A. Zavagno (2010, July). Filamentary structures and compact objects in the Aquila and Polaris clouds observed by Herschel. A&A *518*, L103+.

Mizuno, A., T. Onishi, Y. Yonekura, T. Nagahama, H. Ogawa, and Y. Fukui (1995, June). Overall distribution of dense molecular gas and star formation in the the Taurus cloud complex. ApJ *445*, L161–L165.

Molinari, S., B. Swinyard, J. Bally, M. Barlow, J. Bernard, P. Martin, T. Moore, A. Noriega-Crespo, R. Plume, L. Testi, A. Zavagno, A. Abergel, B. Ali, L. Anderson, P. André, J. Baluteau, C. Battersby, M. T. Beltrán, M. Benedettini, N. Billot, J. Blommaert, S. Bontemps, F. Boulanger, J. Brand, C. Brunt, M. Burton, L. Calzoletti, S. Carey, P. Caselli, R. Cesaroni, J. Cernicharo, S. Chakrabarti, A. Chrysostomou, M. Cohen, M. Compiegne, P. de Bernardis, G. de Gasperis, A. M. di Giorgio, D. Elia, F. Faustini, N. Flagey, Y. Fukui, G. A. Fuller, K. Ganga, P. Garcia-Lario, J. Glenn, P. F. Goldsmith, M. Griffin, M. Hoare, M. Huang, D. Ikhenaode, C. Joblin, G. Joncas, M. Juvela, J. M. Kirk, G. Lagache, J. Z. Li, T. L. Lim, S. D. Lord, M. Marengo, D. J. Marshall, S. Masi, F. Massi, M. Matsuura, V. Minier, M. Miville-Deschênes, L. A. Montier, L. Morgan, F. Motte, J. C. Mottram, T. G. Müller, P. Natoli, J. Neves, L. Olmi, R. Paladini, D. Paradis, H. Parsons, N. Peretto, M. Pestalozzi, S. Pezzuto, F. Piacentini, L. Piazzo, D. Polychroni, M. Pomarès, C. C. Popescu, W. T. Reach, I. Ristorcelli, J. Robitaille, T. Robitaille, J. A. Rodón, A. Roy, P. Royer, D. Russeil, P. Saraceno, M. Sauvage, P. Schilke, E. Schisano, N. Schneider, F. Schuller, B. Schulz, B. Sibthorpe, H. A. Smith, M. D. Smith, L. Spinoglio, D. Stamatellos, F. Strafella, G. S. Stringfellow, E. Sturm, R. Taylor, M. A. Thompson, A. Traficante, R. J. Tuffs, G. Umana, L. Valenziano,

R. Vavrek, M. Veneziani, S. Viti, C. Waelkens, D. Ward-Thompson, G. White, L. A. Wilcock, F. Wyrowski, H. W. Yorke, and Q. Zhang (2010, July). Clouds, filaments, and protostars: The Herschel Hi-GAL Milky Way. A&A *518*, L100+.

Motte, F., P. Andre, and R. Neri (1998, August). The initial conditions of star formation in the rho Ophiuchi main cloud: wide-field millimeter continuum mapping. A&A *336*, 150–172.

Myers, P. C. (1983, July). Dense cores in dark clouds. III - Subsonic turbulence. ApJ *270*, 105–118.

Myers, P. C. (2009, August). Filamentary Structure of Star-forming Complexes. ApJ *700*, 1609–1625.

Myers, P. C. and P. J. Benson (1983, March). Dense cores in dark clouds. II - NH3 observations and star formation. ApJ *266*, 309–320.

Myers, P. C., G. A. Fuller, A. A. Goodman, and P. J. Benson (1991, August). Dense cores in dark clouds. VI - Shapes. ApJ *376*, 561–572.

Myers, P. C., R. A. Linke, and P. J. Benson (1983, January). Dense cores in dark clouds. I - CO observations and column densities of high-extinction regions. ApJ *264*, 517–537.

Narayanan, G., M. H. Heyer, C. Brunt, P. F. Goldsmith, R. Snell, and D. Li (2008, July). The Five College Radio Astronomy Observatory CO Mapping Survey of the Taurus Molecular Cloud. ApJS *177*, 341–361.

Öberg, K. I., F. van Broekhuizen, H. J. Fraser, S. E. Bisschop, E. F. van Dishoeck, and S. Schlemmer (2005, March). Competition between CO and N_2 Desorption from Interstellar Ices. ApJ *621*, L33–L36.

Ochsenbein, F., P. Bauer, and J. Marcout (2000, April). The VizieR database of astronomical catalogues. A&AS *143*, 23–32.

Onishi, T., A. Mizuno, A. Kawamura, H. Ogawa, and Y. Fukui (1998, July). A C 18O Survey of Dense Cloud Cores in Taurus: Star Formation. ApJ *502*, 296–+.

Onishi, T., A. Mizuno, A. Kawamura, K. Tachihara, and Y. Fukui (2002, August). A Complete Search for Dense Cloud Cores in Taurus. ApJ *575*, 950–973.

Ossenkopf, V. and T. Henning (1994, November). Dust opacities for protostellar cores. A&A *291*, 943–959.

Ostriker, J. (1964, October). The Equilibrium of Polytropic and Isothermal Cylinders. ApJ *140*, 1056–+.

Pagani, L., J. Steinacker, A. Bacmann, A. Stutz, and T. Henning (2010, September). The Ubiquity of Micrometer-Sized Dust Grains in the Dense Interstellar Medium. *Science 329*, 1622–.

Palla, F. and S. W. Stahler (2002, December). Star Formation in Space and Time: Taurus-Auriga. ApJ *581*, 1194–1203.

Pavlyuchenkov, Y., D. Wiebe, R. Launhardt, and T. Henning (2006, July). CB 17: Inferring the Dynamical History of a Prestellar Core with Chemodynamical Models. ApJ *645*, 1212–1226.

Pavlyuchenkov, Y., D. Wiebe, B. Shustov, T. Henning, R. Launhardt, and D. Semenov (2008, December). Molecular Emission Line Formation in Prestellar Cores. ApJ *689*, 335–350.

Perryman, M. A. C., L. Lindegren, J. Kovalevsky, E. Hoeg, U. Bastian, P. L. Bernacca, M. Crézé, F. Donati, M. Grenon, F. van Leeuwen, H. van der Marel, F. Mignard, C. A. Murray, R. S. Le Poole, H. Schrijver, C. Turon, F. Arenou, M. Froeschlé, and C. S. Petersen (1997, July). The HIPPARCOS Catalogue. A&A *323*, L49–L52.

Pilbratt, G. L., J. R. Riedinger, T. Passvogel, G. Crone, D. Doyle, U. Gageur, A. M. Heras, C. Jewell, L. Metcalfe, S. Ott, and M. Schmidt (2010, July). Herschel Space Observatory. An ESA facility for far-infrared and submillimetre astronomy. A&A *518*, L1+.

Pineda, J. E., P. Caselli, and A. A. Goodman (2008, May). CO Isotopologues in the Perseus Molecular Cloud Complex: the X-factor and Regional Variations. ApJ *679*, 481–496.

Pineda, J. E., A. A. Goodman, H. G. Arce, P. Caselli, J. B. Foster, P. C. Myers, and E. W. Rosolowsky (2010, March). Direct Observation of a Sharp Transition to Coherence in Dense Cores. ApJ *712*, L116–L121.

Pineda, J. E., E. W. Rosolowsky, and A. A. Goodman (2009, July). The Perils of Clumpfind: The Mass Spectrum of Substructures in Molecular Clouds. ApJ *699*, L134–L138.

Poglitsch, A., C. Waelkens, N. Geis, H. Feuchtgruber, B. Vandenbussche, L. Rodriguez, O. Krause, E. Renotte, C. van Hoof, P. Saraceno, J. Cepa, F. Kerschbaum, P. Agnèse, B. Ali, B. Altieri, P. Andreani, J. Augueres, Z. Balog, L. Barl, O. H. Bauer, N. Belbachir, M. Benedettini, N. Billot, O. Boulade, H. Bischof, J. Blommaert, E. Callut, C. Cara, R. Cerulli, D. Cesarsky, A. Contursi, Y. Creten, W. De Meester, V. Doublier, E. Doumayrou, L. Duband, K. Exter, R. Genzel, J. Gillis, U. Grözinger, T. Henning, J. Herreros, R. Huygen, M. Inguscio, G. Jakob, C. Jamar, C. Jean, J. de Jong, R. Katterloher, C. Kiss, U. Klaas, D. Lemke, D. Lutz, S. Madden, B. Marquet, J. Martignac, A. Mazy, P. Merken, F. Montfort, L. Morbidelli, T. Müller, M. Nielbock, K. Okumura, R. Orfei, R. Ottensamer, S. Pezzuto, P. Popesso, J. Putzeys, S. Regibo, V. Reveret, P. Royer, M. Sauvage, J. Schreiber, J. Stegmaier, D. Schmitt, J. Schubert, E. Sturm, M. Thiel, G. Tofani, R. Vavrek, M. Wetzstein, E. Wieprecht, and E. Wiezorrek (2010, July). The Photodetector Array Camera and Spectrometer (PACS) on the Herschel Space Observatory. A&A *518*, L2+.

Quanz, S. P., B. Goldman, T. Henning, W. Brandner, A. Burrows, and L. W. Hofstetter (2010, January). Search for Very Low-Mass Brown Dwarfs and Free-Floating Planetary-Mass Objects in Taurus. ApJ *708*, 770–784.

Rathborne, J. M., C. J. Lada, A. A. Muench, J. F. Alves, J. Kainulainen, and M. Lombardi (2009, July). Dense Cores in The Pipe Nebula: An Improved Core Mass Function. ApJ *699*, 742–753.

Rebull, L. M., D. L. Padgett, C. McCabe, L. A. Hillenbrand, K. R. Stapelfeldt, A. Noriega-Crespo, S. J. Carey, T. Brooke, T. Huard, S. Terebey, M. Audard, J. Monin, M. Fukagawa, M. Güdel, G. R. Knapp, F. Menard, L. E. Allen, J. R. Angione, C. Baldovin-Saavedra, J. Bouvier, K. Briggs, C. Dougados, N. J. Evans, N. Flagey, S. Guieu, N. Grosso, A. M. Glauser, P. Harvey, D. Hines, W. B. Latter, S. L. Skinner, S. Strom, J. Tromp, and S. Wolf (2010, February). The Taurus Spitzer Survey: New Candidate Taurus Members Selected Using Sensitive Mid-Infrared Photometry. ApJS *186*, 259–307.

Redman, M. P., J. M. C. Rawlings, D. J. Nutter, D. Ward-Thompson, and D. A. Williams (2002, December). Molecular gas freeze-out in the pre-stellar core L1689B. MNRAS *337*, L17–L21.

Rieke, G. H. and M. J. Lebofsky (1985, January). The interstellar extinction law from 1 to 13 microns. ApJ *288*, 618–621.

Rohlfs, K. and T. L. Wilson (2004). *Tools of radio astronomy*.

Román-Zúñiga, C. G., C. J. Lada, and J. F. Alves (2009, October). High Resolution Near-Infrared Survey of the Pipe Nebula. I. A Deep Infrared Extinction Map of Barnard 59. ApJ *704*, 183–195.

Rosolowsky, E. W., J. E. Pineda, J. Kauffmann, and A. A. Goodman (2008, June). Structural Analysis of Molecular Clouds: Dendrograms. ApJ *679*, 1338–1351.

Ryden, B. S. (1996, November). The Shapes of Dense Cores and BOK Globules. ApJ *471*, 822–+.

Sadavoy, S. I., J. Di Francesco, S. Bontemps, S. T. Megeath, L. M. Rebull, E. Allgaier, S. Carey, R. Gutermuth, J. Hora, T. Huard, C. McCabe, J. Muzerolle, A. Noriega-Crespo, D. Padgett, and S. Terebey (2010, February). The Mass Distribution of Starless and Protostellar Cores in Gould Belt Clouds. ApJ *710*, 1247–1270.

Salpeter, E. E. (1955, January). The Luminosity Function and Stellar Evolution. ApJ *121*, 161–+.

Schmalzl, M., J. Kainulainen, S. P. Quanz, J. Alves, A. A. Goodman, T. Henning, R. Launhardt, J. E. Pineda, and C. G. Román-Zúñiga (2010, December). Star Formation in the Taurus Filament L 1495: From Dense Cores to Stars. ApJ *725*, 1327–1336.

Schneider, S. and B. G. Elmegreen (1979, September). A catalog of dark globular filaments. ApJS *41*, 87–95.

Schöier, F. L., J. K. Jørgensen, E. F. van Dishoeck, and G. A. Blake (2002, August). Does IRAS 16293-2422 have a hot core? Chemical inventory and abundance changes in its protostellar environment. A&A *390*, 1001–1021.

Semenov, D., D. Wiebe, and T. Henning (2004, April). Reduction of chemical networks. II. Analysis of the fractional ionisation in protoplanetary discs. A&A *417*, 93–106.

Shu, F. H. (1977, June). Self-similar collapse of isothermal spheres and star formation. ApJ *214*, 488–497.

Siess, L., E. Dufour, and M. Forestini (2000, June). An internet server for pre-main sequence tracks of low- and intermediate-mass stars. A&A *358*, 593–599.

Skrutskie, M. F., R. M. Cutri, R. Stiening, M. D. Weinberg, S. Schneider, J. M. Carpenter, C. Beichman, R. Capps, T. Chester, J. Elias, J. Huchra, J. Liebert, C. Lonsdale, D. G. Monet, S. Price, P. Seitzer, T. Jarrett, J. D. Kirkpatrick, J. E. Gizis, E. Howard, T. Evans, J. Fowler, L. Fullmer, R. Hurt, R. Light, E. L. Kopan, K. A. Marsh, H. L. McCallon, R. Tam, S. Van Dyk, and S. Wheelock (2006, February). The Two Micron All Sky Survey (2MASS). AJ *131*, 1163–1183.

Sodroski, T. J., N. Odegard, R. G. Arendt, E. Dwek, J. L. Weiland, M. G. Hauser, and T. Kelsall (1997, May). A Three-dimensional Decomposition of the Infrared Emission from Dust in the Milky Way. ApJ *480*, 173–+.

Stahler, S. W. and F. Palla (2005, January). *The Formation of Stars*.

Stamatellos, D., A. P. Whitworth, and D. Ward-Thompson (2007, August). The dust temperatures of the pre-stellar cores in the ρ Oph main cloud and in other star-forming regions: consequences for the core mass function. MNRAS *379*, 1390–1400.

Stutz, A., R. Launhardt, H. Linz, O. Krause, T. Henning, J. Kainulainen, M. Nielbock, J. Steinacker, and P. André (2010, July). Dust-temperature of an isolated star-forming cloud: Herschel observations of the Bok globule CB244. A&A *518*, L87+.

Stutzki, J., F. Bensch, A. Heithausen, V. Ossenkopf, and M. Zielinsky (1998, August). On the fractal structure of molecular clouds. A&A *336*, 697–720.

Stutzki, J. and R. Guesten (1990, June). High spatial resolution isotopic CO and CS observations of M17 SW - The clumpy structure of the molecular cloud core. ApJ *356*, 513–533.

Tafalla, M., P. C. Myers, P. Caselli, and C. M. Walmsley (2004, March). On the internal structure of starless cores. I. Physical conditions and the distribution of CO, CS, N_2H^+, and NH_3 in L1498 and L1517B. A&A *416*, 191–212.

Tafalla, M., P. C. Myers, P. Caselli, C. M. Walmsley, and C. Comito (2002, April). Systematic Molecular Differentiation in Starless Cores. ApJ *569*, 815–835.

Tan, J. C. and C. F. McKee (2008, March). Star Formation at Zero and Very Low Metallicities. In B. W. O'Shea & A. Heger (Ed.), *First Stars III*, Volume 990 of *American Institute of Physics Conference Series*, pp. 47–62.

Tassis, K., D. A. Christie, A. Urban, J. L. Pineda, T. C. Mouschovias, H. W. Yorke, and H. Martel (2010, October). Do lognormal column-density distributions in molecular clouds imply supersonic turbulence? MNRAS *408*, 1089–1094.

Terebey, S., M. Fich, A. Noriega-Crespo, D. Padgett, and Taurus Spitzer Legacy Team (2010, January). Dense Cold Cores Identified at 160 Microns in the Taurus Spitzer Legacy Survey. In *Bulletin of the American Astronomical Society*, Volume 41 of *Bulletin of the American Astronomical Society*, pp. 559–+.

Torres, R. M., L. Loinard, A. J. Mioduszewski, and L. F. Rodríguez (2007, December). VLBA Determination of the Distance to Nearby Star-forming Regions. II. Hubble 4 and HDE 283572 in Taurus. ApJ *671*, 1813–1819.

Torres, R. M., L. Loinard, A. J. Mioduszewski, and L. F. Rodríguez (2009, June). VLBA Determination of the Distance to Nearby Star-Forming Regions. III. HP TAU/G2 and the Three-Dimensional Structure of Taurus. ApJ *698*, 242–249.

Vastel, C., P. Caselli, C. Ceccarelli, T. Phillips, M. C. Wiedner, R. Peng, M. Houde, and C. Dominik (2006, July). The Distribution of Ortho-$H_2D^+(1_{1,0}$-$1_{1,1})$ in L1544: Tracing the Deuteration Factory in Prestellar Cores. ApJ *645*, 1198–1211.

Vasyunina, T., H. Linz, T. Henning, B. Stecklum, S. Klose, and L. Nyman (2009, May). Physical properties of Southern infrared dark clouds. A&A *499*, 149–161.

Ward-Thompson, D., P. André, and J. M. Kirk (2002, January). The initial conditions of isolated star formation - V. ISOPHOT imaging and the temperature and energy balance of pre-stellar cores. MNRAS *329*, 257–276.

Werner, M. W., T. L. Roellig, F. J. Low, G. H. Rieke, M. Rieke, W. F. Hoffmann, E. Young, J. R. Houck, B. Brandl, G. G. Fazio, J. L. Hora, R. D. Gehrz, G. Helou, B. T. Soifer, J. Stauffer, J. Keene, P. Eisenhardt, D. Gallagher, T. N. Gautier, W. Irace, C. R. Lawrence, L. Simmons, J. E. Van Cleve, M. Jura, E. L. Wright, and D. P. Cruikshank (2004, September). The Spitzer Space Telescope Mission. ApJS *154*, 1–9.

Wiebe, D., D. Semenov, and T. Henning (2003, February). Reduction of chemical networks. I. The case of molecular clouds. A&A *399*, 197–210.

Williams, J. P., E. J. de Geus, and L. Blitz (1994, June). Determining structure in molecular clouds. ApJ *428*, 693–712.

Wilson, T. L. and R. Rood (1994). Abundances in the Interstellar Medium. ARA&A *32*, 191–226.

Woitke, P., E. Sedlmayr, and B. Lopez (2000, June). Dust cloud formation in stellar environments. I. A radiative/thermal instability of dust forming gases. A&A *358*, 665–670.

Woodall, J., M. Agúndez, A. J. Markwick-Kemper, and T. J. Millar (2007, May). The UMIST database for astrochemistry 2006. A&A *466*, 1197–1204.